Universiteit Gent
Faculteit van de Toegepaste Wetenschappen
Vakgroep Informatietechnologie

Ontwikkeling van een MOCVD-proces op lage temperatuur voor GaInNAs materialen

Development of a low temperature MOCVD process for GaInNAs materials

---

Joff Derluyn

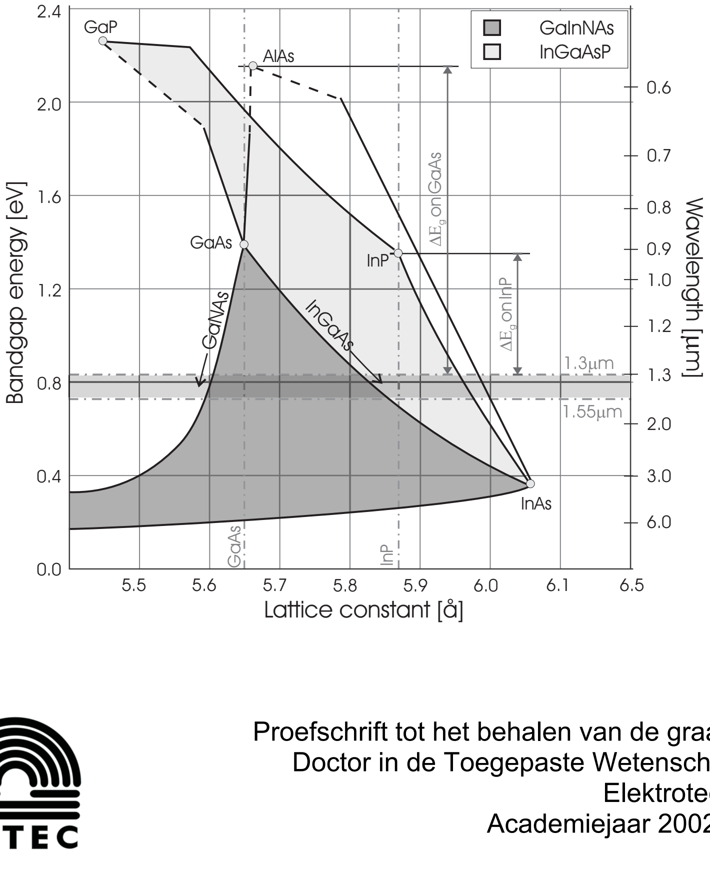

Proefschrift tot het behalen van de graad van
Doctor in de Toegepaste Wetenschappen
Elektrotechniek
Academiejaar 2002-2003

Promotor: Prof. dr. ir. Ingrid Moerman

Universiteit Gent

Faculteit van de Toegepaste Wetenschappen

Vakgroep Informatietechnologie

Sint-Pietersnieuwstraat 41
B-9000 Gent, België

Tel.: +32 (0)9 264 33 16
Fax : +32 (0)9 264 35 93

Dit werk kwam tot stand in het kader van een specialisatiebeurs, toegekend door het Instituut voor de aanmoediging van Innovatie door Wetenschap en Technologie in Vlaanderen (IWT).

DANKWOORD

Traditioneel is het dankwoord de meest gelezen passage uit een doctoraat. Er is nog meer gebruikelijk als het op het dankwoord aankomt, zoals de volgorde waarin de te bedanken personen aan bod komen. Dergelijke gewoontes zijn er natuurlijk enkel om doorbroken te worden.

Daarom: first things first. Op de eerste plaats wil ik dit dankwoord benutten om mijn diepe dankbaarheid en genegenheid uit te drukken voor Nanna, zonder wiens steun en warmte (ondanks roots in sneeuw en ijs) ik het waarschijnlijk nooit tot een dankwoord en het hierop volgende had gebracht. In dezelfde adem wil ik ook familie bedanken; mijn ouders, zus Wies met David en sinds kort Billie, en daarnaast de rest van de verdere familie.

Ex aequo op de tweede plaats wens ik nog de volgende personen binnen en buiten Intec te bedanken, te beginnen met Paul Lagasse voor het ter beschikking stellen van de infrastructuur en de mogelijkheid om een doctoraatstudie te beginnen. Ik wens Staf Borghs te bedanken die deze taak op zich nam na de verhuis. Direktere steun mocht ik ondervinden van mijn promotoren. In den beginne was er Piet Demeester, die mij in de doctoraats-“val” kon lokken en op weg zette. De hoofdbrok was voor Ingrid Moerman die de Gentse periode voor haar rekening nam en ook het uiterste deed om in woelige omstandigheden strategische beslissingen aan de man te brengen. In laatste instantie is er ook nog Maarten Leys als schaduw-promotor, gesierd door jaren groei-ervaring maar nog steeds young at heart. Bij deze ook een woord van dank voor Peter Van Daele en Roel Baets voor indirekte steun.

Ik wens uiteraard het Instituut voor de aanmoediging van Innovatie door Wetenschap en Technologie in Vlaanderen (IWT) bedanken voor de financiële steun gedurende vier jaar.

A part of this work was done in the framework of the European Commission’s IST-GIFT programme. I would like to thank all partners involved for sharing their knowledge, doing their excellent work and providing their help. Special thanks to G. Patriarche and G. Sęk for characterisation and François Alexandre for useful suggestions for improving this manuscript.

Dan, nog steeds op nummer twee, zijn er nog de mensen op wie men als doctoraatstudentje steeds kan rekenen: Luc, expert in pompen, waterkoelingen en alles daartussen om de systemen draaiende te houden; Marc voor de foto’s en gesoldeer en Eddy voor de bibliotheek. En natuurlijk de hele staff van het secretariaat (Marleen, Ilse V., Isabelle, Karien, Bernadette, Ilse M., An, Monic en Berenice), auditief steeds van ver herkenbaar, maar altijd daar voor adminstratief stunt- en vliegwerk. En uiteraard Kristien die zonder klagen alle pc-gezaag over zich liet gaan en Guy's netwerk draaiende wist te houden.

Er is in dit tweede deel nog ruimschoots plaats voor het mede-grut: een samenraapsel van groeiers, bureaugenoten, voetballers, OCS'ers en processingslui. De groeiers verdienen uiteraard een speciale vermelding, met de oude garde op kop. Ik wil expliciet papier en inkt verspillen aan stipte Mark en Modak, "mannen van de drie", Tom, Carl, Bart, Mr. Yu, Giovanni en Koen VH, "mannen van den twee", blauwe Wim "van den een", Ilse en Jan, bijna-groeiers, en Koen J., lotsgenoot en berucht koppelaar. Meer nog dan hun nuttige inbreng en suggesties koester ik hun companie en gezwans. Ook kijk ik uit naar de nieuwe garde, Yves, Kristof, Stefan, Steven en Marianne, die het vuur brandende moet houden (waarvoor de MOCVD-bronnen uitermate geschikt zijn).

Het geklooi boven bracht soms resultaat op, wat direkt werd doorgespeeld aan de goede zorgen van Steven VS, Kristien, Steven VP, Liesbet, Peter en Joël. Aan de karakterisatie-kant passeerde met de tijd een hele resem de revue: Hendrik, Charlie, Joachim en Dimitri.

Tussen dat alles in zag ik mij genoodzaakt tijd te spenderen op den buro, een oude leszaal bevolkt door een wilde variëteit persoonlijkheden, een kerstplant en rondvliegende rugbyballen. Omdat er nog steeds geheugen tussen de gaten rest (de drank? de ouderdom!) meen ik me Zahia, Marko, Mingshan, Karuna en de legendarische Ranjeman (aka Thierry) te kunnen herinneren. Verser in het geheugen liggen Günther en de Wouters. Vooral voor deze laatsten en mocht u het zelf nog niet weten: FC Lachgas rules!

Al deze mensen (en diegenen die ik ondanks intens wroeten in de grijze cellen toch vergeten ben) hebben ervoor gezorgd dat ik me al die tijd goed heb gevoeld op *'t labo*.

U was een fijn publiek.

Bedankt.

Joff

TABLE OF CONTENTS

DANKWOORD

INHOUDSTABEL

LIJST MET AFKORTINGEN

NEDERLANDSTALIGE SAMENVATTING

1. INLEIDING

2. FUNDAMENTELE EIGENSCHAPPEN VAN GAINNAS

ENGLISH TEXT

CHAPTER 1 INTRODUCTION

CHAPTER 2 PROPERTIES OF GAINNAS

CHAPTER 3 LOW TEMPERATURE GROWTH

CHAPTER 4 DEVELOPMENT OF A TBAS PROCESS

CHAPTER 5 GROWTH OF DILUTE NITRIDES

CHAPTER 6 CONCLUSIONS AND OUTLOOK

APPENDIX GROWTH CONDITIONS

1. REACTOR DESIGN
2. FIXED GROWTH PARAMETERS
3. SPECIFIC GROWTH CONDITIONS

LIST OF ABBREVIATIONS

APD	Antiphase domains
AR	Anti-reflection
BAM	Band anticrossing model
BSF	Back surface field
CB	Conduction band
CBE	Chemical beam epitaxy
DBR	Distributed Bragg reflector
DEZn	Di-ethyl-zinc
DLTS	Deep level transient spectroscopy
DMHy	Di-methyl-hydrazine
DVD	Digital versatile disk
FTIR	Fourier transform infrared spectroscopy
FWHM	Full width at half maximum
GRINSCH	Graded index separate confinement heterostructure
GSM	Global system for mobile communication
HR	High-reflectivity
IQE	Internal quantum efficiency
Laser	Light amplification by stimulated emission of radiation
LDA	Local density approximations
LE	Localised exciton
MBE	Molecular beam epitaxy
MC-LED	Micro-cavity light emitting diode
MOCVD	Metal-organic chemical vapour deposition
MOVPE	Metal-organic vapour phase epitaxy
MQW	Multiple quantum well

NRA	Nuclear reaction analysis
ODCR	Optically detected cyclotron resonance
ODMR	Optically detected magnetoresonance
PL	Photoluminescence
PLE	Photoluminescence excitation
PR	Photoreflectance
QW	Quantum well
RBS	Rutherford backscattering
RSM	Reciprocal space mapping
SCH	Separate confinement heterostructure
SIMS	Secondary ion mass spectroscopy
SQW	Single quantum well
SS-MBE	Solid source molecular beam epitaxy
STM	Scanning tunnelling microscopy
TBAs	Tertiary-butyl-arsine
TEGa	Tri-ethyl-gallium
TEM	Transmission electron microscopy
TLV	Threshold limit value
TMGa	Tri-methyl-gallium
TMIn	Tri-methyl-indium
VB	Valence band
VCSEL	Vertical cavity surface emitting laser
WDM	Wavelength division multiplexing
XRD	X-ray diffraction

NEDERLANDSTALIGE TEKST

NEDERLANDSTALIGE SAMENVATTING

Voor de consistentie is de nummering van de hoofdstukken en paragrafen overgenomen vanuit de Engelstalige tekst. Slechts een gedeelte van de figuren uit de Engelstalige tekst zijn letterlijk overgenomen. Ze worden aangeduid met een letter. Voor de overige figuren verwijzen we (via hun nummer) naar het Engelstalige gedeelte.

1. Inleiding

1.1 Een korte geschiedenis van de telecommunicatie

Doorheen de geschiedenis heeft de mens steeds gecommuniceerd. Met behulp van steeds ingenieuzere technologieën kon aan steeds zwaardere criteria worden voldaan. Als voorbeelden vernoemen we de telegraaf van Morse, de telefoon van Bell, de eerste draadloze verbindingen van Marconi en tenslotte de lancering van de Sputnik.

De rode draad doorheen deze evolutie is in eerste instantie het overbruggen van de afstand die de twee partijen scheidt. Daarnaast, onder invloed van doorbraken op andere terreinen zoals bijvoorbeeld de computertechnologie, is er ook vraag naar een steeds grotere bandbreedte, meer vertrouwelijkheid en veiligheid van berichten, het verkorten van de latentie tussen versturen en ontvangen van berichten en uiteraard naar de reductie van de kost van de communicatie.

Wanneer we nader ingaan op de eisen die we kunnen stellen aan communicatiemiddelen (zie tabel 1.1), dan stellen we vast dat de klassieke elektrische oplossingen niet meer voldoen.

1.2 Optischevezelcommunicatie

1.2.1 Totale interne reflectie

In 1870 demonstreerde John Tyndall met behulp van een lekkende emmer hoe licht het gebogen pad van het ontsnappende water volgt. De idee van totale interne reflectie is gemakkelijk te begrijpen aan de hand van de wet van

Snellius. Deze wet definieert de zogenoemde kritische hoek. Licht dat vanuit een medium met bepaalde brekingsindex onder een hoek groter dan de kritische hoek invalt op de scheiding met een tweede medium met lagere brekingsindex zal niet in het tweede medium propageren, maar totaal intern gereflecteerd worden zonder vermogensverlies.

Dit principe wordt toegepast in de optische vezel. Hier omvat een keerlaag met lage brekingsindex een cilindrische kernlaag met hogere brekinsgindex. Wanneer we licht onder een gunstige hoek kunnen inkoppelen in de kernlaag zal het door totale interne reflectie doorheen de optische vezel geleid worden.

1.2.2 Absorptie

Alhoewel het licht niet verloren gaat door het mechanisme van de interne reflectie, zal steeds een gedeelte van het licht geabsorbeerd worden door vervuiling en de eigenlijke bestanddelen van het glas waaruit de vezel bestaat. Er is aangetoond dat optische vezels slechts bruikbaar zijn voor optische communicatie wanneer de verliezen in de vezel beperkt blijven tot minder dan twintig decibel per kilometer.

In de jaren zeventig slaagden materiaalonderzoekers erin om deze doelstelling te halen, en door moderne productietechieken is de kwaliteit van de vezels alleen maar verbeterd.

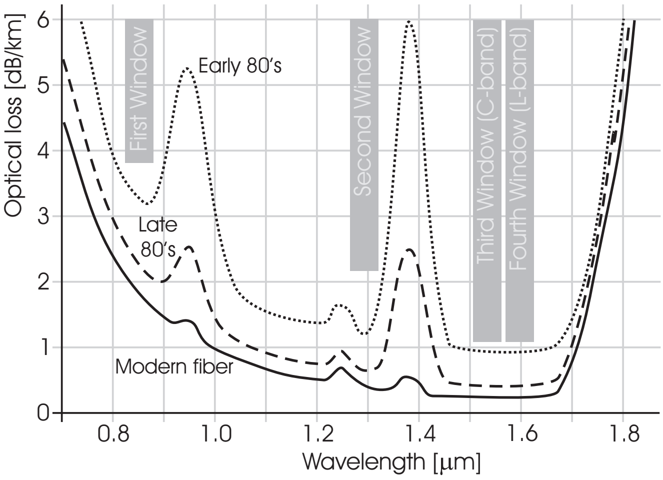

Figuur a Optische verliezen in een glasvezel (zie figuur 1.2)

Het is belangrijk in te zien dat de laagste attenuatie niet voorkomt in het zichtbaar gebied van het optisch spectrum, maar slechts bij golflengten rond 1.3 µm en 1.55 µm in het nabije infrarood (zie figuur a). Dit is een gevolg van de

Rayleighverstrooiing die ons bij kortere golflengtes parten speelt en de intrinsieke infrarood-absorptie van glas bij de langere golflengtes.

Tegenwoordig vindt men optische vezels met een verlies van minder dan 0.1dB/km. Dit betekent dat na tien kilometer propagatie slechts één vijfde van het licht verloren is gegaan.

1.2.3 Dispersie

Een ander belangrijk fenomeen is dat van de dispersie. Het verwijst naar het vervormen van propagerende golven. Dispersie zorgt ervoor dat pulsen tijdens de propagatie gaan uitdeinen. Wanneer we trachten teveel pulsen door te sturen zullen deze in elkaar uitvloeien en wordt het onmogelijk deze van elkaar te onderscheiden. Dus legt dispersie een bovenlimiet op aan de bandbreedte van de optische vezel. Drie soorten dispersie zijn modale dispersie, materiaaldispersie en golfgeleiderdispersie. Ze zorgen ervoor dat de groepssnelheid van het licht niet constant is. Belangrijk in dit opzicht is de spectrale breedte van het licht dat door een vezel wordt gestuurd. In het algemeen is een kleine spectrale breedte bevorderlijk in de strijd tegen de dispersie. De lichtbron die het best aan deze eis voldoet is de laser, die intens coherent licht produceert, gefocust in een kleine straal en met een nauwe lijnbreedte.

1.2.4 Lasertechnologie

Alhoewel reeds theoretisch voorgesteld door Einstein in het begin van de twinitigste eeuw, duurde het tot 1960 voor Maiman zijn optisch gepompte robijnlaser kon realiseren. Twee jaar later was het de beurt aan Hall met een GaAs halfgeleider-laser. Sindsdien is de lasertechnologie haar kinderschoenen ontgroeid.

De groep van halfgeleiders die het meest geschikt zijn voor opto-elektronische toepassingen zijn de III-V halfgeleiders, zo genoemd naar de groepen uit Mendeljev's tabel waaruit ze opgebouwd zijn.

Uit technologisch oogpunt zijn twee parameters primordiaal. De eerste is de roosterkonstante en staat voor de gemiddelde afstand tussen atomen in een halfgeleiderkristal. Lagen verschillende materialen kunnen slechts tot eenzelfde kristal behoren wanneer de respectieve roosterkonstantes niet al te veel van elkaar verschillen (typisch minder dan 2%). De keuze van het substraat zal dus reeds een eerste beperking vormen.

De tweede parameter is de bandafstand. Elektronen in een halfgeleider kunnen niet om het even welke energie aannemen, maar slechts waarden uit bepaalde zones of banden. De twee belangrijkste banden zijn de conductie- en valentieband. Voordat elektronen kunnen deelnemen aan het conductieproces, moeten ze eerst de sprong maken naar de conductieband. Daarvoor hebben ze een extra energie nodig die minimum zo groot is als de grootte van de bandafstand. Wanneer de elektronen de sprong maken zullen ze dus deze energie opnemen of afgeven. Dit kan gebeuren door interactie met een foton. Belangrijk is dat de golflengte van het foton omgekeerd evenredig is met de energie van de elektronensprong en dus van de bandafstand.

In figuur 1.4 worden de twee parameters tegen elkaar uitgezet voor een aantal III-V materialen. Wanneer we de beperkingen van de substraatkeuze in het achterhoofd houden dan zien we dat voor de telecom-golflengtes 1.3 µm en 1.55 µm eigenlijk alleen maar kunnen kiezen voor InP, omdat het golflengte gebied van materialen op GaAs beperkt is tot kortere golflengtes.

1.2.5 Geavanceerde optische toepassingen

Optische vezels werden eerst gebruikt om ruggengraat-verbindingen van netwerken te vervangen. Deze verbindingen verbinden één punt met een ander en dragen een hoge-bandbreedte elektrisch gemultiplexeerd signaal. De capaciteit van een vezel kan echter beter benut worden, wanneer verschillende van dergelijke elektrische signalen op optische dragers met verschillende golflengtes gemoduleerd worden. Om de connectiviteit te verhogen of de betrouwbaarheid van het netwerk te verhogen door het invoeren van redundantie, kan men overstappen van enkele verbindingen naar meervoudige verbindingen in ring- of vermaasde netwerken. Elk knooppunt moet nu ook een schakelfunctionaliteit hebben. Traditioneel wordt dit schakelen uitgevoerd in het elektrisch domein. Het is echter efficiënter, sneller en eleganter om het te transferen naar het optisch domein. Dit vergt opnieuw een uitgebreide graad van passief-aktiefintegratie. Daarnaast kan men ook signaal-onderhoud uitvoeren door signalen te versterken of regenereren. Opnieuw kan dit in het elektrisch domein of volledig optisch. Een probleem dat hier de kop opsteekt is dat van de chip-vezelkoppeling. Doordat de modes van de optische vezel en de richel-golfgeleiders op de chip zeer verschillend zijn zal een koppeling steeds een groot verlies teweeg brengen. Een mogelijk oplossing is het gebruik van bundelexpansiestructuren in de golfgeleiders.

Al deze technieken vereisen echter passieve optische componenten zoals golfgeleiders, filters en multiplexers in combinatie met de actieve componenten zoals lichtbronnen, detectors en schakelaars, liefst dan nog gefabriceerd op dezelfde chip. Dit vereist een lokale controle over de grootte van de verboden zone en heeft men het liefst een zo groot mogelijk keuze.

Nu gebruikt men optische vezels nog enkel in de ruggengraatverbindingen van telefoon-, televisie- en datacommunicatienetwerken. Wanneer men echter ook de lokale lus, dit is de verbinding tussen de gebruiker en de eerste schakelcomponent en nu typisch in coaxiale kabel of gevlochten koperparen, door optische vezels zou willen vervangen, heeft men nood aan nieuwe verticaal emitterende componenten zoals VCSEL's of MC-LED's die goedkoper te fabriceren en gebruiken zijn. Deze componenten bevatten gedistribueerde Braggreflectoren. Hun efficiëntie is sterk afhankelijk van het brekingsindexcontrast tussen verschillende spiegellagen. Aangezien de brekingsindex afhankelijk is van de energie van de verboden zone, zal opnieuw een zo groot mogelijk bereik gewenst zijn.

1.2.6 Het nabije infrarood op GaAs: GaInNAs

We maken opnieuw de vergelijking tussen GaAs en InP (zie figuur b) en tabel 1.2). Het valt op dat indien we GaAs zouden kunnen gebruiken voor telecom-toepassingen, we zowel op vlak van de verboden zone energie als het brekingsindexcontrast een grote stap vooruit kunnen zetten.

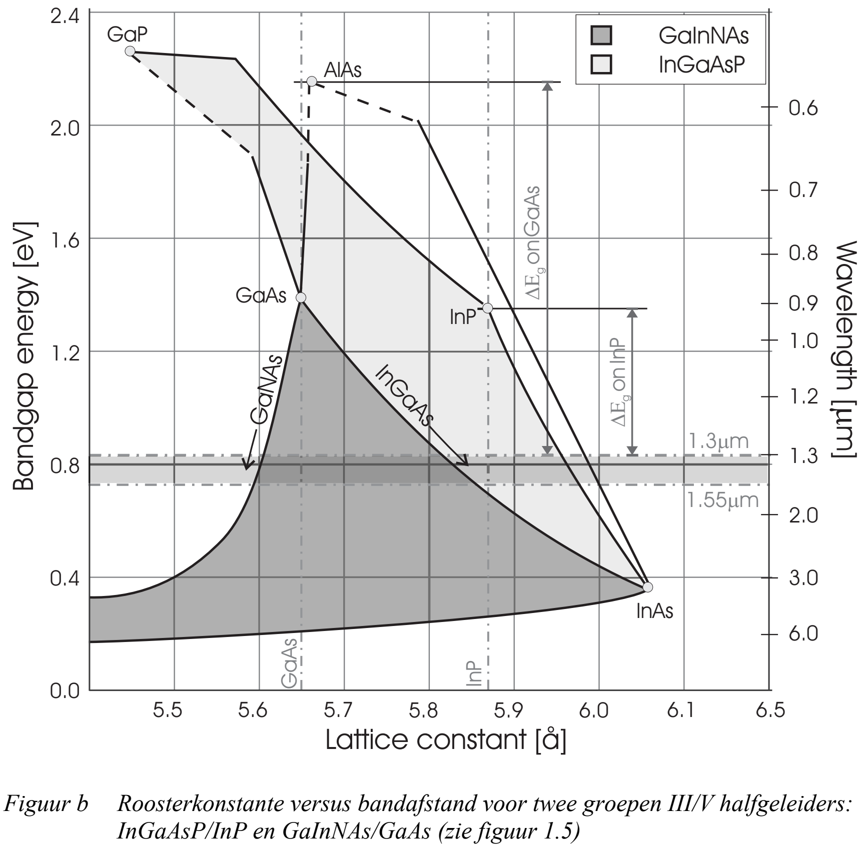

Figuur b Roosterkonstante versus bandafstand voor twee groepen III/V halfgeleiders: InGaAsP/InP en GaInNAs/GaAs (zie figuur 1.5)

En inderdaad in 1992 publiceren Weyers et al. een paper over het toevoegen van kleine fracties stikstof aan GaAs. In tegenstelling tot wat werd verwacht, blijkt de bandafstand niet toe te nemen naargelang men stikstof toevoegt, maar is er een sterke roodverschuiving merkbaar. Voortbouwend op dit feit, beschrijft Kondow in 1996 de mogelijkheid van het GaInNAs-materiaal. Doordat indium en stikstof eenzelfde invloed hebben op de verboden zone energie maar de roosterkonstante in tegenstelde richting beïnvloeden, kan men het materiaal roosteraangepast op GaAs laten groeien, met een kleinere bandafstand dan GaAs.

1.2.7 Epitaxiaalgroeitechnieken

Om dergelijke materialen te kunnen produceren hebben we uiteraard nood aan een geschikte technologie. We wensen te benadrukken dat we niet willekeurig material op een oppervlak deponeren, maar dat het nieuw aangebrachte material geïntegreerd wordt in het kristalrooster van het substraat en dit zo verder uitbreidt.

De door ons gebruikte techniek heet metallorganische gasfaseëpitaxie (MOCVD). Hierin worden de bronmaterialen in gasvormige toestand in een reactor gebracht. Op een temperatuur rond 700ºC, zullen de bronmaterialen dan reageren en bepaalde atomen uit de verbinding op het oppervlak achterlaten.

De bronmaterialen, meestal hydrides of metallorganische verbindingen zijn ofwel gasvormig ofwel vast of vloeibaar onder de gekozen omstandigheden. In deze laatste gevallen zal men daarom waterstof door de bronmaterialen sturen, zodat dit gesatureerd wordt en zo materiaal in de reactor transporteert.

MOCVD is de geprefereerde techniek in de industrie en het onderzoek, maar er zijn ook concurrerende technologieën zoals de ultrahoogvacuumtechnieken MBE en CBE.

1.2.8 Andere toepassingen en concurrerende technologieën

Een kleine verboden zone is niet alleen interessant voor componenten voor de telecommunicatie. Een verboden zone energie van 1 eV in een van de juncties van een zonnecel zou toelaten om een groter deel van het optisch spectrum op te vangen en dus de efficiëntie van dergelijke meervoudige-junctiecellen vergroten. Ook voor de basis van bipolaire transistoren is een materiaal met kleine verboden zone interessant voor het verlagen van de vermogendissipatie.

Er zijn weinig alternatieven om GaAs-technologie te combineren met de telecom-golflengtes. De meest belovende echter is die van de quantumpunten, waarbij kleine cellen InAs met uniforme grootte gebruikt worden als aktief gebied. Een tweede mogelijkheid is de groei van gespannen GaAsSb-lagen.

1.3 Overzicht van het werk

Het doel van dit werk is het ontwikkelen van GaInNAs materialen met behulp van MOCVD.

In een eerste hoofdstuk geven we een overzicht van de communicatietechnologie en relateren we verschillende aspecten van de optischevezelcommunicatie met het eigenlijke onderwerp van deze thesis.

In een tweede hoofdstuk gaan we nader in op de theoretische en experimentele eigenschappen van het GaInNAs-materiaal. Het is hoofdzakelijk een literatuuroverzicht. In een laatste paragraaf bieden we een blik op de stand van zaken inzake op dit materiaal gebaseerde componenten.

Het derde hoofdstuk beschrijft de ontwikkeling van epitaxiaalgroei op lage temperatuur. Dit is noodzakelijk wegens het incorporatiegedrag van stikstof maar is een uitdaging omdat enkele ongewenste parasitische effecten de kop opsteken.

In een vierde hoofdstuk gaan we verder op de ingeslagen weg. Lage temperatuursgroei vereist immers nieuwe precursoren. Een ervan is TBAs. Zijn invloed op het groeiproces is zodanig dat het onderwerp een eigen hoofdstuk verdient.

Het vijfde hoofdstuk tenslotte behandelt de eigenlijke groei van GaInNAs. We bekijken het gedrag van de stikstofintegratie en zijn effect op allerhande materiaaleigenschappen.

In een laatste hoofdstuk formuleren we een aantal besluiten en bieden we enkele toekomstperspectieven.

1.4 Lijst met publicaties

Als afsluiter geven we nog een overzicht van papers in internationale tijdschriften en papers voor workshops en conferenties die in het kader van dit werk zijn gepresenteerd.

2. Fundamentele eigenschappen van GaInNAs

2.1 Abstract

2.2 Inleiding

Onderzoek naar de gemengde nitride-groep V materialen is jong, maar de laatste tijd zeer populair dankzij de intrigerende fysische eigenschappen en de rijkdom aan mogelijke toepassingen.

In conventionele materialen is de bandafstand van ternaire materialen het gewogen gemiddelde van die van de binaire bestanddelen (zie figuur c). Het toevoegen van stikstof aan GaAs of InGaAs echter zorgt voor een gigantische buiging van deze tendens. Langs de andere kant varieert de roosterconstante zoals verwacht volgens de wet van Vegard.

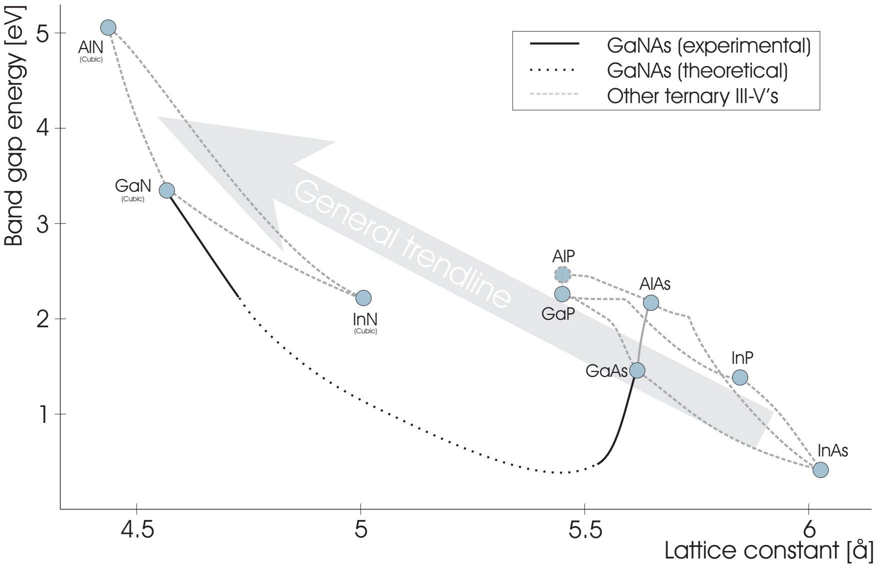

Figuur c Verband tussen roosterkonstante en bandafstand voor enkele typische III/V halfgeleiders (zie figuur 2.1)

De oorzaak van de bandbuiging is lange tijd onduidelijk gebleven. Het wordt toegeschreven aan de eigenaardige eigenschappen van stikstof zoals zijn relatief kleine formaat en zijn elektronegativiteit. Een belangrijk neveneffect is de grote effectieve massa van de elektronen. Langs de andere kant is er de observatie dat de efficiëntie van de luminescentie drastisch daalt wanneer we stikstof toevoegen en zullen thermische nabehandelingen noodzakelijk zijn.

2.3 Bandstructuur

2.3.1 Gigantisch buigen van de bandafstand

In alle gevallen zal, wanneer we in een kristalrooster een element vervangen door een ander met kleinere ionische radius, de bandafstand toenemen, omdat de gemiddelde potentiaal voor electronen toeneemt. Het succes van de fabricatie van III-V halfgeleiders en de doorbraak van de groep III-nitrides leidde in de jaren negentig tot onderzoek naar gemengde III-V-N verbindingen.

Absorptiemetingen (zie figuur 2.2) toonden aan dat GaNAs inderdaad over een directe bandafstandsovergang beschikt maar dat de energie verbonden met deze overgang afneemt in plaats van toeneemt, naargelang men meer stikstof toevoegt. Daarenboven is de verandering per atomaire fractie meer dan tien keer zo groot als normaal.

De eerste theoretische beschrijving van het fenomeen vindt plaats binnen het kader van het model van Van Vechten. Ten gevolge van de grote elektronegativiteit van stikstof voorspelt het een bandbuiging met een buigingscoëfficient van –20eV. Maar het model voorspelt tevens een negatiever verboden zone energie voor grotere stikstoffracties, hetgeen in latere experimenten ontkracht wordt. Twee andere modellen, benaderende lokaledichtheidsberekeningen en het bandenantikruisingsmodel van Shan, geven echter een betere beschrijving. Zij worden beschreven in wat volgt.

2.3.2 Conductiebandtoestanden: stikstofgeaktiveerde E_- en E_+ niveaus

De ontdekking van een extra kenmerk in de fotoreflectantie spectra (zie figuur 2.4), E_+, leidde tot verder inzicht in de aard van de energietoestanden in III-V-N verbindingen.

De drie fundamentele overgangen zijn zichtbaar. Een eerste, E_-, is de fundamentele verboden zone overgang. De tweede, $E_-+\Delta_0$, is de afgesplitste spin-orbit valentieband transitie. De derde, E_+, komt voor in de spectra van GaNAs en GaInNAs voor stikstof-concentraties van respectievelijk 0.8% en 1.2%.

Uit de metingen komt waardevolle informatie over de elektronenstructuur van het materiaal. Zo is de spin-orbit splitting Δ_0 onafhankelijk van de stikstofconcentratie, hetgeen erop wijst dat stikstof de valentieband in slechts minieme mate beïnvloedt en dat het E_+ niveau een bovenliggend niveau van de conductieband is. De positie van het E_- niveau verschuift naar lagere energieën, overeenstemmend met de buiging van de bandafstand, terwijl de kloof met het E_+ niveau lineair toeneemt met de stikstofinhoud.

Eveneens interessant is de studie van de drukafhankelijkheid van de niveaus E_- en E_+ (figuren 2.5 en 2.6). Door materiaal aan vrij grote hydrostatische drukken (orde GPa) te onderwerpen, kunnen we de roosterkonstante van het materiaal beïnvloeden. In tegenstelling met (In)GaAs, waar de bandafstand lineair toeneemt met de hydrostatische druk, vertonen de twee niveaus een gebogen en onderling tegengesteld gedrag, wat erop wijst dat de aard van de niveaus verandert met de druk.

Deze bevindingen geven een direkt bewijs dat een door stikstof veroorzaakte interactie tussen de twee niveaus E_- en E_+ de oorzaak is van de reductie van de verboden zone energie. De onderliggende oorzaak is nog steeds onderwerp van discussie. Twee modellen staan tegenwoordig in het middelpunt van de aandacht. Ze gaan beide uit van het bestaan van een stikstofgeïnduceerd resonantie niveau in de bandenstructuur. Omdat stikstof zo veel kleiner en electronegatiever is dan het arseen dat het vervangt, mengen de energietoestanden van stikstof niet gelijkmatig met die van de (In)GaAs matrix. In de plaats wordt een smalle gelocaliseerde band gevormd, E_N, een paar tienden van een electronvolt boven de conductieband. Het niveau blijft vast ten opzichte van de valentieband is zeer sterk gelocaliseerd van aard.

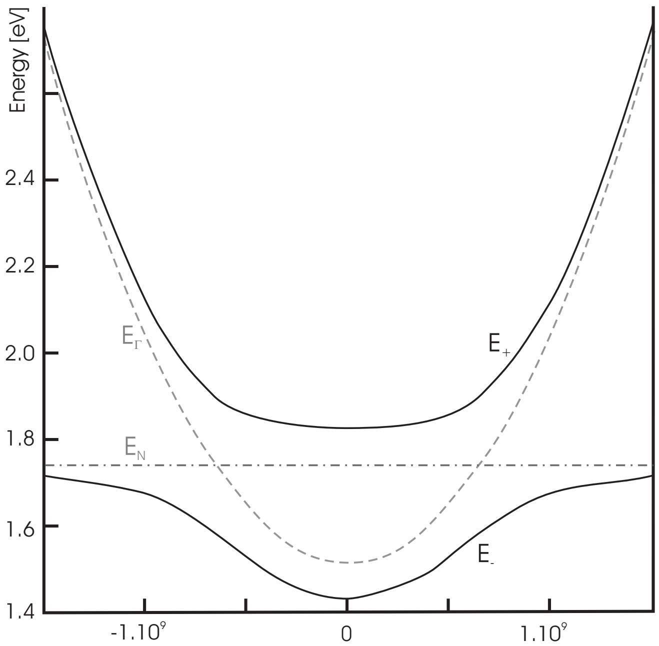

Figuur d Voorstelling van het bandenantikruisingsmodel (zie figuur 2.7)

Het eerste model dat we bespreken is het bandenantikruisingsmodel, voorgesteld in figuur d. Het is bekend dat wanneer twee interagerende quantummechanische toestanden elkaar benaderen in energie, ze elkaar gaan afstoten. In het geval van Ga(In)Nas zijn het de gelokaliseerde stikstoftoestanden, E_N, die interageren met de toestanden van de conductieband met energie E_Γ. Dit heeft een opsplitsing tot gevolg van de conductieband en dus het ontstaan van E_- en E_+. Hoe grotere de stikstofinhoud, hoe groter de interactie en dus de repulsie van de niveaus. Daarnaast zal dit alles leiden tot een afplatting en niet-paraboliciteit van de conductieband wat op zich weer leidt tot een toename van de effectieve massa van de electronen. Ook het gedrag van het materiaal onder invloed van hydrostatische druk kan met dit model verklaard worden.

Een tweede model is gebaseerde op numerieke berekeningen aan de hand van lokaledichtheidsapproximaties (LDA). Hier interageert het stikstofniveau E_N niet direct met het conductiebandsminimum E_Γ maar veroorzaakt het een opsplitsing van de indirecte toestanden. Deze interageren dan weer onderling en met het stikstofniveau en creëren zo de niveaus E_- en E_+. Het model is gebaseerd op de sterk gelokaliseerde perturbatie die veroorzaakt worden door het stikstof. Het model voorspelt twee zones in de verandering van de bandafstand met de stikstofconcentratie. Indien men ook de spanning in de laag in rekening brengt stemt de theorie nog beter overeen met de experimentele data.

2.3.3 *Dispersie van de conductieband*

Een ander substantieel verschil tussen de III-V-N materialen en hun conventionele tegenhangers is het ongewone gedrag van de effectieve massa van de elektronen. Gewoonlijk neemt deze effectieve massa af met afnemende bandafstand, terwijl ze hier juist toeneemt.

De situatie waar de effectieve massa's voor holen en elektronen elkaar benaderen is gunstig voor toepassing in lasers. Dit wordt geschetst in figuur 2.8. Door de asymmetrie in het geval waar beide massa's van elkaar verschillen, zal de transparantie dichtheid toenemen ten opzichte van het symmetrische geval.

De toename van de effectieve massa voor elektronen is experimenteel bevestigd, zowel voor GaNAs quantum putten als voor GaInNAs materiaal tot waardes van 0.19 keer m_0, de massa van een vrij elektron, voor $GaN_{0.02}As_{0.98}$ en zelfs 0.4m_0 voor $Ga_{0.92}In_{0.08}N_{0.033}As_{0.967}$.

2.3.4 *Bandenalignering van Ga(In)Nas/GaAs heterostructuren*

Voor praktische toepassingen is de gedetailleerde kennis van de eigenschappen van heterostructuren zoals bandenalignering en de waardes van de band-discontinuïteiten van uiterst groot belang.

Een nog onopgeloste vraag inzake GaNAs/GaAs quantumputten is die van de bandalignering. Algemeen wordt aanvaard dat stikstofincorporatie vooral de conductieband aantast, wat resulteert in een grote conductiebandoffset en slechts een minimale valentiebandoffset. Het is dan maar ook de vraag of de bandalignering van type I dan wel type II is (zie figuur e).

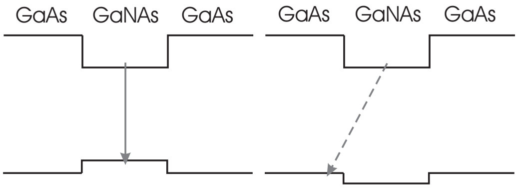

Band scheme	Type I	Type II
Optical transitions	Direct	Indirect
Radiative PL decay	Fast	Slow
Hole location	GaNAs	GaAs

Figuur e Mogelijke bandenalignering in GaNAs/GaAs heterojuncties (zie figuur 2.8)

Verschillende modellen en berekeningen leidden tot tegenstrijdige conclusies (figuur 2.9) en ook experimentele gegevens zijn niet eenduidig, ook al omdat de interpretatie in sommige gevallen veel hypotheses vereist.

Bij GaInNAs/GaAs heterostructuren is de situatie gunstiger. Dit wordt getoond in figuur 2.10. Ook al is de GaNAs/GaAs alignering in het ergste geval type II, dan nog wordt dit door het toevoegen van indium ruimschoots gecompenseerd. Daarbij moet men zich nog realiseren dat in de praktijk vooral compressief gespannen quantumputten worden gebruikt en dat men de holen kan inperken met behulp van AlGaAs barrière lagen.

Experimentele data bevestigen dat er bij GaInNAs quantumputten met 38% indium en 1.5% stikstof een type I alignering is met een valentiebandoffset van 65 meV.

2.4 Recombinatie processen

2.4.1 Radiatieve recombinatie

Het lage-temperatuursfotoluminescentie (PL) spectrum van GaNAs wordt gekarakteriseerd door een asymmetrische piek met maximum bij een golflengte dat naar lagere energieën verschuift naarmate de stikstofconcentratie toeneemt. Ook fotoluminescentie excitatie (PLE) metingen bevestigen dat de absorptie rand van het materiaal naar kleinere energieën verschuift met de toename van stikstof in het materiaal.

Het PL-spectrum van het GaNAs valt typisch scherp af aan de hoge-energie-zijde, maar heeft een exponentieel verloop aan de andere kant. Met toenemende temperatuur verschuift de maximum positie naar langere golflengtes, terwijl een toenemend excitatievermogen het omgekeerde effect heeft. Dit komt niet voor in de PLE spectra, zodat het effect niet het gevolg is van een verandering van de bandafstand (zie figuur 2.17). Het vervalgedrag van de ladingsdragers is verschillend voor de hoge en lage energie-zijde van het spectrum.

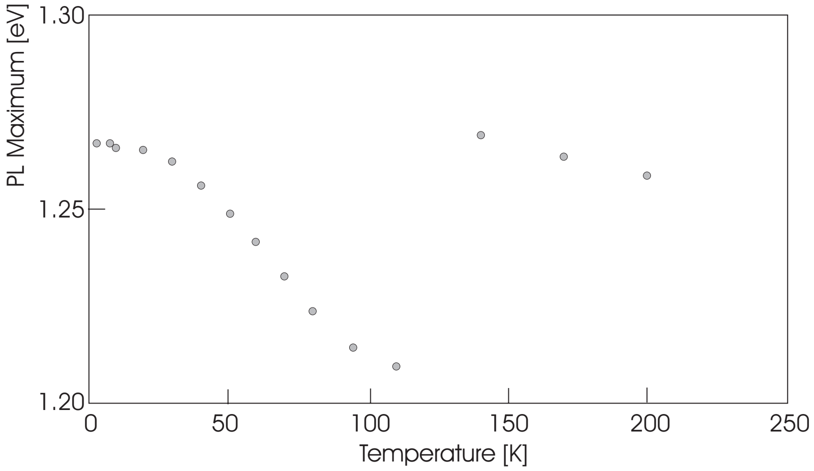

Figuur f Temperatuursafhankelijkheid van het PL-maximum van GaNAs-lagen (zie figuur 2.13)

Deze eigenschappen van de GaNAs emissie kunnen verklaard worden aan de hand van sterke exciton localisatie die aanleiding geven tot gelocaliseerde exciton (LE) recombinatie. Het sterkste bewijs voor deze stelling vindt men terug in het temperatuursgedrag van de PL-emissie (figuur f). Met toenemende temperatuur zullen de ladingsdragers geaktiveerd worden in gedelokaliseerde toestanden. Voor deze vrije ladingsdragers bestaan nu zowel radiatieve als niet-radiatieve recombinatiemechanismen, zodat de fotoluminescentie uitdooft. Aangezien eerst de ladingsdragers met hogere energie zullen ontsnappen zal de LE recombinatie nu een maximum bereiken bij lagere energieën. Wanneer de recombinatie van vrije ladingsdragers het dominerende mechanisme wordt, valt het maximum van de piek weer terug naar zijn oude positie, zodat er een geïnverteerde N-vorm ontstaat. Men kan uit de grafiek ook een lokalisatiepotentiaal afleiden, die voor GaNAs rond 50 meV ligt. Deze waarde kan door thermische nabehandelingen verkleind worden, maar is nog steeds veel hoger dan in andere III-V verbindingen. Daar wordt een dergelijke localisatie veroorzaakt door willekeurige samenstellingswanorde, terwijl het in het geval van GaNAs waarschijnlijker te wijten is aan de lokalisatie van de elektronen rond de stikstof atomen.

Ook bij GaInNAs is de LE recombinatie aangetoond voor zowel quantumputten als dikke epitaxiaallagen. Figuur 2.14 toont het temperatuursgedrag van PL- en PR-maxima. Ook de andere tendensen (verval, excitatievermogen, vorm van het spectrum) van de recombinatie lopen gelijk met die in het GaNAs.

2.4.2 *Niet-radiatieve recombinatie en thermische nabehandeling*

Talrijke optische experimenten hebben het grootste probleem van de arseenverdunde nitrides aangetoond, namelijk het snelle degraderen van de radiatieve efficiëntie met de stikstofincorporatie. De PL-intensiteit neemt drastisch af met de toename van het stikstofgehalte, gewoonlijk met een of twee grootteordes per percent toegevoegde stikstof.

Theoretische beschouwingen op basis van het veranderende karakter van de conductiebandtoestanden leiden tot de voorspelling van een verlaagde optische efficiëntie, maar het effect is veel kleiner dan het experimenteel vastgestelde. Gewoonlijk wijt men het effect aan de lage groeitemperatuur, die nodig is om stikstof beter te incorporeren maar leidt tot een lagere structurele kwaliteit.

Een manier om de inherent slechte kwaliteit van Ga(In)Nas materiaal te verbeteren is het toepassen van thermische nabehandelingen. Deze leiden tot een sterke toename van de PL-intensiteit en het versmallen van het spectrum, maar eveneens tot het verschuiven van het spectrum naar hogere energieën. Ook de diffusielengtes van de ladingsdragers worden langer. Het onderliggende mechanisme zijn lange tijd een mysterie geweest en werd toegeschreven aan de eliminatie van concurrerende niet-radiatieve kanalen.

Aanvankelijk werd gepostuleerd dat een van deze ladingsdragersvallen het gevolg was van waterstofonzuiverheden. Een aantal groepen kon een verband aantonen tussen thermische nabehandelingen en het verminderen van de waterstofachtergrond. Ook werd aangetoond dat waterstof intrinsieke eigenschappen van stikstof kan beïnvloeden en zelfs passiveren.

Maar ook in inherent waterstofvrije epitaxiaalgroeitechnieken zoals MBE met een RF-plasma stikstofkraker wordt hetzelfde effect van de thermische nabehandeling vastgesteld. Daarom moeten nog andere ladingsdragersvallen in het materiaal aanwezig zijn. Zo toonde men aan dat ook zuurstof een recombinatiecentrum in het midden van de verboden zone veroorzaakt.

Een andere onderzoeksgroep identificeerde vier verschillende vallen voor gaten in pasgegroeid GaInNAs, van dewelke drie thermisch onstabiel waren. Als oorzaak wijzen ze puntdefecten aan, vermoedelijk een interstitieel Ga_i atoom.

Een ander puntdefect werd geïdentificeerd als zijnde een interstitieel stikstof-atoom. Voor kristallen waar arseenatomen vervangen worden door stikstof werd theoretisch aangetoond dat de wet van Vegard van toepassing is. Figuur 2.15

toont echter hoe het GaInNAs materiaal daarvan afwijkt. Hoewel stikstof inderdaad preferentieel substitutioneel op de arseensite gaat zitten, kan ze verkiezen uit energetische redenen om in een naburige interstitiele site te gaan. Berekeningen tonen aan dat een enkel interstitieel stikstof atoom energetisch onwaarschijnlijk is, maar dat in de plaats een gesplitst interstitieel gevormd wordt zoals geïllustreerd in figuur 2.16.

Naast het reduceren van de concentratie van puntdefecten hebben de thermische nabehandelingen ook een drastisch effect op de bandafstand van de arseenverdunde nitrides en vergroten die met zo'n 100 meV. Er worden twee mogelijke redenen geciteerd. Een is de uitdiffusie van stikstof, de andere is het microscopisch herschikken van atomen en de daaruit volgende veranderingen in de stikstofbindingen.

Van de eerste mogelijkheid zijn in de literatuur zowel voor- als tegenstanders te vinden, elk met hun eigen argumenten. De tweede mogelijkheid voorziet in een ordening op korte schaal, of anders gezegd verschillende configuraties voor de naaste atomen, gallium of indium, rond het stikstof. Voor microscopisch evenwicht is een balans nodig tussen spanningsenergie in het rooster enerzijds en de chemische energie van de atoombindingen anderzijds. Tijdens epitaxiaalgroei domineert vooral de chemische energie, maar tijdens het thermisch nabehandelen zal de lokale spanning verminderd worden. Elk van de configuraties heeft echter een andere energieniveau voor het stikstof geïnduceerd resonantieniveau (zie figuur g), zodat de overgang van de ene configuratie naar een andere de verschuiving van de bandafstand kan verklaren.

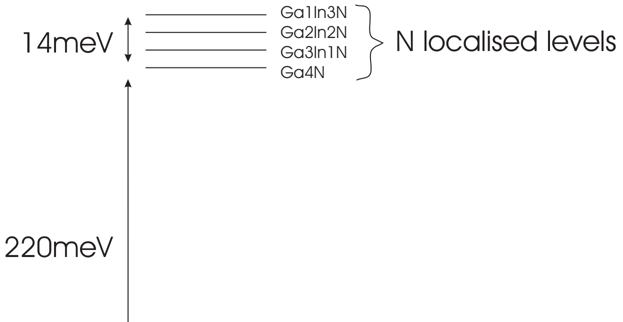

Figuur g Energieniveaus van verschillende gallium-indiumconfiguraties rond stikstof (zie figuur 2.17)

2.5 Overzicht van de beste componenten in de literatuur

2.5.1 Zijdelings emitterende lasers

In deze paragraaf geven we een overzicht van welke componenten reeds werden voorgesteld in de literatuur. Een belangrijke parameter hierbij is de karakteristieke temperatuur T_0, die aangeeft hoeveel de drempelstroom verandert als functie van de temperatuur. Tabellen 2.3 en 2.4 geven een overzicht van de eigenschappen van bredeoppervlakte- en richellasers. In figuur 2.23 tonen we hoe ook de drempelstroomdichtheid toeneemt met de emissiegolflengte en dus ook met stikstofinhoud. Dit toont opnieuw aan dat het toevoegen van stikstof de optische kwaliteit nadelig beïnvloedt.

2.5.2 Vertikaal emitterende lasers

Het verschijnen van monolithische GaInNAs-gebaseerde VCSEL's is het ontegensprekelijke bewijs van het potentieel van het materiaal en de immense progressie dat het onderzoek in korte tijd heeft gemaakt. De excellente eigenschappen van de componenten staat samengevat in tabel 2.5.

3. Epitaxiaalgroei op lage temperatuur

3.1 Abstract

3.2 Inleiding en motivering

Epitaxiaalgroei van lagen zoals GaAs, AlGaAs en InGaAs gebeurt normaal bij temperaturen tussen 600ºC en 750ºC. De reacties op het groeioppervlak verlopen snel, de bronmaterialen ondergaan volledige pyrolyse en samenstelling en groeisnelheid zijn onafhankelijk van de groeitemperatuur.

Er zijn echter twee goede redenen om epitaxiaalgroei op lage temperatuur te gaan bestuderen. Vooreerst, zoals we zullen aantonen in het vijfde hoofdstuk, is een lage temperatuur de eerste vereiste om stikstof te kunnen incorporeren in (In)GaAs materiaal.

Maar zoals bekend is stikstof nefast voor de optische kwaliteit van de lagen. Daarom gaan we het stikstofgehalte zoveel mogelijk beperken in in eerste instantie zelfs elimineren. Uiteraard hebben we nu met extreem gespannen lagen te maken. Ook deze lagen kunnen beter op lage temperatuur gegroeid worden.

Dit is echter niet triviaal aangezien nu parasitische effecten de kop opsteken, en we zelfs alternatieven moeten zoeken voor de klassieke bronmaterialen zoals trimethylgallium (TMGa) en arsine (AsH_3).

3.3 Langegolflengte InGaAs: de spanningsbarrière

Wanneer we indium toevoegen aan GaAs om de bandafstand te verkleinen, zal ook de roosterconstante toenemen. Deze roostermisaanpassing geeft aanleiding tot twee ongewenste effecten: de introductie van misaanpassingsdislocaties en het ontstaan van driedimensionele groei.

3.3.1 Kritische dikte

Wanneer we een epitaxiaallaag aanbrengen op een substraat met andere roosteraanpassing zal die eerst elastisch vervormen. Haar roosterconstante in het vlak zal die van het substraat overnemen, terwijl die in de loodrechte richting zal veranderen om het behoud van volume te verzekeren. Op een gegeven punt zal de opgebouwde spanningsenergie te groot worden en de laag zal relaxeren door het vormen van misaanpassingsdislocaties (zie figuur 3.1).

Relaxatie kan verschillende soort roosterdefecten veroorzaken. De tweedimensionele defecten omvatten stapeldefecten, antifasedomeinen (zie hoofdstuk 4) en zelfs polykristallijne korrels. De twee basistypes van de lineaire defecten worden grafisch voorgesteld in figuur h, samen met het algoritme om de karakteristieke Burgersvector en dislocatielijn te bepalen. Deze twee begrippen definiëren het glijvlak van de dislocatie.

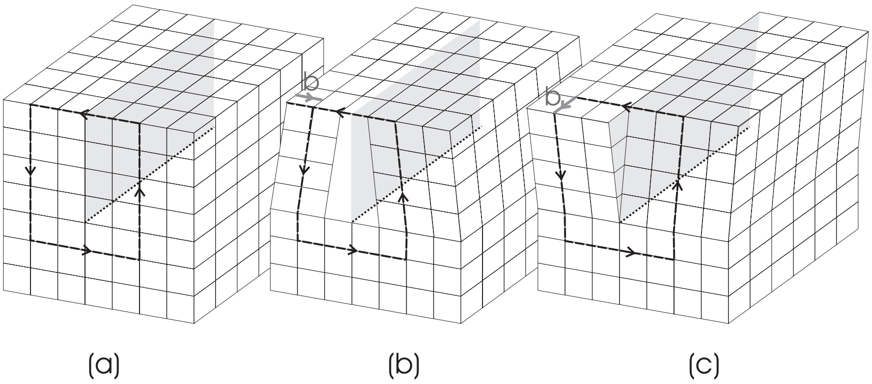

Figuur h *Basistypes van tweedimensionale roosterfouten met een perfect kristal (a), een randdislocatie (b) en een schroefdislocatie (c) (zie figuur 3.2)*

Rand- en schroefdislocaties zijn echter niet de enige voorkomende types. Dislocaties kunnen ook samengesteld zijn uit verschillende andere dislocaties op voorwaarde dat ze dezelfde dislocatielijn hebben. Hun Burgers vector is dan de som van de Burgersvector van de samenstellende dislocaties. In GaAs is vooral de 60º dislocatie van belang, genoemd naar de hoek tussen dislocatielijn en Burgers vector.

Gebaseerd op de idee van glijdende dislocaties ontwikkelden Matthews and Blakeslee een model voor het bepalen van de kritische dikte. Dit is de dikte waarop de spanningsenergie te groot wordt en dislocaties beginnen te vormen (figuur 3.3). People en Bean baseerden hun kritische dikte model op het evenwicht tussen de ingebouwdespanningsenergie en de energie die nodig is om een nieuwe dislocatie te vormen.

Met deze modellen kunnen we nu een theoretische kritische dikte bepalen voor InGaAs lagen die gesandwiched worden tussen GaAs in functie van het indiumgehalte. Ook kunnen we dan weergeven wat de emissiegolflengte is voor quantumputten met die bepaalde samenstelling en (kritische) dikte. Dit wordt weergegeven in figuur i. Alhoewel beide modellen licht van elkaar afwijken is het duidelijk dat met InGaAs de maximum golflengte beperkt is tot 1.2 µm. Het is belangrijk om op te merken dat de ware kritische dikte zal onderhevig zijn aan groeiparameters als temperatuur en groeisnelheid.

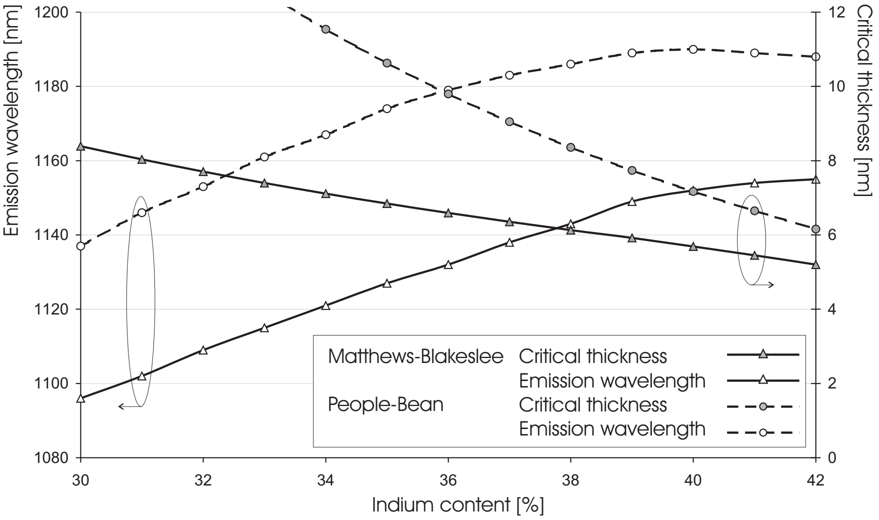

Figuur i *Kritsiche dikte van InGaAs-lagen volgens de modellen van Matthews-Blakeslee en People-Bean, samen met de maximum emissiegolflengte (zie figuur 3.4)*

3.3.2 Afbeeldingen in de reciproke ruimte

Het middel bij uitstek om relaxatie van epitaxiaallagen te bestuderen is x-straal diffractie en meer bepaald de techniek van de afbeeldingen in reciproke ruimte (RSM). Een stukje materiaal wordt gebombardeerd met x-stralen met welbepaalde golflengte. Voor een welbepaalde combinatie van invalshoek en spatiëring tussen de reflectievlakken treedt constructieve interferentie op en zal een groot signaal gedetecteerd worden onder de uitvalshoek. Deze conditie heet de Braggvoorwaarde (zie figuur 3.5).

Om de interpretatie te vergemakkelijken, bestaat een interessante transformatie naar de reciproke ruimte (zie figuur 3.6). De voorwaarde voor constructieve interferentie wordt in deze ruimte omgevormd tot de conditie van Laue. Deze is de basis voor de constructie van de bol van Ewald (zie figuur j). Reflectievlakken worden in de reciproke ruimte getransformeerd naar punten, met een positie die afhankelijk is van de roosterparameters. Wanneer men een deel van de reciproke ruimte zal aflopen, krijgt men voor verschillende roosterparameters verschillende reflecties. Men zal nu eenvoudig relaxatie kunnen vaststellen wanneer al dan niet de reflecties voorkomen voor dezelfde waarde van de vectoren in het vlak (zie figuur 3.8). Door fysische beperkingen van het x-straaldiffractieapparaat kan niet de hele reciproke ruimte afgebeeld worden maar slechts een subruimte zodat de afbeelding goed moet worden gekozen (typisch <–1 15>).

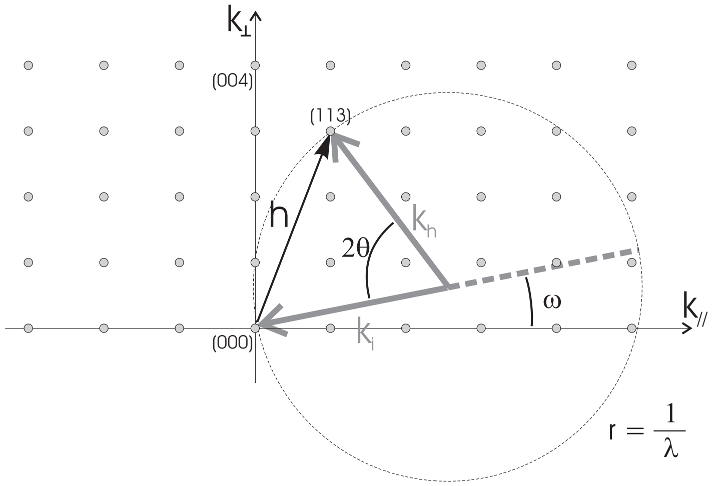

Figuur j Constructie van de Ewaldbol (zie figuur 3.7)

3.3.3 Modi van de epitaxiaalgroei

Een tweede degradatiemechanisme voor sterk gespannen lagen is dat van de driedimensionele groei. Epitaxiaalgroei wordt normaal geklassificeerd volgens drie verschillende groeimodi (zie figuur 3.9). De eerste is de normale tweedimensionele Frank-Van Der Merwe modus. De epitaxiaalgroei verloopt aan de hand van de vorming van eilanden van een enkele atoomlaag groot die zijdelings uitbreiden en samensmelten, zodat de groei laag per laag verloopt. Het andere extreem is dat van Volmer-Weber. Over het hele opppervlak worden pyramidale structuren gevormd die zich nu zowel in het vlak als transversaal uitbreiden. Een derde vorm ligt daartussen. Bij de Stanski-Krastanov modus begint de groei eerst in het tweedimensionele regime om dan na een paar atoomlagen over te gaan in driedimensionele modus.

De overgang van de eerste modus naar de andere is vooral afhankelijk van de roostermisaanpassing (typisch meer dan twee procent), van de nucleatiesnelheid en de mobiliteit van de atomen op het oppervlak. Ze kan onderdrukt worden door een lage groeitemperatuur, hoge groeisnelheid en hoge V/III verhouding.

3.4 Epitaxiaalgroei in het kinetisch gelimiteerd regime

Voor beide degradatiemechanismes is het gunstig om de groeitemperatuur te verlagen. Helaas is dit niet zo eenvoudig. Immers, ook al wordt MOCVD geregeerd door thermodynamica, is het geen evenwichtsproces. Thermodynamica legt limieten op aan het proces en bepaalt de initiële en finale toestand, maar kan geen informatie geven over de snelheid waarop een evenwicht bereikt wordt. De kinetiek van de oppervlaktereacties en het massatransport in de gasfase zijn niet snel genoeg om een evenwicht te vestigen in het hele systeem.

Een normaal groeiregime (zie figuur k) vindt plaats in een temperatuursgebied waar reacties aan het oppervlak veel sneller verlopen dan de diffusieprocessen in de gasfase. Dit diffusieproces en dus het hele MOCVD-proces zijn dan vrijwel temperatuursonafhankelijk. Bij hogere temperaturen wordt het proces gehinderd door thermodynamica of door de depletie van de reactantia. Wanneer we echter de temperatuur verlagen beneden een bepaald punt, wordt de snelheid van de reacties aan het groeioppervlak de beperkende factor, omdat de vorming van bepaalde producten in de gasfase of op het oppervlak te traag verloopt. Dit is uiteraard afhankelijk van de gebruikte bronmaterialen.

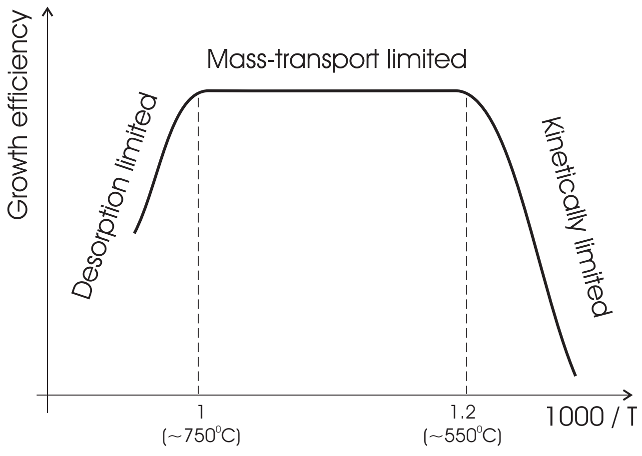

Figuur k Verschillende groeiregimes voor MOCVD (zie figuur 3.10)

Zo zal de pyrolyse van de bronmaterialen beneden een bepaalde temperatuur niet meer volledig verlopen. Voor arsine begint dit proces beneden 550ºC. De beschrijving van de studie waarbij arsine vervangen wordt door een alternatieve bron wordt beschreven in het volgende hoofdstuk. Ook de groep III bronmaterialen zijn onderhevig aan dit effect. Het valt onmiddellijk af te leiden uit het verminderen van de groeisnelheid, zoals getoond in figuur 3.11 voor GaAs gegroeid met trimethylgallium (TMGa). Het verminderd thermisch kraken van het TMGa geeft ook aanleiding tot koolstof achtergrondvervuiling. Bij onvolledig gekraakt TMGa, blijven immers methylgroepen achter op het galliumatoom op het groeioppervlak die in de epitaxiaallaag bedolven worden.

Daarom wordt TMGa vaak vervangen door triethylgallium (TEGa). Omdat TEGa helemaal anders en op lagere temperaturen dissocieert dan TMGa, zal het minder koolstofvervuiling veroorzaken. In figuur 3.12 tonen we de koolstofachtergrond, zoals gemeten met SIMS, in GaNAs gegroeid op identieke temperatuur met beide bronnen en waarin TEGa duidelijk beter scoort.

Uiteraard heeft dit ook zo zijn gevolgen op de optische kwaliteit (zie figuur 3.13), waar we de fotoluminescentie tonen van InGaAs quantumputten die in gelijkaardige omstandigheden werden gegroeid maar met de twee galliumbronnen.

Naast de achtergrondvervuiling beïnvloedt een lagere groeitemperatuur ook kristalliniteit van de epitaxiaallaag. Figuur l toont de fotoluminescentiespectra van InGaAs quantumputten die werden gegroeid op verschillende temperaturen. Twee tegensgestelde effecten zorgen ervoor dat er een optimale groeitemperatuur bestaat rond 525ºC.

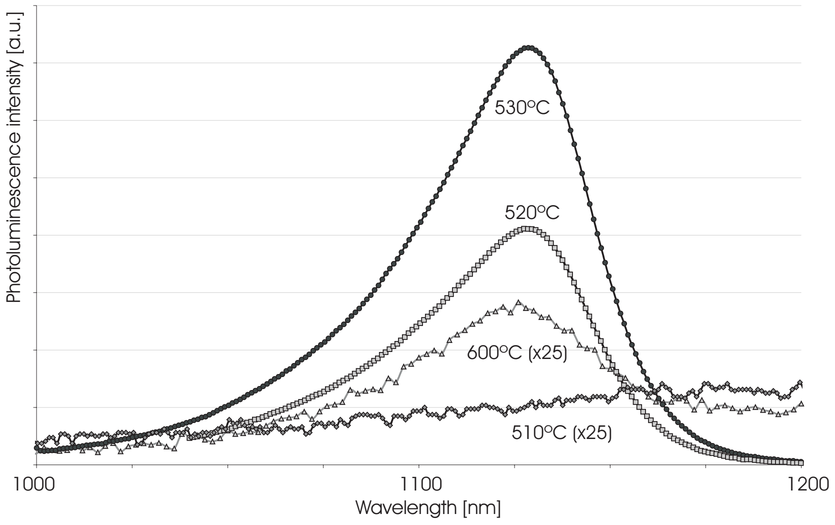

Figuur l Invloed van de groeitemperatuur op de optische kwaliteit van hooggespannen InGaAs quantumputten (zie figuur 3.14)

Langs de ene kant zal een te hoge temperatuur ervoor zorgen dat de gespannen laag gemakkelijker relaxeert. Dit wordt aangetoond in figuur 3.15 (groei op 530ºC) en figuur 3.16 (groei op 600ºC). De lage temperatuurslaag is perfect gespannen, de andere partieel gerelaxeerd. Wanneer we de temperatuur echter te ver verlagen zal de kristalliniteit dermate degraderen dat de impact op de optische eigenschappen nefast is (zie figuur 3.17).

Het belang van de V/III verhouding wordt geïllustreerd in figuur 3.18. Omdat de aanwezigheid van arseen op het oppervlak de mobiliteit van de gallium en indium atomen beperkt, gaat een hoge V/III verhouding relaxatie tegen. In dit opzicht verwijzen we naar hoofdstuk vier, waar we een alternatieve arseen-precursor bestuderen. Tertiairbutylarsine zal beter thermisch kraken wat bij een zelfde molaire stroom resulteert in een hogere effectieve V/III-verhouding.

3.5 Randemitterende lasers

Met de aktieve gebieden die hierboven ontwikkeld werden werden tenslotte ook componenten gemaakt. Zonder in detail op de halfgeleiderlaser te willen ingaan, geven we hier toch een overzicht van de basisprincipes.

Een laser heeft twee belangrijke kenmerken. Ten eerste moet ze een optische oscillator bevatten, en ten tweede moet ze het licht in de oscillator kunnen versterken.

De oscillator is in dit type laser uitgevoerd als een golfgeleider die getermineerd wordt door twee parallelle gekliefde vlakken die als spiegel dienst doen.

Winst in de laser wordt bekomen door gestimuleerde emissie. Figuur 3.19 toont de drie basisinteracties tussen fotonen en elektronen in het halfgeleidermateriaal. Wanneer in de halfgeleider zowel elektronen als gaten geïnjecteerd worden in respectievelijk conductie- en valentieband, kunnen deze spontaan recombineren en hun overtollige energie als foton uitstoten. Deze overgang kan echter ook uitgelokt worden door een passerend foton. Interessant is dat het pas gecreëerde foton exact de eigenschappen van het eerst foton imiteert. Men spreekt over gestimuleerde emissie. Ook het omgekeerde doet zich voor, waar een foton door de materiaal geabsorbeerd wordt en zijn energie gebruikt wordt om een hol-elektronpaar te creëren.

Men kan aantonen dat er netto optische winst geboekt wordt wanneer de elektronenbezetting van het hogere energieniveau (de conductieband) groter is dan die van het lagere niveau (de valentieband). Men spreekt dan van populatie-inversie. De voorwaarde voor optische winst kan worden neergeschreven aan de hand van de expressie van Bernard-Duraffourg. Deze drukt duidelijk uit dat in evenwicht nooit winst kan optreden en dat we dus de structuur altijd moeten pompen. In deze toestand van winst is niet gelijk aan laserwerking; het halfgeleidermedium is enkel van een verlies- in een winstmedium veranderd.

Om laserwerking te beschrijven dienen we ook de optische caviteit in acht te nemen. Immers, het licht zal zowel intern als aan de spiegels verliezen ondervinden. Laserwerking begint dan op het moment dat de winst van het medium groot genoeg is om na een weg-en-weer doorgang door de caviteit dezelfde lichtintensiteit te behouden.

Wanneer we dit verder uitwerken, vindt men een aantal nuttige uitdrukking die leiden tot het extraheren van parameters zoals voorgesteld in figuur 3.20.

Bij het ontwerpen van een laserstructuur dienen we rekening te houden met zowel optische als elektrische inperking. Ladingsdragers worden in het aktieve gebied geïnjecteerd en mogen deze niet kunnen verlaten. Dit gebeurt gewoonlijk via heterostructuren. Ook de fotonen moeten in een golfgeleiderstructuur zitten om de optische verliezen te beperken.

Een probleem met heterostructuren is dat wanneer men hun dwarse afmetingen verkleint om quantumputten te vormen de ladingsdragers gemakkelijker uit de structuur ontsnappen en dus niet langer meewerken aan het recombinatieproces. Figuur 3.21 toont een aantal mogelijke oplossingen.

De structuren die we voor deze studie hebben gebruikt zijn gebaseerd op de standaardlasers die op het laboratorium ontwikkeld werden voor emissie bij 980nm. De transversale dimensies werden geschaald met de emissiegolflengte en daarna met specifiek software geoptimaliseerd (zie figuur m). Er werd een direkte vergelijking gemaakt tussen aktieve gebieden die gegroeid werden met TMGa en TEGa. In dit laatste geval diende de groei onderbroken te worden om over te gaan van de ene naar de andere bron, hetgeen niet ideaal is.

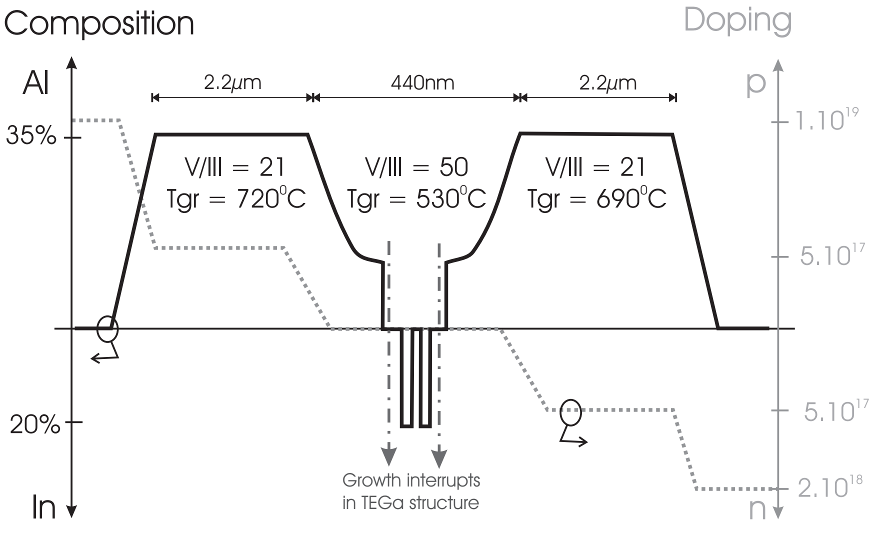

Figuur m   Structuur van de InGaAs laserdiodes (zie figuur 3.22)

Het verdere standaard bewerkingsschema voor de lasers wordt geïllustreerd in figuur 3.23. In figuur 3.24 en tabel 3.1 tenslotte worden de resultaten van beide types lasers weergegeven. Ze zijn nogal middelmatig, maar we will erop wijzen dat het hier gaat over zeer gespannen lagen. Daarenboven bevinden zich in het actieve gebied van de lasers twee quantum putten, in plaats van slechts een in de calibratiemonsters, om een hogere optische winst te kunnen halen. De nabijheid van de twee gespannen lagen maakt ze meer gevoelig voor relaxatie. Ook de invloed van de groeionderbreking op de verliezen in de TEGa structuur zijn duidelijk.

4. Ontwikkeling van een TBAs-proces

4.1 Abstract

4.2 Inleiding en motivering

Klassiek worden voor MOCVD epitaxiaalgroei voor de groep V elementen hydrides gebruikt, waarin het nuttig element gebonden is op waterstofatomen. De groep III elementen komen in zogenaamde organometallische verbindingen voor, met organische groepen (methyl, ethyl, butyl, etc.) als ligand voor het groep III element. Deze materialen waren immers al beschikbaar voor andere industrieën. Pas later heeft men de beperkingen begrepen die door de beperkte keuze aan bronmaterialen werd opgelegd.

De hydrides echter zijn zeer toxisch. Zo is arsine acuut dodelijk in doses van 250ppm. De concentratie waarin men dag-in dag-uit mag worden blootgesteld is zelfs maar 50ppb en er is sprake om dit nog verder te verlagen naar 3ppb. Dit heeft uiteraard grote gevolgen voor de kost inzake veiligheidsvoorzieningen en opleiding van personeel. Daarnaast heeft het ook enkele groeitechnische beperkingen.

In de loop van dit doctoraatswerk werd dan ook het besluit genomen om de hydrides te vervangen door alternatieve precursoren. Dit heeft als gevolg dat het hele groeiproces opnieuw moet worden vastgelegd, ook van materialen als GaAs, AlGaAs en InGaAs.

De eisen die men echter aan groep V bronmaterialen stelt zijn zeer hoog. Tabel 4.1 heeft een overzicht van enkele opties. Uit de tabel komt tertiairbutylarsine (TBAs) als de meest gunstige naar voor. De keuze was dan ook meteen gemaakt. Het is minder toxisch dan arsine en heeft een lagere dampdruk. Ook verhindert het meer dan bij arsine het geval is koolstofvervuiling en het laat toe bij lagere temperaturen te groeien omdat het anders reageert met de andere bronmaterialen. Langs de andere kant is het duurder en minder gemakkelijk te verkrijgen in een voldoende zuivere vorm.

4.3 Tertiairbutylarsine versus arsine

Tabel 4.2 heeft een overzicht van de eigenschappen van beide precursoren. Op de TBAs-molecule is een van arsine's waterstofatomen vervangen door een tertiairbutylgroep (zie figuur 4.1). De binding tussen deze groep en het arseen atoom is aanzienlijk zwakker dan de binding tussen arseen en waterstof. Dit maakt dat het TBAs een lagere decompositietemperatuur heeft. Ook wordt de molecule veel zwaarder hetgeen de dampdruk naar beneden haalt. TBAs op zich is niet zoveel minder toxisch dan arsine, maar het heeft een veel lagere dampdruk, waardoor het zich in geval van een ongeluk minder snel en ver kan verspreiden. Een laatste aspect is de economische kant van de zaak. TBAs is ongeveer tien keer duurder dan arsine. Langs de andere kant laat TBAs toe te groeien bij een lagere V/III verhouding (zie figuur 4.2) zodat de meerkost in de praktijk maar een factor drie bedraagt.

Maar ook het groeimechanisme met beide precursoren is vrij verschillend. Beide materialen kraken aan de hand van een heterogene reactie aan het groeioppervlak. De aanwezigheid van TMGa zal daarbij de decompositie van arsine beïnvloeden, maar die van TBAs niet. De beperkende stap in het geval van arsine is het afsplitsen van het eerste waterstofatoom. Dit waterstof zal dan de methylgroepen van het TMGa aanvallen om vluchtig CH_4 te vormen. Wanneer er door het verlagen van de temperatuur of molaire arsinestroom minder waterstof beschikbaar is blijven de methylgroepen op het oppervlak en veroorzaken er koolstofvervuiling.

Het is onduidelijk hoe de pyrolyse van TBAs exact verloopt. Wel heeft men vastgesteld dat er AsH_x radicalen worden gevormd. De waterstofatomen ervan zijn zeer efficiënt in het vangen van de methylgroepen waardoor er minder op het oppervlak achterblijven.

4.4 MOCVD-epitaxiaalgroei met TBAs

In wat volgt bestuderen we de eigenschappen van GaAs, AlGaAs en InGaAs. We gaan dieper in op de morfologie, achtergrondvervuiling, optische kwaliteit en electrische eigenschappen.

4.4.1 Experimenteel

Alle lagen werden gegroeid in de verticale roterende reactor van Thomas Swan. De reactordruk is typisch 76torr, bij een temperatuur tussen de 500ºC en 760ºC en waterstofdragerstromen van 5.6 millimol per seconde. De susceptor roteert met een snelheid van 300 rotaties per minuut.

4.4.2 Morfologie

Voor de morfologie is vooral de V/III verhouding van belang. Uit thermodynamische overwegingen kan men al aantonen dat deze groter moet zijn dan een, wil men een enkele vaste halfgeleiderfase bekomen. Is dit niet het geval bij bvb. GaAs, dan vormen zich snorharen met een galliumdruppel op het uiteinde. Om het halfgeleiderkristal te stabiliseren zal men de V/III verhouding dus typisch hoog genoeg kiezen. Alle hierna beschreven epitaxiaallagen waren glad en spiegelend.

4.4.3 Achtergrondvervuiling

Door intrinsieke eigenschappen van de bronmaterialen of door vervuiling en onvoldoende purificatie tijdens het productieproces ervan zullen sporen van atomaire onzuiverheden nalaten in de epitaxiaallagen. Deze geven aanleiding tot ongewenste effecten zoals het verstrooien van ladingsdragers, ongewenste dotering van de laag of het vormen van diepe niveaus die ladingsdragers kunnen vangen of niet-radiatieve recombinatie promoten.

We hebben deze vervuiling bestudeerd aan de hand van SIMS. Hierbij wordt het oppervlak gebombardeerd met zware ionen, typisch Cs+, en wordt met een massaspectrometer bekeken welke atomen uit het monster worden weggeslagen.

Figuur 4.3 en 4.4 tonen de SIMS-resultaten voor koolstof en zuurstof. Voor koolstof liggen alle signalen nabij de detectielimiet van het apparaat. Toch is TBAs een iets betere keuze. Ook zullen een hogere V/III en hogere temperatuur guinstig zijn, omdat dan de arseenbronnen bij het kraken meer waterstofradikalen produceren. Voor zuurstof liggen de niveaus zelfs beneden de detectielimiet.

AlGaAs is al wat moeilijker om te groeien. De eenvoudige reden ligt bij het aluminium dat sterke verbindingen vormt met zowel zuurstoof als koolstof. Figuur n en 4.6 tonen de SIMS-data voor koolstof en zuurstof in $Al_{35}Ga_{65}As$-lagen. De koolstofniveaus liggen relatief hoog, ook al worden dezelfde algemene trends gevolgd als bij GaAs. Bij eenzelfde V/III verhouding en temperatuur zal TBAs minder vervuilen met koolstof dan arsine, om dezelfde reden als bij GaAs.

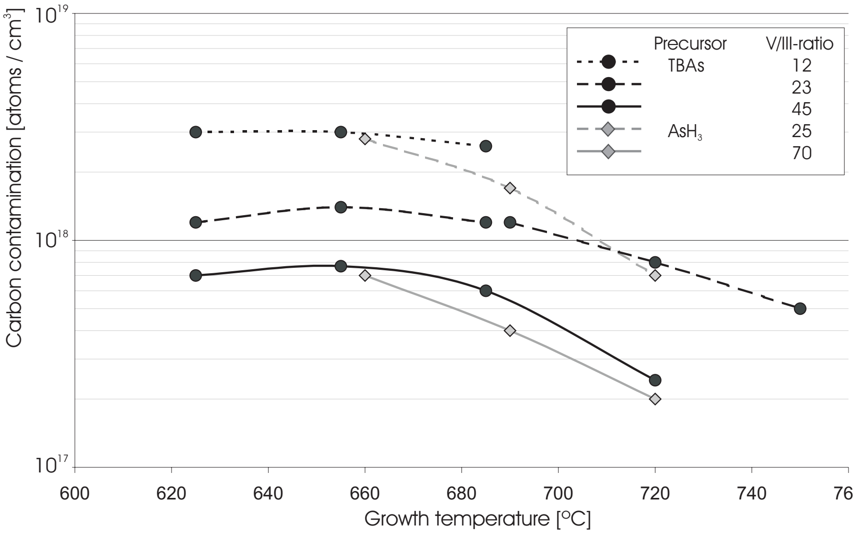

Figuur n *SIMS-data van de koolstofachtergrond in* $Al_{35}Ga_{65}As$ *materiaal (zie figuur 4.5)*

Het grootste probleem voor AlGaAs echter is zuurstof. Er is aangetoond dat 1 ppm zuurstof in de gasfase een vervuiling veroorzaakt van 10^{19} atomen per kubieke centimeter. Daarom moeten extreme maatregelen getroffen worden om alle zuurstof uit de reactor en gastoevoer te verwijderen. Opnieuw presteert TBAs beter dan arsine, al moet er opgemerkt worden dat de data voor arsine niet 100% betrouwbaar kunnen zijn.

We hebben ook de invloed van de groeisnelheid op de achtergrondvervuiling nagegaan. Daarvoor beschouwen we twee gevallen. In het eerste geval varieert de TBAs-flow mee met de groep-III flow en hebben we dus een konstante V/III verhouding; in het tweede houden we gewoon de TBAs-flow konstant. De resultaten staan in figuur 4.7 en 4.8. Wat opvalt is dat koolstof en zuurstof fundamenteel tegengestelde tendensen volgen. Koolstof is immers een intrinsiek deel van de groep-III bronmolecule. Hoe lager de groeisnelheid, hoe meer tijd de metylgroep krijgt om een waterstofradicaal aan de haak te slaan. Bij zuurstof daarentegen is niet de desorptie de beperkende factor, maar adsorptie. Eens het de kans krijgt zich aan een aluminiumatoom te binden zal het die binding moeilijk doorbreken. Daarom zal een hogere groeisnelheid ervoor zorgen dat gemiddeld minder aluminium-zuurstofverbindingen ontstaan.

Dit patroon vindt men ook terug wanneer men de invloed van de groep V overdruk beschouwt. Een lage koolstofachtergrond vereist een hoge V/III verhouding terwijl voor zuurstof vooral een hoge absolute groep V flow van belang is. Voor koolstof is dit mechanisme duidelijk. Bij zuurstof is het een geval van concurrentie. Meer arseen verhoogt de kans dat het aluminium zich bindt op een arseen en niet op zuurstof.

Natuurlijk, hoe hoger het aluminiumgehalte, hoe moeilijker het wordt om zuiver materiaal te groeien. Dit wordt geïllustreerd in figuur 4.9 en 4.10 voor $Al_{80}Ga_{20}As$. Ook al zijn de niveuas hoog in absolute termen, ze zijn zeer aanvaardbaar gezien het hoge aluminiumgehalte. Opnieuw doet TBAs beter dan arsine bij eenzelfde V/III verhouding.

Gebaseerd op deze SIMS-studies hebben we dan een aantal standaard groeicondities gedefinieerd voor verschillende materiaal-samenstellingen en doperingen. Deze worden samengevat in tabel 4.3. Voor de V/III verhouding zijn dit minimumwaardes, omdat een hogere waarde typisch betere resultaten geeft.

4.4.4 Optische kwaliteit

Uiteraard is voor lichtemitterende componenten de kwaliteit van het aktief gebied zeer belangrijk. Daarom hebben we de efficiëntie van de radiatieve recombinatie van de veel gebruikte GaAs/AlGaAs en InGaAs/GaAs quantumputten gekarakteriseerd aan de hand van fotoluminescentie. De gebruikte structuur en groeiparameters zijn weergegeven in tabel 4.4 voor de GaAs/AlGaAs quantumputten. De gebruikte V/III verhouding voor TBAs is ongeveer de helft van de waarde die we voor arsine gebruiken. Figuur o geeft de

PL-spectra weer. Zowel in termen van intensiteit als lijnbreedte zijn de beide processen evenwaardig.

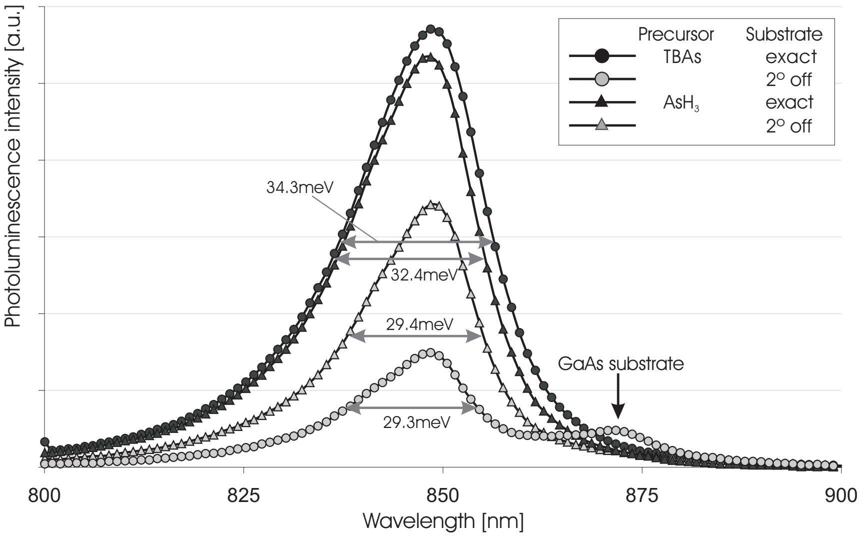

Figuur o *Vergelijking van de PL-spectra van 850 nm GaAs/ALGaAs quantumputten (zie figuur 4.11)*

Tabel 4.5 geeft de structuur weer van de InGaAs/GaAs quantumputten. Opnieuw gebruikten we voor TBAs de helft van de V/III verhouding in vergelijking met het arsine proces. Figuur p toont dat beide processen een zeer vergelijkbaar resultaat opleveren.

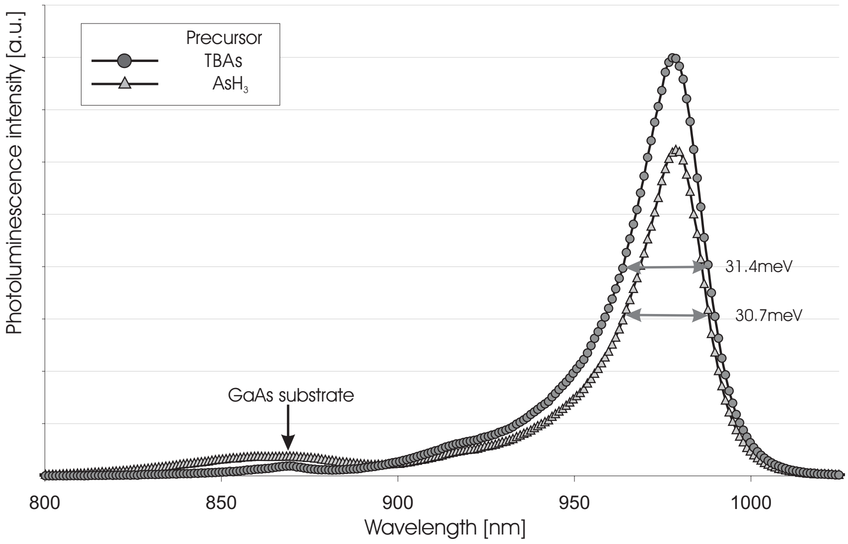

Figuur p Vergelijking van de PL-spectra van 980 nm InGaAs/GaAs quantumputten (zie figuur 4.12)

4.4.5 Electrische eigenschappen en dotering

Nog een stapje dichter bij componenten staat de studie van elektrische eigenschappen en gecontroleerde dotering van de materialen. Het bestaande arsineproces voor (Al)GaAs-lagen gebruikte daartoe de bronmaterialen diethylzink (DEZn) en silaan (SiH_4) en werd vrij goed begrepen en gecontroleerd.

Zink gedraagt zich als een p-type additief. Het diffundeert sterk op hoge temperatuur en in hoge concentraties. Een mogelijk alternatief is het gebruik van koolstof, ofwel met een extra bronmateriaal, ofwel door een intelligent gebruik van groeiparameters.

Silicium is een element uit groep IV en kan zich daarom amfoteer gedragen. Hoewel het preferentieel een kristalplaats van de groep III elementen inpalmt om dan een n-type donor te worden, zal het bij verzadiging ook de groep V plaatsen bezetten en zich als p-type gedragen. Zodoende compenseert het zijn eigen n-dopering en wordt het halen van hoge n-type dopeerniveaus onmogelijk. In de praktijk verzadigt het n-niveau rond 2.10^{18} a 4.10^{18}. Met selenium zijn hogere niveaus haalbaar, maar dit element diffundeert opnieuw zeer gemakkelijk.

Figuur 4.13 toont het dopeergedrag van GaAs met DEZn voor zowel arsine als TBAs. De incorporatie gebeurt sublineair en neemt af met stijgende temperatuur. Met TBAs is de incorporatie ongeveer twee keer zo efficiënt.

Bij silaan is het verschil nog groter (figuur 4.14). De incorporatie is nu een factor tien hoger bij TBAs dan bij arsine. Dit wordt verklaard door het feit dat silaan op groeitemperatuur niet volledig gekraakt is. TBAs heeft een catalyserend effekt op de pyrolyse, weer omdat het zeer efficiënt waterstofradikalen produceert.

Metingen van lagen die aluminium bevatten met polaron zijn een stuk moeilijker omdat het aluminium reageert met het electroliet. Ook is de koolstofachtergrond hoger zodat we een p-type materiaal krijgen van ongeveer $2.5.10^{17}$ voor $Al_{35}Ga_{65}As$.

De data voor het doteren met zink staan in figuur 4.15. De resultaten lopen gelijk met wat we kenden uit het arsineproces. Het is interessanter om de data van het n-type doteren te gaan bekijken omdat we nu het effect van compensatie en amfotericiteit kunnen zien (figuur 4.16). Deze effecten maken het doteren in hogere en lagere concentraties minder eenvoudig.

4.4.6 Besluiten

In een direkte vergelijking tussen de twee processen zien we dat TBAs toelaat te groeien op lagere temperaturen en bij lagere V/III verhoudingen. Het proces laat ook toe materiaal te verkrijgen met aanvaardbare elektrische en optische kwaliteiten. Maar de echte test voor het proces komt er pas wanneer we het gaan gebruiken voor componenten.

4.5 Validatie van het nieuwe proces

4.5.1 GaAs/AlGaAs zonnecellen met een enkele junctie

Parallel aan de studie van de epitaxiaalgroei met TBAs liep er op het laboratorium ook een programma voor de ontwikkeling van GaAs-zonnecellen en groei op germaniumsubstraten. Toepassing van het vorige op deze programma's laat toe om de kwaliteit ervan te toetsen in een praktische toepassing.

De eenvoudigste zonnecel is eigenlijk een gewone p-n diode. Wanneer de diode belicht worden zullen fotonen met voldoende energie interageren met de halfgeleider en er elektron-gatparen creëren. Deze kunnen vrijuit bewegen tot ze het ingebouwde elektrische veld van de diode voelen en van elkaar gescheiden worden om tenslotte aan de contacten verzameld te worden.

Het meest kritische is de diffusie van de elektronen in p-type en de gaten in n-type materiaal. Minoritairen zijn zeer gevoelig aan elke vorm van verstoring in het rooster, daar er een grote hoeveelheid majoritairen aanwezig is om mee te recombineren.

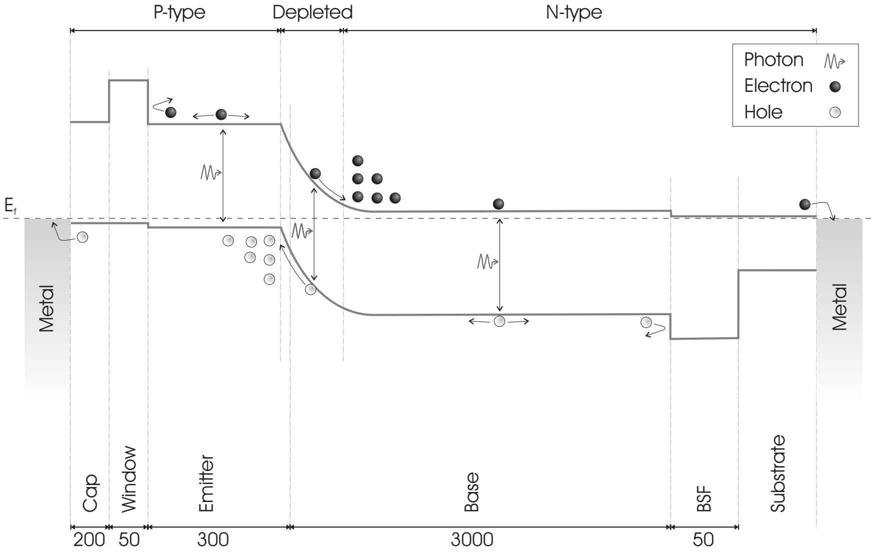

Figuur q Bandenstructuur van de gebruikte zonnecel (zie figuur 4.17)

De cel die we gebruikten voor deze studie is een beetje complexer (zie figuur q). Immers, zelfs wanneer de materiaalkwaliteit goed is zullen de oppervlakken aan voor- en achterzijde voor grote verliezen zorgen. Vooral de achterzijde die volledig gemetalliseerd is voor ohmse contacten is een probleem. Dit wordt opgelost door het invoegen van een extra “back surface field” die de gaten tegenhoudt. Aan de voorzijde is dit niet zo’n groot probleem omdat de contactoppervlakte kleiner is, maar ook de GaAs-lucht interface zorgt voor een belangrijke bron van recombinatie. Dit wordt verholpen met een vensterlaag die het onderliggende GaAs passiveert en door een goedgekozen samenstelling weinig licht absorbeert.

Het gedrag van een zonnecel kan volledig beschreven worden aan de hand van zijn I-V karakteristiek. Figuur r toont deze, samen met de belangrijkste parameters zoals kortsluitstroom, openklemspanning en vulfactor.

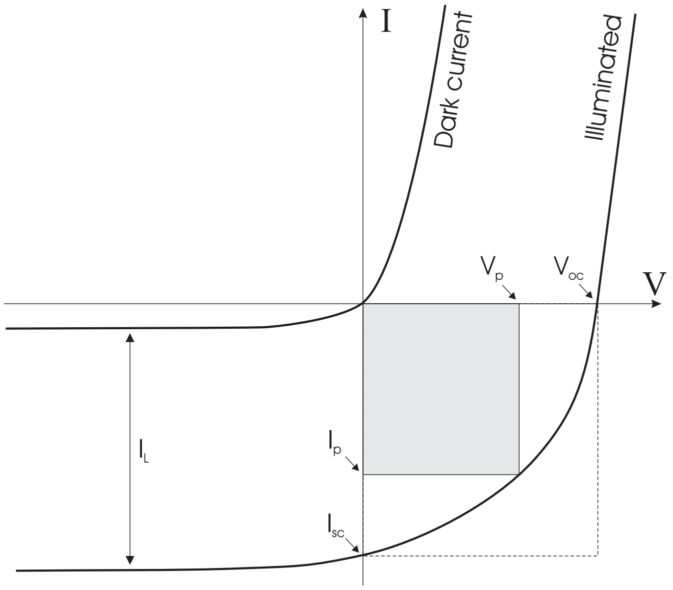

Figuur r IV-karakteristiek van een zonnecel (zie figuur 4.18)

Ook de groei op germanium schept zo zijn eigen problemen. III-V halfgeleiders zijn immers een polaire verbinding, terwijl dit bij germanium niet het geval is. Dit kan aanleiding geven tot antifasedomeinen (zie figuur 4.19). Men kan dit fenomeen onderdrukken door een gepaste keuze voor de off-oriëntatie van het substraat en de GaAs nucleatielaag.

Andere problemen die zich kunnen voordoen zijn autodotering en crossdotering van de gegroeide laag. Ook zijn de roosterkonstantes niet helemaal identiek. Voor dikke structuren zoals de zonnecel kan het nodig zijn om een fractie indium toe te voegen en zo de roosterkonstante te beïnvloeden.

Een ideale studie zou bestaan uit een vergelijking van zowel GaAs en germanium substraten als van de twee arseenbronnen in een identieke structuur en processing. Helaas is dit niet altijd mogelijk omdat in de loop van de groeistudie ook het een en ander werd geoptimaliseerd aan de processing.

Tabel 4.6 geeft een overzicht van de verschillen in de zonnecelstructuur en de gebruikte substraten en precursoren. Tabel 4.7 geeft een uitgebreid overzicht van de gebruikte groeicondities. Behalve de triviale verschillen wijzen we nog op het verschil in de dikte van de emitter. Een dikkere emitter heeft immers een lagere serieweerstand. Deze was nodig omdat het masker eigenlijk ontworpen is voor een n-op-p structuur. Als we zoals hier een p-op-n structuur gebruiken moet de lage mobiliteit van de gaten gecompenseerd worden.

Ook hier wijzen we erop dat de cellen van het arsineproces niet in optimale condities werden gegroeid. Na het weghalen van de arsine konden de experimenten niet meer herhaald worden.

Tenslotte zijn er ook verschillen in het processingschema. Deze staan samengevat in tabel 4.8 en slaan vooral op het gebruikte maskerset en de keuze en diktes van de antireflectielaag (AR). Figuur 4.20 beschrijft de processing zelf.

De belangrijkste opmerking die we willen maken bij het bespreken van de karakterisatie van de cellen is dat bij de cellen op germanium een kleine hoeveelheid indium is toegevoegd om roosteraanpassing te verkrijgen. Deze zal de bandafstand met zo’n 15 meV verkleinen en dus het absorptiebereik van de cel naar langere golflengtes uitbreiden. Figuur 4.21 toont hoe dat een toename van de kortsluitstroomdichtheid van 1.5 mA/cm^2 zal opleveren.

Daarnaast zijn bijna alle gemeten parameters functie van de specifieke processing van de cel. Door de onderlinge variatie is een direkte vergelijking zeer moeilijk. In plaats zullen we als vergelijking de interne quantumefficiëntie bekijken. Hieruit kunnen we ook een berekende kortsluitstroomdichtheid afleiden die minder afhankelijk is van de processing.

De parameters van de verschillende cellen staan in tabel 4.9. De verschillen tussen de gemeten en berekende kortsluitstroomdichtheid zijn duidelijk te wijten aan de verschillende reflectiviteit van de respectievelijke AR-lagen. De belangrijkste parameter in verband met materiaalkwaliteit is de open-klem spanning. Zijn waarde wordt echter beïnvloed door het toevoegen van indium. De waarde van de vulfactor (FF) is sterk verwant aan de serieweerstand van de emitter. Een dikkere emitter heeft dan ook een gunstig effect.

Wanneer we germanium en GaAs substraten willen vergelijken, dan moeten we kijken naar structuren A vs. B en D vs. E. Figuur s toont de interne quantumefficiëntie van de structuren D en E. Aan de kant van de langere golflengtes valt onmiddellijk het effect van het indium op. In de tabel 4.9 wijzen we opnieuw op het effect van indium op de kortsluitstroomdichtheid en openklemspanning.

De conversieefficiëntie tenslotte is het moeilijkst te vergelijken omdat ze afhangt van zowel structuur, materiaalkwaliteit als processing. Zo hebben de cellen die gegroeid werden met arsine vooral last van een minderwaardige processing. Figuur t toont echter de interne quantumefficiëntie van een cel uit het arsineproces en een uit het TBAs-proces. De resultaten zijn moeilijk van elkaar te onderscheiden. Vergelijken we cellen D en E die een gelijkwaardige processing hebben ondergaan, dan zien we dat het effect van indium op de kortsluitstroom die op de openklemspanning domineert.

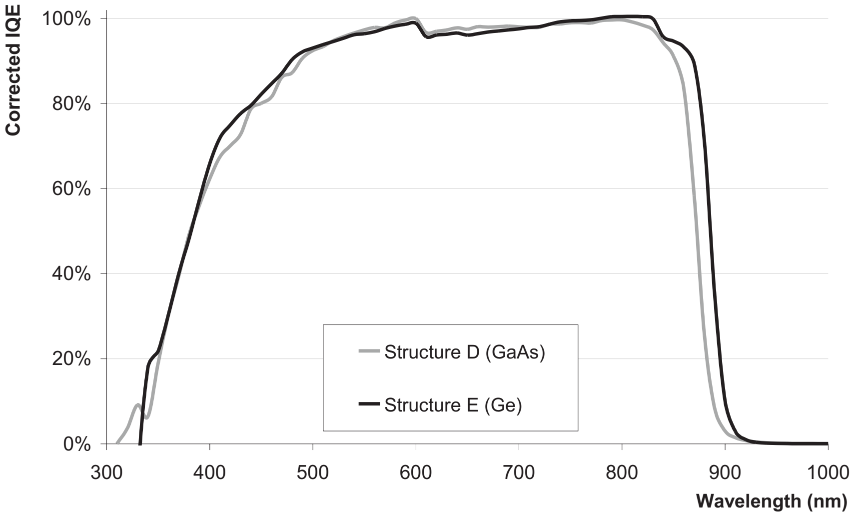

Figuur s *Interne quantumefficiëntie van vergelijkbare zonnecellen gegroeid op GaAs en germanium (zie figuur 4.22)*

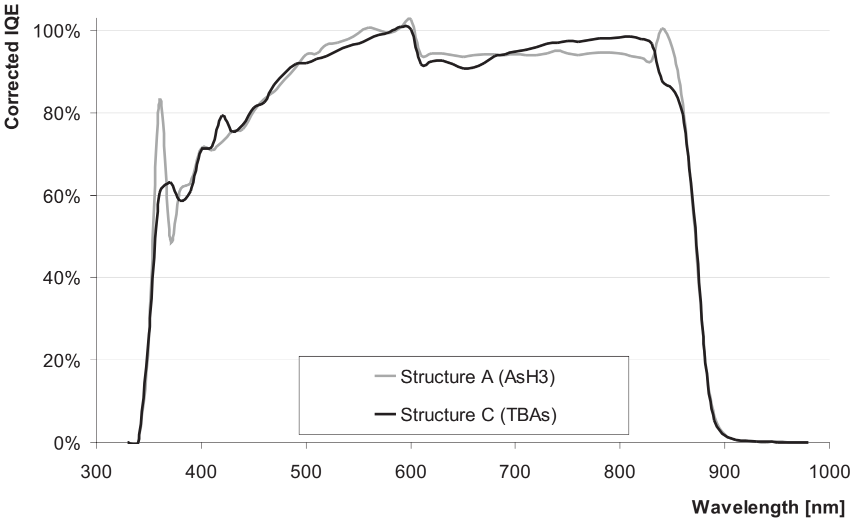

Figuur t *Interne quantumefficiëntie van vergelijkbare zonnecellen gegroeid met arsine en TBAs (zie figuur 4.23)*

We mogen echter besluiten dat we met het TBAs-proces en gebruik makend van de goedkopere en robustere germanium substraten erin geslaagd zijn zonnecellen te maken van heel hoge kwaliteit. Het Fraunhofer instituut te Freiburg heeft bevestigd dat de conversie efficiëntie van 24.4% onder het AM1.5 zonnespectrum een wereldrecord waarde is voor een p-op-n GaAs zonnecel op germanium!

4.5.2 InGaAs randemitterende lasers bij 980nm golflengte

Een tweede deel van de validatie van het TBAs-proces omvat de fabricatie van standaard 980nm InGaAs lasers. Het betreft een ontwerp dat alle geruime tijd op het laboratorium wordt gebruikt en waarvan de processing goed gecontroleerd wordt. De structuur wordt geïllustreerd in figuur 4.24. Daarnaast is er ook een tweede structuur gegroeid met als bedoeling een lagere drempelstroom te bekomen. Die bevat 65% aluminium in de keerlagen en slechts een quantum put.

De resultaten van de karakterisatie worden samengevat in 4.25 en tabel 4. 10. De eerste componenten hebben last van een hoge serieweerstand in de keerlagen. De geëxtrapoleerde drempelstroomdichtheid voor oneindige lengte echter is zeer laag (220A/cm^2).

Een tweede iteratie van het proces leverde de resultaten uit tabel 4.11 op. Ondanks een trade-off inzake interne verliezen zijn we er echter in geslaagd om componenten te maken met goede karakteristieken zoals een interne quantum efficiëntie van meer dan 90 procent.

5. Epitaxiaalgroei van arseenverdunde nitrides.

5.1 Abstract

5.2 Inleiding

In het tweede hoofdstuk hebben we reeds een uiteenzetting gegeven van de buitengewone eigenschappen van het GaNAs en GaInNAs materiaal. In dit hoofdstuk gaan we dieper in op de experimentele resultaten van de epitaxiaalgroei van het materiaal.

Eerst wijzen we erop hoe de resultaten uit de vorige twee hoofdstukken, waar we lage temperatuursgroei en de TBAs-ontwikkeling bespreken een ideale voorbereiding zijn voor deze studie.

We geven ook een overzicht van de groeicondities die gebruikt worden door andere onderzoeksgroepen. Figuur 5.1 toont het effect van de groeitemperatuur op de stikstofincorporatie. Bij een temperatuur die hoger ligt dan 535ºC treedt desorptie op van het stikstof aan het groeioppervlak.

Het effect van de relatieve verhouding van DMHy en TBAs flows, die meestal wordt uitgedrukt in de relatieve DMHy flow (DMHy/DMHy+TBAs) wordt getoond in figuur 5.2. Deze figuur toont tevens hoe ook het indiumgehalte van de laag de stikstofincorporatie beïnvloedt.

Een laatste punt is dat van de groeisnelheid (zie figuur 5.3) en het bestaan van een stikstofvangend effect.

5.3 Stikstofbronnen

Vooraleer we de epitaxiaalgroei kunnen aanvatten, dienen we uiteraard een geschikt bronmateriaal te selecteren. Net als bij de selectie van de arseen-bron moet het materiaal aan een aantal criteria voldoen. Uit een vergelijking van meerdere bronnen kiezen we uiteindelijk voor het onsymmetrisch dimethylhydrazine (DMHy). De DMHy-molecule en zijn belangrijkste eigenschappen zijn weergegeven in figuur 5.4 en tabel 5.1

5.4 Eerste resultaten met arsine

5.4.1 Experimentele condities

De standaard groeicondities bestaan uit een reactordruk van 76torr, met een susceptorrotatie van 300rpm en een draaggasflow van twee keer acht gasliter per minuut per manifold. Als bronmaterialen gebruiken we arsine, trimethylindium, trimethylgallium en het dimethylhydrazine. Voor sommige experimenten zijn atmosfeerdruk en triethylgallium gebruikt, maar dit wordt dan expliciet vermeld.

Thermisch nabehandelen gebeurde ofwel ex-situ in een RTA oven met een GaAs arsenide wafer als bescherming bovenop het monster; ofwel in-situ in de reactor onder een arseen overdruk. Typisch duurt een behandeling tien minuten op 760ºC.

5.4.2 GaNAs

De eerste experimenten zijn gefocuseerd op stikstofincorporatie in GaAs. De gegroeide lagen zijn 800nm dik. Morfologisch gezien zijn de monsters perfect, behalve bij hele hoge stikstofinhoud waar dan cross-hatch optreedt. Uit XRD-metingen blijkt dat alle lagen perfect gespannen zijn.

We kunnen voor deze lagen de stikstofinhoud bepalen aan de hand van x-straaldiffractie. De belangrijkste parameters zijn de temperatuur en de verhouding van arsine- en DMHy-flows. Figuur 5.5 toont het temperatuursafhankelijkheid van de stikstofincorporatie. Vanaf 530ºC zakt deze dramatisch. Figuur l toont de stikstofinhoud als functie van de relatieve DMHy-flow. Alleen bij zeer hoge waardes van deze relatieve flow komt er stikstof in de laag. Om een minimum aan kwaliteit te garanderen is er een onderdrempel aan de arsineflow. Dit betekent dus dat de DMHy-flow dan zeer hoog moet zijn.

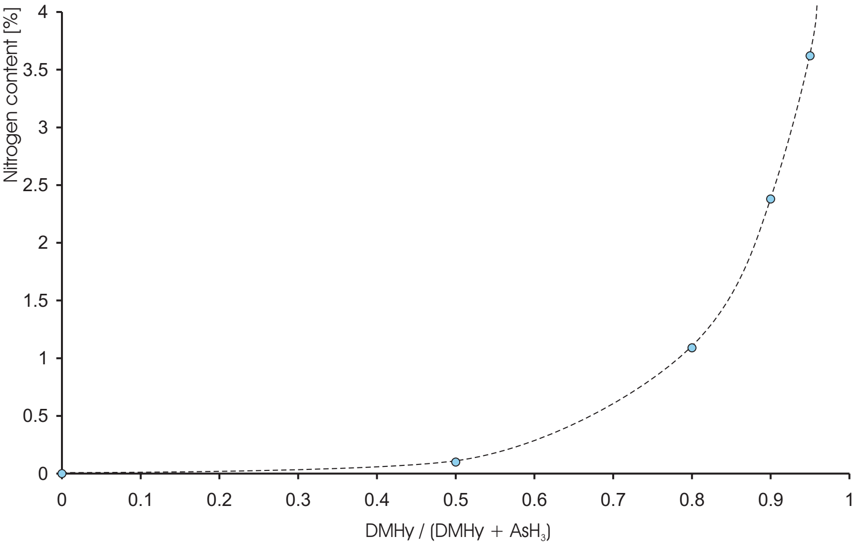

Figuur u Stikstofincorporatie in GaAs als functie van de verhouding DMHy/(DMHy+TBAs), gegroeid op 535°C met arsine (zie figuur 5.6)

Ook al is het mogelijk om een redelijk percentage stikstof te halen, het effect van de stikstof op de optische kwaliteit is dramatisch. Figuur 5.7 toon een photoluminescentiespectrum van een GaNAs sample met 0.6% stikstof. De intensiteitsschaal is genormeerd naar de intensiteit die we mogen verwachten van een GaAs bulk laag. De gemeten intensiteit is ongeveer drie grootteordes lager!

5.4.3 GaInNAs

Een eerste probleem dat opgelost dient te worden wanneer we quaternaire lagen gaan bestuderen, is het bepalen van de samenstelling van de gegroeide quantumputten. Er zijn dan namelijk drie onafhankelijke parameters te bepalen: indium-galliumgehalte, stikstof-arseengehalte en de dikte. Met x-straaldiffractie kunnen we er twee aan elkaar linken, en een derde (de dikte) bepalen zij het relatief onnauwkeurig.

Soms neemt men de indiuminhoud en dikte over van een calibratiemonster. Dit is echter een gevaarlijke veronderstelling omdat geweten is dat de introductie van DMHy beide beïnvloedt.

Daarom moet men een tweede verband opleggen aan de hand van een bepaling van de bandafstand door een optische meting. We gebruiken dan een empirisch verband uit de literatuur om de uit de emissiegolflengte het stikstofgehalte te bepalen. Figuur 5.8 toont dit verband voor een quantumput met 37.5% indium en 0.5% stikstof.

Bij de groei zelf komen twee problemen voor. Het eerste is het uitdoven van de PL-emissie met toenemende stikstofinhoud, het tweede is de moeilijkheid om zelfs een kleine fractie stikstof in de laag te krijgen.

Figuur v toont de PL van een referentie InGaAs quantumput en twee GaInNAs quantumputten met 0.33% en 0.45% stikstof. Een van de monsters onderging een thermische behandeling. De PL van dit monster neemt na de behandeling weer toe in intensiteit maar verschuift ook terug naar de kortere golflengtes.

Een mogelijke oorzaak voor de slechte optische kwaliteit werd bestudeerd met TEM (zie figuur 5.10). Aan de interfaces van de quantumputten verschijnt een tussenlaag (indiumarm of stikstofrijk). Dit probeerden we door het invoegen van een groeionderbreking te onderdrukken. Figuur 5.11 toont hoe dit zorgt voor het ontstaan van dikteïnhomogeniteiten.

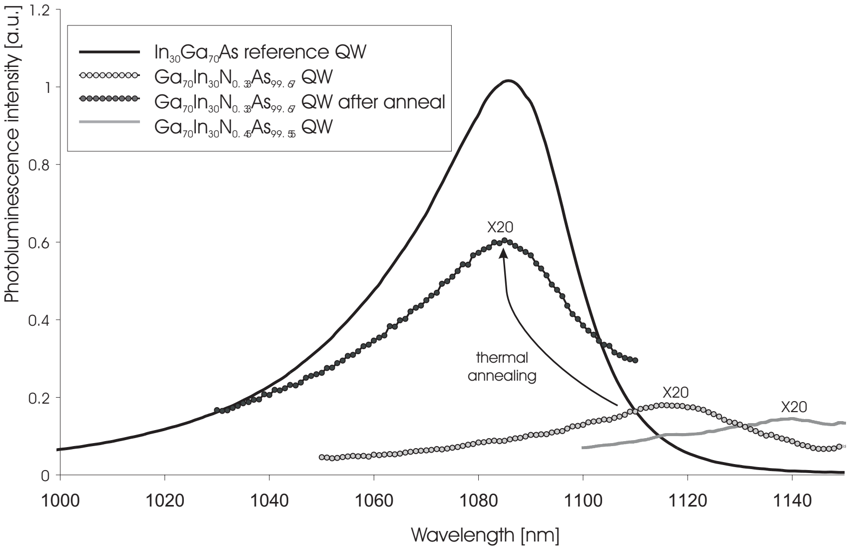

Figuur v *Fotoluminescentie van GaInNAs quantumputten gegroeid op 76torr en 535°C met arsine (zie figuur 5.9)*

We onderzochten verder de invloed van de reactordruk. Bij groei op atmosfeerdruk (700torr) zal een bepaalde molaire flow een grotere partieeldruk vertegenwoordigen en het halfgeleidermateriaal beter kunnen stabiliseren. Langs de andere kant zijn prereacties meer waarschijnlijk omdat de molecules een hogere botswaarschijnlijkheid hebben. Figuur 5.12 toont de PL-spectra van drie representatieve monsters met opnieuw het uitdoven van de PL-efficiëntie door slechts een fractie stikstof.

Figuur 5.13 toont daarenboven nog het effect van de onverwacht lage stikstofincorporatie. We merken op dat het onmogelijk is om de DMHy/groepV verhouding nog verder te verhogen omdat dit impliceert dat de arsine flow dan te laag wordt.

Een laatste opmerking in dit verband willen we maken met betrekking tot de soms dubieuze kwaliteit van het DMHy. Figuur 5.14 toont de PL van twee keer twee identieke structuren, maar gegroeid met DMHy van verschillende leveranciers. In het ene geval is de optische kwaliteit een grootteorde lager, hetgeen te wijten is aan contaminatie van de bron.

5.5 Epitaxiaalgroei van arseenverdunde nitrides met TBAs

5.5.1 Experimentele condities

De standaard groeicondities bestaan uit een reactordruk van 76torr, met een susceptorrotatie van 300rpm en een draaggasflow van twee keer acht gasliter per minuut per manifold. Als bronmaterialen gebruiken we tertiairbutylarsine, trimethylindium, triethylgallium en het dimethylhydrazine. De groeitemperatuur is typisch 535ºC. Thermisch nabehandelen gebeurde voor de GaInNAs quantumputten in-situ in de reactor onder een TBAs overdruk, gedurende tien minuten op 760ºC te houden. Als groeisnelheid gebruiken we 1.08µm per uur voor GaNAs en 0.07µm per uur voor GaInNAs. Als substraat gebruiken we (1 0 0) exact georiënteerde ongedopeerde GaAs-wafers.

GaNAs-monsters groeien we 300nm dik met een 30nm GaAs toplaag er boven op. De enkele GaInNAs quantumputten zijn nominaal 6.5nm dik met een 100nm GaAs toplaag. Er zijn geen groeionderbrekingen.

5.5.2 GaNAs

Ook hier bepalen we de stikstofinhoud aan de hand van hoge-resolutie x-straal diffractie in combinatie met simulatie m.b.v. dynamische simulatie theorie. Figuur 5.15 toont een voorbeeld van een dergelijke meting met simulatie voor een GaNAs laag met 2.4% stikstof. Aan de hand van afbeeldingen uit de reciproke ruimte rond asymmetrische reflecties (zie figuur w) kunnen we afleiden dat de lagen steeds 100% gespannen zijn.

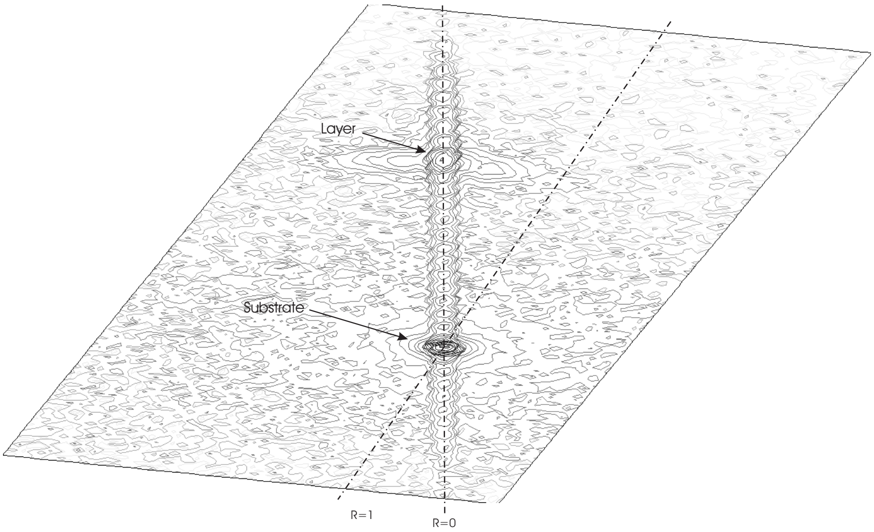

Figuur w XRD afbeelding in de reciproke ruimte rond de <-1 1 5> reflectie van een GaNAs monster met 1.5% stikstof (zie figuur 5.16)

De eerste parameter onder beschouwing is de groeitemperatuur. We hebben een interval rond het 530ºC punt afgegaan (cfr. de studie met arsine en figuur 5.5). De resultaten staan weergegeven in figuur 5.17 en tonen dat eenzelfde desorptiegedrag optreedt, wat erop wijst dat we niet met een chemische (pre-)reactie te maken hebben maar met een fysisch (thermodynamisch) fenomeen.

In tegenstelling tot wat in de literatuur wordt beweerd, vinden we in deze studie dat het stikstofincorporatiegedrag niet eenduidig wordt bepaald door de DMHy over groep V verhouding. Figuur x toont onze bevindingen. Voor verschillende waardes van de TBAs-flow vinden we verschillende curves in het diagramma. Dit wordt nader toegelicht in figuur 5.19, waar we dezelfde data uitzetten, maar nu als functie van de TBAs-flow en dit voor verschillende DMHy-flows. Het stikstof-gehalte neemt duidelijk toe met toenemende TBAs-flow tot op een zeker punt waar het terug naar beneden valt. Deze tendens werd ook bevestigd door bepalingen van de optische absorptie rand van het materiaal zoals bepaald met fotoreflectantiemetingen (zie figuur 5.20). Langs de andere kant toont figuur 5.21 hoe de stikstofincorporatie lineair afhankelijk is van de DMHy-flow, voor verschillende waardes van de TBAs-flow.

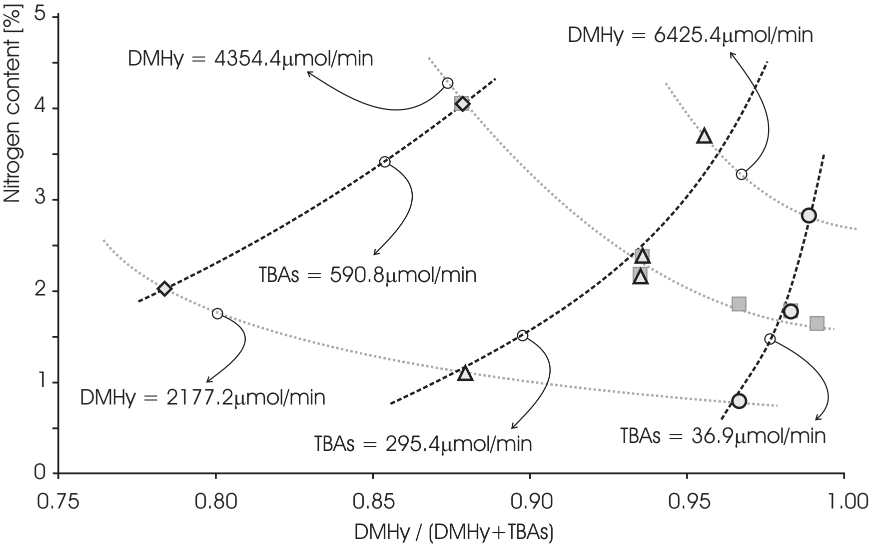

Figuur x Stikstofincorporatie in GaNAs, gegroeid bij 535°C met TBAs (zie figuur 5.19)

Dit afwijkende gedrag kan niet verklaard worden door gasfase gerelateerde effecten en moet dus zijn oorzaak hebben in een effect aan het groeioppervlak. Een mogelijke verklaring is dat een met arseen bedekt oppervlak de adsorptie en reactie van DMHy-moleculen stimuleert. Langs de andere kant zal bij een te hoge bedekkingsgraad het DMHy eerder desorberen.

5.5.3 *GaInNAs*

Vervolgens voerden we een gelijkaardige studie uit bij GaInNAs lagen. We gebruikten data uit TEM, PL, XRD en PR.

De TEM-foto's onthulden geen verspreide defecten of variaties in de quantumputten. Aan de hand van het kontrastprofiel kunnen we twee parameters extraheren: de breedte op het halve maximum die een maat is voor de dikte van de put en de breedte aan de basis, die ons iets vertelt over de abruptheid van de interface. Dit wordt weergegeven in figuur 5.22. Het is duidelijk dat voor hogere TBAs-flows de overgang meer abrupt wordt.

Vervolgens werden de monsters optisch onderzocht met PL en PR. De meetresultaten op kamertemperatuur vinden we terug in figuur 5.23. De energie van de optische overgangen bij zowel PL als PR dalen met toenemende TBAs-flow, consistent met een toenemend stikstofgehalte. Figuur 5.24 toont de energie van de overgangen, samen met de breedte van de spectra. Deze breedtes zijn een maat voor de optische kwaliteit van de quantumput. Ze nemen af met de TBAs-flow tot op een bepaald punt waar de grote stikstofinhoud gaat domineren en de optische kwaliteit opnieuw afneemt.

We hebben dezelfde trends waargenomen in lagetemperatuursmetingen. Deze worden weergegeven in figuur y. Uit deze metingen kunnen we een extra parameter afleiden, namelijk de Stokesverschuiving. Het is het verschil tussen de energie van een de absorptierand van het materiaal en de energie van de geëmitteerde fotonen en is opnieuw een maat voor de optische kwaliteit. De tendens en verklaring is dezelfde als voor de kamertemperatuurmetingen.

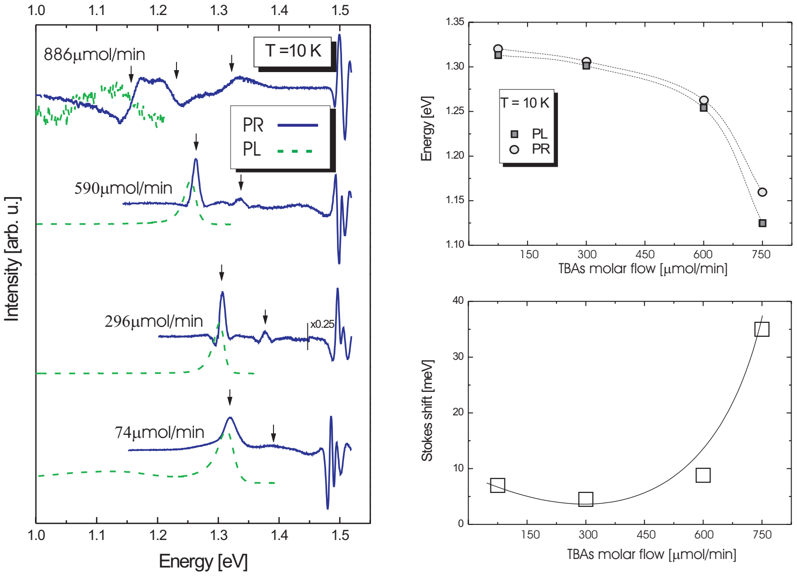

Figuur y Lage temperatuurs PL en PR spectra van GaInNAs quantumputten (zie figuur 5.24)

Om de materiaalsamenstelling te bepalen gaan we gebruik maken van deze transitie-energieën samen met de diktes zoals die bepaald zijn met TEM. Daarenboven gaan we ervan uit dat de indium-\concentratie 18.5% bedraagt. Dit kan omdat de reproduceerbaarheid van de reactor zeer goed is en vooral omdat de DMHy-flow, die ervoor verantwoordelijk wordt geacht invloed uit te oefenen op dikte en samenstelling, konstant blijft. Het resultaat van de berekening staat in figuur 5.26.

Daarnaast bekijken we de invloed van indium op de stikstofincorporatie. Het is welbekend dat door de zwakkere indium-stikstofverbinding in vergelijking met de gallium-stikstofverbinding stikstof gemakkelijker desorbeert indien het indiumgehalte toeneemt. We hebben dit fenomeen onderzocht aan de hand van een speciale structuur waarin InGaAs en GaInNAs quantumputten met gelijke indiuminhoud elkaar afwisselen. Deze structuur leent er zich toe om aan de hand van XRD metingen de stikstofinhoud te bepalen, omdat de verandering van de roosterkonstante van de quantumputten die stikstof bevatten de periodiciteit verstoort (zie figuren 5.28 en 5.30 evenals figuur z). Door de opeenstapeling van de gespannen lagen en als gevolg relaxatie is er geen spoor van fotoluminescentie. Dit wordt geïllustreerd in figuur 5.31 waar we TEM-foto’s laten zien van de structuur. Het monster met 35% indium vertoont golvingen die progressief erger worden.

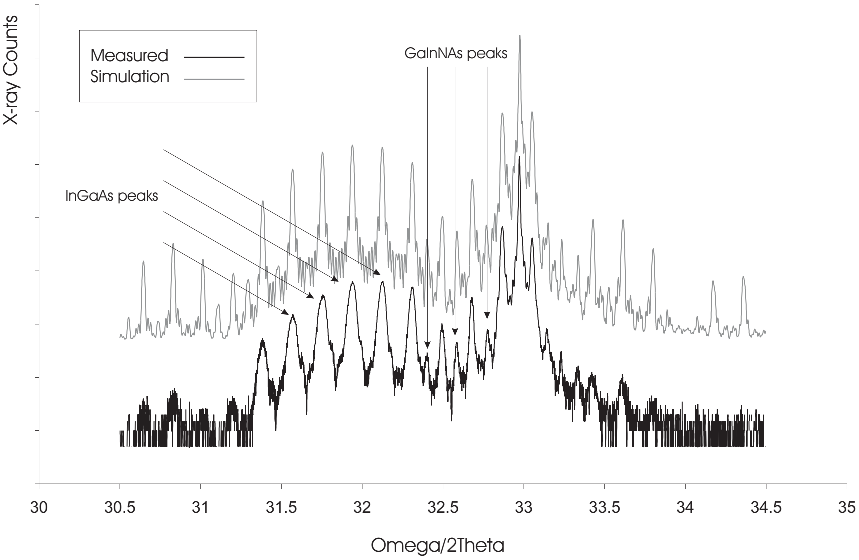

Figuur z XRD-meting en simulatie van de het InGaAs/GaInNAs superrooster (zie figuur 5.29)

Wel leiden we uit de metingen een factor af die uitdrukt hoe de indiumconcentratie de stikstofincorporatie onderdrukt. Deze wordt geïllustreerd in figuur 5.32.

5.5.4 Besluit

Uitgaande van GaAs en InGaAs hebben we de stikstofincorporatie bestudeerd met DMHy in combinatie met arsine of TBAs. Voor arsine gedraagt het groeiproces zich zoals verwacht, terwijl dit voor TBAs niet langer het geval is. Ook het effect van de stikstof op de optische kwaliteit kwam ter sprake.

6. Conclusies en toekomstperspectieven

6.1 Conclusies

Dit werk was toegespitst op de groei van arseenverdunde nitrides, met als belangrijke voorbereidende stap het ontwikkelen van een daartoe geschikt groeiprocede. Daarin hebben we de groei op lage temperatuur onderzocht evenals drie nieuwe precursoren geïntroduceerd. We hebben aangetoond hoe we zeer gespannen stikstofvrije lagen op lage temperatuur kunnen groeien wat leidde tot laserdiodes bij 1190nm.

In de loop van het werk hebben we een aantal excellente resultaten behaald, vooral dan in het kader van de TBAs-ontwikkeling. De GaAs zonnecellen op germanium hebben een wereldrecord conversie-efficiëntie. Ook de 980nm laserdiodes hebben goede karakteristieken qua drempelstroom en interne quantumefficiëntie.

Minder spectaculair, maar niettemin interessant zijn de resultaten van de arseen-verdunde nitrides zelf. Het proces met arseen komen overeen met de verwachtingen, terwijl bij het TBAs-proces een eigenaardig stikstofincorporatiegedrag werd geconstateerd.

6.2 Toekomstperspectieven

Voor al deze onderwerpen kunnen we ons natuurlijk wel inbeelden hoe ze verder ontwikkeld kunnen worden. Voor de lage temperatuursgroei denken we bijvoorbeeld aan de bewuste koolstofdopering met TMGa. Op die manier kunnen we zeer abrupte en hoge p-type concentraties bekomen. In combinatie met een hoge n-type dopering kunnen we dan tunnel-juncties maken. Deze worden gebruikt in zonnecellen om meerdere juncties en serie te kunnen schakelen. Uiteraard is ook dit een uitloper van het zonnecelwerk dat we in het kader van de TBAs-ontwikkeling hebben gedaan.

Vooraleer de hydrides uit het laboratorium werden verbannen, was er een ruime know-how aanwezig voor verscheidene materialen. Hoewel voor het GaAs systeem de meeste kennis werd overgedragen, is dit nog niet het geval voor de materialen met fosfor in het rooster. Het loont dan ook de moeite om ook voor fosfine een alternatief te vinden, bvb. teriairbutylfosfine (TBP), en het groeiproces van InGaAsP/InP en InAlGaP/GaAs opnieuw te optimaliseren.

Het onderzoek naar langegolflengte opto-elektronische componenten zit sinds een paar jaar in een stroomversnelling. De doorbraak kwam er met de monolithische GaInNAs VCSEL bij 1300nm, zowel gebaseerd op MBE als MOCVD technologie. Het feit dat MOCVD MBE heeft bijgehaald wijst op de vooruitgang die met de techniek is gemaakt, bijvoorbeeld ook op het terrein van bronmaterialen. Zonder twijfel zal het onderzoek leiden tot een beter begrip van het materiaal en verbetering van de eigenschappen, bvb. in termen van de diffusielengte der minoritairen. Op die manier worden nieuwe toepassingen mogelijk, zoals bvb. een extra 1eV GaInNAs junctie in zonnecellen. Anderzijds wijzen we op de laserdiode met geïntegreerde bundelexpansiestructuur. Een dergelijke component werd reeds gemaakt voor een golflengte van 980nm. De gebruikte technologie zoals natte selectieve oxidatie van AlGaAs is direct bruikbaar in combinatie met GaInNAs aktieve gebieden.

ENGLISH TEXT

CHAPTER 1

INTRODUCTION

1.1. A short history of communication

Since the Dawn of Man, the human race has exchanged information through communication. The key evolution involved is language. Some experts, such as paleo-anthropologists, have stated that the development of language was part of a genetic mutation. It is widely accepted that language triggered the development of abstract thinking, making it a distinct human feature. From about 3000 B.C. on, spoken language was complemented with writing, evolving from pictures combined with simple numeric systems for managing inventory and trade to symbols that represent sounds to record history and mythology. For thousands of years, the exchange of written messages by messengers or carrier pigeons was the principal means of long-distance communication. Some of these forms of transferring information are still in use [1].

The use of electronic equipment to send and receive messages is called telecommunications and was pioneered by Samuel F.B. Morse. On May 24, 1844, he electrically transmitted his famous message "What hath God wrought?" from Washington to Baltimore and the telegraph was born. Telegraph lines soon extended westward, and within Morse's own lifetime they connected the continents of Europe and America.

The next step on the time-line is the telephone, invented by Graham Bell. According to the famous story, the first fully intelligible telephone call occurred on March 6, 1876, when Bell, in one room, called to his assistant in another room. "Come here, Watson, I want you."

In 1895 Italian inventor Guglielmo Marconi built the equipment and transmitted electrical signals through the air from one end of his house to the other, and then from the house to the garden. These experiments were, in effect, the dawn of practical wireless telegraphy or radio. Following the successes of his experiments at home, Marconi became obsessed with the idea of sending messages across the Atlantic. He built a transmitter, 100 times more powerful than any previous station, at Poldhu, on the southwest tip of England, and installed a receiving station at St. John's Newfoundland. On December 12, 1901, he received signals from across the ocean.

Further progress was made with the launch of earth's first artificial satellite, the Sputnik module on October 4, 1957. It allowed around the world communication independent of atmospheric conditions. Progress in overland communications was less drastic and consisted mainly of an increase of connected telephones together with evolutionary upgrades to the switching infrastructure and wiring. It was not until the early nineteen-eighties that new applications fuelled the demand for bandwidth.

Technology	Distance [km]	Bandwidth [bits/s]	Product [bits·km/s]	Security	Latency [s]
Vocal	0.025	±25	0.525	--	±5
5 page letter sent to Australia in 3 days	20.000	±0.125	2.5k	-	260k
Truck filled with DVD's	100km	±100G	10T	+	50k
Twisted pair	2	1M	2M	-	< 0.1
Coaxial cable	1	10M	10M	-	< 0.1
Wireless (e.g. GSM)	5	56.6k	250k	--	< 0.1
WDM Optical fibre	100	100G	10T	+	< 0.1

Table 1-1 Overview of the properties of some means of communication

Even though overcoming distance was the first effort of the early inventors, it is not the only criterion for communication technology (Table 1-1). Adding repeaters and amplifiers to the network can enlarge the distance, but this will increase the complexity and the cost and decrease the reliablity as there is now one more possible point for failure. For military and strategic purposes, the security and confidentiality of messages remains important. All communication solutions mentioned are extremely vulnerable to eavesdropping or even tampering with the content of the messages. Solving this requires complicated cryptographic protocols. Obviously another criterion is the cost of sending messages. The arrival of the digital age was the start of an exponential increase in demand for bandwidth. Bandwidth is the amount of information that can be squeezed through in a given amount of time. Bandwidth will be limited by dispersion: the broadening of pulses as they propagate. Clearly, pulses will spread more, the further they travel. For any physical medium, bandwidth is therefore strongly related (usually inversely proportional) to the distance. Hence the notion of bandwidth-distance product is introduced. In electrical systems this product is relatively small. Even though it is nowadays possible for processors to generate huge internal bandwidths (e.g. the 32bit Pentium4 processors operating at 3GHz) it is very hard to transmit that information off the chip. An important but often neglected concept is that of latency. It is the time that passes between the request for and obtaining of information. A messenger carrying a box of DVD's will score high in terms of bandwidth but the latency of the information will be high compared to e.g. a leased line. It is clear from the table that the common electrical solutions will not suffice once bandwidth requirements grow.

1.2. Optical fibre communication

Even though not mentioned in the short overview above, a number of optical techniques have been used in communication. All of them are line-of-sight methods and vary in their degree of ingenuity. The use of smoke signalling by native American tribes and semaphores in naval environments are well known. But there were also more complicated and extensive systems, such as the grid of bonfires built by Queen Elisabeth I to warn against a Spanish invasion. Graham Bell's "photophone" even used deformable mirrors and a light-sensitive selenium resistor to transfer telephone conversations optically. Truly practical optical technology only became possible with the advent of two important realisations: low-loss optical fibres and Maiman's laser.

1.2.1. Total internal reflection

In 1870, John Tyndall, using a jet of water that flowed from one bucket to another and a beam of light, demonstrated that light used internal reflection to follow a specific path. As water poured out through the spout of the first container, Tyndall directed a beam of sunlight onto the water in the top bucket. The light followed the curved path inside the water leaving the bucket.

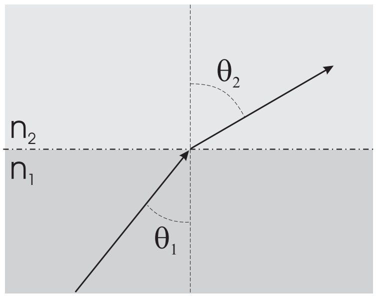

Figure 1-1 Breaking of a ray of light: Snell's law

The idea of total internal reflection is easily understood from Snell's law (see Figure 1-1). Imagine a ray of light in a medium with refractive index n_1 that encounters a transition to a medium with refractive index n_2. If it falls onto the interface between the two under an angle θ_1, then the ray will be broken and enters the second medium under angle θ_2 determined by the following relation:

$$n_1 \cdot \sin(\theta_1) = n_2 \cdot \sin(\theta_2)$$

If n_1 is bigger than n_2, then there exists a certain critical angle θ_1 for which θ_2 attains the value of 90º. At this angle, the ray will not cross the boundary but instead be reflected without losing its energy.

It is this principle that is used in an optical fibre, where a low refractive index cladding surrounds a high refractive index cylindrical core. When we couple light into the core under a suitable angle, it will be guided by total internal reflection. This makes wire-tapping of optical fibres also a lot harder than is the case with electrical connections. In theory, one could even make optical fibres 100% secure by using quantum cryptography and encoding information on e.g. the polarisation of single photons. However, for the moment this kind of experiments only exists in a laboratory-scale state.

1.2.2. Absorption

Even though the light is not lost while it reflects as it passes through the fibre, impurities in the glass and constituents of the glass itself absorb some of the propagating light. Conventional window glass, whether it is soda-lime glass or borosilicate (Pyrex), is not really very transparent. It only appears so because we usually use it in thin sheets – typically a few millimetres thick. Charles Kao and Charles Hockham, working at the Standard Telecommunication Laboratory in England in 1966, published a landmark paper [2] proposing that optical fibre might be a suitable transmission medium if its attenuation could be kept under 20 decibels per kilometre (dB/km). At the time of this proposal, optical fibres exhibited losses of 1,000 dB/ km or more.

Kao and Hockham’s work spurred the efforts of others and in 1970 scientists Donald Keck, Robert Maurer, and Peter Schultz at Corning Glass achieved the attenuation figure of 20 dB/km. Reductions in attenuation of modern fibres (see Figure 1-2) have been accomplished by developing optical fibres fabrication techniques that eliminate impurities, particularly hydroxyl ions when the lowest attenuations are required.

It should be acknowledged that the lowest attenuation levels have not been achieved for visible light but at two wavelengths in the near-infrared part of the spectrum, near 1.3μm and 1.55μm. This is due to the remaining significant, unavoidable attenuation mechanism in the fibre: Rayleigh scattering. It is the natural tendency for any atom or module to reradiate in all directions a part of the electromagnetic radiation incident on it. The magnitude of this scattering increases dramatically at shorter wavelengths ($\sim 1/\lambda^4$), and is enhanced by the random structural character of glass. Indeed it is this phenomenon that causes the sky to appear blue: the shorter wavelengths in sunlight (the blue light) scatter more strongly than other colours. Microscopic variations in material density in a glass fibre lead to concomitant variations in refractive index that enhance Rayleigh scattering. Drawing the fibre during production so as to minimize compositional variations can minimize this loss. Beyond the near-infrared region, the attenuation increases irrevocably due to the absorption of photons by the inter-atom bonds of the basic constituents of glass.

Nowadays, losses in fibres can be as low as 0.1dB/km. This means that after 10km of propagation, only 20% of the input optical power is lost.

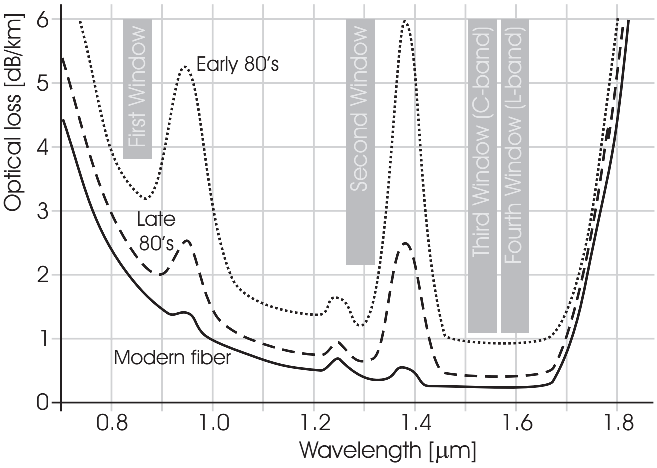

Figure 1-2 Spectral absorption in an optical fibre in the near infrared region

1.2.3. Dispersion

Dispersion refers to the distortion of a propagating wave. When pulses are sent through a waveguide, the waveform can be expanded in two different terms. One is a fast-varying term, the carrier, which propagates with phase velocity. The other is a more slowly varying envelope that travels with the group velocity. Dispersion-less transmission in general requires a constant group velocity. Since dispersion causes pulse broadening, if we attempt to transmit too many pulses per second, they will spread and interfere with each other. Hence dispersion imposes an upper limit to the bandwidth.

Modal dispersion is caused when a propagating wave is comprised of several different modes with different propagation characteristics. If we use the ray model for propagating waves, different modes correspond to different angles of incidence at the core-cladding boundary. Those with steeper angles have lower group velocity. Modal dispersion can (in principle) be eliminated using single-mode fibers that have a cross-section close to the wavelength of the light and are common at 1300nm and 850nm.

Material dispersion is caused by imperfect materials whose refractive index depends on the wavelength. This effect is usually an order of magnitude smaller than modal dispersion.

A third type of dispersion is waveguide dispersion, caused by non-constant group velocity as a function of the wavelength for a fixed mode. It is caused by the different field patterns that each wavelength takes and hence the different effective refractive index it experiences.

In quantifying dispersion, an important consideration is the spectral width of the light signal. In general, a small spectral width is beneficial to limit dispersion. There is one particular type of light source that is extremely suitable in this sense: the laser. It produces coherent light with very narrow line width. Moreover, lasers create light with high intensities in very narrow beam. These features allow light to be coupled into fibres very efficiently.

1.2.4. Laser technology

Although the physical principles underlying the laser, the famous rate equations, were first explained by Albert Einstein early in this century, it was not until the spring of 1960 that Theodore Maiman, working at the Hughes Research Laboratories in Malibu, California, produced the first operating laser [3]. It consisted of a ruby crystal surrounded by a helicoidal flash tube enclosed within a polished aluminium cylindrical cavity cooled by forced air. The ruby cylinder forms a Fabry-Perot cavity by optically polishing the ends to be parallel to within a third of a wavelength of light. Each end was coated with evaporated silver; one end was made less reflective to allow some radiation to escape as a beam. Photo-pumped by a fast discharge flash-lamp, the first ruby lasers operated in pulsed mode for reasons of heat dissipation and the need for high pumping powers.

Two years later, Robert Hall created the first semiconductor laser. Using p-n junctions in gallium arsenide, cooled to 77K, Hall's laser output a light with a wavelength of 840 nm. Unfortunately, this laser required a current density of 10,000 ampere per square centimetre, and generated so much heat that it could only operate in a pulsed mode at 77K. These childhood problems have since been overcome by many smart innovations. For one of these, semiconductor heterostructures, Herbert Kroemer and Zhores Alferov received the Nobel Prize for Physics in 2000.

The group of semiconductors that are most suitable for opto-electronic applications are the III-V semiconductors, named after the respective groups of chemical elements in the Mendeljev’s periodic table that these semiconductors consist of. Each group provides exactly half of the atoms in the semiconductor monocrystal.

Two basic physical material properties impose the boundary conditions for the application of these materials (see Figure 1-3 and Figure 1-4).

The first is the lattice constant, a measure for the average distance between the atoms in the crystal lattice. Layers of different materials can only be integrated into the same crystal when their lattice constant is not too different (usually within 2% of each other's value). Thus, the selection of the substrate imposes limits on the choice of semiconductors that can be used in conjunction.

The second property is the value of the band-gap energy (see Figure 1-3). The energies of electrons in semiconductors can only take values in certain distinct ranges or energy bands. The two most important are the valence band and the higher-lying conduction band. In the semiconductor's lowest state of energy, all electrons completely fill up the so-called valence band. Because this band is completely full and because of Pauli's exclusion principle, electrons cannot move freely through the crystal and thus do not participate in the conduction process. Only when an electron gains more energy it can make the jump to the empty conduction band. It is clear that in an empty band the electron can move (more) freely around. Also, the empty place in the valence band the electron used to occupy now allows some limited conduction processes there. It is crucial to realize that the electron's energy in a perfect crystal can never be in the forbidden region between the valence and conduction band. The magnitude of the gap between both bands is the band-gap energy (E_g). It is an extremely important figure, because when an electron makes the jump from one band to the other, it determines the excess energy of the process. Under certain conditions, this energy can be provided by or to a photon, the optical quantum, and will determine the wavelength (λ) of that photon through the following relation:

$$\lambda\ [\mu m] = 1.24 / E_g\ [eV]$$

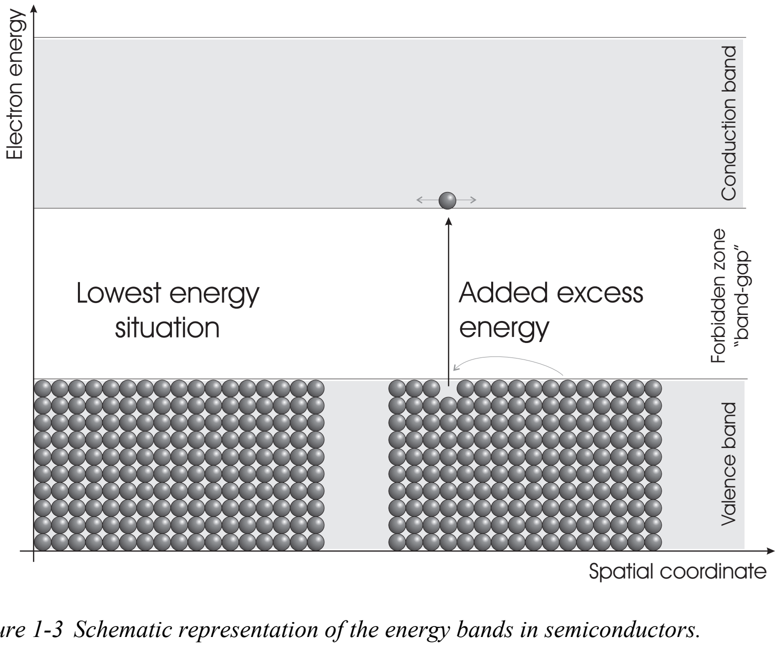

Figure 1-3 Schematic representation of the energy bands in semiconductors.

In figure 4 we show the relation between band-gap energy and lattice constant for the most common III-V semiconductors.. In binary materials such as GaAs or InP, stoichiometry dictates the exact composition and there are no degrees of freedom. These materials are represented by dots. In ternary materials, such as $In_xGa_{1-x}As$ there is one degree of freedom (as an element from one Mendeljev group can only replace an element of the same group). They are shown as solid lines. They also form the boundary for the two-dimensional area that stands for the quaternary materials. These have two degrees of freedom, so that (in theory) one can independently select both lattice constant and band-gap energy.

From the concepts set out above and from Figure 1-4 we see that for the wavelengths in the optical fibre windows, 1.3µm and 1.55µm, *classically* only the InGaAsP material grown on InP substrates was suitable. On GaAs there was simply no material available with sufficiently small band-gap energy.

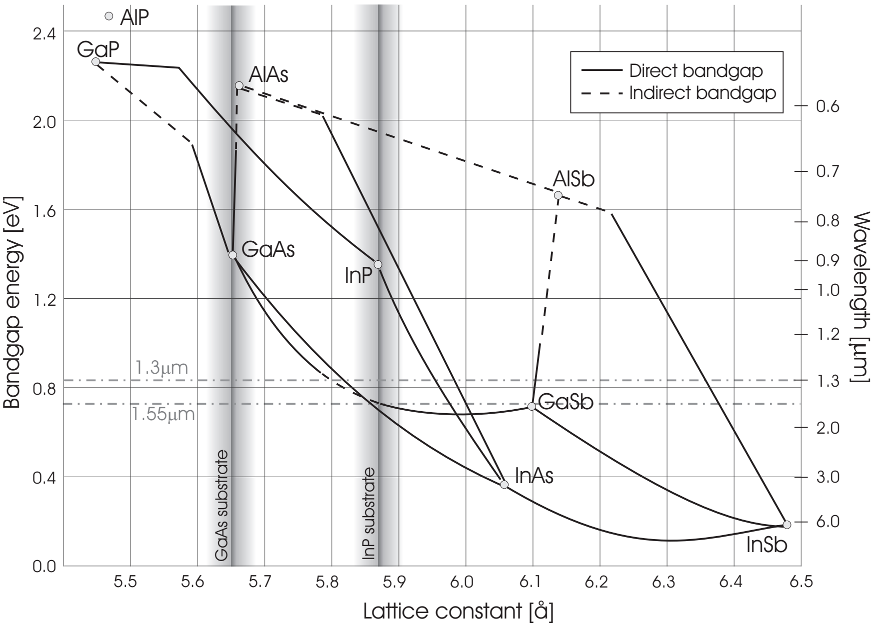

Figure 1-4 Lattice constant and band-gap energy of III-V semiconductors. The vertical grey areas illustrate application area of GaAs and InP substrates.

1.2.5. Advanced optical applications

At first optical fibres were used to replace the backbone connections between the main network switches. These first optical links were just point-to-point links, carrying a high-bandwidth electrically multiplexed signal. However, the capacity of an optical fibre is much larger than this and can be used more efficiently by modulating different signals on different carrier wavelengths. This method is called wavelength division multiplexing and requires optical multiplexers and wavelength filters. In the ideal case they are fabricated on the same chip and in the same process as the active components such as lasers and detectors.

To improve connectivity and for reasons of reliability, e.g. to facilitate recovery when a cable is cut, point-to-point links were replaced by ring- or mesh-like networks. As a result each node now needs some switching capability. In the simplest form, the optical fibres are terminated and the signal is switched electrically before it is send back into another fibre. However, it is more elegant to transfer the switching into the optical domain. This requires the combination of passive functionality, like waveguides or passive couplers, and active components like an optical switch. One can also imagine to fight dispersion by optically regenerating a digital signal, again without first taking it into the electrical domain. One problem to be solved here is the coupling of the optical mode in the fibre into the differently shaped modes of the waveguides on a chip. One solution is the use of tapered waveguides that transform the optical mode of a ridge waveguide into a shape that is better matched to the fibre's mode.

Nowadays the entire backbone network of the telephone, television and data-communication systems use optical fibres. Only the local loop, the interconnection between the subscriber and the nearest switch, still uses copper twisted-pair or coax cables. If this last stretch is to be replaced by optical fibres in a fibre-to-the-curb or fibre-to-the-home philosophy, the cost of the active components has to be reduced. It is often suggested to use devices with a vertical cavity, such as vertical cavity surface emitting lasers (VCSEL's) or micro-cavity light emitting diodes (MC-LED's). The mirrors of the VCSEL's are no longer defined by cleaving but by using distributed Bragg mirrors, a periodic stack of quarter-wavelength layers. The optical mode is then defined by etching a suitably shaped mesa, instead of being bound by the dimensions of a ridge waveguide on top of a substrate. As a result, processing is simplified and less labour-intensive, testing can happen on-chip and the optical mode can be perfectly circular which is beneficial for fibre coupling. Making such VCSEL's or MC-LED's requires mirror technology that combines good electrical, optical and thermal qualities and is feasible to fabricate.

In order to make devices of the complexity described above, band-gap engineering is needed. It is the art to locally change the composition and hence the band-gap energy and refractive index of materials. In the transversal direction this just requires the choice of a suitable material, whereas in the in-plane direction one has to resort to selective growth schemes or employ complex processing schemes. Flexibility in the choice of band-gaps is also beneficial for the electrical and thermal properties of semiconductors. Indeed, heterostructures with large band offsets will do a better job at confining electrons.

Closely related to the band-gap energy (through the Kramers-Krönig integral) is the refractive index of a material. Also here, a large contrast between different materials allows better mirrors or waveguiding.

1.2.6. Near infrared wavelengths on GaAs: GaInNAs

Figure 1-5 shows a simplified version of the band-gap versus lattice constant relation for materials grown on GaAs and InP substrates. Light with a wavelength of 1.3µm (or photon energy of 0.95eV) will pass through any material that has higher band-gap energy. In the case of InGaAsP on InP, this leaves only a range of about 0.4eV. If we would be able to have a 1.3µm active region on GaAs in conjunction with AlGaAs or InAlGaP material, this range spans over 1.25eV.

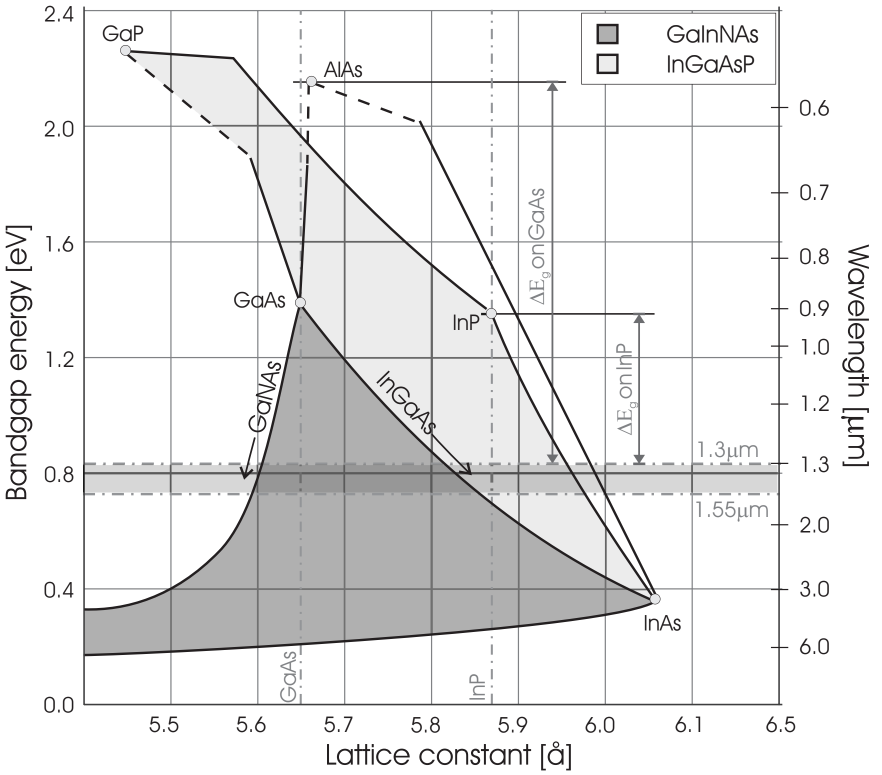

Figure 1-5 III-V semiconductors: reprise. The light-grey area represents the InGaAsP material; the darker grey the novel GaInNAs system.

In terms of refractive index (n_r) contrasts the situation is even more outspoken. It is possible to convert AlGaAs with sufficiently high aluminium content into aluminium oxide in a controlled wet oxidation process. This oxide has an extremely low refractive index. Moreover, it will act as an electrical insulator, which makes current confinement a lot easier. Table 1-2 gives an overview. For devices such as VCSEL's, the reflectivity of the mirrors has to be higher than 99.9%, which is why these devices in the InGaAsP system usually have fused dielectric mirrors instead.

Technology	ΔE_g	Minimal n_r	Maximal n_r	Contrast	#DBR pairs
InP (1.55µm)	0.4eV	3.21 (InP)	3.42 (InGaAsP)	0.21	38
GaAs (1.3µm)	1.25eV	2.94 (AlAs)	3.32 (GaAs)	0.38	20
	1.25eV	1.60 (AlOx)	3.32 (GaAs)	1.72	4

Table 1-2 Refractive index contrast at a wavelength of 1.3µm for the InGaAsP/InP and AlGaAs/GaAs systems. The last column shows the number of DBR pairs that is required to obtain a reflectivity higher than 99%.

In 1992 Weyers et al. investigated the growth of GaAs with small nitrogen content [4]. To their and everybody else's surprise, the band-gap energy does not increase from the value of GaAs towards the band-gap of GaN. Instead a large red shift is observed even for small amounts of incorporated nitrogen. At the same time, the lattice constant does decrease as expected.

In 1996 Kondow et al. pointed out the possibility of growing GaInNAs, lattice matched to GaAs [5]. Adding indium to GaAs makes the lattice constant bigger, whereas nitrogen leads to a smaller lattice constant. Both elements though cause the band-gap energy to shrink. And thus, there is now an opportunity to combine telecom wavelengths with the GaAs technology. The paper spurred a great interest in the material, both from a theoretical as applied point of view. Even though it is hard to incorporate nitrogen in the material and the optical quality suffers drastically from the addition of nitrogen, several groups have since succeeded in making high-performance edge-emitting lasers and VCSEL's.

1.2.7. Epitaxial techniques

Of course, we need a suitable technology to produce these semiconductor layers on top of a substrate. It should be stressed that we do not just randomly deposit material on any surface, but that we aim to expand the substrate's mono-crystal with new material. This epitaxial process is often referred to as "growing" (a word not easily translated into Dutch due to the grammatical difference of transitivity of the verbs involved).

There are a number of different techniques that can achieve this task. The one at hand in the laboratory is metal-organic chemical vapour deposition (MOCVD), also referred to as metal-organic vapour phase epitaxy (MOVPE). It requires the substrate to be introduced into a temperature- and pressure-controlled reactor into which a number of chemical species are fed in gaseous form (see Figure 1-6). At elevated temperatures (usually 650ºC to 750ºC), the source-materials' molecules will react and leave specific constituent atoms behind on the surface. In this way the crystal "grows" in a layer-by-layer fashion. Usually the process occurs at pressures between a tenth of and one times atmospheric pressure.

Clearly, the choice of the source materials or precursors is very important. Most commonly, a series of compounds are used in which metallic elements of the third and fifth groups of Mendeljev's table are bound to organic groups, or in its simplest form to hydrogen to form the so-called hydrides. Even though precursors are fed into the reactor as a vapour, some of them, especially the metal-organics, exist as a liquid (e.g. TMGa and TMAl) or solid (TMIn) under the conditions used. To use these sources, hydrogen is "bubbled" through the source material on its way to the reactor. The equilibrium vapour pressure of the source material will saturate the hydrogen flow, which will in turn transport the material into the reactor. Gaseous sources, such as the hydride arsine, are much simpler in use.

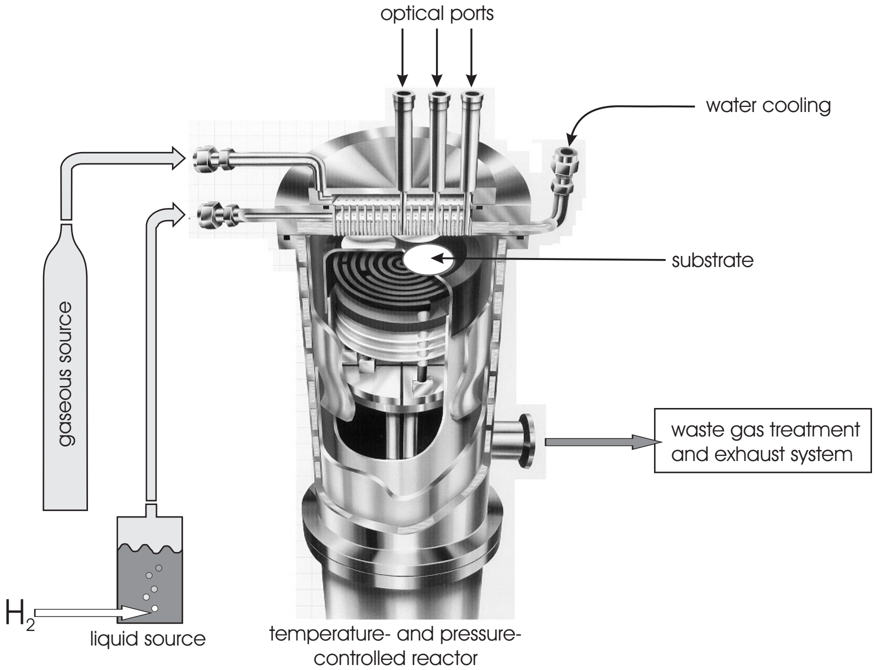

Figure 1-6 Principle of operation of an MOCVD reactor.

MOCVD is the preferred technology in industry for III-V semiconductors, as it combines high uniformity, flexibility and relatively simple reactor design. Its negative points include the high usage of expensive and often dangerous source materials and the limited availability of in-situ characterisation. The biggest competing technology is molecular beam epitaxy. It is a high vacuum technique, in which source elements are introduced in their elemental form from effusion cells. Disadvantages of the technique are a limited growth velocity and uniformity and the overhead of the vacuum technology. On the other hand, it allows very abrupt interfaces and in-situ characterisation techniques (e.g. reflection high energy electron diffraction or RHEED). Cross-breed technologies are chemical beam epitaxy (CBE), metal-organic molecular beam epitaxy (MOMBE) and gas source molecular beam epitaxy (GS-MBE).

1.2.8. Other applications and competing material systems

A low band-gap material on GaAs is not only interesting for telecommunication. A 1eV band-gap junction in solar cells would allow capturing of a wider range of the optical spectrum and hence increase the efficiency of multi-junction cells. In bipolar transistors, a low band-gap base material reduces the switch-on voltage of such devices and thus limits the power dissipation.

There are only a few technologies that compete to deliver near infrared wavelengths on GaAs substrates. So far the most promising is the growth of InAs quantum dots. It is challenging to grow these quantum dots with uniform size and gain easily saturates unless several quantum dot layers are stacked. Progress in this field has already led to a 1.3µm VCSEL with excellent characteristics.

Another option is the growth of gallium antimonides. Adding antimony to GaAs will increase the lattice constant and decrease the band-gap energy. As with GaInNAs, this material has a large miscibility gap. Also, as it cannot be grown lattice matched, the layers are always highly strained. On the other hand less strain is required for an equal decrease in band-gap energy as compared to InGaAs. Even though there is still some discussion concerning the topic, most people accept that GaAsSb/GaAs heterostructures are of type II, meaning that the charge carriers (esp. holes) will not be confined to the GaAsSb layer. In a recent evolution, experiments have been reported where people add both nitrogen and antimony to GaAs to form GaNAsSb.

1.3. Overview of the work

The aim of this work is the study of GaInNAs material grown on GaAs substrates and the development of a growth process in order to do so. Layers of GaInNAs have been grown epitaxially on GaAs substrates by means of metal-organic chemical vapour deposition (MOCVD).

This chapter means to give an introduction into the subject and relate it with other aspects of optical telecommunication.

Chapter two is mainly a survey of what has been published concerning the material. It focuses on theoretical as well as experimental data. A state of the art of its application in devices concludes the chapter.

Chapter three discusses the development of a low temperature growth regime for layers without nitrogen. Low temperature is not only necessary for the nitrogen incorporation, but also allows growing highly strained layers. On the other hand, it induces a number of unwanted parasitic effects.

The fourth chapter treats the development of a growth process using an alternative arsenic precursor: TBAs. Fundamental differences in growth mechanics as compared to the alternative arsine ask for a complete re-establishing of the growth process.

Growth of GaNAs and GaInNAs is then reviewed in chapter five. It will look into the growth characteristics of nitrogen-containing layers and the structural and optical quality of such layers.

A final chapter draws some conclusions. At the same time it will look out into future prospects for GaInNAs research.

1.4. Publication list

1.4.1. Papers in international journals

J. Derluyn, K. Dessein, G. Flamand, Y. Mols, J. Poortmans, G. Borghs, I. Moerman, "Comparison of MOVPE grown GaAs solar cells using different substrates and group-V precursors", Journal of Crystal Growth, Vol. 247, Nr. 3-4, January 2003, pp. 237-244.

J. Derluyn, I. Moerman, M. Leys, G. Patriarche, G. Sęk, R. Kudrawiec, W. Rudno-Rudziński, K. Ryczko, J. Misiewicz, “Control of nitrogen incorporation in MOCVD-grown GaInNAs”, submitted to Journal of Applied Physics.

R. Bockstaele, J. Derluyn, C. Sys, S. Verstuyft, I. Moerman, P. Van Daele, R. Baets, "Realisation of highly efficient 850nm top emitting resonant cavity light emitting diodes", Electronics Letters, Vol. 35, Nr. 18, 2 September 1999, pp. 1564-1565.

G. Flamand, I. Moerman, J. Derluyn, K. Dessein, M. Van Bavel, "A safer, efficient MOCVD process for GaAs solar cell growth", Photovoltaics Bulletin, ISSN 1473-8325, August 2002, pp. 7-9.

1.4.2. Workshops and conferences

J. Derluyn, G. Patriarche, I. Moerman, "Development of a low temperature growth regime for GaInNAs", 9th European Workshop on Metal-Organic

Vapour Phase Epitaxy and Related Growth Techniques, 10-13 June 2001, Wrexham, North Wales, United Kingdom, pp. 37.

J. Derluyn, K. Dessein, G. Flamand, Y. Mols, J. Poortmans, G. Borghs, I. Moerman, "Comprehensive MOVPE study of GaAs solar cells using different substrates and group-V precursors", 11th International Conference on Metalorganic Vapour Phase Epitaxy, 3-7 June 2002, Berlin, Germany, pp. 85.

J. Derluyn, I. Christiaens, I. Moerman, "GaInNAS: a novel material for long-wavelength applications", 1st FTW PHD Symposium, Interactive Poster Session, Paper 47 (Proceedings available on CD-ROM), 5 December 2000, Gent, Belgium.

G. Flamand, K. De Mesel, J. Derluyn, I. Moerman, B. Dhoedt, R. Baets, P. Demeester, P. Van Daele, "InP-based modulator array antennas at 1.06 mm", 1998 Annual IEEE/LEOS Benelux Chapter Workshop - Integrated Optics and Passive Micro-Optics, 16 June 1998, Brugge, Belgium, pp. 19.

M. D'Hondt, J. Derluyn, I. Moerman, S. Verstuyft, P. Van Daele, P. Demeester, P. Mijlemans, "Germanium as a growth substrate for high quality AlGaAs/InGaAs laser diodes", Proc. of the Third Annual Symposium of the IEEE/LEOS Benelux Chapter, 26 November 1998, Gent, Belgium, pp. 9-12.

P. Bienstman, W. Bogaerts, R. Bockstaele, D. Delbeke, S. Goeman, B. Depreter, J. Derluyn, C. Sys, L. Vanwassenhove, B. Dhoedt, I. Moerman, P. Van Daele, R. Baets, "Microcavity and PBG-related activities at the University of Gent", COST 268 Wavelength Scale Photonic Components for Telecommunications (Workshop & Management Committee Meeting), 15-17 March 1999, Stockholm, Sweden.

P. Modak, J. Derluyn, M. D'Hondt, P. Mijlemans, I. Moerman, P. Demeester, "High quality AlGaInP layers on GaAs and Ge grown by MOVPE", Proceedings of the 8th European Workshop on MOVPE, 8-11 June 1999, Prague, Czech Republic, pp. 139-142.

T. Coosemans, A. Van Hove, R. Bockstaele, J. Derluyn, I. Moerman, R. Baets, P. Van Daele, "Optical data communication using substrate removed 850 nm RCLEDS and small core (63/125 mm) plastic optical fibres", Proceedings of the 8th International POF Conference, 14-16 July 1999, Makuhari Messe, Chiba, Japan, pp. 246.

T. Coosemans, R. Bockstaele, A. Van Hove, K. Naessens, J. Derluyn, L. Vanwassenhove, P. Van Daele, I. Moerman, R. Baets, "Substrate removed 850nm RCLED's and small core (63/125mm) Plastic Optical Fibers for optical data communication (Invited Paper)", Proceedings of the SPIE Conference on Light-Emitting Diodes: Research, Manufacturing, and Applications IV, Vol. 3938, 26-27 January 2000, San Jose, California, USA, pp. 160-168.

References

[1] D. Waitzman, “IP Datagrams on Avian Carriers”, Internet Engineering Task Force RFC1149 (1990)

[2] C.K. Kao, G.A. Hockham, “Dielectric-Fiber Surface Waveguides for Optical Frequencies”, Proc. IEEE, vol. 113 n° 7, pp. 1151-1158 (1966)

[3] T. H. Maiman, "Stimulated Optical Radiation in Ruby." Nature 187, 493-494 (1960)

[4] M. Weyers, M. Sato, Appl. Phys. Lett. 62, p1396 (1993)

[5] M. Kondow, K. Uomi, A. Niwa, T. Kitatani, S. Watahiki, Y. Yazawa, Jpn. J. Appl. Phys. 35, p1273 (1996)

CHAPTER 2

PROPERTIES OF GAINNAS

2.1. Abstract

In this chapter important fundamental properties of the Ga(In)NAs material system are analysed with the emphasis on the nature of the giant band-gap bowing and the nitrogen-induced modifications of the electronic structure of the conduction band. We will review the current knowledge of the key material parameters, relevant for device applications, such as electron effective mass, recombination processes and band alignment in common heterostructures, mainly from an experimental point of view. We will focus on material with low nitrogen content (< 10%) where most of the experimental research has been done.

By far the most interesting property of the material is the nature of the giant band gap bowing in the alloy. The bowing mainly occurs in the conduction band, so the emphasis will be on the nitrogen-induced modification of the conduction band states as revealed by various experiments. The other key material parameters for device applications such as effective electron mass and band alignment in Ga(In)NAs/GaAs heterostructures, will also be reviewed.

Since the main motivation for the alloy fabrication is to improve the performance of opto-electronic devices, the second part of the chapter will deal with recombination processes in Ga(In)NAs. The bulk of the discussion will be on radiative recombination processes in the material, which are relatively well understood, but also non-radiative processes will be briefly touched. As it is an important issue in relation with the luminescence, we will also deal with the impact of thermal annealing on the previously discussed properties.

In the last paragraph of the chapter we will describe the performance of devices and their state of the art.

2.2. Introduction

Mixed nitride-group V alloys, such as GaN(In)As, GaN(In)P and In(Al)As(P)N have in recent years emerged as a subject of considerable theoretical and experimental research interest, due to their unique physical properties and the wide range of application possibilities. Due to the novelty of the research area, there is still a lot of discussion on the origins of and the mechanisms behind many of the experimental findings.

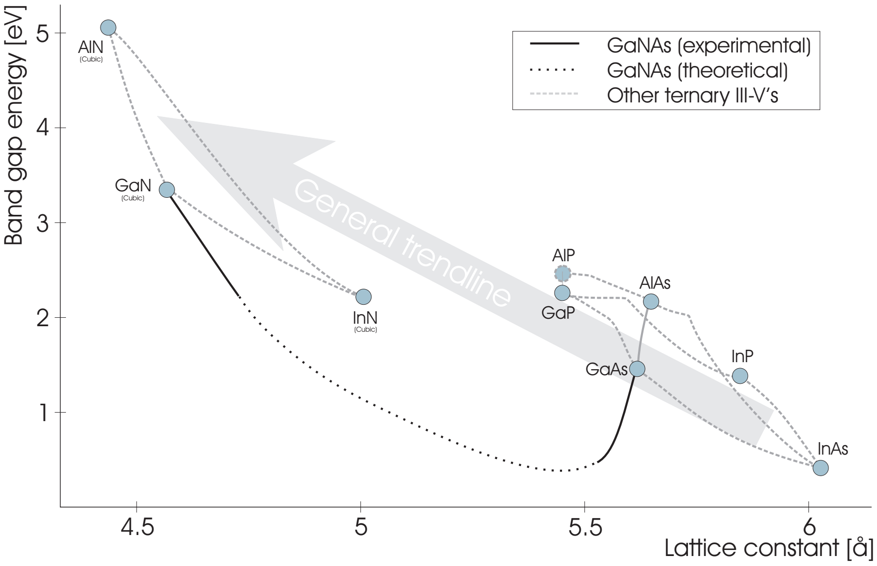

Figure 2-1 Band-gap energy versus lattice constant for a few of the most common III-V semiconductors in a cubic lattice.

In conventional III-V semiconductor alloys, such as AlGaAs, InGaAs or InGaP, etc., the band gap energy of the alloy can be reasonably approximated by the weighted linear average of the binary constituents (see Figure 2-1). Surprisingly, N-containing anion-mixed III-V alloys exhibit a huge bowing of the band-gap energy ([1] [2] [3] [4] [5] [6] [7] [8] [9] [10] [11] [12]). For instance, the addition of only 2% of nitrogen to GaAs causes a dramatic *decrease* of the band-gap energy by about 0.4eV. For comparison, to reach a similar increase in band-gap energy by 0.4eV in the GaAsP-system one has to replace 35% of the arsenic atoms in GaAs by smaller phosporous atoms. The variation of the lattice constant on the other hand, is in accordance with Vegard's law as expected [13]. These remarkable fundamental properties of the GaN(In)As ternary and quaternary alloys provide an opportunity to tailor the material properties respective to the desired applications based on III-V materials.

The origin of the band-bowing effect has long remained unclear and has been attributed to the peculiar characteristics of the nitrogen atom as compared to other group V elements, such as its large electro-negativity and its small size. As a consequence, the perturbation caused by the introduction of nitrogen into a crystal lattice alters the conduction band. An important property for applications is the high effective electron mass, causing more symmetric band structures and density of states, which leads to lower transparency carrier densities and higher differential gain [14].

On the downside however is the observation that the luminescence efficiency drops drastically when nitrogen is introduced into the alloy. Thermal annealing has proved useful to reduce the concentration of non-radiative recombination centres and gradually the nature of these centres is better understood.

2.3. Band structure

2.3.1. Giant bowing of the band-gap energy

In all known cases, when an element in a semiconductor lattice is replaced by another with a smaller ionic radius, the band-gap is increased. Indeed, a decreased interatomic spacing increases the average potential sensed by the electrons in the material, which in turn enlarges the size of the energy band-gap. The success in fabrication of high quality III-V alloys based on the (Al, Ga, In)(As, P) material system, as well as the advent and break-through in the growth of III-Nitrides in the early nineties has encouraged the growth of mixed III-V-N alloys. The motivation to do this was to close the gap between nitrides and arsenides, and thus to cover the complete visible spectrum, based on direct band-gap III-V semiconductors.

Early absorption measurements ([3] [4] [5] [6]) show that GaNAs indeed has a direct band-gap. However, instead of the expected blue-shift from the GaAs band-gap, the alloy shows a considerable red-shift in absorption and photoluminescence near the band edge, suggesting a decrease in the band-gap energy with increasing nitrogen composition (see Figure 2-2). Moreover, the change of the band-gap energy per atomic percentage is more than a tenfold larger than what is observed in other semiconductor alloys.

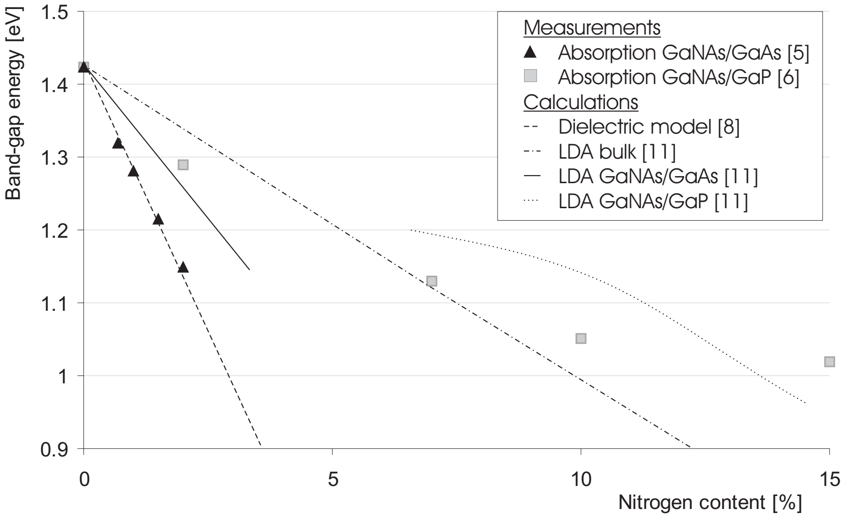

Figure 2-2 Experimental results on the compositional dependence of the band-gap energy of GaN_xAs_{1-x} *on the nitrogen content*

The band-gap energy $E_g(x)$ of an $AB_{1-x}C_x$ semiconductor alloy usually deviates from the average gap $E_g(x) = (1-x).E_g(AB) + x.E_g(AC)$. The deviation of the band-gap energy from the composition weighted linear average band-gaps of the parental binary compounds forming the alloy is usually described by a correction term

$$\Delta E_g(x) = b.x.(1-x)$$

where the bowing coefficient b is typically only a fraction of an electron-volt and is composition independent. However, in dilute III-V-N materials, the optical bowing coefficient is negative and huge, i.e. in the order of –18eV to -20eV for x smaller than a few percent, and strongly dependent on nitrogen content. The rather different behaviour of the band-gap energy for layers grown on GaAs or GaP substrates implies that the bowing coefficient also depends on the internal strain in the GaNAs layer. Strain relaxation in the rather thick GaNAs layers, commonly used for absorption measurements, can then explain the kink in Figure 2-1 in the slope of the compositional dependence of the band-gap energy at a value for x of around 3 to 4 percent.

The first theoretical explanation of the observed effect has been provided [8] within the Van Vechten model ([15] [16] [17]). This is a dielectric two-band model, which only needs the density and the dielectrically defined electronegativity difference as input parameters to predict ionisation potentials and electronic band structures. The large electronegativity of the nitrogen (cf. Figure 2-3) atoms has been shown to cause bowing in the conduction band (CB) energy of the alloy with a bowing coefficient of -20eV. This dielectric model provides very good agreement with the experimental results for the lowest nitrogen fractions (i.e. < 2%). However, it predicts a negative band-gap, i.e. semimetal behaviour, in most of the compositional range (9.5 - 86.7%) based on a constant value of the bowing coefficient. This prediction has been disproved by later experiments ([6] [7]).

III	V
B 159 2.04	N 110 3.04
Al 286 1.61	P 221 2.19
Ga 244 1.81	As 249 2.18
In 325 1.78	Sb 290 2.05

Bond length [pm]
Electronegativity [Pauling]

Figure 2-3 Comparison of relevant chemical parameters of elements of group III and V

The reduction of the bowing coefficient for higher nitrogen fractions has been explained by the first-principle local-density approximation (LDA) calculations of the band structure ([10] [11] [12] [13]) as well as by the band anticrossing model of Shan and Walukiewicz [18]. These models will be introduced next.

2.3.2. Conduction band states: nitrogen-activated E_- and E_+ levels

Further insight in the nature of band states in III-V-N alloys has been gained after the discovery of an additional feature (denoted as E_+) in the electro- [19] and photoreflectance spectra ([20] [21] [22]) of Ga(In)N_xAs_{1-x} alloys with $x > 1\%$. Typical reflectance spectra, taken from [19], are shown in Figure 2-4.

Three fundamental transitions are clearly seen. The first, denoted E_-, is the band gap transition. The second is a transition intrinsic to all zinc-blende III-V semiconductors. It is denoted $E_-+\Delta_0$ and stands for the spin-orbit split-off valence band transition. An additional third feature, denoted E_+, appears in the spectra of GaN_xAs_{1-x} samples with $x \geq 0.8\%$ and $GaInN_xAs_{1-x}$ layers with $x \geq 1.2\%$. These measurements provide valuable information on the electronic structure of Ga(In)NAs. First of all, the independence of the spin-orbit splitting Δ_0 on nitrogen concentration gives a direct experimental evidence for the negligible effect of nitrogen incorporation on the electronic structure of the valence band states in the alloy. It also shows that the E_+ level represents an upper lying subband of the conduction band. With increasing nitrogen content the spectral position of the E_- transition shifts towards lower energies, representing the band gap bowing effect, which was discussed above. The E_+ level on the other hand shifts towards higher energies with increasing x. The E_+-E_- splitting is linearly dependent on the nitrogen composition.

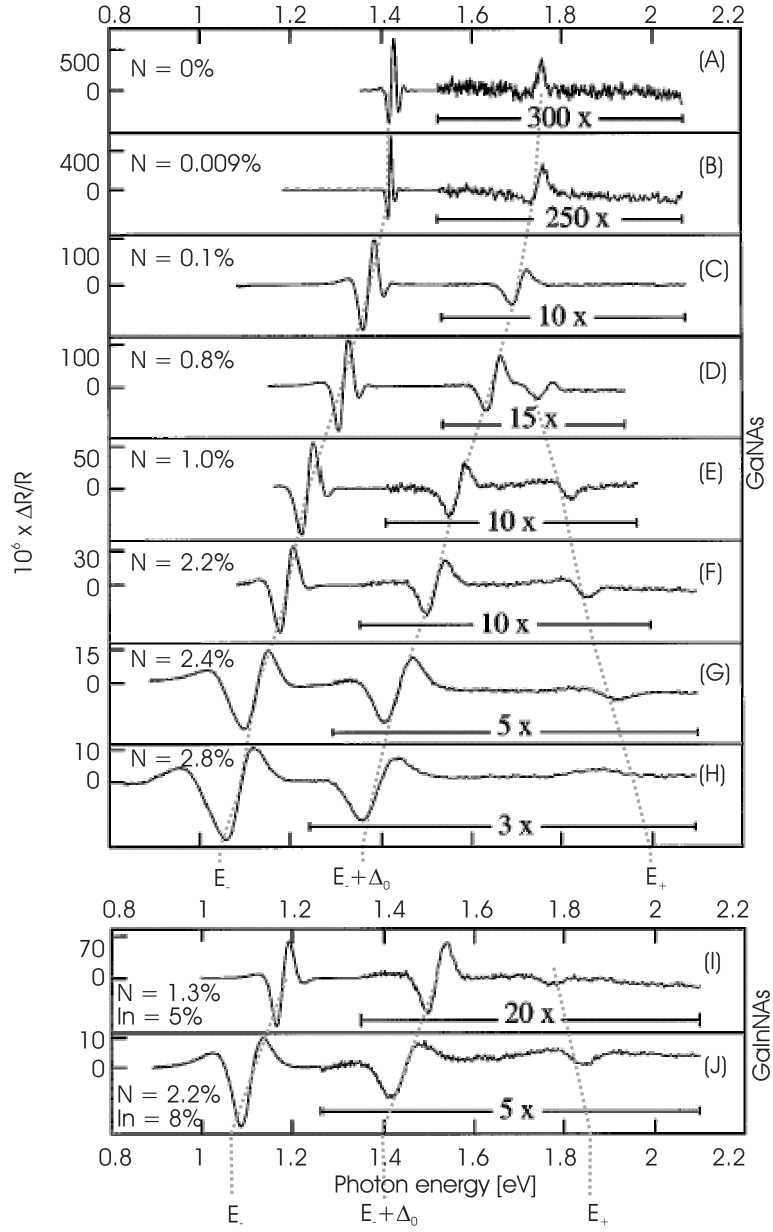

Figure 2-4 Electroreflectance spectra at room temperature for thick GaNAs (a) – (h) and GaInNAs (i) - (j) layers grown on a GaAs substrate (after [19])

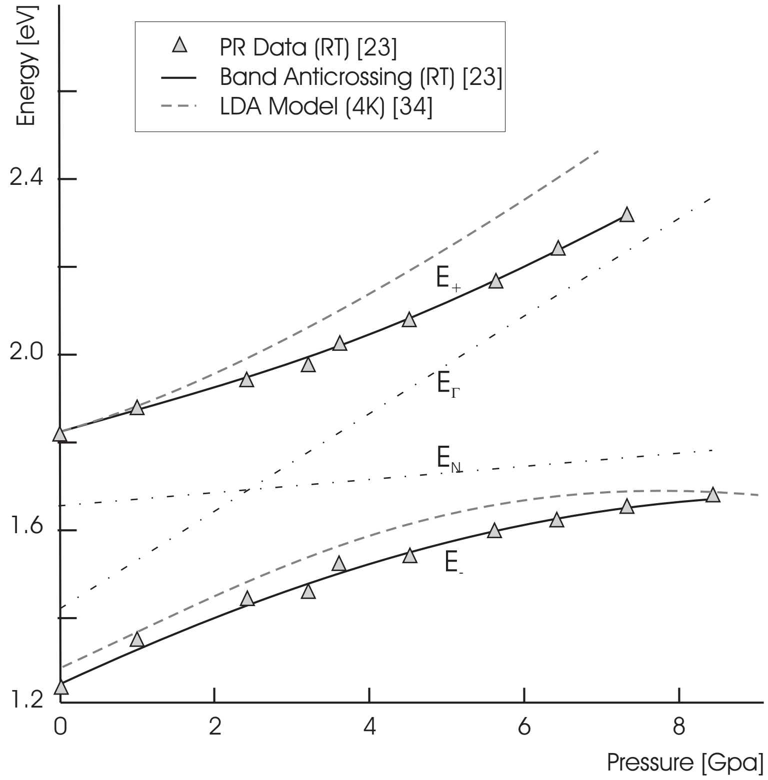

Figure 2-5 Energy levels E_- and E_+ as a function of hydrostatic pressure in GaNAs

Equally interesting is the observation of the unusual pressure dependence of the alloy band-gap ([20] [21] [22] [23] [24] [25]). By applying hydrostatic pressures of several tens of thousands of atmospheres, one can control the lattice constant of the alloy under investigation while at the same time measuring the relative positions of the energy levels using photoreflectance ([20] [21] [22]) or photoluminescence ([23] [24] [25]). Some experimental data has been collected in Figure 2-5 and Figure 2-6. In contrast to the parent Ga(In)As material, where the fundamental band-gap energy increases linearly under hydrostatic pressure, the band-gap energy of nitrogen-containing alloys (corresponding to the E_- transitions) exhibits a much weaker sublinear pressure dependency with a tendency to saturate at high pressures. The pressure dependence of the E_+ level on the other hand exhibits the reverse behaviour: a low dependency at low pressures that changes into a linear dependence at the higher pressures. Also the intensity of the E_+ transition at high pressures increases drastically ([20] [21]), which implies a change in the character of the E_+ subband.

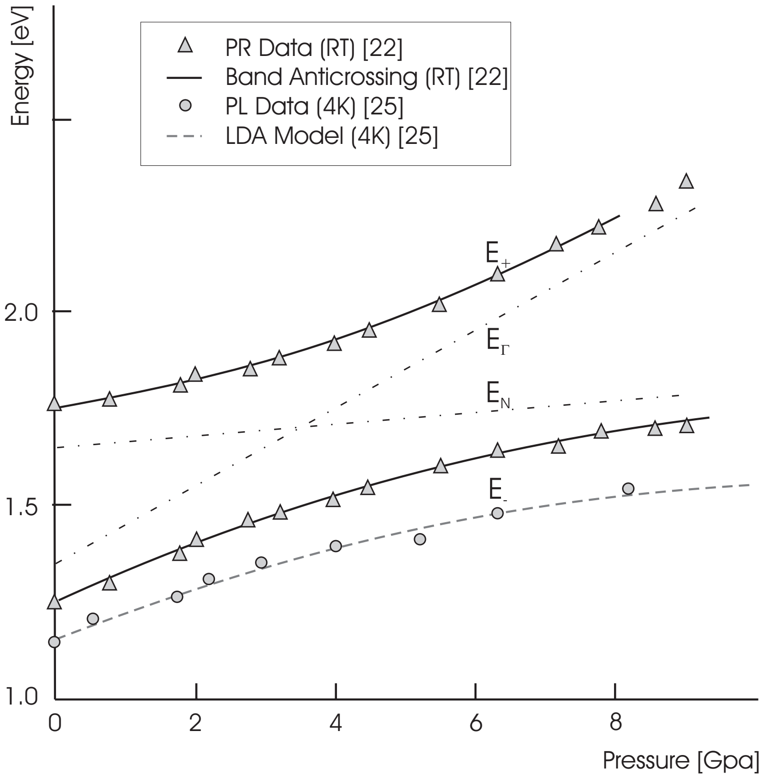

Figure 2-6 Energy levels E_- and E_+ as a function of hydrostatic pressure in GaInNAs

These experiments provide direct evidence that the nitrogen-induced interaction between the E- and E+ energy levels causes the reduction of the band-gap. The physical origin of the phenomenon remains the subject of debate. Two models, each with a different character of the conduction band states, are currently in the picture. Both start from the premise of the existence of a nitrogen-induced resonance level in the band structure [19]. Because nitrogen is much smaller and much more electronegative than the arsenic it replaces, its states do not mix smoothly into those of the Ga(In)As matrix as in common semiconductor alloying [26]. Instead, the electrons from the nitrogen form a narrow, localised band, E_N, located a few tenths of an electron-volt above the conduction band edge. The transformation of nitrogen acting as an isoelectronic impurity to the band formation takes place at a nitrogen content of about 0.2%. The level does not shift with respect to the valence band as a function of nitrogen concentration and is strongly localised in nature [27].

The first model is the empirical band-anticrossing model (BAM) ([20] [21] [22]). It is schematically depicted in Figure 2-7. It is well known that when two interacting quantum-mechanical states are brought close together in energy, there is a repulsive interaction or anti-crossing that tends to push them apart. In the case of Ga(In)NAs alloys, it is the localised nitrogen states that mixes with the conduction band with energy level E_Γ and splits it into two distinct energy levels, one pushed down and one pushed up in energy. The strength of the E_Γ-E_N interaction is described by the interband matrix element V_{MN}. An increase of the V_{MN} value with increasing nitrogen content leads to a stronger repulsion between the E_+ and E_- states and thus the band-gap bowing accompanied by a blue-shift of the E_+ state. The interaction also leads to a considerable increase of the electron effective mass and a strong non-parabolicity of the conduction band. The anticrossing model makes specific predictions of the relative changes of the energy levels with applied hydrostatic pressure [20], which are in excellent agreement with experimental data (see Figure 2-5). This unusual behaviour is explained by the change of the character of the states from extended to localised (and vice versa). There have been efforts to support this model from a theoretical background ([28] [29]).

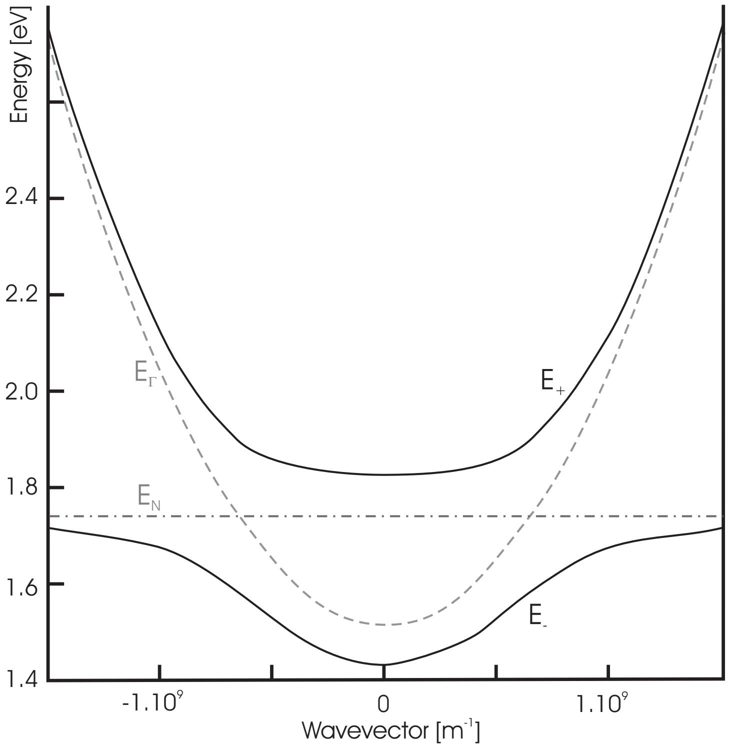

Figure 2-7 Schematic of the conduction band in the band anticrossing model (after [22])

The second model to explain the existence of the two energy levels uses pseudopotential LDA calculations ([23] [24] [30]). Nitrogen incorporation predominantly induces a strong perturbation in the host crystal states leading to symmetry breaking. This causes splitting of the indirect conduction band states. Mixing of these split subbands and the nitrogen-induced resonant level E_N then causes the creation of E_- and E_+. The interaction between the nitrogen level and the direct conduction band states only has a minor contribution [30]. The model is based on the analysis of the highly localised nature of the perturbations introduced by nitrogen atoms. Due to a large chemical and size difference between nitrogen and the other group V anions it replaces, two regions in the band-gap variation as a function of composition of the III-V-N alloys have been predicted. An impurity-like region with a large and composition-dependent bowing coefficient is expected for the low nitrogen contents up to 10%, whereas a band-like region with a much smaller and nearly constant bowing coefficient is predicted for the intermediate compositions from 10 to 40% [13]. By considering the effect of the residual strain on the alloy properties, even better agreement between the LDA theory and the experiments can be achieved [11].

Both models provide qualitative agreement with experimental data and can account for the compositional and pressure dependencies of the E_- and E_+ levels. They can also qualitatively describe the observed increase of electron effective mass with increasing nitrogen composition or pressure. However, the two models do predict a different nature (localised-like vs. extended-like) of the states of the higher split energy band and experimentally obtained data regarding this matter are not conclusive ([31] [32] [33] [34]).

2.3.3. Conduction band dispersion.

Another difference between the III-V-N material and its conventional counterparts is the unusual behaviour of the electron effective mass. Usually the value of the effective mass decreases with decreasing band-gap energy, whereas in this case it increases with nitrogen content (in the low composition range). What’s more, the conduction band of the alloy is predicted to be strongly non-parabolic, leading to an energy dependence of the effective mass.

This situation where the values of the electron and hole effective mass approach each other is beneficial for application in laser devices. Consider a quantum well at the transparency condition. Due to pumping, either electrically or optically, a highly non-equilibrium condition is created such that a high electron and hole density can coexist. From the expression for gain one can deduce that when the separation of the quasi-fermi levels E_{fc} and E_{fv} is equal to the band-gap energy, the material will become transparent for photon energies equal to the band-gap energy. This electron and hole carrier density is known as the transparency carrier density N_{tr}. Its magnitude is fundamentally related to the densities of states ρ_c and ρ_v of a given material. Two situations, one with equal effective masses and one where the effective masses are different, are sketched in Figure 2-8. The area of the shaded regions represents the total carrier density in the band. Starting from the symmetric case, increasing the effective hole mass will also increase the density of states ρ_v in the valence band. The asymmetry shifts both Fermi-functions f_c and f_v towards the band with lower effective mass in order to maintain equal number of carriers in both bands. The result is a larger transparency carrier density than in the symmetric case [14]. One can also easily deduce that the differential gain is higher in the symmetric case by contemplating on the band edge carrier density and the slope of the Fermi-functions.

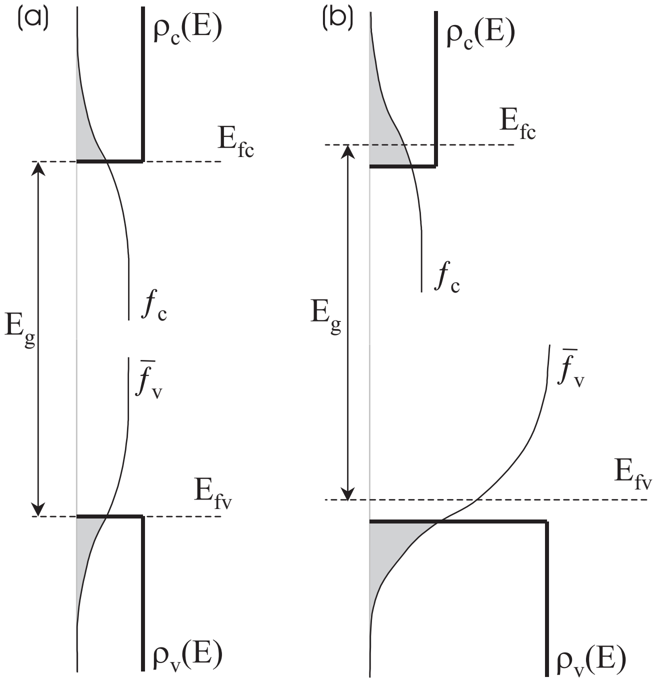

Figure 2-8 Transparency condition in a quantum well with equal effective carrier masses (a) and unequal effective carrier masses (b).

For GaNAs/GaAs quantum well structures, the compositional dependence of the electron effective mass has been directly studied by using optically detected cyclotron resonance (ODCR) [35]. Based on the clear compositional dependence of the ODCR maximum position measured under such resonant excitation of the GaNAs, the electron effective mass has been found to increase from a value of about 0.063 m_0 up to 0.19 m_0 for a nitrogen content of 2%. This is in agreement with the theoretical predictions, even though the determined values are somewhat higher than 0.11 m_0 expected from the band anticrossing model. A strong broadening of the ODCR spectra with nitrogen content indicates a decrease of the scattering time, which contributes in conjunction with the increased effective mass to a decrease of the electron mobility in GaNAs.

In the case of GaInNAs experimental data has been obtained from infrared reflection [36]. The results show an increase of the electron effective mass with the addition of nitrogen and with electron concentration in a heavily Se-doped GaInNAs samples, up to 0.4 m_0 for $Ga_{0.92}In_{0.08}As_{0.967}N_{0.033}$ with an electron concentration of $6.10^{19}cm^{-3}$. The observed dependence of the effective mass on carrier concentration is the first direct evidence for an enhanced non-parabolicity of the conduction band in the alloy. The results have been interpreted in terms of the band anticrossing model and are in accordance with earlier results ([23] [24]). Also, in a different report, the fitting of data obtained through polarised photoluminescence excitation measurements [37] on $Ga_{0.62}In_{0.38}N_{0.015}As_{0.985}$ quantum wells was improved by increasing the value of the electron effective mass by $0.03m_0$ over the value of the nitrogen-free material.

2.3.4. Band alignment in Ga(In)NAs/GaAs hetero-structures

The great range of applications of the Ga(In)NAs alloy system cannot be realised without a detailed knowledge of the fundamental properties related to the corresponding heterostructures, such as band alignment in quantum structures and band offset values. This information is also important for the validity of approximations made in theoretical models and thus the understanding of the electronic band structures of the material.

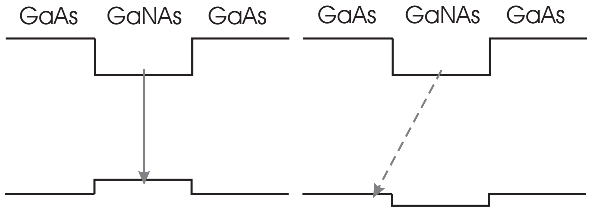

Band scheme	Type I	Type II
Optical transitions	Direct	Indirect
Radiative PL decay	Fast	Slow
Hole location	GaNAs	GaAs

Figure 2-9 Possible band alignments and properties of GaNAs/GaAs heterojunctions.

One of the remaining unsolved issues regarding GaNAs/GaAs quantum well structures involves the band edge alignment. It is commonly accepted that the incorporation of nitrogen mainly affects the conduction band states resulting in a large conduction band and only a small valence band offset. However it remains unclear, whether the band alignment is fundamentally type I or II.

Earlier studies with the dielectric model have predicted the negligible effect of the band-gap bowing on the valence band states which resulted in a type II alignment over the entire range of nitrogen compositions as is shown in Figure 2-10. On the other hand, first principle ([10] [11]) and sp^3s^* tight-binding calculations [29] have concluded an increase of the valence band edge with nitrogen content and as a result a type I line-up in strain-free heterostructures with low nitrogen content.

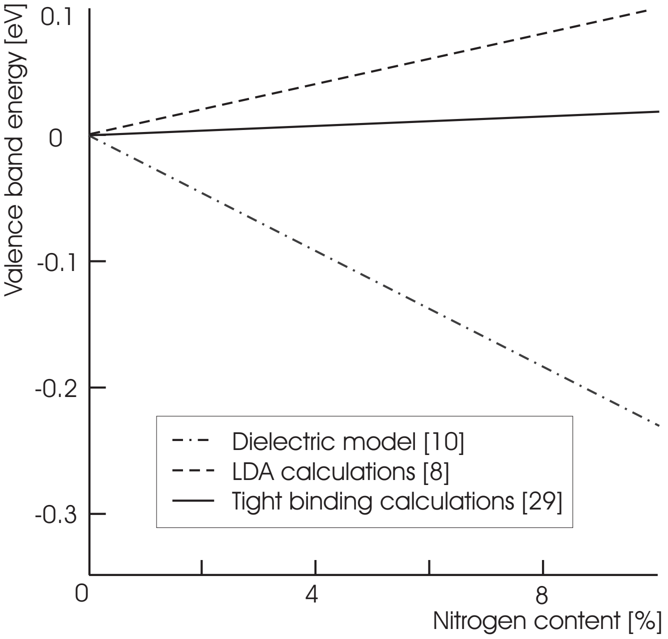

Figure 2-10 Theoretical valence band energy as a function of nitrogen content.

Unfortunately, experimental data on the subject is as contradictory as the theoretical predictions. Attempts have been made to evaluate the band alignment based on the effect of quantum confinement on the energy of optical transitions, studied under ambient and hydrostatic pressure. Depending on the source, values were published ranging from a type I alignment with ΔE_C equal to 17% of band-gap discontinuity at x = 1.6% [38] and ΔE_V = 30% at x = 1.8% [27] to a type II alignment with a value for ΔE_V of 30meV [39] to 40meV [40]. The differences between these results are probably due to the difficult interpretation of the data, since parameters such as effective carrier mass and the origin of the topmost valence band states (light hole vs. heavy hole) greatly influence the outcome of the calculation. Qualitative information has been obtained using a combination of three complementary optical techniques [41] (time-resolved photoluminescence, photoluminescence polarisation and optically detected cyclotron resonance) as well as from capacitance-voltage measurements [42] and favours a type I band alignment.

The issue of the influence of nitrogen on the band alignment is less critical for GaInNAs/GaAs heterostructures. Kondow already pointed out the advantage of the increased electron confinement as compared to InGaAsP-based devices leading to improved thermal characteristics. The increased conduction band offset is a direct consequence of the large band-gap bowing, as discussed before. In a worst case scenario, assuming a negligible bowing of the valence band as predicted by the dielectric model [8], the valence band of GaInNAs material lattice matched to GaAs should still be at the same energy as the GaAs valence band (see Figure 2-11). Hole confinement can be realised using GaInNAs/AlGaAs structures. One should take into account that for laser applications indium-rich, thus heavily compressively strained quantum wells are common which implies a type I band alignment. If the valence band increases with nitrogen content as predicted with LDA calculations for the GaNAs alloy ([10] [29]), hole confinement is already realised even for lattice-matched material.

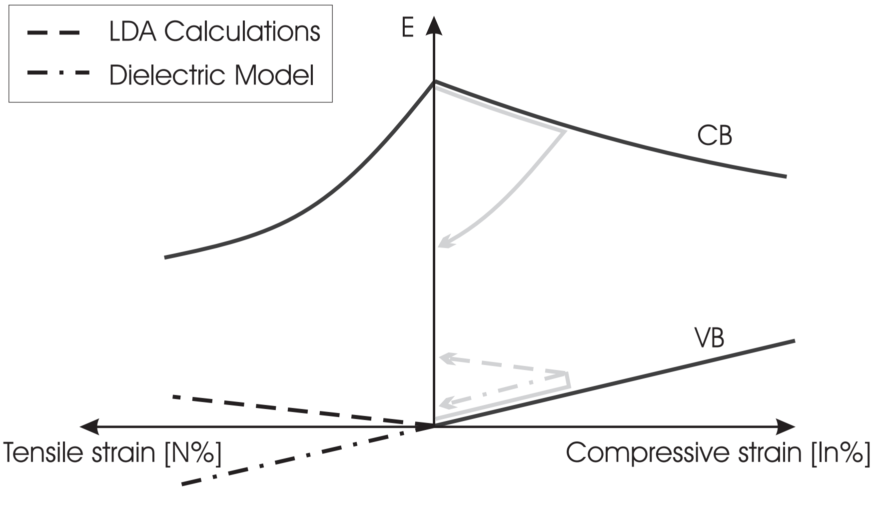

Figure 2-11 Schematic diagram of band alignment for GaNAs and InGaAs. The grey, arrow-headed lines indicate how we lattice-match GaInNAs material lattice matched to GaAs (by first adding indium and then nitrogen)

Experimental data regarding the electronic structure of strained GaInNAs/GaAs quantum wells has been obtained by polarised photoluminescence excitation spectroscopy [37]. The use of polarisation measurements has allowed analysis of the quantum confinement effects on the valence band states via direct identification of various features in the measured spectra as related to heavy hole and light hole transitions. A type I alignment was demonstrated for quantum wells with 38% of indium and 1.5% of nitrogen which corresponds to an emission wavelength of 1.3μm. The estimated offset for the lowest heavy-hole subband is ΔE_V = 65meV, whereas for the light-hole subband a flat alignment has been concluded.

2.4. Recombination processes

Besides the potential of GaInNAs as an active material in solar cells, the main motivation for the extensive research on the material system is the possibility of its application in light emitting devices in the near-infrared region. Therefore, improving optical quality and identifying the dominant mechanisms of the light emission have been, are and will remain to be a big issue in research on dilute nitrides. In the next paragraphs, we will discuss the radiative and non-radiative processes in GaNAs and GaInNAs alloys. Even though the mechanisms involved in the two materials are very similar, we will discuss them one after the other.

2.4.1. Radiative recombination

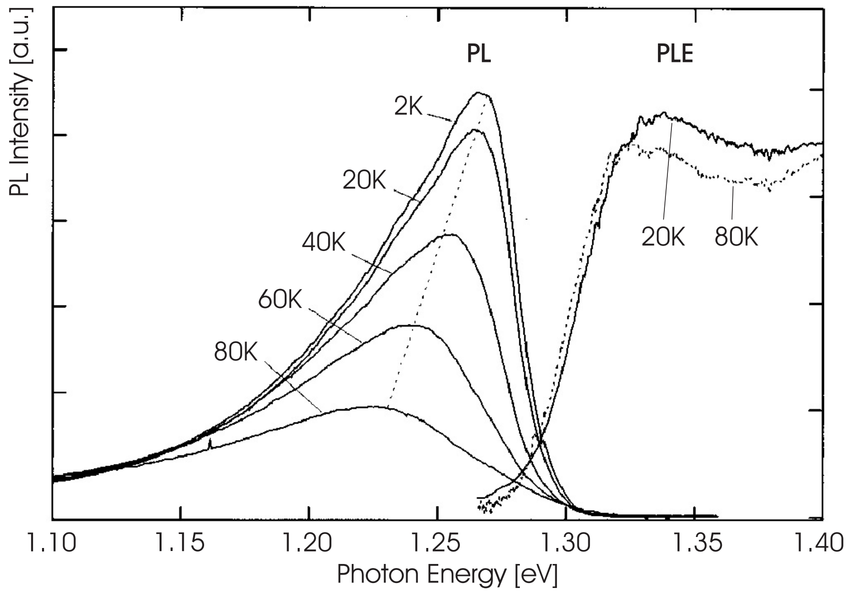

Figure 2-12 Photoluminescence and photoluminescence excitation spectra at low temperatures of GaNAs/GaAs MQW's [44]

The low-temperature photoluminescence (PL) spectra of GaNAs alloys in the near-band-gap spectral region are characterised by an asymmetric PL band with a maximum at a wavelength that shifts towards lower energies with increasing nitrogen content. This PL shift has been shown to correlate with the red shift of the absorption edge in the material and thus has been attributed to the expected decrease of the band-gap energy ([3] [43] [44] [45]). This has further been confirmed by PL excitation measurements, showing that the low-energy cut-off of the PLE spectra shifts towards lower energies to a degree corresponding to the nitrogen concentration ([44] [45]).

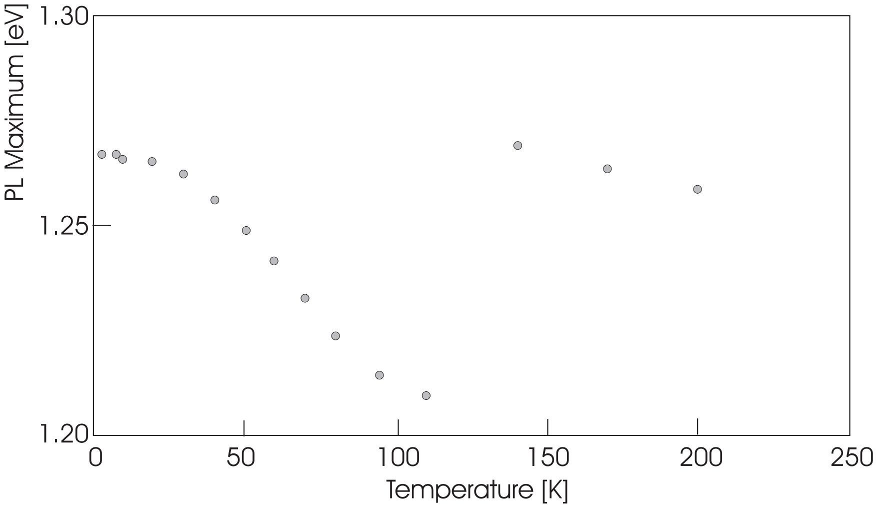

Figure 2-13 Temperature variation of the PL peak energy [1].

Typically GaNAs-related emission has the characteristic properties as shown in Figure 2-12. The PL emission has an asymmetric line-shape with a sharp high-energy cut-off and an exponential low-energy tail. A strong red shift of the PL maximum position occurs with increasing temperature, which is not observed in the PLE spectra. Hence, the shift is not related to a temperature-induced change of the band-gap energy. Increasing the optical excitation power leads to a blue shift of the PL-maximum and the decay of the photoluminescence is characterised by a single exponential with a short decay time (~350ps) at the high-energy side to a longer time (~5ns) at the low emission energies [44].

These properties of the GaNAs emission at low temperatures can be explained in terms of strong exciton localisation by potential fluctuations at the band edges: localised exciton (LE) recombination. The spectral shape of LE emission is very asymmetric. The low energy side of the spectrum can be approximated by an exponential function, which reflects the energy distribution of the density of states within the band tails, whereas the high energy cut-off corresponds to a mobility edge, separating the localised and delocalised states [46]. Also, gradual filling of the energy states within the band tails with increasing optical excitation power can cause a blue shift of the peak position of the LE emission. The temperature behaviour of the PL emission (Figure 2-13) also provides evidence for the exciton localisation. With increasing temperature, trapped carriers can be activated into delocalised states. This will both activate radiative recombination related to free carriers as well as cause thermal quenching of the PL when competing non-radiative processes are important. Since the remaining emission originates from the localised excitons, located deeper in the band tails, at first a red shift of the PL-maximum with temperature is observed. When radiative free carrier recombination becomes the dominant PL mechanism at elevated temperatures, the PL-maximum shifts back, leading to an apparent inverted N-shape [1]. The PL transient data further supports the LE proposition, with a slow decay, typical of LE, at low energies and an increasing contribution of faster free carrier processes at the high-energy side [47].

From the slope of the PL low-energy tail on a semi-logarithmic scale, one can roughly estimate the localisation potential [46]. The estimated value for this potential is in the order of 50meV. One can reduce the value by increasing growth temperature [48] or by post-growth high-temperature treatment [49], but it still remains much higher than in conventional alloy systems. In those alloys, the localisation is caused mainly by random compositional disorder and is rather shallow (about 10meV). One possible reason for this can be clustering of nitrogen atoms ([45] [50]), even though recently scanning tunneling microscopy (STM) analysis of GaNAs did not find any evidence of such clusters [51]. Another possibility is that due to the high electronegativity of nitrogen and the increase of the length of the Ga-N bond in the nitrogen-poor GaNAs-lattice as compared its original value, electron localisation on the nitrogen atoms is enhanced [52].

A similar strong exciton localisation has been demonstrated for GaInNAs/GaAs strained quantum well (QW) structures ([34] [54] [55]) and thick epitaxial layers lattice-matched to GaAs [57]. As with GaNAs, the near-band-gap PL emission has an asymmetric lineshape and has thermal, excitation power and temporal dependencies inherent for LE emission. The PL maximum position is non-monotonically dependent on increasing temperature [55]. Data from PL and PR measurements is shown in Figure 2-14. Besides a shift in the band-gap energy, thermal annealing does not influence the temperature behaviour of the PL maximum position. Also indicated is the expected behaviour for the PL and PR maximum position according to the empirical Varshni relation [56]. There is a blue shift of the PL maximum position with increasing excitation power ([34] [54] [55] [57]). The PL decay has a slow exponential character with a decay time that decreases at the high-energy side of the spectrum [57].

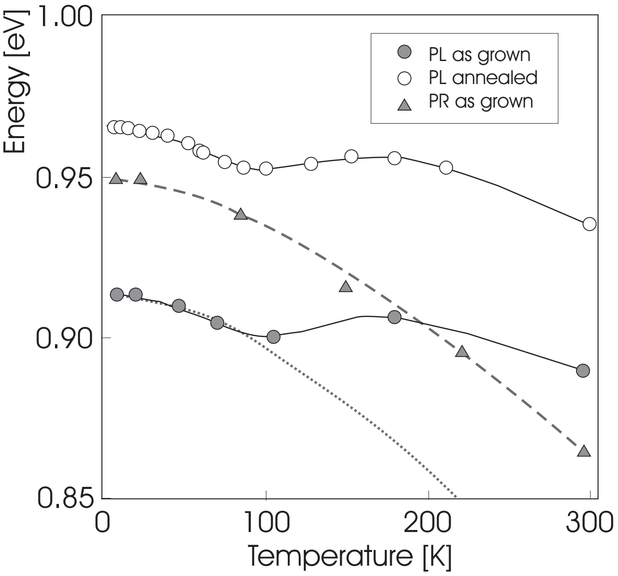

Figure 2-14 Temperature variation of PL and PR peak energy for GaInNAs/GaAs quantum wells [55]. The black lines are a guide to the eye. The dashed and dotted lines are interpolations based on the empirical formula by Varshni [56].

The origin of the large localisation in GaInNAs is at least partly attributed to compositional and strain-non-uniformity of the alloy. It can be influenced by growth conditions or post-growth annealing ([54] [55]).

2.4.2. Non-radiative recombination and thermal annealing

Numerous optical experiments have demonstrated the biggest problem for the growth of dilute nitrides, i.e. the rapidly degrading radiative efficiency of the alloy with nitrogen incorporation ([2] [3] [43] [44]). PL intensity is drastically reduced with increasing nitrogen composition, usually by one to two orders of magnitude per percent of nitrogen. Similarly, adding nitrogen causes a strong reduction in the quantum efficiency of solar cells with a GaInNAs active region ([58] [59]).

Theoretical considerations based on the changing character of conduction band states as nitrogen content increases, have led to the prediction of a reduced optical efficiency. However, the predicted reduction of about 60% for a content of 5% of nitrogen cannot account for the observed experimental effect [12]. Instead, the effect is usually attributed to the low growth temperature, which is needed to obtain a higher nitrogen uptake but leads to poor structural quality.

One way to cure the inherently low optical quality of the as-grown Ga(In)NAs material are post-growth thermal treatments . Its effects are a strong increase in PL intensity and a decrease of the PL linewidth but at the same time a strong blue shift of the spectrum is observed ([43] [42] [49]). Also, the carrier diffusion length increases several times in the annealed structures [59]. The mechanisms that govern the annealing have long remained unclear and have been attributed to the elimination of some grown-in competing non-radiative channels. Recently a number of studies have provided insight in the matter.

At first, it was postulated that one of these traps might be due to hydrogen impurities, when a number of groups linked the improvement of optical quality to a decrease in hydrogen contamination with higher growth temperature or after a thermal annealing step ([60] [61] [62]). All growth techniques used for these studies supply hydrogen or a hydrogen complex when source materials decompose. Hydrogen is well known to be a highly diffusive element in III-V semiconductors and to interact with extended and point defects. This interaction often results in the passivation of their electrical activity. The interaction of nitrogen and hydrogen is an important issue since intrinsic properties can be altered by the presence of hydrogen [63]. The presence of N-H_n complexes was first suspected in MOCVD-grown GaNAs layers. It was speculated that such complexes could act as non-radiative centres [62]. Far infrared absorption measurements revealed the presence of N-H bonds in thick GaInNAs layers, as observed through their local vibration modes [64]. In another study the effect of hydrogen on GaInNAs quantum wells was investigated by a deliberate and controlled introduction of hydrogen after growth. It reports striking effects on the electronic properties of this material after hydrogen irradiation and interprets the results as a passivation of the nitrogen-related states through the formation of N-H complexes ([65] [66]).

However, using techniques that are inherently hydrogen-free, such as MBE with an rf plasma nitrogen cracker, the same effect of annealing has been observed ([42] [67]). Therefore, there are still other traps in the material that are affected by the annealing procedure.

The importance of oxygen as an efficient recombination centre in GaInNAs solar cells has also been underlined. By comparing deep-level transient spectroscopy (DLTS) measurements on as-grown and oxygen-implanted samples, an efficient oxygen-related mid-gap recombination centre has been identified [68].

Kwon et al. performed deep level transient spectroscopy (DLTS) experiments and discovered four distinct hole traps in as-grown lattice matched GaInNAs material. Upon thermal anneal, only one of these appeared to be thermally stable and the overall trap density was reduced by a factor of two. The trap that is dominant in as-grown samples is no longer dominant after annealing [69]. It is also concluded that point defects or point defect clusters and not dislocation-related traps are responsible for the hole traps. Optically detected magnetoresonance (ODMR) characterisation of GaNAs samples attribute the point defect to either a Ga_i interstitial or an As_{Ga} antisite, where the latter is argued to be the more likely candidate [70], whereas positron annihilation spectroscopy measurements favour the Ga_i interstitial [71].

More recently, yet another point defect in as-grown materials was identified as interstitial nitrogen or interstitial nitrogen complexes by a combination of Rutherford backscattering (RBS) and nuclear reaction analysis (NRA) ([42] [71] [72]). When comparing data from x-ray diffraction (XRD) and secondary ion mass spectroscopy (SIMS) as shown in Figure 2-15, a deviation from Vegard's law is observed ([42] [72]), even though theoretical calculations show that this law should be respected when arsenic atoms are replaced by nitrogen atoms [13].

Although most nitrogen atoms are believed to occupy predominantly the arsenic sublattice, they may energetically prefer to move out of the substitutional into neighbouring interstitial sites when the nitrogen incorporation exceeds a certain level. Calculations show that the formation of isolated interstitial nitrogen in GaNAs is highly unlikely due to the high formation energy. Instead, nitrogen complexes, such as As-N and N-N split interstitials (shown in Figure 2-16) are energetically favoured to form [72]. Li et al. [71] estimate the density of interstitial nitrogen is $1.7\text{x}10^{19}\text{cm}^{-3}$ in as-grown $GaN_{0.03}As_{0.97}$ or 2.5% of the total amount of nitrogen. After annealing, this concentration drops to $2\text{x}10^{18}\text{cm}^{-3}$ or 0.3%. Spruytte et al. [42] do not quantify densities, nor do they identify the possible chemical states of the interstitial nitrogen, but they do clearly observe the presence of interstitial nitrogen and a significant decrease thereof after anneal.

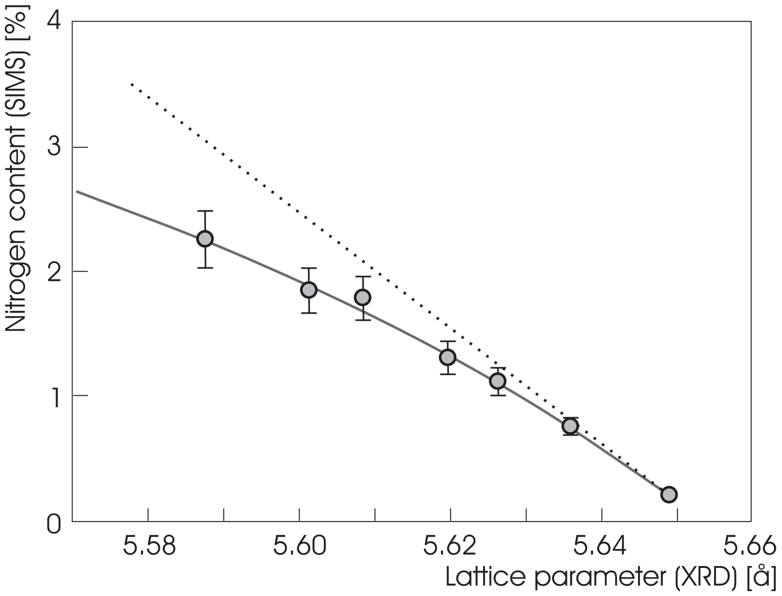

Figure 2-15 Dependence of the lattice parameter in the growth direction of GaNAs on the nitrogen content. The dashed line represents Vegard's law between GaAs and cubic GaN (after [72])

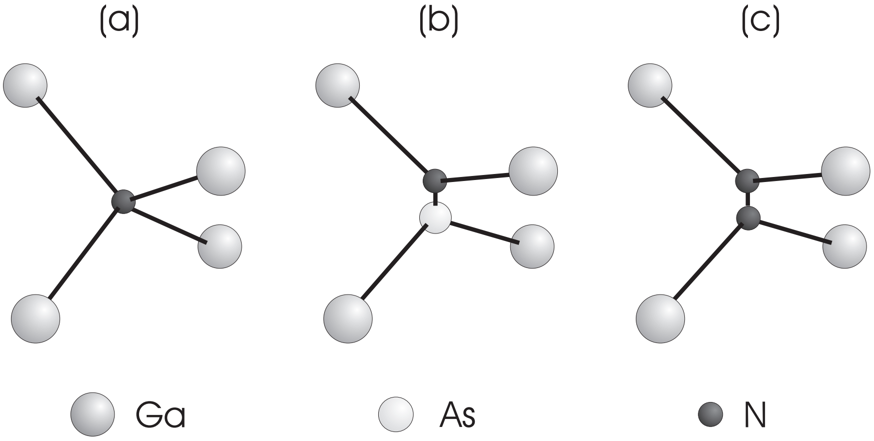

Figure 2-16 Atomic structures for the normal case (a) and split interstitial complexes As-N (b) and N-N (c), after [72]

Besides reducing the concentration of point defects, thermal treatments have a drastic effect on the band-gap energy of the dilute nitrides and cause a blue shift of roughly 100meV. Two major reasons have been suggested as a cause. The obvious one is out-diffusion of nitrogen; the other is a change in the microscopic arrangement of nitrogen atoms and the consequent changes of the bonding state of the nitrogen.

Spruytte et al. [42] report that the out-diffusion of nitrogen atoms from GaInNAs/GaAs quantum well structures is the major cause of the blue shift during annealing. The out-diffusion of nitrogen may be facilitated by the vacancy-type defects that were described before. However, other groups claim the composition of their quantum wells remains unchanged after annealing and therefore look for other mechanisms of the blue shift [52].

The second possibility is that there is a short range ordering or differently put, different configurations for the nearest neighbours of the nitrogen atoms, that influence the band-gap energy. Kim and Zunger [73] point out that to obtain the more stable microscopic configuration, there has to be a balance between strain energy in the lattice and chemical bond energy. To minimise the first part, nitrogen is preferentially bound to indium and gallium to arsenic, whereas to minimise the chemical energy, the opposite is true (GaN+InAs). When calculating the minimal total energy for lattice-matched $Ga_{0.89}In_{0.11}N_{0.04}As_{0.96}$ they find that starting from a random alloy where nitrogen is bound to four gallium atoms (Ga4N), the best configuration is Ga1In3N. These different binding configurations each have a different energy level of the nitrogen-induced resonant band (cf. Figure 2-17). When more indium-atoms are bound to nitrogen, the coupling between these nitrogen-localised states and the Γ-state becomes weaker, which in turn leads to less bowing and thus a band-gap blue shift of about 100meV for the Ga1In3N configuration.

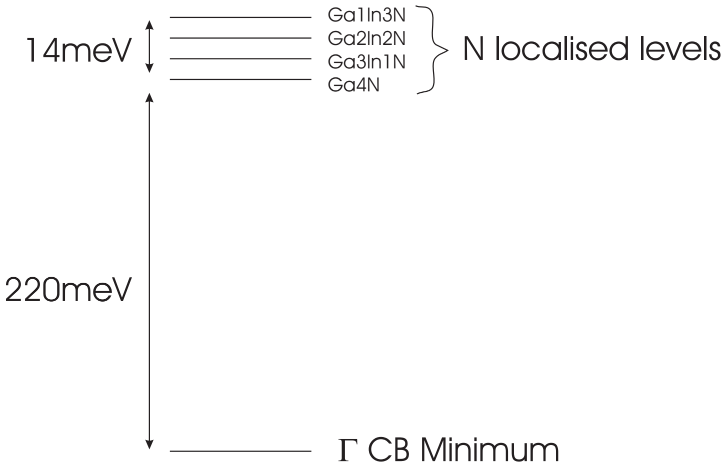

Figure 2-17 Energy levels of N localised levels relative to the GaAs conduction band minimum for different binding configurations, after [73]

During epitaxial growth the dominant parameter is the chemical bond energy, which promotes the formation of a gallium-rich environment for nitrogen. This results in a high local strain. During the post-growth anneal, the point defects caused by low-temperature growth stimulate a changeover in the nitrogen-bonding configuration toward a more indium-rich environment with lower local strain [74]. There is some experimental data to support this last hypothesis. Resonant Raman scattering [75] and Fourier transform infrared (FTIR) spectroscopy [76] shows that annealing causes the formation of In-N bonds in as-grown material where Ga-N bonds dominate. It is also shown that the existing Ga-N bonds are subject to less strain after annealing, suggesting a shorter bond length [76]. This shortening of the Ga-N bond length upon annealing is also observed by infrared absorption spectroscopy [77].

2.5. State of the art of devices

To conclude this chapter, we will review the characteristics of GaInNAs devices. Since Kondow's pioneering research and given the interest of most groups, the main part focuses on edge emitting lasers in the near infrared region. These results however have paved the way for the production of monolithic VCSEL's, lasing in the same wavelength region, which hold the promise of becoming the material's killer-application.

2.5.1. Edge emitting lasers

Kondow already pointed out the importance of the potentially better thermal characteristics of GaInNAs-based lasers. Because of the large conduction band discontinuity of GaInNAs/GaAs heterojunctions compared to e.g. junctions in the InGaAsP-system, electrons need more thermal excitation to be able to hop over the barriers out of the quantum well. This way, electrons no longer contribute to the recombination current, which results in an increase of the threshold current. Usually this parameterised by the characteristic temperature T_0 that expresses the sensitivity of the threshold current to temperature:

$$I_{th} = I_0 \, . \, \exp(T_s / T_0)$$

Group	Technology	λ [μm]	η_{ext} [W/A]	J_{th} [kA/cm2]	T_0 [K]	Ref.
Hitachi	MBE	1.18		1.83	126	[78]
Tokyo Ins. Techn.	CBE	1.20		0.96	270	[79]
	MOCVD	1.28		0.45	130	[80]
	MOCVD	1.3		0.39		[81]
Columbia Univ.	SS-MBE	1.20	0.15	0.52		[82]
Infineon	SS-MBE	1.30	0.59	0.68	75	[83]
Nanoplus	MBE	1.28	0.22	0.78		[84]
Philips Univ. Marburg	MOCVD	1.28	0.18	0.80	100	[85]
Columbia Univ.	SS-MBE	1.30	0.12	1.02	64	[86]
Tampere Univ. Techn.	SS-MBE	1.32	0.28	0.564	104	[87]
Univ. of Wisconsin	MOCVD	1.29		0.4	110	[88]
	MOCVD	1.294		0.27		[89]
	MOCVD	1.295		0.229	75	[90]
Furukawa	GS-MBE	1.305		0.46		[91]
Agilent	MOCVD	1.29		0.58		[92]
InGaAsP ref. (5QW)	MOCVD	1.30	0.20	0.50	60	

Table 2-1 Overview of the best broad area laser results published to date.

The relevant device parameters are set out in Table 2-1 and Table 2-2. Although MBE and related techniques seems to be the prevailing growth technology, MOCVD has closed the gap in recent years. The best example is the co-operation between the groups at Infineon and Marburg that has produced comparable laser results with both technologies. Compared to InGaAsP based lasers, GaInNAs lasers have comparable efficiencies and threshold current densities, but a far greater T_0 value.

Group	Technology	λ [µm]	η_{ext} [W/A]	J_{th} [kA/cm2]	T_0 [K]	Ref.
Infineon	SS-MBE	1.29	0.35	1.63	100	[93]
Ricoh	MOCVD	1.29	0.14	1.00	148	[94]
Nanoplus	SS-MBE	1.29	0.52	0.875	160	[95]
Hitachi	MBE	1.30	0.16	6.75		[96]
Princeton	GS-MBE	1.30	0.28	2.70	140	[97]
Hitachi	MBE	1.32	0.06	3.20	214	[98]
Stanford	SS-MBE	1.39	0.67	1.50		[99]

Table 2-2 Overview of the best ridge laser results published to date.

The evolution of the threshold current densities of the lasers with lasing wavelength is shown in Figure 2-18. Even though the current density of the best GaInNAs lasers rivals that of InGaAsP lasers around 1.3µm, it becomes worse with increasing wavelength, showing that increasing the nitrogen content is deteriorating optical quality.

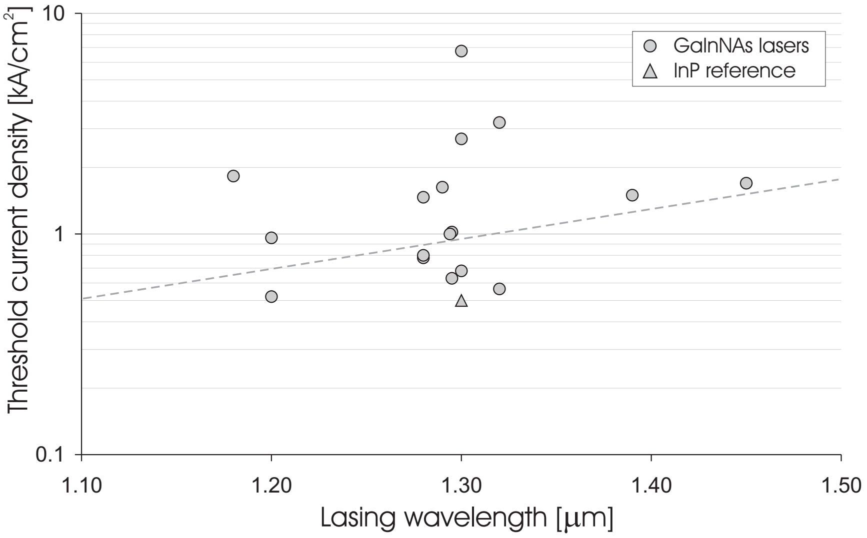

Figure 2-18 Threshold current density of GaInNAs and InGaAsP lasers emitting in the 1.3μm region. The dashed line is a guide to the eye only.

2.5.2. VCSEL's

The appearance on the market of GaInNAs-based VCSEL's has irrefutably shown the true potential of the material system and the immense progress that has been made in the research on the topic. The excellent characteristics of the devices are summarised Table 2-3. It also shows how the quality of MOCVD-grown active regions has caught up with that of MBE-material.

Currently commercial devices emitting at 1.3 μm are available from two different sources. One is the result of a co-operation between Cielo Inc. and the Sandia Labs, the other has come from a co-operation between the Philips University at Marburg and Infineon GmbH. The devices perform very well, compared with existing non-GaInNAs devices. Cornell's VCSEL which uses fused mirrors (one GaAs/AlAs, one dielectric) and an InGaAsP active region has a threshold current of less than 1 mA, but a maximum output power of only 35 μW. Mitel's similar structure at 1550 nm attains 0.5 mW output power. In the Gore approach an 850 nm VCSEL and a long wavelength VCSEL are combined in one structure. The electrically operated 850 nm device then optically pumps the 1.3μm VCSEL. The threshold current density is 5 mA, but 2 mW of output power can be reached. We stress that these devices lack a simple growth sequence and subsequent processing.

Group	Technology	λ [µm]	η_{ext} [W/A]	I_{th} [mA]	P_{max} [W]	Ref.
TIT	CBE	1.20	0.23	1.2	1	[100]
Stanford	SS-MBE	1.2	0.09	1.2	0.1	[101]
Ricoh & Tokyo I.T.	MOCVD	1.26	0.1	7.6	0.1	[102]
Cielo Inc. & Sandia	SS-MBE	1.268	0.27	1.2	1.2	[103]
Furukawa	GS-MBE	1.3	0.2		1	[104]
Agilent	MOCVD	1.28			3	[105]
IQE	MOCVD	1.27		2		[106]
Infineon & Marburg	MOCVD	1.293	0.15	1.25	1.4	[107]

Table 2-3 Overview of GaInNAs VCSEL results to date. All devices are electrically pumped and operate in continuous wave mode at room temperature.

2.5.3. Other devices

GaInNAs has also attracted interest for application in other types of devices. A junction with a band-gap of 1 eV is of great interest for multi-junction solar cells, because it would allow capturing a greater part of the solar spectrum. Also GaInNAs has been studied as a base material for bipolar transistors. The performance of these devices to date is poor due to the low diffusion length of minoritary carriers. As a result the first characterisation of GaInNAs solar cells reports an internal quantum efficiency of less than 60% [108].

References

[1] I. A. Buyanova, W. M. Chen, B. Monemar, MRS Internet J. Nitride Semicond. Res. 6, 2 (2001).

[2] Markus Weyers, Michio Sato , Appl. Phys. Lett. 62, 1396-1398 (1993).

[3] Markus Weyers, Michio Sato, Hiroaki Ando, Jpn. J. Appl. Phys. 31, L853 (1992).

[4] M. Sato, Mater. Res. Soc. Symp. Proc. 395, 285 (1996).

[5] Masahiko Kondow, Kazuhisa Uomi, Kazuhiko Hosomi, Teruo Mozume, Jpn. J. Appl. Phys. 33, L1056 (1994).

[6] WG Bi, CW Tu, Appl. Phys. Lett. 70, 1608-1610 (1997).

[7] K. Uesugi, I. Suemune, Jpn. J. Appl. Phys. 36, L1572 (1997).

[8] Shiro Sakai, Yoshihiro Ueta, Yoji Terauchi, Jpn. J. Appl. Phys. 32, 4413 (1993).

[9] Su-Huai Wei, Alex Zunger , Phys. Rev. Lett. 76, 664-667 (1996).

[10] L. Bellaiche, S. -H. Wei, A. Zunger, Phys. Rev. B 54, 17568 (1996).

[11] L. Bellaiche, S.-H. Wei, A. Zunger, Appl. Phys. Lett. 70, 3558-3560 (1997).

[12] L. Bellaiche, S. -H. Wei, A. Zunger, Phys. Rev. B 56, 10233 (1997).

[13] J. Neugebauer, C. Van de Walle, Phys. Rev. B 51, 10568 (1995)

[14] P. S. Zory (ed.), Quantum Well Lasers, Academic Press (1993).

[15] J.A. Van Vechten, Phys. Rev. 182 (3), 891-904 (1969).

[16] J.A. Van Vechten, Phys. Rev. 187 (3), 1007-1020 (1969).

[17] J.A. Van Vechten, T.K. Bergstresser, Phys. Rev. B 1 (8) , 3351-3358 (1970).

[18] W. Walukiewicz, Proceedings of SIMC-XI (2001).

[19] J. D. Perkins, A. Mascarenhas, Y. Zhang, J. F. Geisz, D. J. Friedman, J. M. Olson, S. R. Kurtz, Phys. Rev. Lett. 82, 3312 (1999).

[20] W. Shan, W. Walukiewicz, J. W. Ager, E. E. Haller, J. F. Geisz, D. J. Friedman, J. M. Olson, S. R. Kurtz, Phys. Rev. Lett. 82, 1221 (1999).

[21] W. Shan, W. Walukiewicz, J. W. Ager, E. E. Haller, J. F. Geisz, D. J. Friedman, J. M. Olson, S. R. Kurtz, J. Appl. Phys. 86, 2349 (1999).

[22] W. Walukiewicz, W. Shan, J. W. Ager, D. R. Chamberlin, E. E. Haller, J. F. Geisz, D. J. Friedman, J. M. Olson, S. R. Kurtz, "Nitrogen-induced modification of the electronic structure of group III-N-V alloys", Proc. 195th Meeting of the Electrochem Soc., Seattle, WA, May2-6, 1999; in"Photovoltaics for the 21st Century", vol.99-11, p. 190 (1999)

[23] E. D. Jones, N. A. Modine, A. A. Allerman, S. R. Kurtz, A. F. Wright, S. T. Torez, X. Wei, Phys. Rev. B 60, 4430 (1999).

[24] E. D. Jones, N. A. Modine, A. A. Allerman, I. J. Fritz, S. R. Kurtz, A. F. Wright, S. T. Torez, X. Wei, Proc. SPIE 3621, 52 (1999).

[25] E. D. Jones, A. A. Allerman, S. R. Kurtz, N. A. Modine, K. K. Bajaj, S. T. Torez, X. Wei, Phys. Rev. B 62, 7144 (2000).

[26] H. P. Hjalmarson, P. Vogl, D. J. Wolford, J. D. Dow, Phys. Rev. Lett. 44, 810 (1980).

[27] P. J. Klar, H. Grüning, W. Heimbrodt, J. Koch, W. Stolz, P. M. A. Vicente, A. M. Kamal Saadi, A. Lindsay, E. P. O'Reilly, Phys. Stat. Sol. B 223, 163 (2001).

[28] B. Gil, Sol. St. Comm. 114, 623 (2000).

[29] A. Lindsay, E. P. O'Reilly, Sol. St. Comm. 112, 443 (1999).

[30] T. Mattila, S. -H. Wei, A. Zunger, Phys. Rev. B 60, R11245 (1999).

[31] M. Kozhevnikov, V. Narayanamurti, C. V. Reddy, H. P. Xin, C. W. Tu, A. Mascarenhas, Y. Zhang, Phys. Rev. B 61, R7861 (2000).

[32] H. M. Cheong, Y. Zhang, A. Mascarenhas, J. F. Geisz, Phys. Rev. B 61, 13687 (2000).

[33] K. Uesugi, I. Suemune, T. Hasegawe, T. Akutagawa, Appl. Phys. Lett. 76, 1285 (2000).

[34] A. Polimeni, M. Cappizzi, M. Geddo, M. Fischer, M. Reinhardt, A. Forchel, Appl. Phys. Lett. 77, 18 (2000).

[35] P. N. Hai, W. M. Chen, I. A. Buyanova, H. P. Xin, C. W. Tu, Appl. Phys. Lett. 77, 1843 (2000).

[36] C. Skierbiszewski, P. Perlin, P. Wisniewski, W. Knap, T. Suski, W. Walukiewicz, W. Shan, K. M. Yu, J. W. Ager, E. E. Haller, J. F. Geisz, J. M. Olson, Appl. Phys. Lett. 76, 2409 (2000).

[37] M. Hetterich, M. D. Dawson, A. Yu. Egorov, D. Bernklau, H. Riechert, Appl. Phys. Lett. 76, 1030 (2000).

[38] Y. Zhang, A. Mascarenhas, H. P. Xin, C. W. Tu, Phys. Rev. B 61, 7479 (2000).

[39] J. Wu, W. Shan, W. Walukiewicz, K. M. Yu, J. W. Ager, E. E. Haller, H. P. Xin, C. W. Tu, unpublished (2001).

[40] B. Q. Sun, D. S. Jiang, X. D. Luo, Y. Z. Xu, Z. Pan, L. H. Li, R. H. Wu, Appl. Phys. Lett. 76, 2862 (2000).

[41] A. Buyanova, G. Pozina, P. N. Hai, W. M. Chen, H. P. Xin, C. W. Tu, Phys. Rev. B 61, 33303 (2001).

[42] S. Spruytte, C. Coldren, J. Harris, W. Wampler, P. Krispin, K. Ploog, M. Larson, J. Appl. Phys. 89, 4401 (2001)

[43] S. Francoeur, G. Sivaraman, Y. Qiu, S. Nikishin, H. Temkin, Appl. Phys. Lett. 72, 1857 (1998).

[44] I. A. Buyanova, W. M. Chen, G. Pozina, J. P. Bergman, B. Monemar, H. P. Xin, C. W. Tu, Appl. Phys. Lett. 75, 501 (1999).

[45] H. Gruning, L. Chen, Th. Hartmann, P. J. Klar, W. Heimbrodt, F. Höhnsdorf, J. Koch, W. Stolz, Phys. Stat. Sol. B 215, 39 (1999)

[46] M. Oueslati, M. Zouaghi, M. Pistol, L. Samuelson, H. Grimmeiss, M. Balkanski, Phys. Rev. B 32, 8220 (1985)

[47] Y. Narukawa, Y. Kawakami, S. Fujita, S. Nakamura, Phys. Rev. B55, R1938 (1997)

[48] I. Buyanova, W. Chen, B. Monemar, H. Xin, C. Tu, Appl. Phys. Lett. 75, 3781 (1999)

[49] I. Buyanova, G. Pozina, P. Hai, N. Thinh, J. Bergman, W. Chen, H. Xin, C. Tu, Appl. Phys. Lett. 77, 2325 (2000)

[50] S. Francoeur, S. Nikishin, C. Jin, Y. Qiu, H. Temkin, Appl. Phys. Lett. 75, 1538 (1999)

[51] H. McKay, Appl. Phys. Lett. 78, 82 (2001)

[52] T. Kitatani, M. Kondow, M. Kudo, Jpn. J. Appl. Phys. 40, 750 (2001)

[53] P. Krispin, S. G. Spruytte, J. S. Harris, K. H. Ploog, J. Appl. Phys. 88, 4153 (2000).

[54] H. Xin, K. Kavanagh, Z. Zhu, C. Tu, Appl. Phys. Lett. 74, 2337 (1997)

[55] L. Grenouillet, C. Bru-Chevalier, G. Guillot, P. Gilet, P. Duvaut, S. Vannuffel, A. Millon, A. Chevenas-Paule, Appl. Phys. Lett. 76, 2241 (2000)

[56] Y. P Varshni, Physica (Utrecht) 34, 149 (1967)

[57] R. Mair, J. Lin, H. Jiang, E. Jones, A. Allerman, S. Kurtz, J. Appl. Phys. 76, 188 (2000)

[58] S. Kurtz, J. Klem, A. Allerman, R. Sieg, C. Seager, E. Jones, Appl. Phys. Lett. 80, 1379 (2002)

[59] S. Kurtz, A. Allerman, E. Jones, J. Gee, J. Banas, B. Hammons, Appl. Phys. Lett 74, 729 (1999)

[60] H. Saito, T. Makimoto, N. Kobayashi, J. Cryst. Growth 195, 416 (1998)

[61] J. Geisz, D. Friedman, J. Olson, S. Kurtz, B. Keyes, J. Cryst. Growth 195, 401 (1998)

[62] E. Rao, A. Ougazzaden, Y. Le Belego, M. Juhel, Appl. Phys. Lett. 72, 1409 (1998)

[63] J.-C. Harmand, A. Caliman, E. Rao, L. Largeau, J. Ramos, R. Teissier, L. Travers, G. Ungaro, B. Theys, I. Dias, Semicond. Sci. Technol. 17, 778 (2002)

[64] S. Kurtz, J. Webb, L. Gedvilas, D. Friedman, J. Geisz, J. Olson, R. King, D. Joslin, N. Karam, Appl. Phys. Lett. 78, 748 (2001)

[65] A. Polimeni, H. Baldassari, M. Bissiri, M. Capizzi, M. Fischer, M. Reinhardt, A. Forchel, Phys. Rev. B 63, R201304 (2001)

[66] H. Baldassari, M. Bissiri, A. Polimeni, M. Capizzi, M. Fischer, M. Reinhardt, A. Forchel, Appl. Phys. Lett. 78, 3472 (2001)

[67] T. Miyamoto, T. Kageyama, S. Makino, D. Schlenker, F. Koyama, K. Iga, J. Cryst. Growth 209, 339 (2000)

[68] A. Balcioglu, R. Ahrenkiel, D. Friedman, Appl. Phys. Lett. 76, 2397 (2000)

[69] D. Kwon, R. Kaplar, S. Ringel, A. Allerman, S. Kurtz, E. Jones, Appl. Phys. Lett. 74, 2830 (1999)

[70] N. Thinh, I. Buyanova, P. Hai, W. Chen, H. Xin, C. Tu, Phys. Rev B 63, 33203 (2001)

[71] W. Li, M. Pessa, T. Ahlgren, J. Decker, Appl. Phys. Lett. 79, 1094 (2001)

[72] W. Li, M. Pessa, J. Likonen, Appl. Phys. Lett. 78, 2864 (2001)

[73] K. Kim, A. Zunger, Phys. Rev. Lett. 86, 2609 (2001)

[74] E. Tournie, M.-A. Pinault, A. Guzman, Appl. Phys. Lett. 80, 4148 (2002)

[75] J. Wagner, T. Geppert, K. Koehler, P. Ganser, N. Herres, J. Appl. Phys. 90, 5027 (2001)

[76] S. Kurtz, J. Webb, L. Gedvilas, D. Friedman, J. Geisz, J. Olson, Appl. Phys. Lett. 78, 748 (2001)

[77] T. Kitatani, M. Kondow, M. Kudo, Jpn. J. Appl. Phys. 40, 750 (2001)

[78] M. Kondow, Electr. Lett. 32, xx (1996)

[79] T. Kageyama, T. Miyamoto, S. Makino, N. Nishiyama, F. Koyama, K. Iga, Phot. Techn. Lett. 12, 10 (2000)

[80] M. Kawaguchi, T. Miyamoto, E. Gouardes, D. Schlenker, T. Kondo, F. Koyama, K. Iga, Jpn. J. Appl. Phys 40, L744 (2001)

[81] T. Miyamoto, Proceedings of Int. Workshop on GaAs-based lasers (Wroclaw), p46 (2003)

[82] X. Yang, M. Jurkovic, J. Heroux, W. Wang, Appl. Phys. Lett. 75, 178 (1999)

[83] Y. Egorov, D. Bernklau, B. Borchert, S. Illek, D. Livshits, A. Rucki, M. Schuster, A. A Kaschner, A. Hoffmann, G. Dumitras, M. Amann, H. Riechert, J. Cryst. Growth 227-228, 545 (2001)

[84] M. Reinhardt, M. Fischer, M. Kamp, J. Hofmann, A. Forchel, Phot. Techn. Lett. 12, 239 (2000)

[85] F. Höhnsdorf, J. Koch, S. Leu, W. Stolz, B. Borchert, M. Druminski, Electr. Lett. 35, 571 (1999)

[86] K. Yang, C. Hains, J. Cheng, Phot. Techn. Lett. 12, 7 (2000)

[87] W. Li, M. Pessa, T. Ahlgren, J. Decker, Appl. Phys. Lett. 79, 1094 (2001)

[88] N. Tansu, L. Mawst, IEEE Phot. Techn. Lett. 14, 444 (2002)

[89] N. Tansu, N. Kirsch, L. Mawst, Proceddings of IC-MOVPE XI (Berlin), p113 (2002)

[90] L. Mawst, Proceedings of IPRM03 (Santa Barbara), p273 (2003)

[91] H. Shimizu, Proceedings of IPRM03 (Santa Barbara), p264 (2003)

[92] S. Kim, Proceedings of LEOS 2001 (La Jolla)

[93] B. Borchert, A. Egorov, S. Illek, H. Riechert, Phot. Techn. Lett. 12, 597 (2000)

[94] S. Sato, S. Satoh, Phot. Techn. Lett. 11, 1560 (1999)

[95] M. Fischer, D. Gollub, M. Reinhardt, A. Forchel, Proc. IPRM-13, p101 (2001)

[96] K. Nakahara, M. Kondow, T. Kitatani, M. Larson, K. Uomi, Phot. Techn. Lett. 10, 487 (1998)

[97] M. Gokhale, J. Wei, H. Wang, S. Forrest, Appl. Phys. Lett. 74, 1287 (1999)

[98] M. Kondow, T. Kitatani, K. Nakahara, T. Tanaka, Jpn. J. Appl. Phys. 38, 1355 (1998)

[99] W. Ha, V. Gambin, M. Wistey, S. Bank, S. Kim, J. Harris, Phot. Techn. Lett. 14, 591 (2002)

[100] S. Makino, T. Miyamoto, T. Kageyama, Y. Ikenaga, N. Nishiyama, A. Matsutani, F. Koyama, K. Iga, Proc. of LEOS 2001

[101] M. Larson, C. Coldren, S. Spruytte, H. Petersen, J. Harris, Phot. Techn. Lett. 12, 1598 (2000)

[102] S. Sato, N. Nishiyama, T. Miyamoto, T. Takahashi, N. Yikutani, M. Arai, A. Matsutani, F. Koyama, K. Iga, Electr. Lett. 36, 2018 (2000)

[103] A. Jackson, R. Naone, M. Dalberth, J. Smith, K. Malone, D. Kisker, J. Klem, K. Choquette, D. Serkland, K. Geib, Electr. Lett. 37, 356 (2001)

[104] H. Shimizu, Proceddings of IPRM03 (Santa Barbara), p264 (2003)

[105] T. Takeuchi, Y.-L. Chang, M. Leary, D. Mars, T. Ashish, R. Twist, S. Belov, D. Bour, M. Tan, D. Roh, Y.-K. Song, L. Mantese, H.-C. Luan, Proceedings of Int. Workshop on GaAs-based lasers (Wroclaw), p21 (2003)

[106] A. Joel, Proceedings of Int. Workshop on GaAs-based lasers (Wroclaw), p22 (2003)

[107] A. Ramakrishnan, G. Steinle, D. Supper, C. Degen, G. Ebbinghaus, Electr. Lett. 38, 322 (2002)

[108] D. Friedman, J. Geisz, S. Kurtz, J. Olson, J. Cryst. Growth 195, 409 (1998)

CHAPTER 3

LOW TEMPERATURE GROWTH

3.1. Abstract

This chapter deals with growth at low temperatures. This is needed to maximise the nitrogen content in the layers (as will be discussed later), but is also beneficial for the growth of highly strained layers.

First we have a look at degradation mechanisms in strained layers such as dislocation formation and three-dimensional growth. We will introduce the notion critical thickness and XRD reciprocal space mappings as a means to study this.

Next, an overview of the growth study will be provided. TEGa is introduced as an alternative to TMGa. The effect of growth temperature on the relaxation and optical properties of highly strained, high-indium-content quantum wells will be shown. Finally, we will have a look at some devices that have been grown with these highly strained layers in the active region.

3.2. Introduction and motivation

GaAs, InGaAs or AlGaAs layers are normally grown at temperatures between 600ºC and 760ºC. Surface reactions are fast, precursors pyrolise completely and growth rate and composition are independent of temperature in this range. However, there are two good reasons to move to a low temperature growth regime.

First, as we will show in a later chapter (chapter 5), the low temperature is needed to incorporate nitrogen in the (In)GaAs layers. This is usually attributed to desorption. Between 530ºC and 560ºC the incorporation already drops by a factor of two.

Also, as discussed in chapter two, the introduction of nitrogen into the lattice has a detrimental effect on the optical quality. This is why we will try to limit the nitrogen content of our active layers and in a first step we will even try without. Of course, now the layers are heavily strained. In this chapter we will explore the limits of nitrogen-free InGaAs material. We will study the possibilities of the material of reaching higher wavelengths without adding nitrogen. Then we will meet the physical limitations of the strained layers and discuss the means to circumvent them.

One such means is growth at low temperatures, which on its turn again leads to new challenges. Even our good old standard precursors TMGa and AsH_3 are no longer safe and will be replaced by more suitable sources.

3.3. Long wavelength InGaAs: meet the strain barrier

As we add indium to GaAs to reduce the band-gap energy, the lattice constant difference with GaAs increases as well. During epitaxy this lattice mismatch will be the cause of two undesirable effects. One is the introduction of misfit dislocations; the other is the start of three-dimensional growth.

Dislocations break the regular crystal lattice and are the cause of dangling bonds. These have free electrons that can easily absorb light or act as traps for free carriers. The creation of misfit dislocations is governed both by the lattice mismatch and by the thickness of the mismatched layer. A small lattice mismatch will cause dislocations only when the layer is thick enough. For an example we refer to the growth of solar cells on germanium (see chapter 4, section 5). These are rather thick structures (~5µm) and there is a small difference between the lattice constants of germanium and GaAs. To avoid crosshatch we add a small amount of indium to obtain a smooth morphology.

Obviously, three-dimensional growth will cause a bad surface morphology and also disrupt the crystal lattice. One notable exception is the growth of quantum dots where the dots are carefully covered with a planarisation layer. The important parameter that determines the growth mode is the lattice mismatch. Three-dimensional growth will only occur when the lattice mismatch is sufficiently large, as e.g. in the case of InAs dots on GaAs.

3.3.1. Critical thickness

When we deposit a layer on a substrate with a different lattice constant, the layer will initially deform elastically so that it continues to follow the substrate's crystal lattice. In the plane it will adapt the substrate's lattice constant but in the perpendicular direction it will deform to try and maintain its volume. At some given point the energy that is built up by the deformation will be too high and the layer will relax by creating misfit dislocations. This is illustrated in Figure 3-1. The condition for relaxation to occur is that the built-in strain has a higher energy than the activation energy for the nucleation of dislocations.

The lattice constant of the substrate and freestanding layer are called a_s and a_r respectively, and $a_{//}$ and $a_\perp$ are the in-plane and perpendicular lattice parameters of the layer on the substrate.

The degree of relaxation R and the mismatch f are then defined as:

$$R = \frac{a_{//} - a_s}{a_r - a_s} \qquad f = \frac{a_r - a_s}{a_s}$$

We can then conclude that for compressively strained material ($a_r > a_s$) and with Poison’s ratio ν we have following cases:

- Perfectly strained: $a_{//} = a_s$
  $$a_\perp = \frac{a_r.(1 + \nu) - 2.\nu.a_{//}}{(1 - \nu)}$$
  thus $R = 0$.
- Partially relaxed: $a_r > a_{//} > a_s$; $a_\perp > a_r$ thus $0 < R < 1$.
- Completely relaxed: $a_{//} = a_\perp = a_r$ thus $R = 1$.

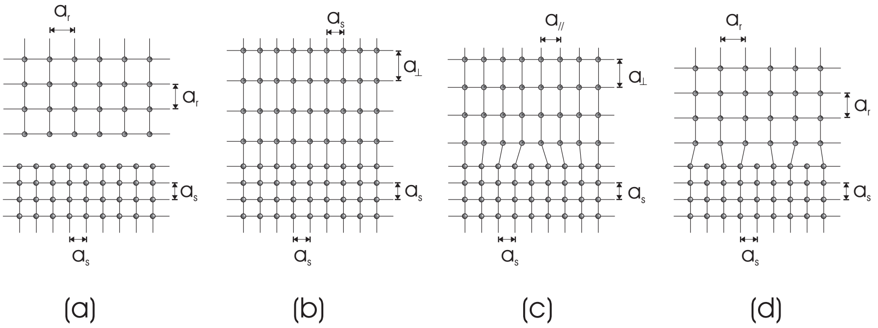

Figure 3-1 A layer with lattice constant a_r is put on top of a substrate with lattice constant a_s (a). Either the layer can be fully strained (b) or partially (c) or completely (d) relaxed.

Relaxation causes various types of lattice defects. In the family of two-dimensional defects we distinguish between stacking defects, anti-phase domains or in the worst-case even polycrystalline grains. Anti-phase domains are not caused by lattice-mismatch, but are a consequence of combining polar and non-polar crystals. They are discussed in the next chapter together with the growth on germanium. Polycrystalline growth doesn’t occur in a standard growth regime. Stacking defects occur when locally a part of a lattice plane is added to or removed from the lattice.

The two basic types of linear defects are shown in Figure 3-2. These dislocations can be characterised by their dislocation line and Burgers vector. In an edge dislocation a half plane of atoms is taken out. The dislocation line is the straight line where this half plane ends. In a screw dislocation the atomic bonds within a half plane are moved one position. The dislocation line is the line around which the screw is formed.

The Burgers vector can be found using a simple algorithm. First we consider a perfect crystal and create a closed Burgers path in a plane perpendicular to the dislocation line, defined by a number of atom-per-atom hops. If we repeat the same recipe in the dislocated lattice, the path will no longer be closed. The vector that is needed to close the path is called the Burgers vector.

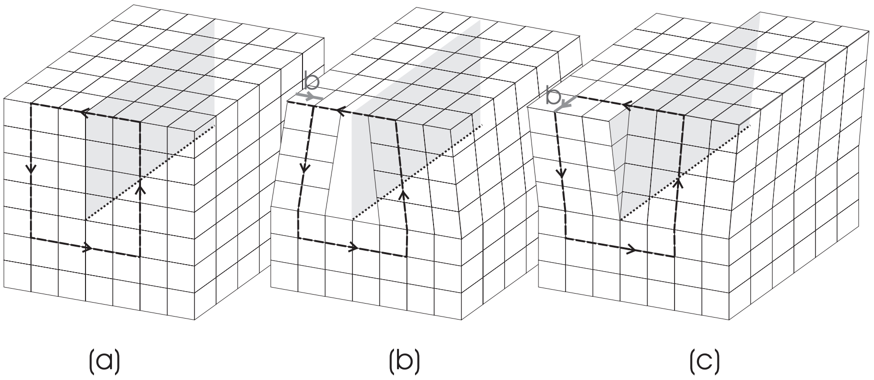

Figure 3-2 Starting from a perfect lattice (a), two basic types of linear lattice defects can occur: the edge dislocation (b) and screw dislocation (c). Also shown are the dislocation line (dotted), the Burgers path (dashed) and Burgers vector (solid grey).

Edge and screw dislocations are not the only types. Dislocations can be combined from different dislocations with a common dislocation line. Its Burgers vector is the sum of all constituents' Burgers vector. As such, the dislocation can have a combined edge and screw character. A typical type of such mixed dislocations in zinc-blende crystals is the so-called 60º type, named after the angle between dislocation line and Burgers vector.

Dislocation lines can only end at the surface of the crystal or on another dislocation line with an identical Burgers vector. In this way, they can form loops or half loops ending at the surface. Dislocations that penetrate the surface will propagate through the layer stack and are called threading dislocations.

The dislocation line and Burgers vector define the gliding plane of a dislocation. When both are parallel, in the case of a screw dislocation in a zinc-blende crystal, the gliding plane is the closest stacked plane that contains the dislocation line, which is the {111} plane. Dislocations can move within their gliding plane under influence of mechanical strain.

Based on the idea of gliding dislocations, a number of models have been proposed to describe the point at which misfit dislocations will be introduced at the interface between the strained and its supporting layer. The thickness at which these misfit dislocations are first formed is called the critical thickness of a layer. The best-known model is that of Matthews and Blakeslee [1]. It is based on the equilibrium of forces and illustrated in Figure 3-3. They presume that there are several threading dislocations in the grown layer that will glide within the gliding plane. To interconnect the threading dislocations in the strained and supporting layers, misfit dislocations at the interfaces will be created and relieve part of the strain.

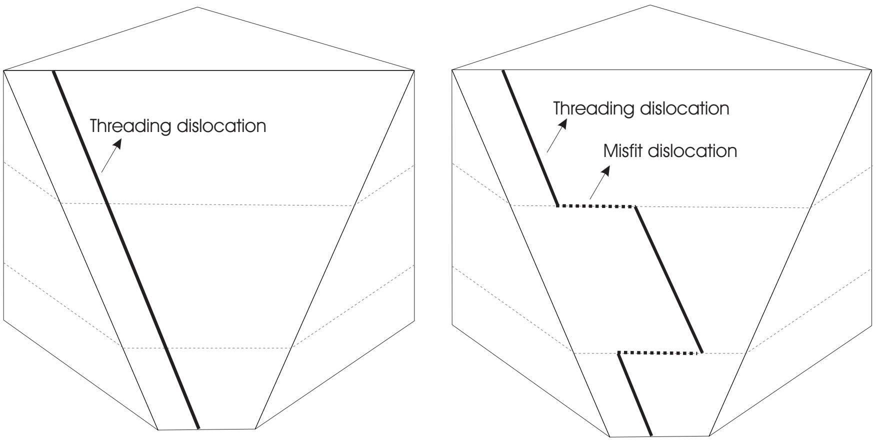

Figure 3-3 Creation of misfit dislocations according to Matthews and Blakeslee.

By calculating the force induced by the strain and the "linear force" of the misfit dislocation and by making a number of assumptions and approximations, they obtain the implicit relationship for the critical thickness h_c:

$$h_c = \frac{a}{\kappa\sqrt{2}\,\pi f}\,\frac{1 - \nu/4}{1+\nu}\left[\ln\left(\frac{h_c\sqrt{2}}{a}\right) + 1\right]$$

In this expression ν is the Poisson ratio and κ a factor that is 2 for a single layer and 4 for a sandwiched layer. Usually the expression is solved iteratively. It usually yields two solutions, so care is needed when interpreting the results. Just recently an analytical solution has been found but as it involves Lambert's transcendental W-function, it is of little practical use [2].

Another commonly used model is that of People and Bean [3]. They consider the equilibrium of the energy of the strained layer and the energy that is needed to create a new dislocation. They assume there are no threading dislocations in the layer and that screw dislocations are the first to form. They also arrive at an implicit relationship:

$$h_c = \frac{a}{32\sqrt{2}\,\pi f^2}\frac{1-\nu}{1+\nu}\ln\left(\frac{h_c\sqrt{2}}{a}\right)$$

This equation could equally well be expressed in an explicit form using the method of Braun [2].

Using these equations we can now quantify the theoretical critical thickness of InGaAs layers sandwiched in between GaAs barrier layers. When we take the strain and quantum well effect into account we can also plot the wavelength related to the transition energy of the InGaAs layer. This is shown in Figure 3-4. The model of People and Bean gives a larger critical thickness than the model of Matthews and Blakeslee. In any case, the maximum wavelength that can be obtained theoretically is smaller than 1.2µm.

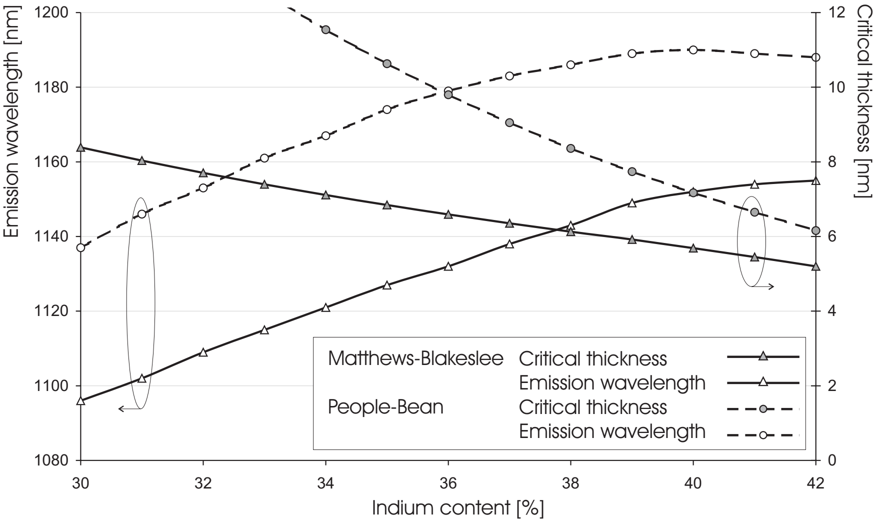

Figure 3-4 Critical thickness of a lattice-mismatched InGaAs layer sandwiched between GaAs layers, calculated by the models of Matthews-Blakeslee and People and Bean.

It is important to point out that the actual critical thickness can differ from the theoretically predicted ones under influence of various growth parameters. Especially such parameters as low temperature and high growth velocity will allow the growth of thicker metastable layers.

3.3.2. Reciprocal space mapping

The tool of choice to examine the relaxation of epitaxial layers is x-ray diffraction (XRD) and more in particular reciprocal space mappings. The principle of XRD is rather simple. The sample is exposed to X-ray radiation that will reflect on a carefully selected crystal plane, which is not necessarily parallel to the sample surface. For certain combinations of input angles and lattice parameters the reflected rays will interfere constructively and a large intensity will be detected at the output angle. This will occur when Bragg's condition is fulfilled (see Figure 3-5).

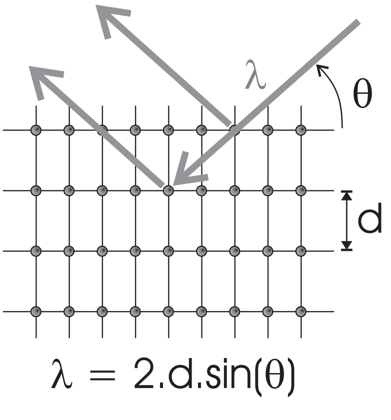

Figure 3-5 Bragg's condition for a ray with wavelength λ coming in under an angle θ onto crystal planes with spacing d for the simplest case of symmetric reflection

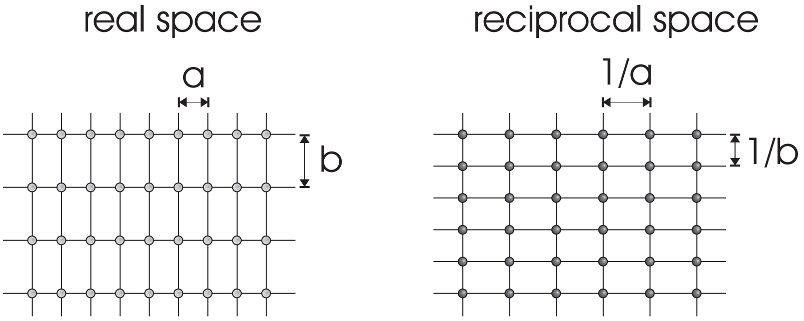

Figure 3-6 Transformation in two dimensions from real space (atomic positions) to reciprocal space (reflections).

Even though this relationship is sufficient to study relaxation (see e.g. [7]), an interesting transformation exists that makes the interpretation easier. Therefore we consider the transformation depicted in Figure 3-6. Starting from a crystal lattice where the atoms are a distance a and b apart we create a new reciprocal lattice with a spacing of 1/a and 1/b. This new lattice is part of the reciprocal space.

In general when we transform a three-dimensional cubic crystal we find a three-dimensional reciprocal cubic lattice where every reciprocal lattice vector h is an integer combination of the reciprocal basis vectors a*, b* and c*.

$$\vec{h} = h.\vec{a}^* + k.\vec{b}^* + l.\vec{c}^*$$

Here the triplet of integers (h, k, l) uniquely characterises each reciprocal lattice vector and its magnitude is inversely proportional to the spacing d of the lattice planes.

It is convenient to introduce the wave vector k_i, which is parallel to the direction of the incident beam. Its magnitude is set as the inverse of the wavelength λ of the incident beam. We define the wave vector k_h in a similar way but parallel to the diffracted beam.

The reciprocal analogue of the Bragg condition is called the Laue condition:

$$\vec{k}_h = \vec{k}_i + \vec{h}$$

The Laue condition is the basis of the construction of the Ewald sphere in reciprocal space (Figure 3-7). The incident and diffracted wave vectors have the same origin and magnitude and thus define a sphere with one point of the circumference in the origin and radius equal to $1/\lambda$. When the diffracted wave vector coincides with a reciprocal lattice vector the Laue condition is met. This occurs in the diagram when the Ewald sphere that hinges around the origin crosses one of the lattice vectors. From the diagram, we can now read the angles ω (between the incident x-rays and the surface) and 2θ (between the incident and diffracted beams) at which the reflection occurs.

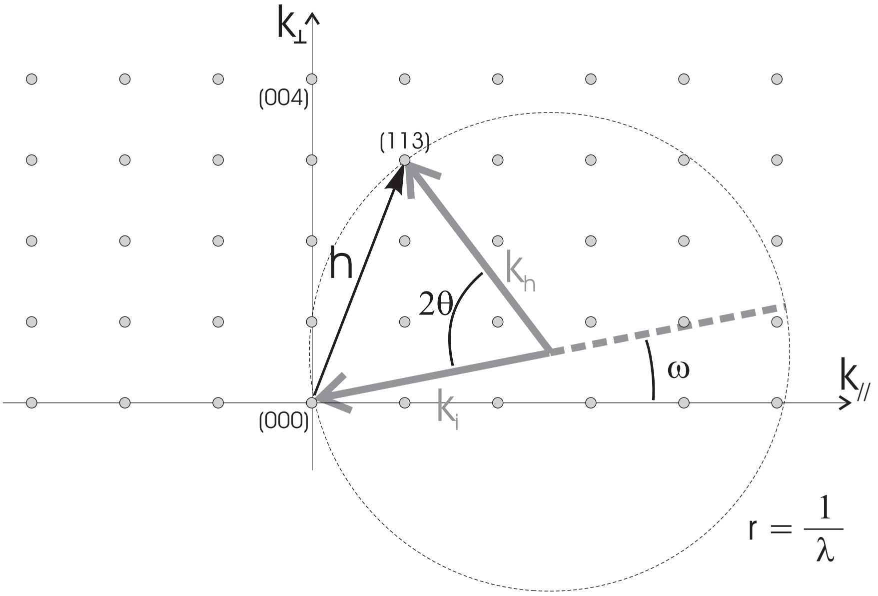

Figure 3-7 The Bragg condition in reciprocal space: construction of the Ewald sphere with the incoming (i), transmitted (t) and reflected beams (r).

Due to physical restrictions of the XRD-machine, such as the XRD-wavelength and angular limits, only a part of the reciprocal space can be scanned. This part is shown as the white area in Figure 3-8, whereas the grey area cannot be scanned. Also, not all reflections are possible due to destructive interference within the crystal (expressed by the structure factor). In a zinc-blende crystal all integers h, k and l need to be simultaneously even or odd. Due to the difference in lattice constants, the positions of the reflections in reciprocal space for different layers will not coincide and one can easily determine the relaxation of layers by their position relative to the substrate's. A perfectly strained layer adapts the substrate's in plane lattice vector and constructive interference will thus occur at the same in plane vector as the substrate's. In practice we will select a limited area in reciprocal space around one of the asymmetric (h and/or k different from 0) lattice vectors.

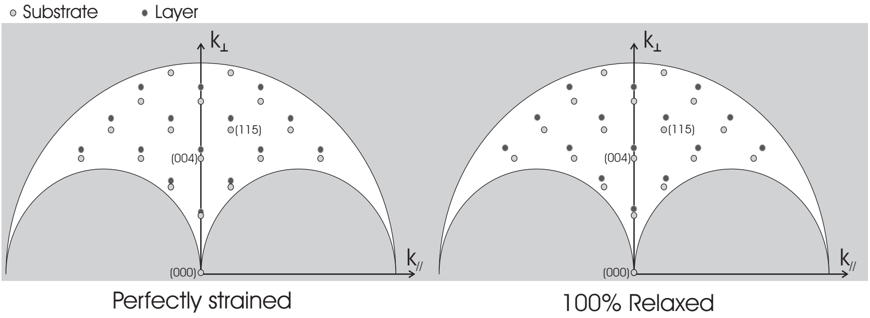

Figure 3-8 View of XRD patterns in scan-able reciprocal space (white). The light round spots are the substrate, the darker spots are tensile strained layers.

3.3.3. Growth modes

Another degradation mechanism when growing highly strained epitaxial layers is three-dimensional growth. Depending on the growth parameters, we can distinguish three different growth modes (see Figure 3-9). First and for all there is the two-dimensional Frank-van der Merwe growth mode, in which growth starts by the formation of mono-layer islands that coalesce laterally. In this way epitaxial layers are deposited one after the other. The other extreme is the Volmer-Weber or three-dimensional growth mode. Again, spread across the surface various pyramid-like islands are formed but these now expand both laterally and in the perpendicular direction. A third growth mode, called Stanski-Krastanov, is a crossbreed form, in which growth first proceeds in the two-dimensional mode, but changes into three-dimensional mode after a few layers.

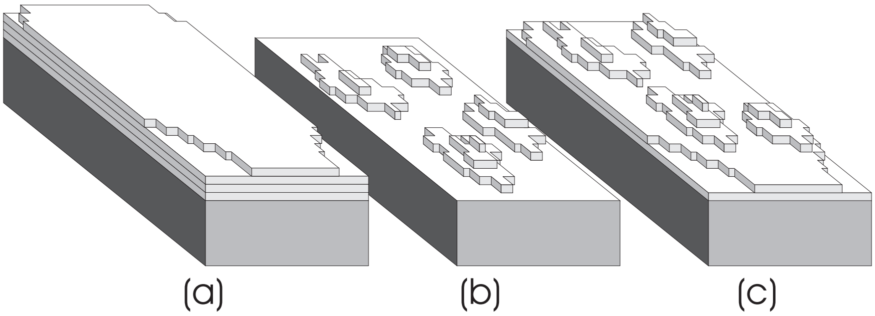

Figure 3-9 Illustration of Frank-van der Merwe (a), Volmer-Weber (b) and Stanski-Krastanov (c) growth modes.

Besides some very specific applications, such as quantum dots in which case it is the aim to have reasonably controlled three-dimensional growth, one will always try to obtain a two-dimensional growth regime. A rule of thumb is that three-dimensional growth may occur when the lattice mismatch exceeds 2%. The actual transition point depends on the nucleation rate and mobility of the atoms on the semiconductor surface. Three-dimensional growth can be suppressed by using a low growth temperature, a high growth rate and a high V/III ratio. The atom migration length has to be sufficiently small to achieve high indium content, but yet large enough to realise good crystal quality [6].

3.4. Growth in the kinetically limited regime

Unfortunately, there is more to reducing the growth temperature than just reducing the power provided to the heater element. Even though MOCVD growth is fundamentally governed by thermodynamics, it is not an equilibrium process. Thermodynamics defines only certain limits for the growth process, such as the driving force, maximum growth rate, number and composition of phases. It gives valuable information about the free energy of the system in the initial and final state. It is however unable to provide information about the time to obtain equilibrium. Kinetics of surface reactions and mass transport through the gas phase are never fast enough to establish equilibrium throughout the system at all times.

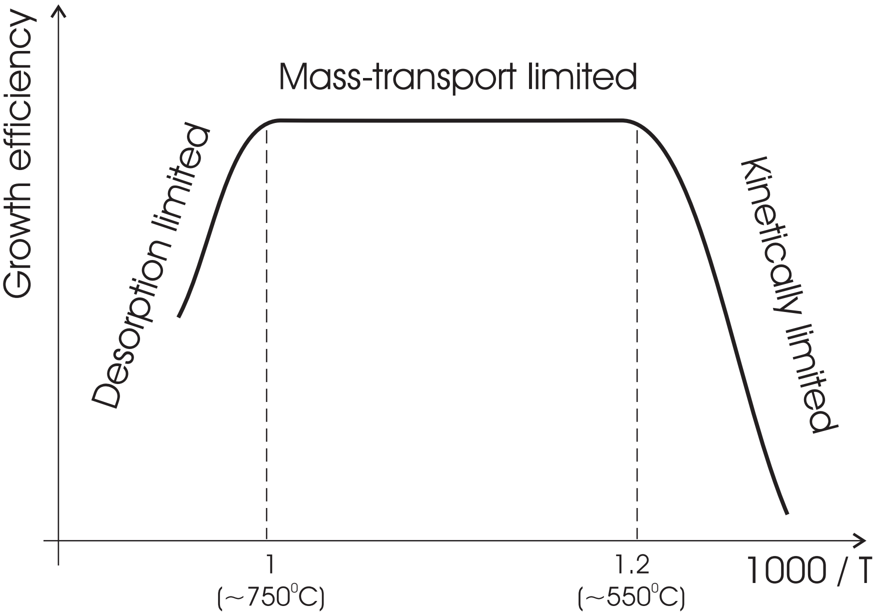

Figure 3-10 Arrhenius plot of the growth rate versus reciprocal temperature. The actual temperatures mentioned refer to growth of GaAs using TMGa and arsine.

The normal situation for MOCVD epitaxial growth (see Figure 3-10) is the temperature range where the interface kinetics is much more rapid than the diffusion kinetics. Since diffusion is a nearly-temperature independent process, growth rate and solid composition are independent of temperature in this regime. At higher temperatures the growth may be limited by thermodynamics or by depletion of the reactants on reactor walls. When we reduce the temperature of the substrate below a certain value, e.g. 550ºC for GaAs grown using TMGa and arsine, it is the surface kinetics that are the limiting step because the formation of certain species in the gas phase or at the interface is too slow. We note that the temperatures at which the transition from one growth mode to another occurs vary from one precursor to another, due to different pyrolysis mechanisms and temperatures.

One negative effect that we observe when we reduce the growth temperature is the decreasing pyrolysis of the source materials. It is not easy to measure the actual pyrolysis of the group V precursor without specialised equipment and experiments. From data in literature [4] it is clear that arsine pyrolises in a negligible way at temperatures below 550ºC. A complete description of growth using arsine's alternative TBAs can be found in the next chapter. The effect of the reduced pyrolysis of the group III reactants is immediately clear from its effect on the growth rate. This is illustrated in Figure 3-11, where we observe the reducing growth rate below 550ºC.

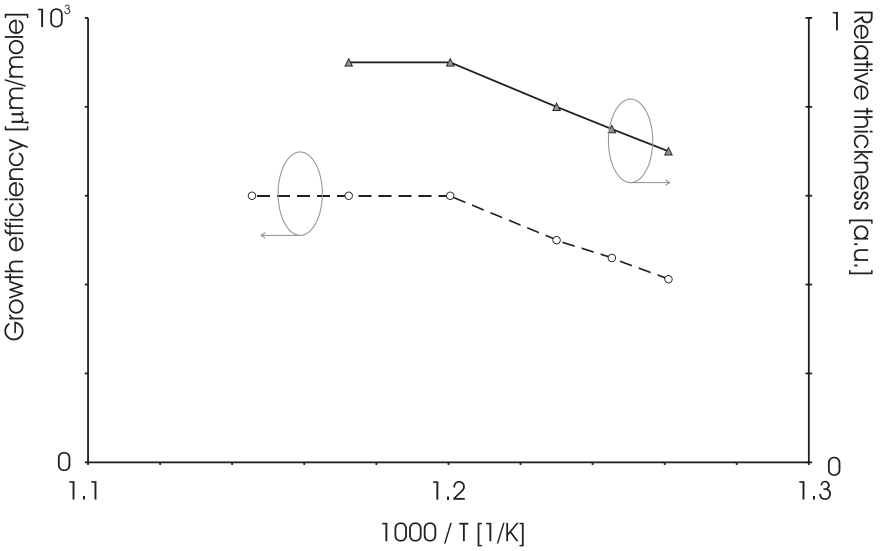

Figure 3-11 Experimental data of the transition into the kinetically limited growth of GaAs using TMGa and AsH_3.

The reducing pyrolysis of TMGa will also cause a substantial increase of the carbon background doping of the grown layers. The primary cause of this is the methyl groups that remain bonded to the Ga-atom on the surface and are consequently incorporated on an arsenic-site into the bulk layer.

The classic replacement for tri-methyl-gallium as a Ga source is tri-ethyl-gallium (TEGa) or $Ga(C_2H_5)_3$. The reduction of carbon doping is attributed to the TEGa pyrolysis mechanism and lower pyrolysis temperature. It does not pyrolise before reaching the surface. Pyrolysis itself occurs first by the β-elimination reaction, making $GaH(C_2H_5)_2$ and may even produce GaH_n in subsequent steps [4]. Literature data suggests that with TEGa, MOCVD epitaxial growth occurs in the mass transport regime down to temperatures around 500ºC [5]. The reduction of the carbon levels is shown in Figure 3-12. Two layers of GaNAs grown at 530ºC and 700torr using TMGa and TEGa respectively in combination with AsH_3 have been characterised using SIMS. The nitrogen content of both layers is comparable. This is an indication that there are no parasitic gas-phase pre-reactions with the group V precursors. Any variation is probably due to a temperature shift or measurement inaccuracy. The carbon concentration is near the detection limit (low 10^{17}) in the case of TEGa growth, but is as high as $3{\cdot}10^{18}$ for the TMGa case.

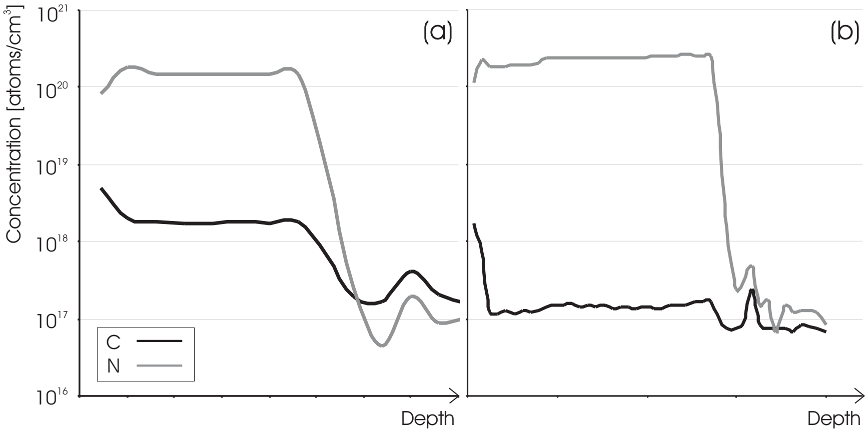

Figure 3-12 SIMS determination of carbon and nitrogen content in a single GaNAs layer grown with TMGa (a) and TEGa (b).

The carbon background also causes the optical quality to deteriorate. Indeed, carbon acts as a p-type dopant. The ionised acceptor induces band tails that easily absorb any light in the vicinity. In Figure 3-13 we compare photoluminescence signals from InGaAs quantum wells grown using both TEGa and TMGa. The TEGa sample is about ten times as bright.

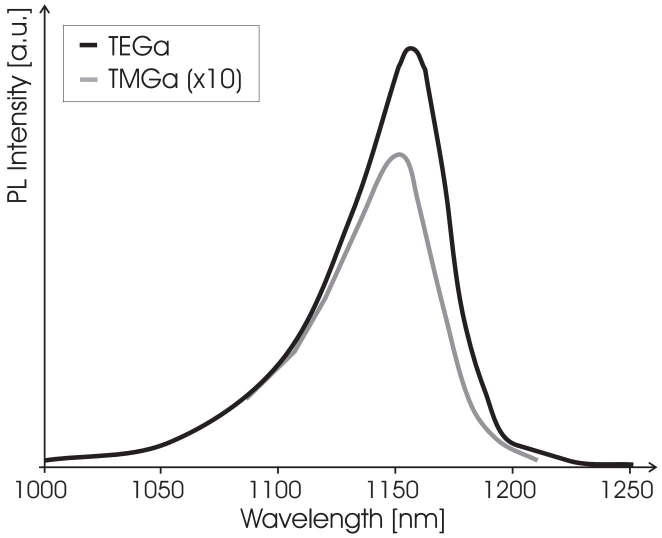

Figure 3-13 Photoluminescence from InGaAs QW's grown using TEGa and TMGa.

Besides this increased contamination, the reduction of the growth temperature will also affect the crystalline quality of the epitaxial layers. This will of course influence the optical quality. This is shown Figure 3-14 where we have plotted the photoluminescence spectra of 6nm thick $In_{35}Ga_{65}As$ single quantum wells grown at different temperatures using TEGa. Even though the critical thickness of layers of this composition is 6.67nm (Matthews-Blakeslee) or 10.63nm (People-Bean), the luminescence efficiency varies greatly between 500ºC and 600ºC, reaching an optimum around 530ºC. At the lower end of the temperature range, the photoluminescence disappears due to the effects mentioned above. However, increasing the temperature is not beneficial to the optical quality either. The increased mobility of the atoms on the surface will make the strained layers relax faster or promote 3-D growth modes.

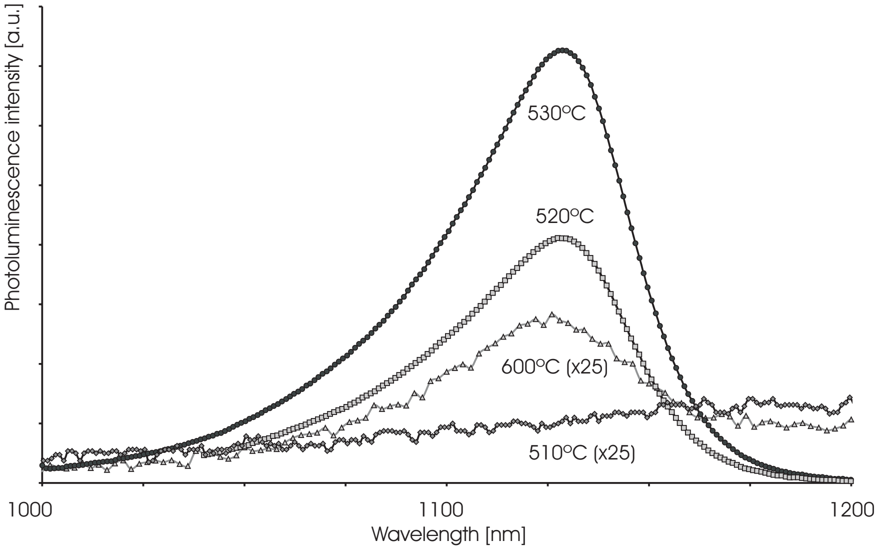

Figure 3-14 PL-spectra of InGaAs SQW's grown at different temperatures (using TEGa)

We have performed XRD reciprocal space mappings of the samples in Figure 3-14. These are shown in Figure 3-15 and Figure 3-16. The sample grown at 530ºC is perfectly strained. The sample that was grown at 600ºC on the other hand is partially relaxed, because the higher temperature will facilitate the nucleation of dislocations.

Whereas high temperature will lead to relaxation, too low temperature is not ideal either, because then the crystalline quality degrades. From the reciprocal space mappings, we observe multiple Pendellösung fringes in the sample grown at the higher temperature but not in the low temperature sample.

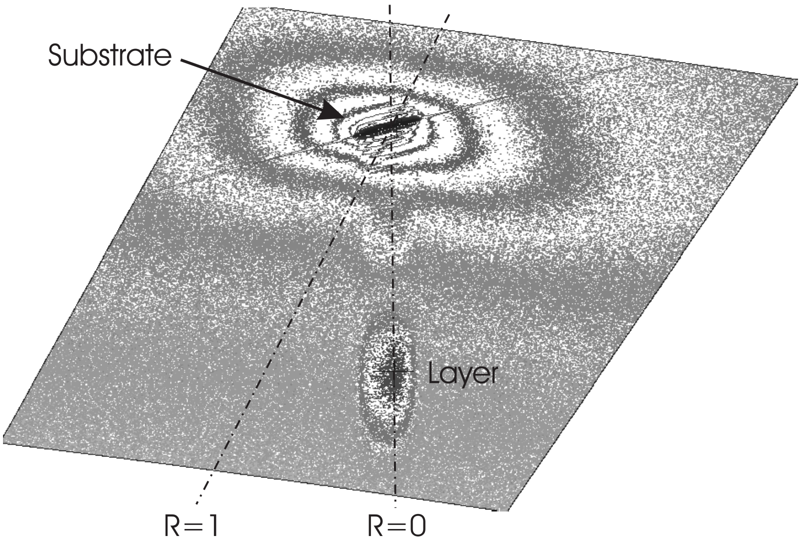

Figure 3-15 *Reciprocal space mapping around the <–1 1 5> reflection of the InGaAs SQW sample grown at 530°C. The layer is perfectly strained.*

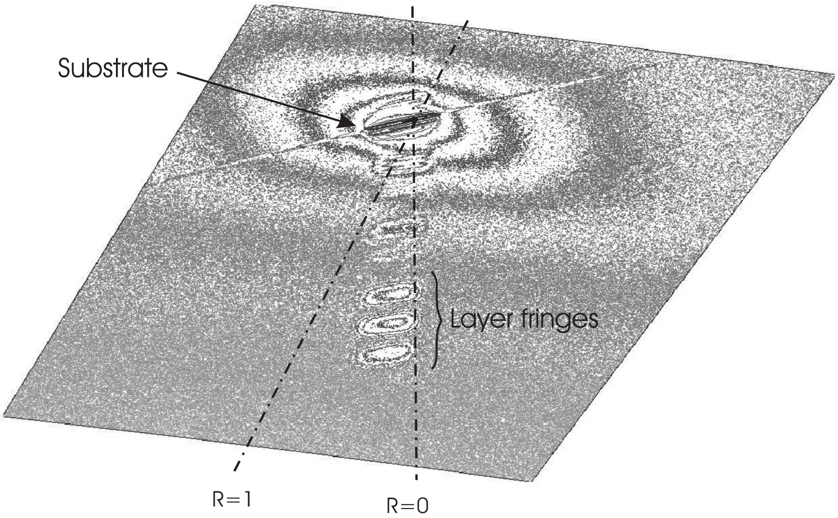

Figure 3-16 *Reciprocal space mapping around the <–1 1 5> reflection of the InGaAs SQW sample grown at 600°C. The layer is partially relaxed.*

This is also illustrated in Figure 3-17, where we show the PL intensity and full width at half maximum (FWHM) for InGaAs quantum wells grown just above 500ºC. Clearly the optical quality reaches an optimum around 525ºC.

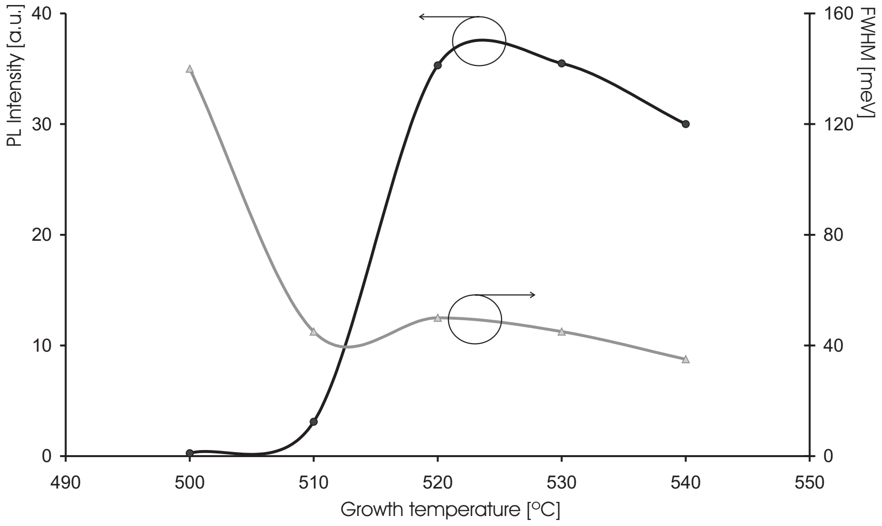

Figure 3-17 PL properties of InGaAs quantum wells. An optimum is found at 525ºC

Concerning the mobility of the gallium atoms, we point out the importance of the V/III ratio, as illustrated in Figure 3-18. The structure consists of a 7nm thick single quantum well with 42% indium grown at 530ºC using TEGa. We note that the critical thickness for such a well is only 5.65nm according to Matthews and Blakeslee and 7.17nm according to People and Bean. The reduction of the V/III ratio by less than a factor two already causes the photoluminescence to disappear almost completely. When the V/III ratio is decreased, the surface-coverage with arsenic decreases as well. This increases the mobility of the gallium atoms on the surface.

As we will show in the next chapter, the arsenic precursor arsine (AsH_3) is not really suitable for growth at these low temperatures. However, at the time of these experiments, the alternative source tertiary-butyl-arsenic (TBAs) was not yet available. Also, the development of epitaxial growth with a group V source is much more elaborate than changing a group III source. The study of growth using TBAs is covered in the next chapter. We only point out here that TBAs decomposes fully at the growth temperatures discussed here and as such an equal molar flow of TBAs as compared to arsine leads to a higher effective V/III ratio.

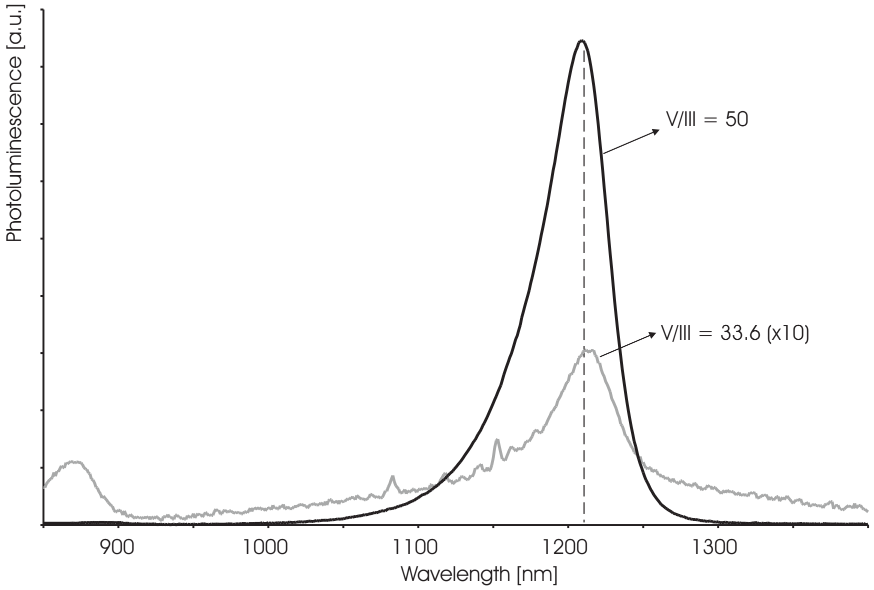

Figure 3-18 Illustration of the effect of the V/III ratio on the photoluminescence of 7nm thick $In_{42}Ga_{58}As$ *single QW's, grown at 530° using TEGa.*

3.5. Edge-emitters

These results have incited us to produce laser diodes with the best quantum wells grown so far. It is by no means our intention to give a broad overview of mechanisms behind the semiconductor laser or to provide an in-depth characterisation of the devices. For this we refer to some standard works in literature ([7] [8] [9] [10]). Instead, our aim is to examine the lasers to extract some basic parameters concerning the quality of the active region and the wave-guide.

3.5.1.1 Principle of operation

A semiconductor laser is a structure that has two important properties. The first is that it consists of an optical oscillator; the second is that it can provide amplification of the light within the oscillator. In standard edge-emitting lasers the oscillator takes the form of a wave-guide confined by two mirrors, usually just implemented as the semiconductor-air interface of two parallel, cleaved planes. Gain in the laser is obtained through stimulated emission of light. In order to do this, the laser is conceived as a p-i-n heterojunction operated in forward bias. This way, electrons and holes are concentrated in the active region. There they can recombine and expel their excess energy as light. The recombination either occurs spontaneously, or triggered by a passer-by photon. In the latter case, we speak of stimulated emission. Interesting to note is that the newly created photon will exactly mimic the properties such as polarisation, wavelength, direction and phase of the trigger-photon.

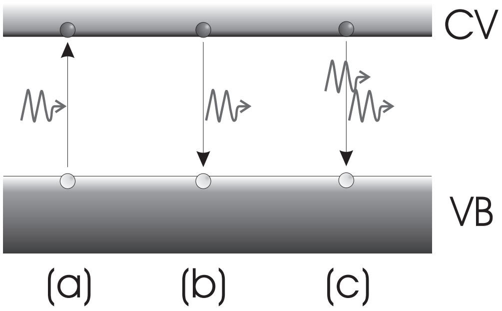

Figure 3-19 Simplified band-diagram depicting absorption (a), spontaneous emission (b) and stimulated emission (c).

However, as in a solar cell, the semiconductor can also absorb a photon and create an electron hole pair and thus cause optical losses (Figure 3-19). The ratio of loss and gain is determined by the electron occupation of the valence and conduction bands. It can be shown that the condition to obtain net gain is met when the higher energy level (i.e. the conduction band) has a higher electron occupation than the lower level (or the valence band). This condition is called population inversion. For a photon energy E = hν one can deduce the following expression for the gain (see e.g. [10]):

$$g(h\nu) = \frac{1}{h\nu} \cdot \frac{q^2.h}{2.c.\varepsilon_0.m_o^2} \cdot \frac{n_g}{n^2} \cdot |M_T|.2.\rho_{red}(h\nu\text{-}E_g').(f_c\text{-}f_v)$$

where q is the electron charge, h the Planck constant, n the refractive index, n_g the group index, c the speed of light in free space, ε_0 the permitivity in vacuum, m_0 the electronic mass, $|M_T|$ the transition matrix element, ρ_{red} the reduced density of states, E_g' the transition energy of the active medium and f_c and f_v the Fermi-functions for electrons and holes. The point where the gain is zero, thus when the material turns from an absorber into a gain material, is called transparency.

To obtain gain, the former expression has to be positive which leads us to the Bernard-Duraffourg condition for gain:

$$E_{fc} - E_{fv} > h\nu > E_g'$$

It is obvious that at equilibrium, when $E_{fc} = E_{fv} = E_f$, there can never be any gain. Note that even when the former condition is fulfilled, there is no laser activity yet; we have just reached the point where the active region turns from an absorber into a gain region.

To achieve lasing, we have to also take the effects of the optical cavity into account. Light propagating in the cavity with length L will feel the effect of intrinsic losses (α_i), will be amplified by the gain section (g) and will be reflected by both mirrors (R_1 and R_2). Of course only the light that is within the active region will be amplified. This is expressed by the confinement factor Γ. Lasing starts when the threshold gain g_{tr} is big enough so that the light intensity is maintained after one round-trip through the cavity:

$$R_1.R_2.\exp(2.L.(g_{tr}.\Gamma\text{-}\alpha_i)) = 1$$

When the current injection increases the gain beyond this point, the roundtrip gain remains fixed at unity, and the excess carriers build up the laser intensity. Part of this power will be dissipated within the cavity (α_i), the rest will leave the cavity through the mirrors (α_m). When the threshold current I_{th} is the current to reach lasing and η_i is the internal quantum efficiency we can express the output power by:

$$P = \eta_i.h\nu.\frac{I - I_{th}}{e} \cdot \frac{\alpha_m}{\alpha_i + \alpha_m} \quad \text{with} \quad \alpha_m = \frac{1}{L}.\ln\left(\frac{1}{\sqrt{R_1.R_2}}\right)$$

A useful expression for parameter extraction is the expression for the external differential quantum efficiency is:

$$\eta_d = \frac{d[P / h\nu]}{d[(I-I_{th}) / e]} = \eta_i . \left[1 + \frac{2.\alpha_i.L}{\ln\left(\frac{1}{R_1.R_2}\right)}\right]^{-1}$$

It allows estimating the internal quantum efficiency and internal losses of the device as is illustrated in Figure 3-20.

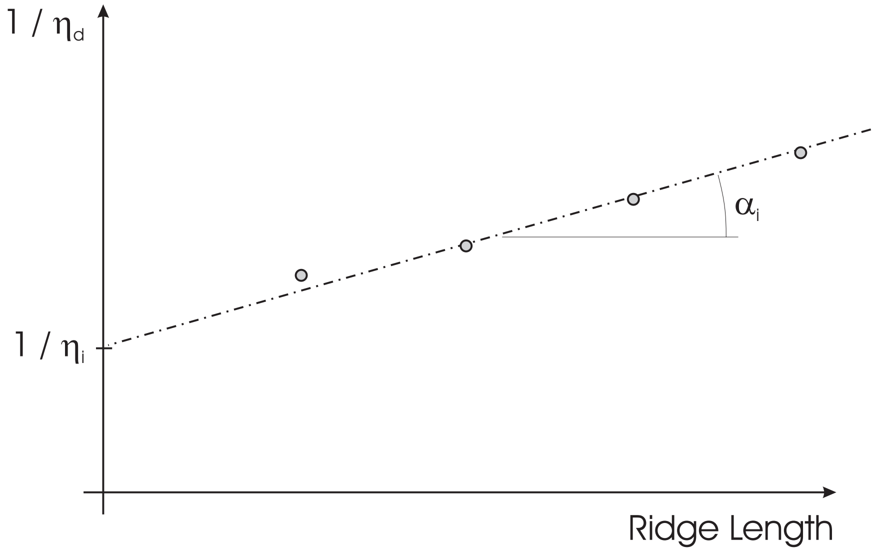

Figure 3-20 Parameter extraction from lasers

3.5.1.2 *Structure, growth and processing.*

When we design a laser structure, we have to take care of the electronic and optical confinement in the structure. Carriers should be injected into the active region and not be allowed to leave it and photons should be kept inside a waveguide structure. This can be done in a double heterostructure where the active region is sandwiched by cladding layers with higher band-gap energy and as a result a lower refractive index.

One problem with heterostructure lasers is that when we reduce the transversal dimension of the active region to form a quantum well, carriers will more easily leak out of the well and not take part in the recombination process. At the same time the reduction of the width will decrease the confinement of the optical mode. One way to counter this effect is the insertion of a separate confinement heterostructure (SCH). Optical confinement can be even higher when we use a graded index separate confinement structure (GRINSCH). This is illustrated in Figure 3-21.

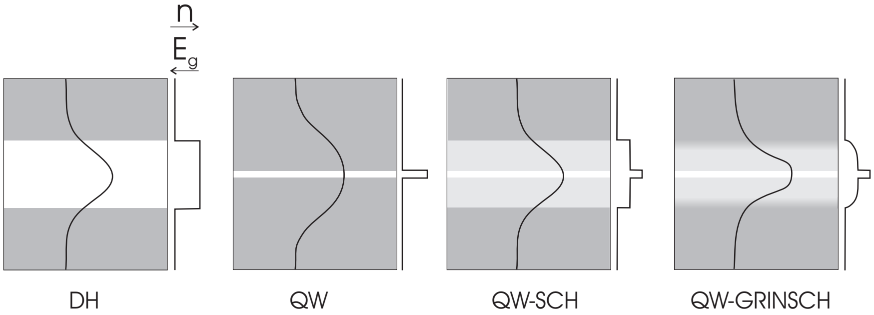

Figure 3-21 Confinement structures for semiconductor lasers. Darker areas have higher band-gap energy and lower refractive index.

The devices we have grown are based on the standard laser structures that are used in the laboratory for emission near 980nm ([8] [9]). These latter devices have 6nm thick $In_{20}Ga_{80}As$ triple quantum wells with GaAs barriers embedded in a GRINSCH structure with $Al_{35}Ga_{65}As$ cladding layers. The structure is optimised for high power output. The cladding layers have a doping level of $5\cdot10^{17}$. The GRINSCH and active region are not intentionally doped whereas the contact and buffer layers are $p = 1\cdot10^{19}$ and $n = 2\cdot10^{18}$ respectively. The structures will be discussed more in detail in the next chapter.

The new laser structures aimed for 1.2µm emission were adapted from the 980nm devices. As a first approach all transversal dimensions are scaled by a factor related to the wavelength (~ 1.2), and after that optimised using a dedicated CAD tool (Fimmwave) to maximise confinement (low loss waveguide) and overlap between optical mode and active region (high gain). Also, only two quantum wells are used because of the high strain in these layers.

Two different types of lasers were grown using both TMGa and TEGa for the active regions. The cladding and contact layers are grown using TMGa because the growth velocity is about three times higher with that source. Also, composition and doping are well calibrated for AlGaAs materials using TMGa, and not using TEGa. Because of the set-up of the system, switching sources during the run for the TEGa quantum wells requires a growth interrupt. In this five to ten minute period there are no group III precursors switched to the reactor, whereas the arsenic source remains switched to the reactor to stabilise the semiconductor crystal at all times.

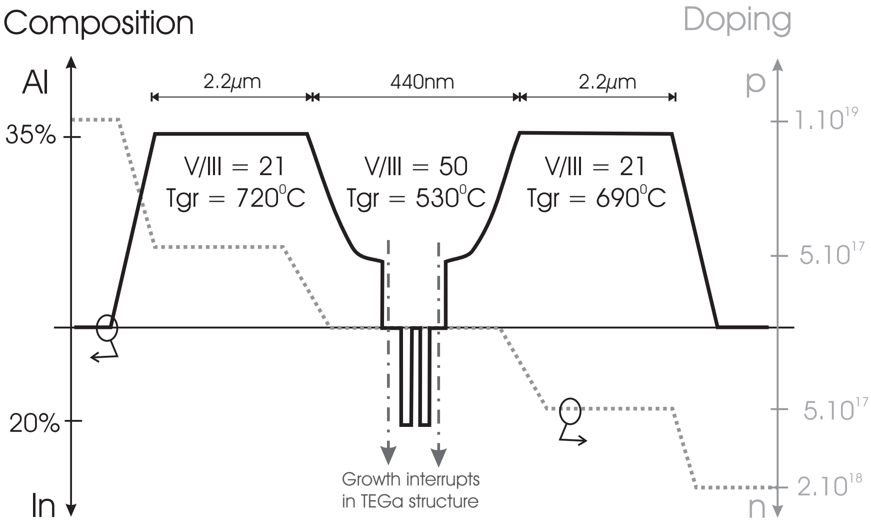

Figure 3-22 Structure of the laser devices with highly strained active regions.

The processing of the lasers is relatively simple (see Figure 3-23). After the epitaxial growth of the layer stack, ridges from 2 to 10 µm wide are defined using standard lithographic techniques and etched away. Then an electrical insulation layer, e.g. silicon-nitride or aluminium-oxide, is deposited on the entire top surface. On top of the mesas the insulation is etched away again using a lithographic mask. Then, the top contact is deposited and removed with the lift-off technique. To facilitate cleaving the substrate is thinned and in a last step a bottom contact is added covering the entire back surface. Then the wafer is ready for cleaving laser bars, which can then be mounted onto copper plates. An extra step could be the deposition of high-reflectivity and/or anti-reflection coatings on the mirrors but for simplicity this was not done.

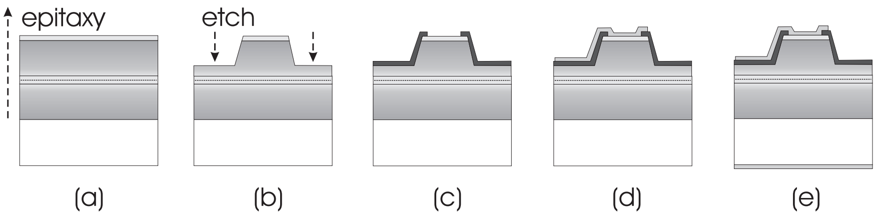

Figure 3-23 Simplified processing scheme for laser diodes. After epitaxial growth (a), a ridge wave-guide is defined (b). Then an isolation layer is deposited (c) after which a top (d) and bottom contact (e) can be evaporated.

The results of the characterisation of the two types of devices are shown in Figure 3-24, where we plot the reciprocal of the external differential quantum efficiency versus the ridge waveguide's length and Table 3-1, in which the most important parameters are summarised. The TEGa structure has better internal quantum efficiency, but suffers as much as the TMGa lasers from high internal losses, threshold current densities and series resistance. The fact that the internal optical losses are even higher than for the TMGa lasers can be explained by the growth interrupt that is necessary for changing gallium-precursors. Indeed, the interfaces that are formed by the interrupt attract a lot of contamination, which lead to a high delta-like doping background.

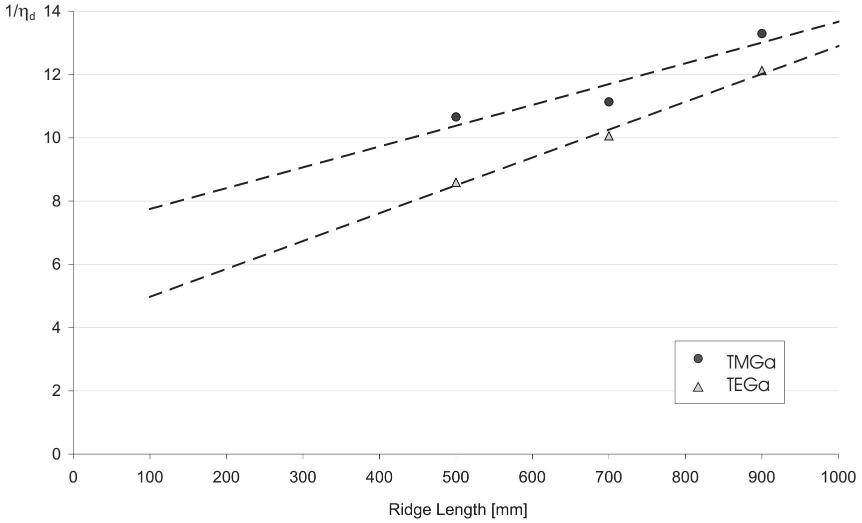

Figure 3-24 Reciprocal of external quantum differential efficiency versus the laser ridge length.

	λ	η_i	α_i	J_{th}	R_s
TEGa structure	1180nm	49.06%	88.4 / cm	1.7 kA/cm^2	9.5 Ω
TMGa structure	1190nm	28.23%	58.7 / cm	2.1 kA/cm^2	10 Ω

Table 3-1 Parameters of the laser diodes

In general the performance of the lasers are rather mediocre, compared with the results obtained by Bugge [11]. Their (rather large) broad area lasers have a slope efficiency of nearly 80% and threshold current densities of only 125A/cm^2, but under pulsed operation and at the lower wavelength of 1170 nm. Other publications focus on the threshold current densities and present similar values ([6] [12]) but no efficiencies are reported.

One should take into account that the active regions used are extremely highly strained. In fact, theoretically these quantum wells should already be relaxed. And whereas the calibration samples only contain a single quantum well, the laser devices have two, in order to have a higher gain. The two closely spaced strained wells will be more susceptible to relaxation than their single counterparts. On the other hand, we have obtained 1.2 µm laser emission without nitrogen in the well.

References

[1] J. Matthews, A. Blakeslee, J. Cryst. Growth 27, 118 (1974)

[2] A. Braun, K. Briggs, P. Böni, J. Cryst. Growth 241, 231 (2002)

[3] R. People, J. Bean, Appl. Phys. Lett. 47, 322 (1985)

[4] G.B.Stringfellow, “Organometallic vapor-phase epitaxy”, Academic Press, San Diego (1989)

[5] N. Ingle, C. Theodoropoulos, T. Mountziaris, R. Wexler, F. Smith, J. Cryst. Growth 167, 543 (1996)

[6] D. Schlenker, T. Miyamoto, Z. Chen, F. Koyama, K. Iga, J. Cryst. Growth 209, p27 (2000)

[7] M. D’Hondt, “Ontwikkeling van MOVPE-gebaseerde InGaAs/InP fotodetectoren en laserdioden voor golflengten boven 1.65µm”, Ph.D. Thesis, Intec-Ghent University (1997)

[8] F. Vermaerke, “Ontwerp en realisatie van hoogperformante InGaAs/AlGaAs halfgeleider laserdiodes”, Ph.D. Thesis, Intec-Ghent University (1996)

[9] G. Vermeire, “Metaalorganische gasfase epitaxiaalgroeitechnieken voor de realisatie van geavanceerde (In)(Al)GaAs/AlGaAs halfgeleiderlasers”, Ph.D. Thesis, Intec-Ghent University (1995)

[10] P. Zory ed., “Quantum Well Lasers”, Academic Press, Boston (1993)

[11] F. Bugge, M. Zorn, U. Zeimer, T. Sharma, H. Kissel, R. Hülsewede, G. Erbert, M. Weyers, J. Cryst. Growth 248, 354 (2003)

[12] T. Takeuchi, Y.-L. Chang, A. Tandon, D. Bour, S. Corzine, R. Twist, M. Tan, H.-C. Luan, Appl. Phys. Lett. 80, 2445 (2002)

CHAPTER 4

DEVELOPMENT OF A TBAS PROCESS

4.1. Abstract

To allow low temperature growth and due to a strategic decision, the MOCVD lab at INTEC was forced to abandon growth using arsine and instead switch to tertiary-butyl-arsine as an alternative. We will first compare both precursors in a general way, discussing their toxicological, chemical and physical, epitaxial and economical properties.

We will describe the growth process using the new precursor with, where possible, direct comparison with the old arsine process. Emphasis will be on morphology, background contamination, optical and electrical properties and doping behaviour.

With the newly developed process we have grown solar cell and edge emitting laser structures. We will discuss the characterisation of the devices. Both types have excellent properties, which is a proof of the high quality we can obtain. One of the solar cells grown using TBAs even exhibits world record conversion efficiency for that particular type of cell.

4.2. Introduction and motivation.

Up to this date, most industrial and even research MOCVD reactors still use the hydrides arsine (AsH_3) and phosphine (PH_3) as group-V precursors. The reason for this is mainly historical. During the initial fifteen-year development period of the growth technology the choice of source molecules was straightforward: only compounds manufactured for other purposes were considered. These generally were simple methyl- and ethyl-metal-compounds for the group-III precursors, whereas the group-V atoms had hydrogen as a ligand. Over time, the restrictions imposed by the limited choice of precursor molecules have been understood better [1].

Arsine and phosphine however are very toxic. Arsine is the most acutely toxic form of arsenic. It is acutely lethal, instantly in doses of 250ppm or in case of exposure during one to two minutes in a concentration of a mere 50ppm. It is already considered life threatening in an exposure level of 10ppm during half an hour. The long-term effects of the substance are unclear, but certain inorganic compounds containing arsenic are known to be carcinogenic. As a result the threshold limit value for the time weighted average (TLV-TWA), which is the maximum allowed concentration for eight hours a day and five days a week exposure, has been set as low as 50 ppb. Recently it has even been suggested to reduce this value down to 3ppb [2]. This is why a considerable fraction of the overall expense of both purchasing and operating a reactor deemed safe by today's standards is devoted to safety features. On top of this comes the fact that hydrides are stored in gas cylinders under high pressure. The threat of release of large quantities in a short time is serious, since it could affect an entire building or, in the extreme case of a laboratory located in the centre of a city, an entire neighbourhood. This raises the need for alternative, less hazardous group-V sources.

During the course of this work, due to these safety concerns, the strategic decision was taken to get rid of the hydrides in the lab's MOVPE-process. Of course, an alternative had to be found and the entire process for GaAs, AlGaAs and InGaAs re-established.

The requirements for group-V precursors are stringent. The precursor must have a reasonable room temperature vapour pressure between 5 and 500Torr. It must be stable at room temperature and yet must pyrolise at the lowest desirable growth temperatures (400ºC). It must not participate in undesired parasitic pre-reactions with the group-III source molecules. And of course it must be available in very pure form, which implies it must be easily purified without decomposing. During epitaxy it must not produce any detectable contamination of the resultant epitaxial layers. For a comparison of precursors we refer to Table 4-1.

In this study we have opted for tertiary-butyl-arsine (TBAs). TBAs is not only less toxic than arsine, but it also has a lower vapour pressure. It also causes lower carbon contamination and allows lower growth temperatures, as it decomposes and reacts with the other precursors in a different way than arsine does. On the other hand, it has the disadvantage of a higher price and a irregular availability in pure form.

Precursor	# H-atoms / molecule	Carbon contamination	Stability	Vapour pressure	Hazard
As	0	- -	+	- -	+ +
AsH_3	3	+ + +	+	+ + +	- - -
TBAs	2	+ + +	+ + +	+ + +	-
$PhAsH_2$	2	+ +	+	- -	?
DMAs	1	- - -	?	+ + +	+
DEAs	1	+	+ + +	-	+
TMAs	0	- - -	-	+ + +	+ + +
TEAs	0	- - -	+	-	+ +

Table 4-1 Comparison of different As-precursors (after [1]). The label "- - -" signifies an extremely undesirable inadequacy, "+ + +" means this property presents no significant problems.

4.3. Tertiary-butyl-arsine vs. arsine

In TBAs, a tertiary butyl group has replaced one of arsine's hydrogen atoms. Both molecules are represented Figure 4-1 and important properties are summarised in Table 4-2. An arsenic-hydrogen bond is significantly stronger than an arsenic-carbon bond, and the latter bond strength becomes even weaker when the carbon atom that is bound to the arsenic atom is also bound to other carbon atoms. Therefore the pyrolysis temperature of TBAs is lower than that of arsine.

In general lighter molecules have a higher vapour pressure, even though intermolecular interactions in the liquid will also have an influence. TBAs is a heavier molecule than arsine is, and as such has a much lower vapour pressure.

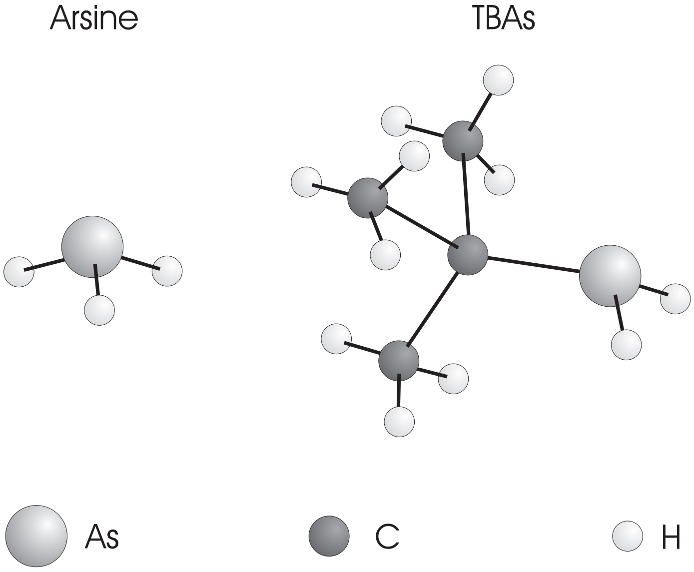

Figure 4-1 Schematic diagrams of arsine and tertiary-butyl-arsine molecules.

Toxicity and safety are described in terms of the LC_{50} value and a figure of merit. The LC_{50} value is the concentration that kills 50% of the test rat population after an exposure for four hours in inhalation experiments. The figure of merit is calculated from the LC_{50} value divided by the vapour pressure. It gives an idea of the safety by taking toxicity and spreading of the substance in case of a leakage into account. TBAs is not that much less toxic as such, but it will not spread as fast and therefore the figure of merit is about two orders of magnitude better.

Another factor to consider is the economical side. Clearly, TBAs of purity suitable for epitaxy is more than a factor of ten more expensive than arsine. On the other hand, the V/III ratios required for high quality layers are much lower for growth using TBAs as compared to using arsine. This is illustrated in Figure 4-2 where we show the photoluminescence intensity for InGaAs quantum wells grown with different V/III ratios with both precursors. The required V/III ratio is three times lower for TBAs to obtain the same result. The same observation will be made in the next paragraphs where we discuss SIMS measurements on GaAs and AlGaAs layers. In the end, TBAs is still about three times more expensive.

		Arsine	TBAs
Pyrolysis temperature	[ºC]	600	425
Vapour pressure at 20ºC	[torr]	7823	148
Molecular weight	[g]	77.9	134.05
Toxicity: LC_{50}	[ppm]	5-50	70
Safety figure of merit (LC_{50} / P_{vap})		0.006	0.47
Price	[€ / Mole]	125	1375

Table 4-2 Properties of arsine and TBAs.

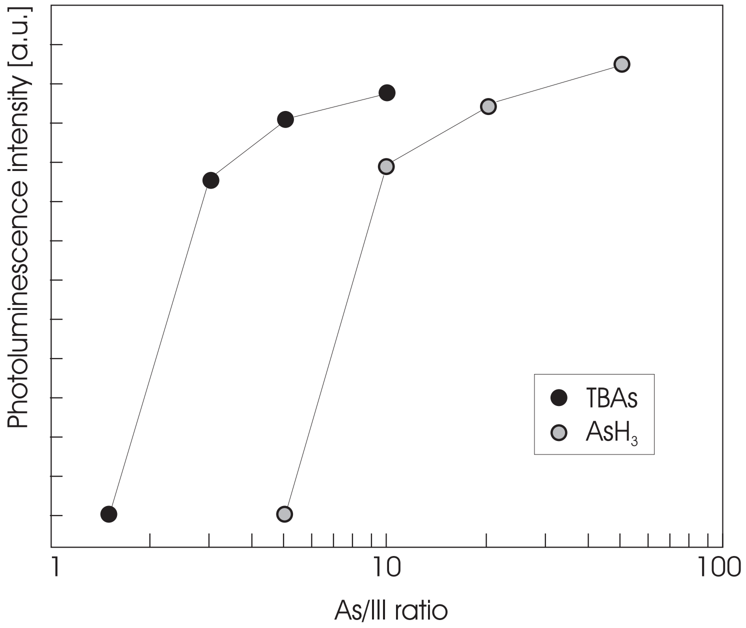

Figure 4-2 Photoluminescence intensity of InGaAs QW's grown with TBAs or arsine as a function of V / III ratio (after [6]).

The growth mechanism when using the two precursors is also quite different. We will focus on the growth of simple GaAs layers with TMGa as group-III precursor. Both TBAs and arsine decompose in a heterogeneous reaction on the III-V surface. TMGa acts as a catalyst for the arsine pyrolysis only but leaves the TBAs decomposition unaffected. This suggests a TMGa-AsH_3 complex is formed at the reaction surface. The rate-limiting step of the pyrolysis of arsine is the cleaving of the first hydrogen atom. This atomic hydrogen is then responsible for reducing the CH_3 radicals from the TMGa source, which are the main responsibles for carbon-contamination of the epitaxial layers, into stable CH_4-molecules. As the growth temperature is reduced and the arsine decomposition becomes less efficient, an increasing amount of the CH_3 radicals is left at the surface [1].

The decomposition of TBAs on the other hand is not influenced by the presence of TMGa, suggesting a homogeneous pyrolysis reaction in the gas-phase occurs. It is yet unclear how the reaction proceeds exactly, but mass spectrometry of the exhaust gases has indicated the existence of reactive AsH and AsH_2 radicals besides AsH_3 in the gas-phase and adsorbed on the surface. The AsH_x radicals are more efficient at eliminating the CH_3 radicals and thus GaAs layers are less contaminated with carbon acceptors ([4] [5]).

4.4. MOCVD growth using TBAs

In the following paragraphs we will discuss the characterisation of epitaxial layers of the GaAs, $Al_xGa_{1-x}As$ and $In_xGa_{1-x}As$ material system. In light emitting devices, the first two are especially important as a cladding, contacting or barrier material, whereas the latter is mostly used as an active material. The biggest chunk of the characterisation will thus encompass GaAs and AlGaAs, including their electrical and doping properties. We will briefly touch upon InGaAs in the optical characterisation.

4.4.1. Experimental

The layers that are described below were grown in a Thomas Swan close-coupled vertical rotating reactor with a capacity of three 2” wafers, one 4” wafer or one 6” wafer. Unless explicitly mentioned, the reactor pressure was maintained at 76torr. The susceptor rotates at 300rpm. The growth temperature varied from 500ºC to 760ºC. The carrier flows through both manifolds at growth conditions are 5.595 millimoles per second of hydrogen each. Molar flows of the precursors will be mentioned below.

4.4.2. Morphology

The main factor that influences the surface morphology is the V/III ratio. It can be shown from thermodynamical considerations that this ratio needs to be higher than unity to obtain a single GaAs solid phase. Otherwise, Ga-droplets or whiskers can be created. Due to inhomogeneous flow patterns or partial depletion of arsenic in the gas-phase the V/III ratio can locally vary. Thus, to stabilise the crystal at elevated temperatures and to prevent occasional out-diffusion of arsenic, the V/III ratio will be chosen even higher. E.g. for growth using arsine, values between 30 and 100 are typical. On the other hand, one wants to limit this ratio for economical reasons.

All layers discussed here were grown smooth and mirror-like. This means that the layers were grown with a sufficiently high V/III ratio.

4.4.3. Background contamination

4.4.3.1 General

Intrinsic chemical properties of the source material and contamination caused by the production process or insufficient purification will leave traces of atomic impurities in the epitaxial layers. Depending on how these atoms are introduced in the III-V crystal, they will cause a variety of undesired effects, such as scattering of carriers, deep levels that act as carrier traps or non-radiative centres, background doping, etc.

One tool to quantify this contamination is secondary ion mass spectroscopy (SIMS), where the III-V crystal is bombarded with heavy element ions (typically Cs+) and the secondary ions that are knocked away from the crystal are detected in a mass spectrometer. The results are expressed in atoms per cubic centimetre and should be compared to the value of $4.42 \cdot 10^{22}$ atoms/cm^3 for pure crystalline GaAs. For $Al_xGa_{1-x}As$ the number of atoms per cubic centimetre is expressed by:

$$(4.42 - 0.17 \cdot x) \cdot 10^{22} \text{ atoms/cm}^3$$

Not all our experimental data is as conclusive because growth has been performed over a rather large time span and many external effects influence the results. One critical item is the palladium diffuser cell that purifies the hydrogen carrier gas but is very fragile. In the course of these experiments it had to be replaced once.

4.4.3.2 GaAs

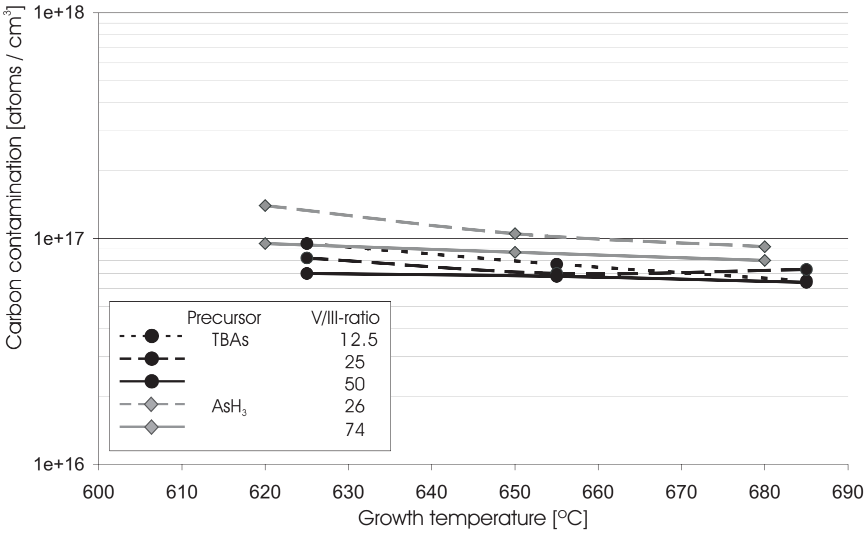

Figure 4-3 Parasitic carbon contamination levels in GaAs epitaxial layers grown using TMGa and either arsine or TBAs, as observed through SIMS.

SIMS data for carbon and oxygen in GaAs layers are shown in Figure 4-3 and Figure 4-4. For carbon all signals are near detection limit of the SIMS equipment. Still, one can see that TBAs performs slightly better than arsine. Also, a larger V/III ratio and a higher growth temperature allow lower carbon levels. More cracked group-V precursor molecules will deliver more atomic hydrogen upon pyrolysis that can attack the CH_3 radicals that come off the TMGa-molecules to form volatile CH_4. For oxygen, all contamination levels are below the detection limit.

The hydrogen content of the layers (not shown) is more or less constant for the varied parameters. Layers grown with TBAs have $5 \cdot 10^{17}$ hydrogen atoms per cubic centimetre, whereas for arsine the value is $2 \cdot 10^{18}$.

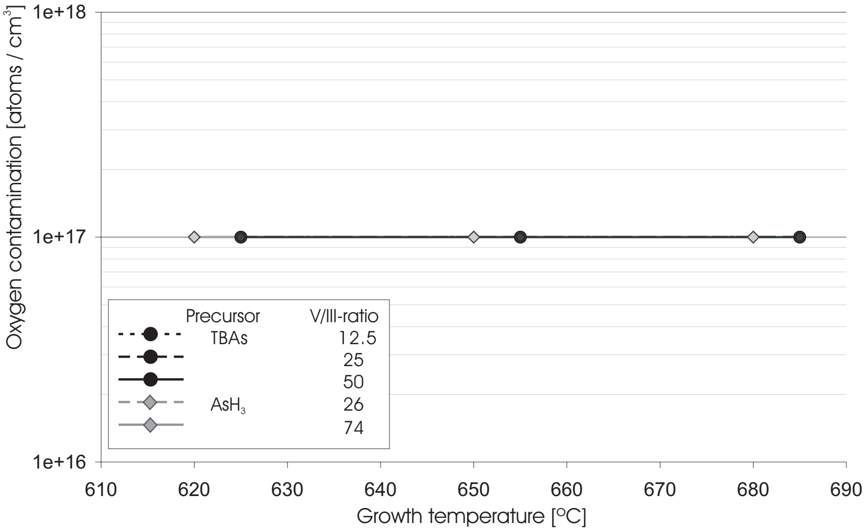

Figure 4-4 Parasitic oxygen contamination levels in GaAs as observed through SIMS.

4.4.3.3 $Al_{35}Ga_{65}As$

AlGaAs has proven to be a more difficult material to grow than GaAs. The simple reason for this is the reactivity of aluminium, which forms strong bonds with both carbon and oxygen. SIMS data for $Al_{35}Ga_{65}As$ is plotted in Figure 4-5 and Figure 4-6.

The carbon levels that are detected are relatively high. Even so, the general trends are comparable to those found for GaAs. Both a higher growth temperature and a higher V/III ratio will influence the contamination levels positively. When we compare AsH_3 to TBAs, we can see that at equal V/III ratios and growth temperatures, TBAs shows lower carbon levels than arsine. This can be explained in the same way as for simple GaAs.

The main problem for aluminium containing layers however is the oxygen background. It was shown that as little as 1ppm of oxygen in the gas phase resulted in extremely high oxygen concentrations in the solid AlGaAs of over

10^{19} cm^{-3} [1]. This calls for extreme measures in terms of equipment and handling. Examples are such as the installation of Pd-diffuser cells in the hydrogen supply lines and glove boxes to isolate the reactor interior from the atmosphere during loading or the growth of layers with high aluminium content before the actual devices structure to absorb any residual oxygen.

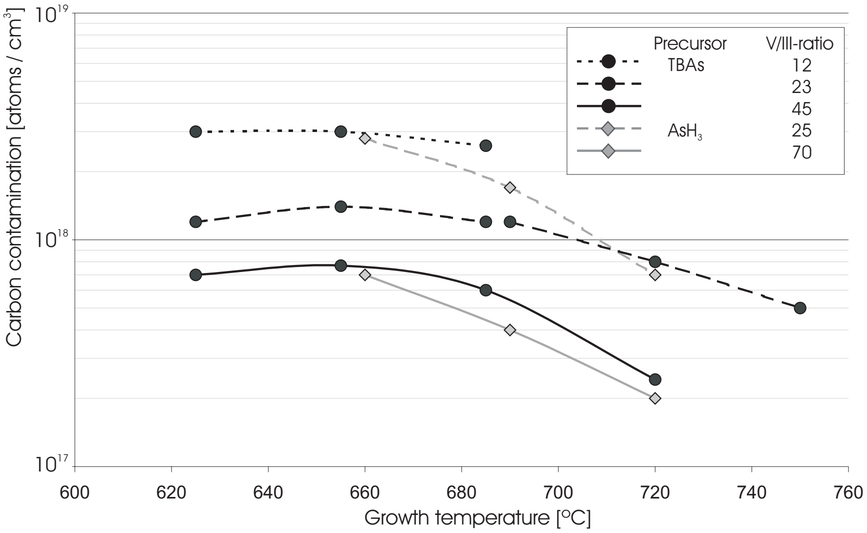

Figure 4-5 Parasitic carbon contamination in $Al_{35}Ga_{65}As$ grown using TMGa, TMAl and either arsine or TBAs, as observed through SIMS.

Unless special precautions are taken concerning purity, also arsine is a well-known source of oxygen. Referring to Figure 4-6, we point out that the arsine data may be unreliable. In the original experiments, when increasing the growth temperature, the oxygen levels flatten out at a level of about $5 \cdot 10^{17}$, both for arsine and TBAs. Unfortunately after the first experiments, we no longer disposed of arsine to repeat the experiment. We did for TBAs and present the results in Figure 4-6.

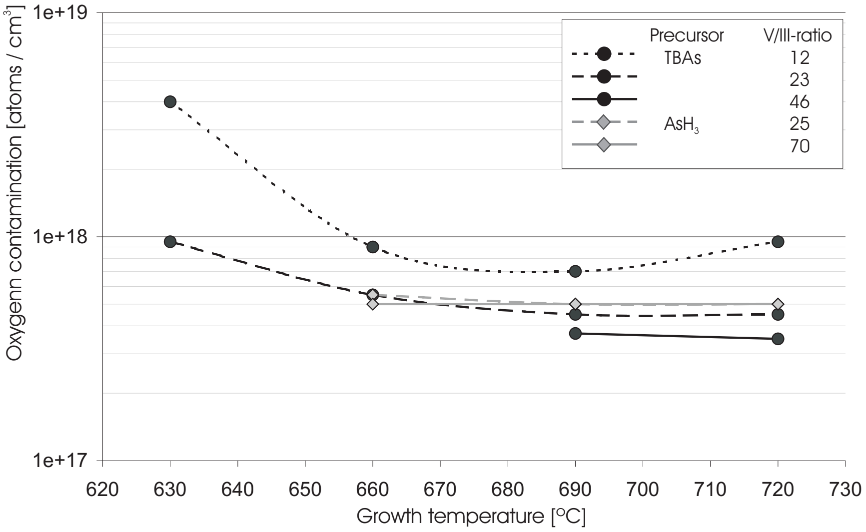

Figure 4-6 Parasitic oxygen contamination in $Al_{35}Ga_{65}As$ as observed through SIMS.

The hydrogen content is constant at a level of $7 \cdot 10^{17}$ for both the arsine as the TBAs process.

It is interesting to observe the effect of the growth velocity on the background contamination. In MOCVD growth velocity depends only on the group III flows as long as the V/III ratio is sufficiently high (> 5). In standard conditions, we achieve a growth rate (V_{gr}) of 2.5µm/hr with a TMGa molar flow of 85.9µmol/min, which means a growth efficiency of 10250µm/mol. This is a somewhat abstract number, but if we take the useful area of the reactor into account (i.e. the surface where we can grow homogeneously or 6") then we find that 28% of all injected TMGa molecules actually causes epitaxial growth.

For the experiment we have constructed two cases: one where the V/III ratio was kept constant and the TBAs flow varies with the group III flow; and one where the TBAs molar flow is kept constant and the V/III ratio decreases with increasing growth rate. The results are shown in Figure 4-7 and Figure 4-8.

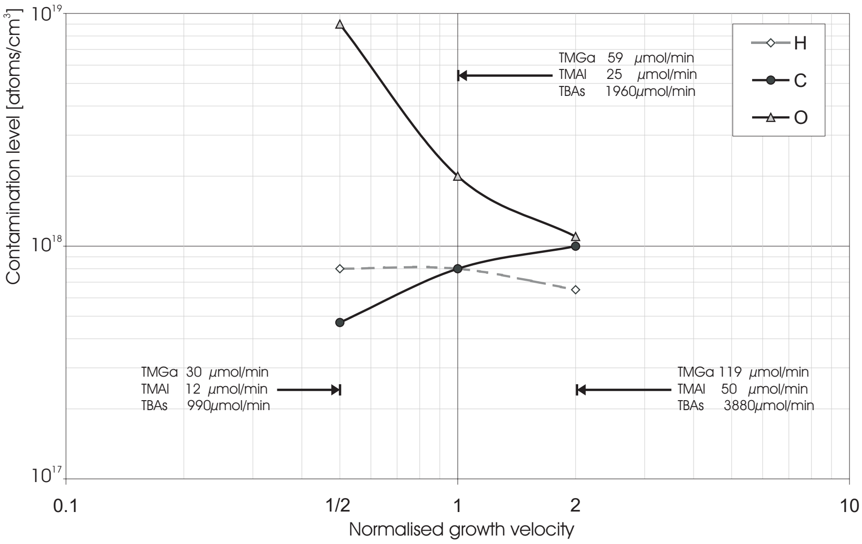

Figure 4-7 Influence of the growth velocity on the contamination levels in $Al_{35}Ga_{65}As$ *with a fixed V/III ratio of 23.2. The normal growth rate is 2.5µm/hr.*

The first thing that catches the eye is that the trends of carbon and oxygen are fundamentally opposed. Carbon is an intrinsic part of the group III precursor molecules and is transported to the growth surface together with the useful group III atom. When the CH_3 radical can react with atomic hydrogen, it can desorb from the surface. The lower the growth rate, the more time it gets to do this. In the case of oxygen the step that limits incorporation is not desorption, but the adsorption of the oxygen. If the oxygen is allowed to reach the surface and bind to an aluminium atom it will stay there unless very high growth temperatures are used, as the aluminium-oxygen bond is extremely strong and the oxide is non-volatile. Therefore a higher growth rate will result in lower average oxygen content.

This is also reflected in the sensitivity of these two contaminants to the group V precursor. Low carbon levels require a high V/III ratio, whereas oxygen is especially sensitive to the absolute group V partial pressure. This can be interpreted from the figures as follows. Carbon levels vary less when the V/III ratio is kept constant (by a factor of two for a variation of V_{gr} by a factor of four) than (by a factor of ten) when this ratio changes linearly with the growth rate. Indeed, per TMGa molecule a certain amount of TBAs is required to reduce the CH_3 to volatile CH_4. Again, in the case of oxygen, the trend is exactly opposite, because a higher TBAs partial pressure in the gas phase (particularly in the boundary layer above the surface) will increase the probability of aluminium bonding to arsenic, rather than oxygen.

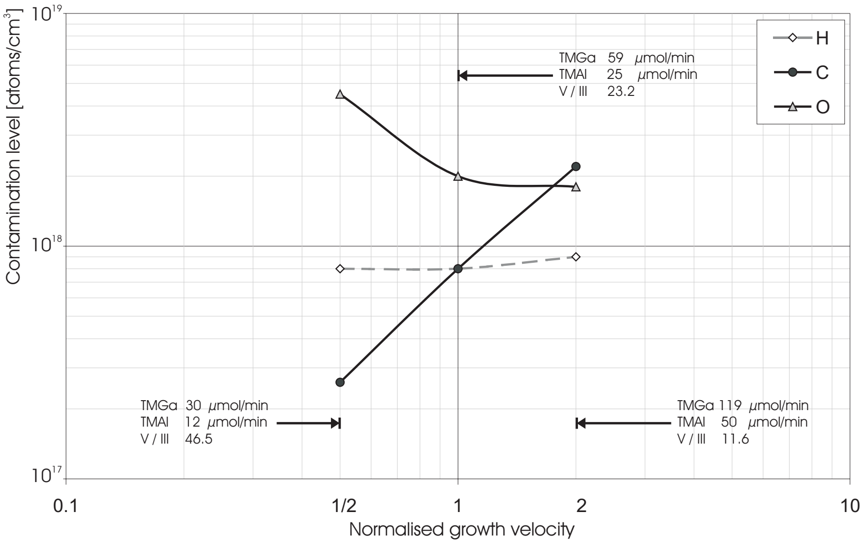

Figure 4-8 Influence of the growth velocity on the contamination levels in $Al_{35}Ga_{65}As$ *with a fixed TBAs flow of 1957µmol/min. The normal growth rate is 2.5µm/hr.*

4.4.3.4 $Al_{80}Ga_{20}As$

Obviously, as the aluminium content goes up, the contamination levels increase as well. SIMS trends for $Al_{80}Ga_{20}As$ are shown in Figure 4-9 and Figure 4-10. Even though the contamination is high in absolute terms, the values obtained are very good considering the high aluminium content of 80%. Again, TBAs outperforms arsine when we look at the same V/III ratios. While carbon occupies the As-site in the lattice and acts as an acceptor, AlGaAs layers are predominantly n-type. This is due to the TMAl source, which contains high concentrations of silicon that compensates the p-type background.

For this composition the hydrogen content of the layers is no longer constant but is proportional to the carbon content. This is indicative of the CH_3 radicals that have not been removed from the growth surface and thus get incorporated into the epitaxial layer. Its value varies between 10^{18} and 10^{19} atoms/cm^3.

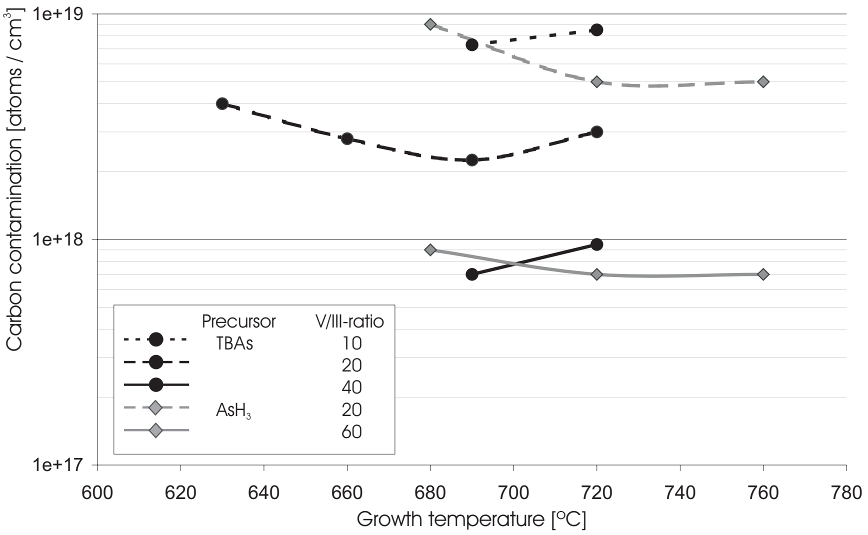

Figure 4-9 Parasitic carbon contamination in $Al_{80}Ga_{20}As$ as observed through SIMS.

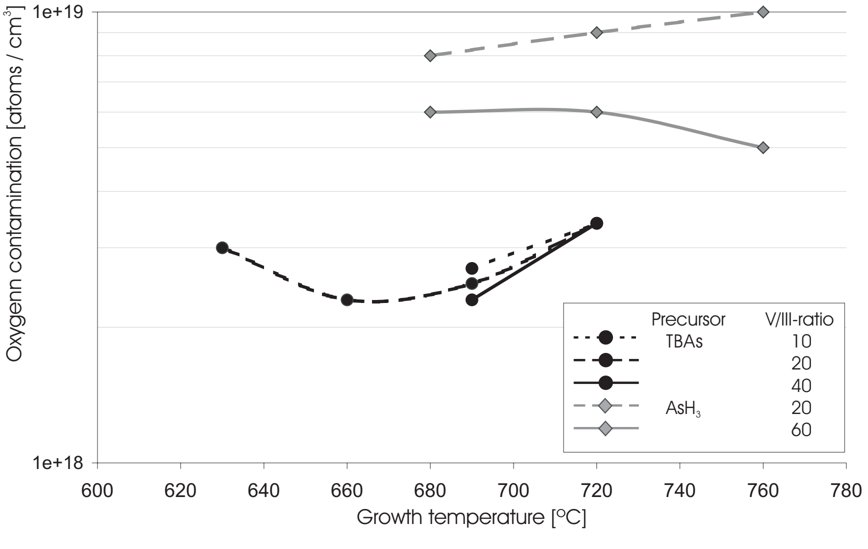

Figure 4-10 Parasitic oxygen contamination in $Al_{80}Ga_{20}As$ as observed through SIMS.

4.4.3.5 *Conclusions*

Based on these SIMS studies we have defined standard growth conditions for different material compositions and different intended doping type. They are summarised in the Table 4-3. One should note that V/III ratios are the minimal value required. For economical reasons the group V flows are kept as low as possible, but sometimes, for practical reasons, one uses a higher value.

Material	Doping	Temperature	TMGa flow	TMAl flow	TBAs flow	V/III
GaAs	any	660ºC	105	0	990	10
$Al_{35}Ga_{65}As$	p	690ºC	59	25	1957	20
$Al_{35}Ga_{65}As$	undoped	720ºC	59	25	3877	40
$Al_{35}Ga_{65}As$	n	720ºC	59	25	3877	40
$Al_{80}Ga_{20}As$	any	690ºC	15	81	3877	40

Table 4-3 An overview of the growth parameters that are used on basis of the SIMS results. The flows mentioned are molar flows and are expressed in µmol/min.

4.4.4. Optical quality

It is obvious that in light emitting devices the quality of the active region is of the utmost importance. We have characterised the radiative recombination efficiency of the commonly used GaAs and InGaAs quantum wells with AlGaAs barriers by photoluminescence spectroscopy.

Material	Thickness	Type	V/III using TBAs	V/III using AsH_3
GaAs	300nm	buffer	39.6	74.3
$Al_{40}Ga_{60}As$	200nm	confinement	22.5	42.2
$Al_{20}Ga_{80}As$	50nm	barrier	30.8	57.8
GaAs	10nm	QW	39.6	74.3
$Al_{20}Ga_{80}As$	6nm	Barrier	30.8	57.8
GaAs	10nm	QW	39.6	74.3
$Al_{20}Ga_{80}As$	6nm	Barrier	30.8	57.8
GaAs	10nm	QW	39.6	74.3
$Al_{20}Ga_{80}As$	50nm	Barrier	30.8	57.8
$Al_{40}Ga_{60}As$	200nm	confinement	22.5	42.2

Table 4-4 GaAs/AlGaAs QW structure for optical characterisation using PL.

The structure of the GaAs quantum wells is summarised in Table 4-4. The growth temperature was 720ºC for the entire stack and the V/III ratio using TBAs is roughly half of what is used for arsine. Note that these values do not correspond exactly with the recommended values from Table 4-3, because the TBAs and arsine flows were kept constant throughout the structure to improve the interfacial quality of the wells.

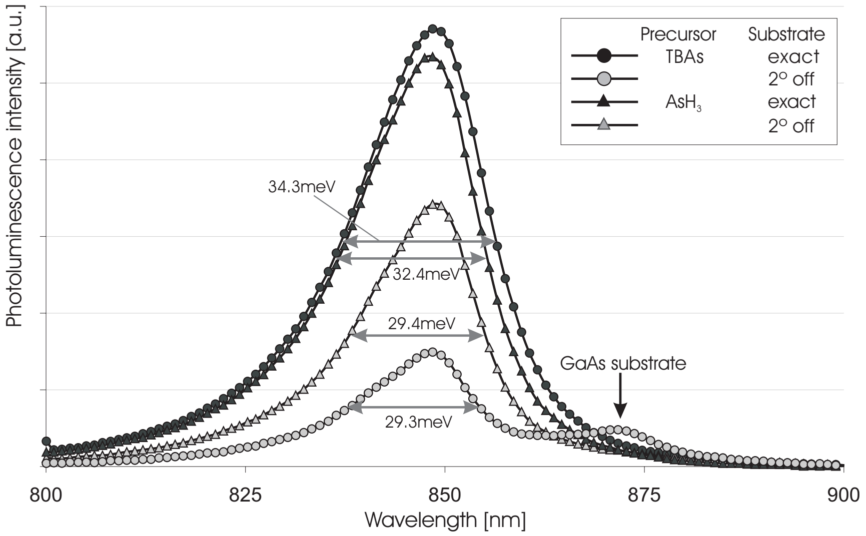

Figure 4-11 Comparison of triple 10nm thick GaAs triple quantum wells with $Al_{20}Ga_{80}As$ barriers, grown on exactly oriented <100> substrates and substrates oriented 2° off to <110> direction using TBAs or arsine.

The photoluminescence spectra of the GaAs quantum wells are shown in Figure 4-11. All spectra are measured in the same batch, as the set-up is very sensitive to alignment. This is also why the linewidth, expressed as the full width at half maximum (FWHM), is a more important parameter than the maximum intensity. For the experiment we have used two types of substrates: one has its surface exactly towards the <100> crystal direction, the other's surface is tilted 2° towards the <110> direction. The quantum wells that were grown on exactly oriented substrates are of comparable quality for both processes, both in terms of intensity as linewidth. The spectra of the 2° off-oriented samples show a decreased intensity but are at the same time less broad. The intensity of the 2° off TBAs sample is lower and even some luminescence from the substrate can be seen.

The structure of the triple InGaAs quantum wells is summarised in Table 4-5. A 2nm thick GaAs layer between the quantum well and the barrier layer is inserted to improve the quality of the interface of the quantum wells. The growth temperature of this structure is kept stable at 650ºC and the V/III ratio for TBAs is about half of the ratio used with arsine. We show the photoluminescence spectra in Figure 4-12. Again, the intensity and linewidth of the spectra obtained with both epitaxial processes is comparable. In summary we claim that in terms of optical quality the two processes can compete, even if we use a lower V/III ratio with TBAs.

Material	Thickness	Type	V/III using TBAs	V/III using AsH_3
GaAs	300nm	buffer	41.9	74.4
$Al_{40}Ga_{60}As$	25nm	confinement	25.0	45.1
$Al_{20}Ga_{80}As$	15nm	barrier	33.7	53.8
GaAs	2nm	interface	41.9	74.4
$In_{20}Ga_{80}As$	6nm	QW	36.0	63.8
GaAs	2nm	interface	41.9	74.4
$Al_{20}Ga_{80}As$	15nm	Barrier	33.7	53.8
GaAs	2nm	interface	41.9	74.4
$In_{20}Ga_{80}As$	6nm	QW	36.0	63.8
GaAs	2nm	interface	41.9	74.4
$Al_{20}Ga_{80}As$	15nm	Barrier	33.7	53.8
GaAs	2nm	interface	41.9	74.4
$In_{20}Ga_{80}As$	6nm	QW	36.0	63.8
GaAs	2nm	interface	41.9	74.4
$Al_{20}Ga_{80}As$	15nm	Barrier	33.7	53.8
$Al_{40}Ga_{60}As$	25nm	confinement	25.0	45.1

Table 4-5 InGaAs/GaAs quantum well structure for optical characterisation using PL. The entire structure was grown at 650°C.

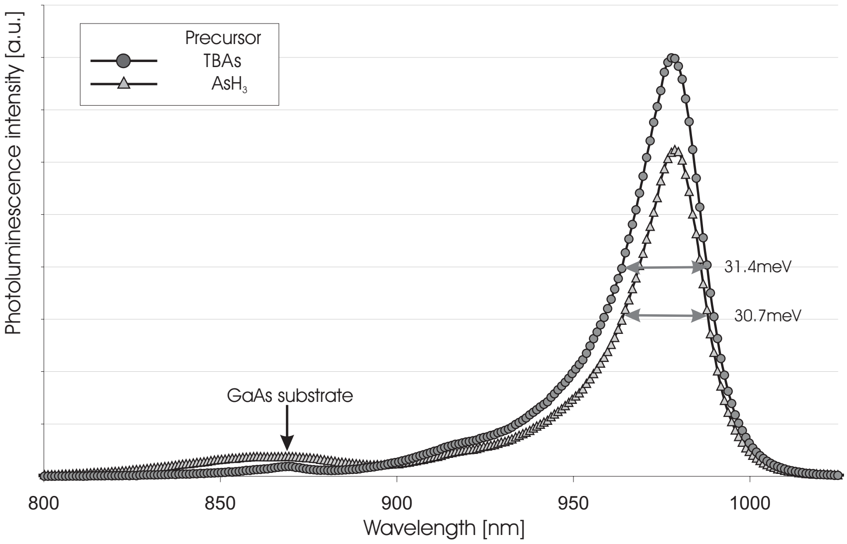

Figure 4-12 Comparison of photoluminescence spectra of triple 6nm thick InGaAs QW's with AlGaAs barriers grown using arsine and TBAs.

4.4.5. Electrical properties and doping

4.4.5.1 General

One step further down the road to devices is the control of intentional doping of the epitaxial layers. The existing arsine process for (Al)GaAs-layers at the lab used silane (SiH_4) and diethylzinc (DEZn) as n-type and p-type dopants respectively and is well understood. That is why the study of the intentional doping will focus on the same dopants, even though they may not be ideal in every case.

Zinc may diffuse when it is used in high doping levels and at high growth temperatures. The doping efficiency also decreases with increasing temperature, making DEZn a low temperature dopant. An interesting alternative to zinc is carbon, which does not diffuse and can be incorporated in very high concentrations. Also, as is clear from the paragraphs before, it can be obtained without extra precursors but by intelligently adapting growth parameters.

Silicon, being a group IV element, has the problem it is an amphoteric dopant. This means that even though it will preferentially occupy a group-III site in the crystal lattice, it will also occupy the group-V site if not enough group-III sites are available. Thus it is hard to reach very high n-type doping levels using silicon. Also the pyrolysis of silane is incomplete in most of the growth temperature range. We have also studied selenium, a group VI element, as an alternative, even though it is a highly diffusive element.

The doping behaviour has been studied using an electrochemical C-V technique (polaron) and Hall-Van der Pauw measurements. Polaron measures the net carrier density ($|N_A\text{-}N_D|$) as a function of depth. Hall measurements allow measuring the majority free carrier concentration as well as their mobility but are limited to a single homogeneous layer of sufficient thickness on semi-insulating substrates.

4.4.5.2 *GaAs doping profiles*

The evolution of the concentration of p-type carriers as a function of the DEZn molar flow is shown in Figure 4-13 for different growth temperatures and the two As-precursors. With TBAs, the doping has a sublinear dependency on the DEZn molar flow. The doping efficiency increases with decreasing temperature as can be expected from thermodynamics [1]. The incorporation efficiency is about twice more efficient with TBAs as it with arsine. For a doping level of $4.7{\cdot}10^{17}$ a room temperature mobility of 210cm^2/Vs was obtained in the TBAs process.

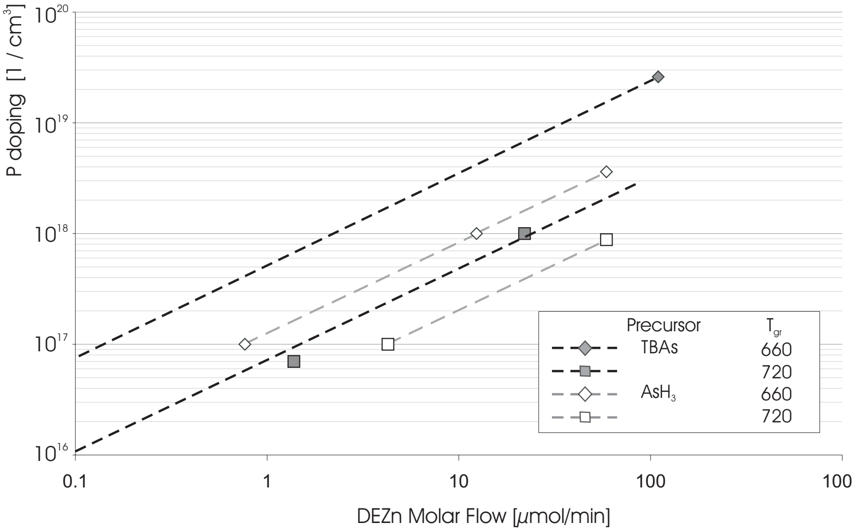

Figure 4-13 P-type doping behaviour of GaAs using DEZn in combination with either arsine or TBAs

This is not the case when we take a look at n-type doping using silane where the doping efficiency is more than a factor of ten times higher using TBAs than it is using arsine, even at a lower growth temperature. This is due to the fact that TBAs acts as a catalyst for the pyrolysis of silane in the same way it helps the pyrolysis of the other hydride arsine.

At the end of the TBAs study we experimented with the precursor H_2Se. The maximum n-type doping level obtained is $7.01 \cdot 10^{18}$ in which case the carriers have a mobility of 1260cm^2/Vs.

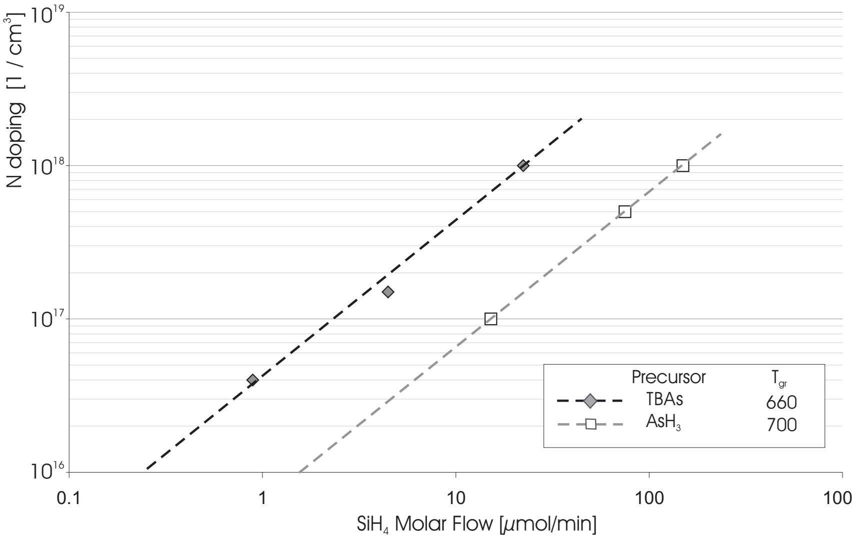

Figure 4-14 N-type doping behaviour of GaAs using silane in combination with either arsine or TBAs

4.4.5.3 $Al_{35}Ga_{65}As$ profiles

Doping calibration with polaron is more difficult for aluminium containing material because the aluminium reacts with the electrolyte solution. Furthermore, as we have seen from SIMS measurements, the aluminium-containing material has a significant amount of carbon impurities which will act as acceptor and render a p-type background. Hall-measurements on an unintentionally doped $Al_{35}Ga_{65}As$ layer grown under optimum conditions still reveal a background level of $2.42 \cdot 10^{17}$ with a room temperature mobility of 98cm^2/Vs.

The data for zinc-doped AlGaAs is shown in Figure 4-15. Even though there is no data shown for the arsine process, the DEZn molar flows and doping levels are in agreement with what can be expected for such a process.

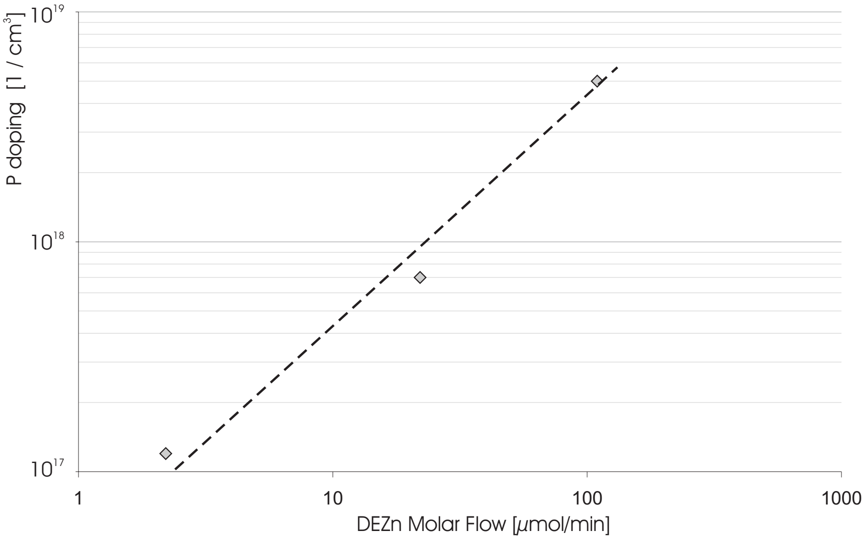

Figure 4-15 *P-type doping behaviour of* $Al_{35}Ga_{65}As$ *using DEZn and TBAs*

It is more interesting to focus on the n-type doping, as is shown in Figure 4-16, because there the influence of the carbon background and the amphoteric nature of silicon can be observed. At high silane molar flows the doping level saturates. At this point silicon starts occupying the group-V sites in the crystal lattice and auto-compensates its own n-type doping. In the region of the low silane molar flows, it is the carbon background compensation that limits the n-type doping. These non-linear effects make the control of doping levels in the low and the higher range more difficult. At a doping level of $4.61 \cdot 10^{17}$, that is in the linear region, the mobility at room temperature reaches a value of 1238cm^2/Vs.

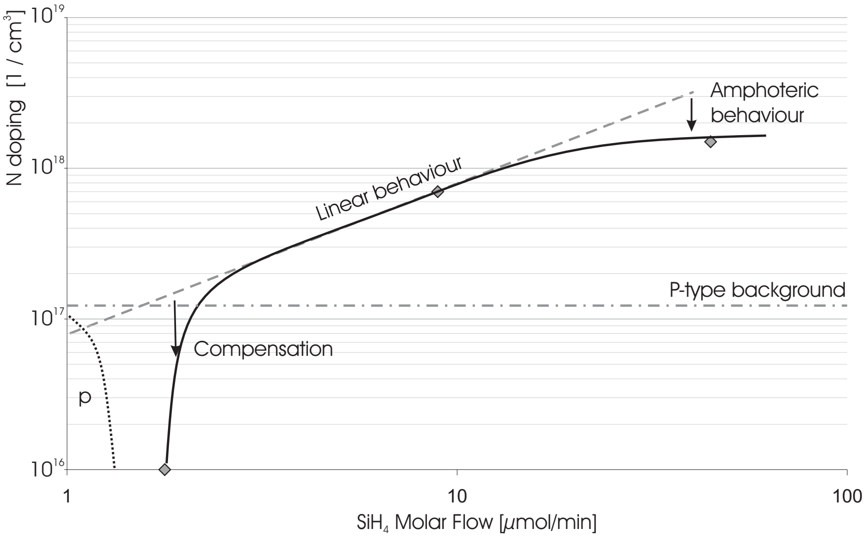

Figure 4-16 *N-type doping behaviour of* $Al_{35}Ga_{65}As$ *using silane and TBAs*

4.4.6. Conclusions

We have performed a direct comparison of the growth with arsine and TBAs. To obtain similar results concerning background contamination and optical quality as in the arsine process, TBAs prefers lower temperatures and allows lower V/III ratios. TBAs does influence the behaviour of the different dopants, but in terms of attainable doping levels and carrier mobility it is again a worthy opponent of the arsine process. In the next part we will put these observations to the test and evaluate the performance of two different types of devices.

4.5. Validation of the process

4.5.1. GaAs/AlGaAs single junction solar cells.

Simultaneous with the switchover of the arsenic precursor, the lab was involved in the development of solar cells[1] as well as the growth on germanium substrates. The application of the acquired knowledge concerning the TBAs process to these projects offered the perfect occasion for a benchmark. The optimum n-on-p structure requires the ability to grow highly n-doped cap-layers, which is not possible using silane. Instead, because the selenium doping process was not yet entirely under control, the solar cells were of the p-on-n type.

4.5.1.1 Principle of operation

The simplest solar cell is in fact a single p-n diode. When the cell is exposed to light, the photons with sufficient energies will interact with the semiconductor to excite hole-electron pairs. These holes and electrons may diffuse freely, until they sense the intrinsic electric field of the p-n junction and drift away from each another, from which point on they can be collected from appropriate contacts.

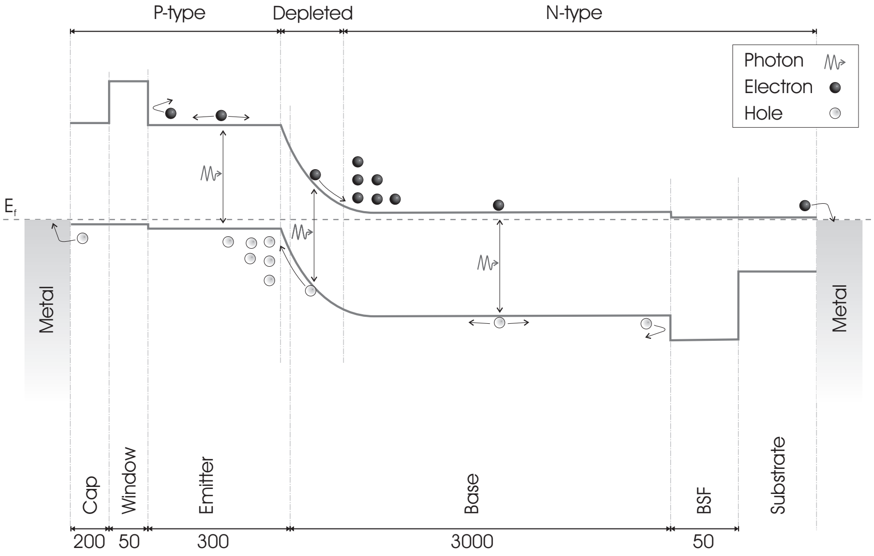

Figure 4-17 Simplified band structure for the p-on-n GaAs solar cells grown on germanium substrates. The layer thickness is expressed in nanometer.

---

[1] Processing and characterisation performed by E. Vanderplas and G. Flamand at IMEC, Leuven

It is important to point out that the diffusion of the electrons through the p-type region and the holes in the n-type region is the most critical. Minority carriers are very sensitive to any kind of disturbance of the crystal, as there are plenty of majority carriers to recombine with. The penetration depth of the incident light is proportional to its wavelength, so that the top part of the structure will mostly capture the high-energy photons and the deeper located base is responsible for capturing the majority of the longer-wavelength light.

The cell that was used for this study is a bit more sophisticated. Its band structure is shown in Figure 4-17. Even when the material quality is good and minority carriers have a long lifetime, an important source of recombination losses is the recombination at the front and back surfaces. The recombination velocity at the back surface is usually very high because the ohmic contacts are covering the entire surface. One way to limit the effective recombination velocity at the back surface is to use a back surface field (BSF) [7]. In our case it is implemented as a layer of AlGaAs, with a doping level and band-gap energy higher than that of the GaAs base layer. As shown in Figure 4-17, this layer will act as a barrier for the minority carriers and repel them from the backside.

The effect is not as pronounced at the front surface because of the lower contact area with the top metal contact. On the other hand, the top GaAs-air surface of the emitter will also cause surface recombination. A similar concept as the BSF is that of the window layer that is inserted at the top of the structure. It is a highly p-doped layer of high band-gap AlGaAs that will passivate the surface of the underlying GaAs emitter and thus effectively reduce the surface recombination velocity [7]. Because the aluminium content is rather high (80%), the band-gap transition is indirect and thus this top layer will only absorb little light.

The performance of a solar cell under illumination can be completely described by its current-voltage dependence. For practical purposes, it is sufficient to characterise it by a few parameters only. A typical voltage-current curve is depicted in Figure 4-18. I_L gives the maximum photocurrent that can be generated in a cell. Two important parameters are the short-circuit current I_{sc} and the open-clamp voltage V_{oc}. For an ideal diode, I_{sc} equals I_L and the open-clamp voltage can be expressed by:

$$V_{oc} = \frac{k_bT}{e} \ln\left(\frac{I_L}{I_s} + 1\right)$$

The diffusion current I_S depends on the physical dimensions and doping levels of the pn-junction.

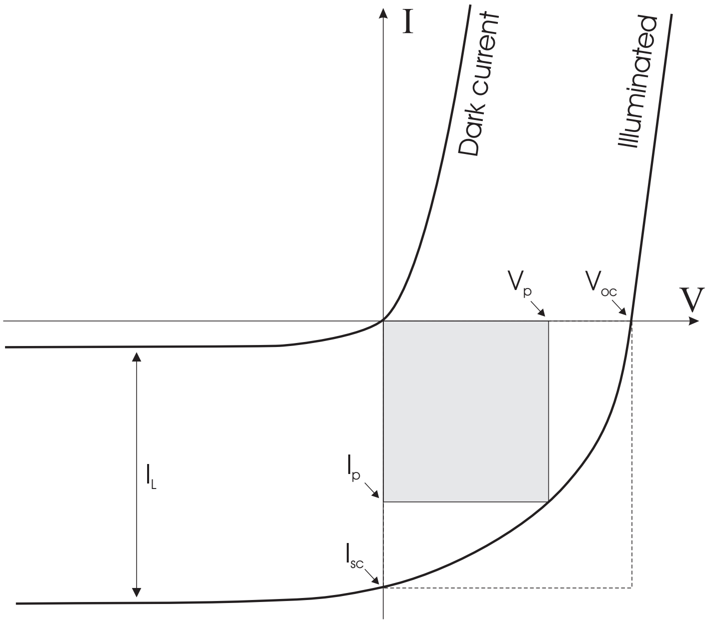

Figure 4-18 IV-characteristic of pn-junction photodiode in the dark and under illumination.

A solar cell in an electrical circuit will produce a lower current, determined by the external load resistance and its corresponding operating point (V_P, I_P) on the curve. The total electrical power generated by a cell can be visualised by the grey rectangle in Figure 4-18. When we assume ideal diode behaviour it can then be expressed as:

$$P = I_P \frac{k.T}{e} \ln \left(\frac{I_P + I_L}{I_s} + 1 \right)$$

In general the cell will be operated under conditions that give the maximum power output. The maximum possible area $P_{max} = V_{mp} \cdot I_{mp}$ determines the fill factor FF, which is defined by:

$$FF = \frac{V_{mp}.I_{mp}}{V_{oc}.I_{sc}}$$

Consequently, the fill factor is the ratio of the two rectangles in Figure 4-18 and is larger the more square-like the IV-curve is.

The three parameters V_{oc}, I_{sc} and FF are sufficient to calculate the energy conversion efficiency of the cell, which is defined as:

$$\eta = \frac{V_{mp}.I_{mp}}{P_{in}} = \frac{FF.V_{oc}.I_{sc}}{P_{in}}$$

where P_{in} is the total power of the incident light. The essential material parameters that determine the efficiency of a particular type of solar cell are the lifetime and the mobility of the minority charge carriers, and the surface recombination velocities [7].

4.5.1.2 *Growth on germanium substrates*

As we mentioned, the solar cell development has to be seen in a larger frame, of which a major part focuses on the epitaxial growth on germanium substrates [8]. A number of problems arise when growing polar III-V semiconductor material on the non-polar germanium.

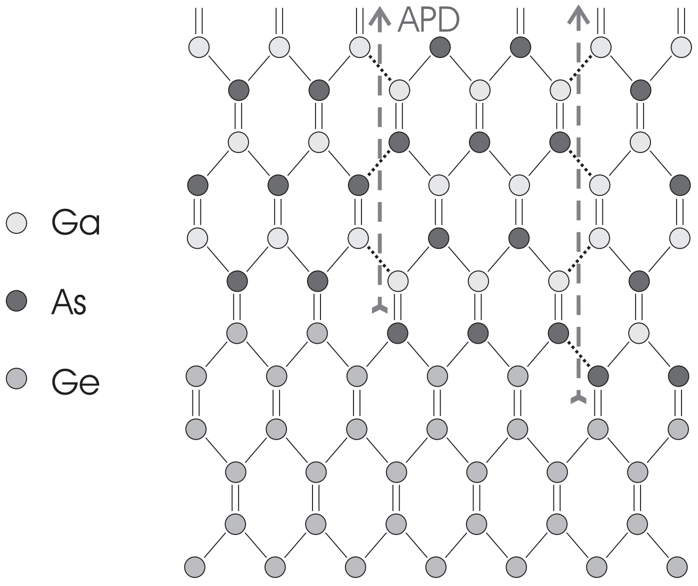

Figure 4-19 The formation of APD when growing GaAs on Ge (after [8])

The most important problem is the occurrence of anti-phase domains (APD). Germanium has a diamond lattice that consists of two sublattices. They only differ from one another in the spatial arrangements of the bond orientation. In

GaAs, the gallium atoms occupy one of the two sublattices, arsenic atoms the other. When the allocation of the atoms to a sublattice changes through the crystal, a two-dimensional structural defect is formed, called anti-phase domain. Now when growing GaAs on germanium, the As-Ge bond is strong whereas the Ga-Ge is not, thus the first atomic layer is expected to be an As-layer. Also, any real surface is not atomically sharp but shows some steps. As is illustrated in Figure 4-19, this will lead to APD with As-As and Ga-Ga bonds. To counter this effect a certain off-orientation of the substrate combined with a suitable nucleation layer are necessary.

There are some other issues. One is the auto-doping of the grown epitaxial layers with out-diffusing germanium. For certain applications, the germanium substrates are back-side coated to prevent this. Another issue is the cross-doping at the interface between the substrate and the epitaxial layers. Also, there is a difference in the lattice constant and the thermal properties. That is why, when growing the thick solar cell structures, a small amount of indium (1-2%) is added to the (Al)GaAs layer stack to provide lattice-matching. For a more thorough study of the growth on germanium we refer to reference [8].

4.5.1.3 Structure-, growth- and processing-parameters

An ideal comparison of the solar cells grown using the two precursors and on the two substrates would comprise of identical structures and processing. Unfortunately, in practice growth and the subsequent processing have been optimised simultaneously. As a result, not all cells are optimal and some of the conclusions are not very “hard”. The layer stack, growth conditions and differences in processing are summarised in Table 4-6, Table 4-7 and Table 4-8.

Sample		**A**	**B**	**C**	**D**	**E**
Cap	GaAs, $p>10^{19}cm^{-3}$	300 nm	300 nm	300 nm	300 nm	300 nm
Window	$Al_{80}Ga_{15}As$, $p=2x10^{18}cm^{-3}$	50 nm	50 nm	50 nm	50 nm	50 nm
Emitter	GaAs, $p=2x10^{18}cm^{-3}$	200 nm	200 nm	200 nm	500 nm	500 nm
Base	GaAs, $n=1x10^{17}cm^{-3}$)	3 µm	3 µm	3 µm	3 µm	3 µm
BSF	$Al_{30}Ga_{70}As$, $n=2x10^{18}cm^{-3}$	50 nm	50 nm	50 nm	50 nm	50 nm
Arsenic-precursor		AsH_3	AsH_3	TBAs	TBAs	TBAs
Substrate	(n-type)	GaAs	Ge	GaAs	GaAs	Ge

Table 4-6 Overview of the layer stack, arsenic-precursor and substrate of the solar cells in the comparison.

Sample	A	B	C	D	E
GaAs (base + emitter)					
TMGa (µmole/min)	106	106	106	106	106
TMIn (µmole/min)	-	2.1	-	-	2.1
AsH_3 (µmole/min)	2061	2061	-	-	-
TBAs (µmole/min)	-	-	923	923	923
T_{growth} (°C) - base	710	710	660	660	660
T_{growth} (°C) - emittor	670	670	660	660	660
V_{gr} (µm/hour)	3.1	3.1	3.1	3.1	3.1
V/III	20	20	8.7	8.7	8.6
$Al_{30}Ga_{70}As$ (BSF)					
TMGa (µmole/min)	79	79	59	59	59
TMAl (µmole/min)	35	35	25	25	25
TMIn (µmole/min)	-	2.1	-	-	2.1
AsH_3 (µmole/min)	2061	2061	-	-	-
TBAs (µmole/min)	-	-	3875	3875	3875
T_{growth} (°C)	730	730	720	720	720
V_{gr} (µm/hour)	2.5	2.5	2.5	2.5	2.5
V/III	24	24	46	46	45
$Al_{80}Ga_{20}As$ (window)					
TMGa (µmole/min)	20	20	20	20	20
TMAl (µmole/min)	78	78	78	78	78
TMIn (µmole/min)	-	2.1	-	-	2.1
AsH_3 (µmole/min)	2061	2061	-	-	-
TBAs (µmole/min)	-	-	3875	3875	3875
T_{growth} (°C)	660	660	720	720	720
V_{gr} (µm/hour)	3	3	3	3	3
V/III	21	21	40	40	39

Table 4-7 Overview of the growth conditions for the different solar cells.

Besides the obvious differences involving the arsenic-precursor and substrate used, we point out the difference in the emitter thickness. A thicker emitter has a lower serial resistance but will also push the junction further away from the illuminated surface. The mask set has been designed for an n-on-p structure. When we use a p-type emitter instead, we have to compensate for the lower mobility of the holes.

Looking at the detailed growth conditions we find that the cells grown using arsine may not have been grown in optimal conditions and thus the performance of these cells will represent a lower limit of the arsine process. It has been impossible however to repeat the experiments under better conditions due to the removal of the arsine from the lab.

Sample	**A**	**B**	**C**	**D**	**E**
Mask set					
Type	Old	Old	New	New	New
Shadowing	9.5%	9.5%	4.5%	4.5%	4.5%
AR coating					
Type	Si_3N_4	Si_3N_4	MgF_2/ZnSe	MgF_2/ZnSe	MgF_2/ZnSe
Reflectivity	10%	18%	6%	6-7%	3%

Table 4-8 Overview of the differences in the processing of the different cells

Also the processing scheme of the solar cells has evolved over time. The first samples used a mask set where the top contacts covered 9.5% of the surface, whereas this shadowing effect was reduced to about half of that value with a new mask set. To limit the reflection at the air-semiconductor interface, an anti-reflection coating is applied. On the first cells this was a single layer of silicon-nitride but this was later improved to a double layer of magnesium-fluoride and zinc-selenide. Tuning the thickness of the layers is the last means of reducing reflectivity.

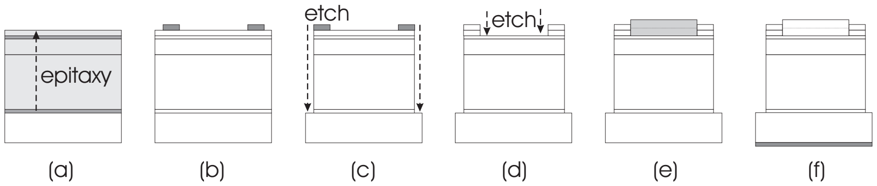

Figure 4-20 Processing principle of the solar cells. After epitaxy of the layer stack (a) and deposition of the top finger-pattern metallisation (b), a mesa is etched (c). Then the cap layer is etched away (d) and finally an anti-reflection coating (e) and a back contact (f) are deposited.

The processing sequence for the solar cells is relatively simple. After epitaxial deposition of the layer stack on the epi-ready substrate a front metallisation is applied (TiW) and plated (Au). This metallisation consists of a "finger-pattern", applied using standard lithography techniques. First a mesa, 3 to 4μm high, is etched to avoid leakage of the light-generated charge. The finger-pattern metallisation is then used as a mask to selectively etch away the highly doped cap layer that would otherwise absorb too much light. Then an antireflection coating is evaporated onto the front surface. In a final step a metallic contact (AuGe/Ni/Au) covers the entire back surface.

4.5.1.4 Device characterisation and comparison

A major difference to take into account when comparing the performance of the cells on different substrates is that the epitaxial layers that are grown on germanium contain a small amount of indium to obtain better lattice-matching. This leads to the reduction of the band-gap by about 15meV and thus the extension of the spectral response towards longer wavelengths. Convolution of the spectral response with the solar spectrum (see Figure 4-21) shows a theoretical improvement of the current density J_{sc} of about 1.5mA/cm^2.

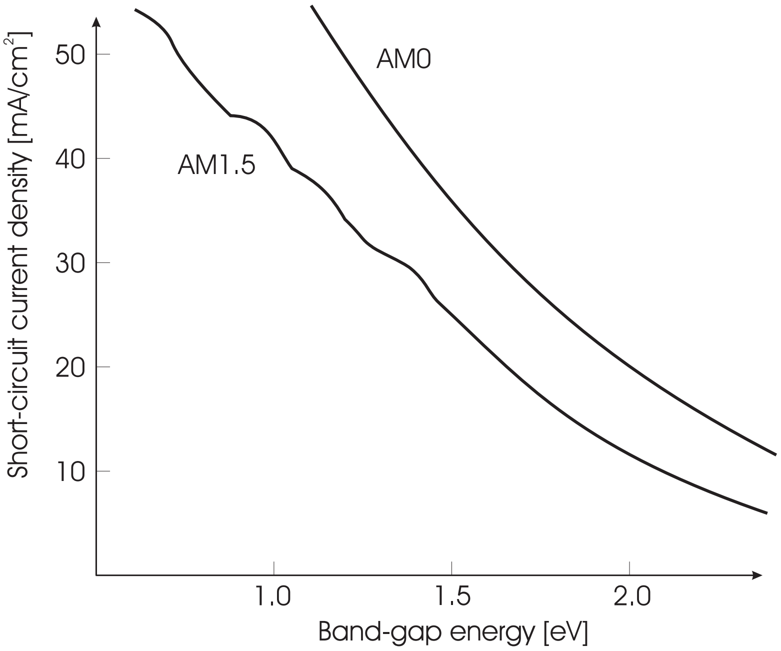

Figure 4-21 Theoretical maximum short-circuit current density as a function of the junction band-gap energy for air mass 1.5 (earth surface) and air mass 0 (outside the atmosphere) after [7].

However, the measured current density J_{sc} obtained from IV-characteristics is dependent on processing parameters (such as AR-coating and the shadowing effect of the mask). In order to make a fair comparison it is better to compare current densities that are extracted from the internal quantum efficiency (IQE) measurements as these are independent on AR-coatings and shadowing effect of the mask. In the following discussion, we will always refer to this calculated current density J_{sc}, unless otherwise mentioned.

Sample	**A**	**B**	**C**	**D**	**E**
$J_{sc,\ meas'd}$ (mA/cm^2)	23.6	23.4	27.2	26.8	28.8
$J_{sc,\ calc'd\ from\ IQE}$ (mA/cm^2)	29.6	30.3	30.5	29.9	31
V_{oc} (mV)	1030	1017	1054	1040	1030
FF (%)	80.1	78.1	79.7	83.7	82.8
Conversion efficiency (%)	19.5	18.6	22.8	23.3	24.4

Table 4-9 Performance under AM1.5 of the different solar cells. The current density in the first row is obtained from IV-measurements, the current density in the second row is calculated from the internal quantum efficiency (see below).

The characteristic parameters of the different cells are summarised in Table 4-9. The difference between the measured and calculated current densities is clearly related to the shadowing effect of the mask and the reflectivity of the antireflection coating. The most important parameter to judge material quality is the open circuit voltage (V_{oc}). Its value will however also be reduced due to the addition of indium to the junction region. The value of the fill-factor is directly related to the resistance of the emitter layer and is indeed improved by increasing emitter thickness (structures A, B, C vs. D, E).

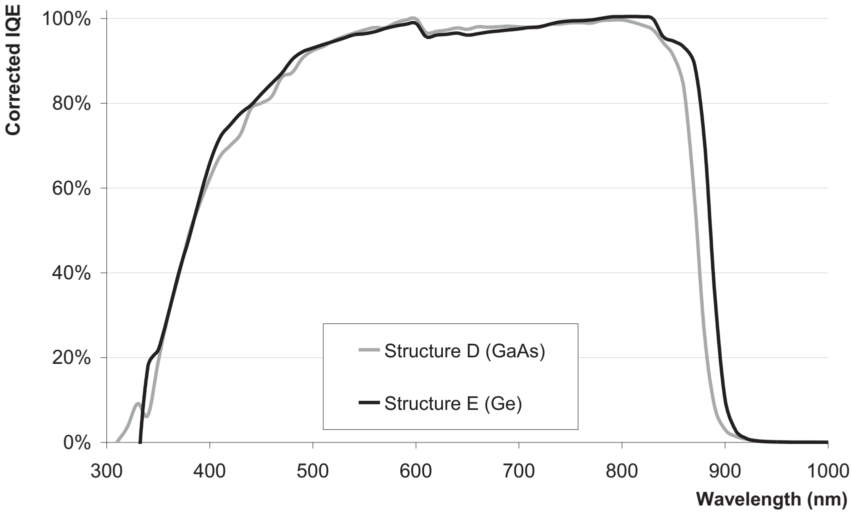

Figure 4-22 Internal quantum efficiency under AM1.5 of identical solar cell structures grown on GaAs (D) and germanium (E) substrates using TBAs.

Now, when we compare germanium and GaAs substrates, we take a look at structures A vs. B and D vs. E respectively. The indium-related spectral response difference of the IQE between structures D and E is shown in Figure 4-22. Also from Table 4-9, can we clearly observe the effect on both V_{oc} and J_{sc}

of adding indium. Note that all values are very high compared to the theoretical maximum value for J_{sc} and V_{oc} of 31.5mA/cm^2 and 1095mV resp. for a GaAs solar cell.

The conversion efficiencies are more difficult to compare, as they not only depend on the intrinsic material quality, but also on the device structure and all processing parameters. Different processing schemes (in particular AR-coating and mask design) have a severe impact on the conversion efficiency. The cells grown with AsH_3 indeed suffer from the highest shadowing and the highest reflectivity of the AR-coating. The cell grown on Ge and with TBAs, exhibiting the largest conversion efficiency, was processed in the most optimum conditions. By comparison of structures D and E, which underwent the more reliable processing scheme, we see that the cells grown on germanium have a better conversion efficiency than the cells on GaAs. This is because the effect on the measured J_{sc} outweighs the effect on V_{oc} and because of the better AR-coating deposited.

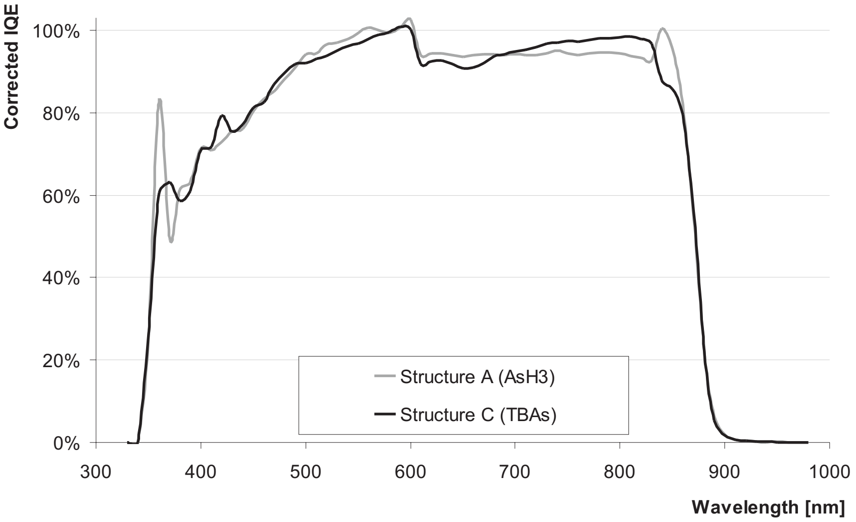

Figure 4-23 Internal quantum efficiency under AM1.5 for identical structures grown using AsH_3 (A) and TBAs (C) on GaAs substrates.

It is difficult to draw any conclusions from the performance characteristics of Table 4-9 when comparing As-precursors. Indeed, such effects as reduced reflectivity in the AR-coating and processing with a mask set with reduced shadowing will influence current densities and fill factors and hence conversion efficiencies. Instead, in Figure 4-23, we show the internal quantum efficiencies (IQE) of the solar cells A and C, and refer to the J_{sc} calculated from this IQE. Material obtained with TBAs is at least of equal quality as the material grown with AsH_3.

In conclusion, we have demonstrated that excellent solar cells can be realised using this TBAs-process and using the cheaper and more robust Ge-substrates instead of the traditional GaAs substrates. An efficiency of 24.4% under the AM1.5 solar spectrum has been measured and confirmed by the Fraunhofer ISE test centre in Freiburg, Germany. This value is to date a world record efficiency for a p-on-n single junction GaAs solar cell on germanium [3].

4.5.2. InGaAs 980nm edge-emitting lasers

4.5.2.1 Laser design

A second part of the validation of the growth process consists of the growth of laser diodes with InGaAs quantum wells as active region emitting at 980nm. Similar devices have been grown for several years at the lab and the know-how of the processing is profound. For the basic mechanism of semiconductor lasers and their design, processing and characterisation we refer to the previous chapter.

The actual structure used, which is in fact the basic structure for the long wavelength lasers of chapter three, is shown in Figure 4-24. The devices we have grown here have 6nm thick $In_{20}Ga_{80}As$ triple quantum wells with GaAs barriers embedded in a GRINSCH structure with $Al_{35}Ga_{65}As$ cladding layers. The cladding layers have a doping level of $5 \cdot 10^{17}$. The GRINSCH and active region is not intentionally doped whereas the contact and buffer layers are $p = 1 \cdot 10^{19}$ and $n = 2 \cdot 10^{18}$ respectively.

We have also grown devices with low threshold current. Their structure is similar to the one before, but now the cladding layers contain 65% of aluminium to maximise overlap of the optical mode and the active region and there is only one quantum well in the active region so less conduction band states have to be filled.

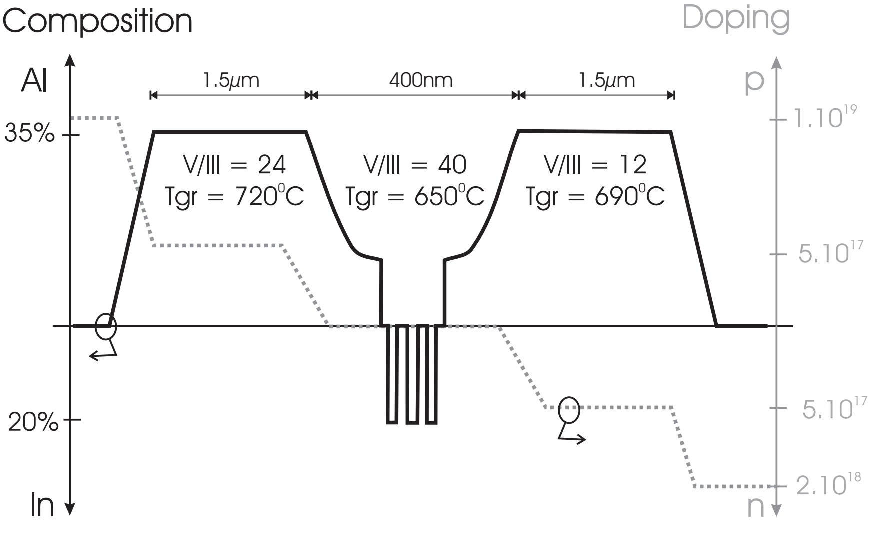

Figure 4-24 Structure, growth parameters and intended doping levels of the edge-emitting laser devices.

4.5.2.2 *Characterisation*

The characterisation of the devices consists of standard continuous wave measurement of the output power and voltage of the device as a function of the current. The heat sink's temperature is fixed at 20ºC. The parameters are extracted as for the lasers in chapter three (see Figure 4-25) and are summarised for ridge widths of 7µm in Table 4-10.

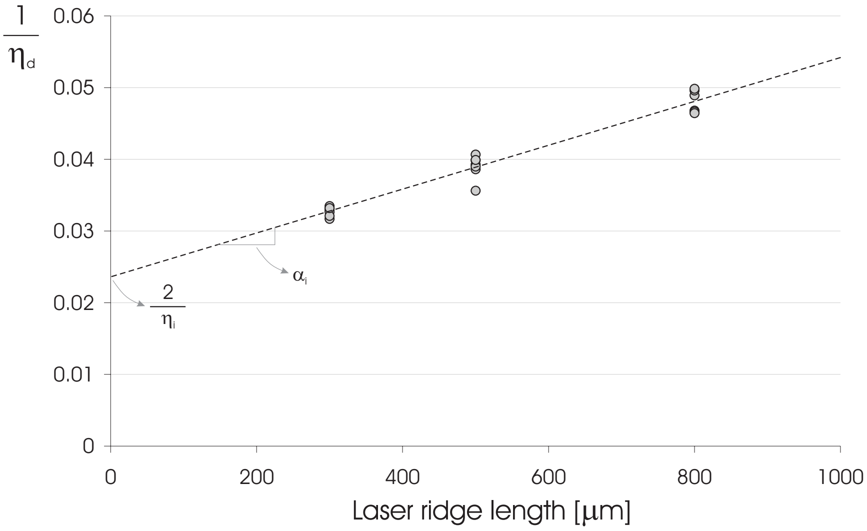

Figure 4-25 A plot of the reciprocal external quantum efficiency per facet versus the laser ridge length (here from the standard structure) allows us to estimate the internal quantum efficiency η_i and the internal losses α_i.

	η_i	**α_i**	**J_{th}**	**R_s**
Standard structure	84.72%	0.31 / cm	0.82 kA/cm^2	10 Ω
Low threshold structure	85.71%	0.71 / cm	0.33 kA/cm^2	20 Ω

Table 4-10 Characteristics of the first series of InGaAs edge-emitters

The threshold current density is extrapolated to be as low as 220A/cm^2 for devices of infinite length. This value can probably be still reduced when we would apply a suitable HR-coating on the facets.

	η_i	α_i	I_{th}	R_s
Standard structure	81.46%	11.74 / cm	65mA	4 Ω
Low threshold structure	91.8%	16.66 / cm	45mA	4 Ω

Table 4-11 Characteristics of the second series of InGaAs edge-emitters

However, the serial resistance is rather high, probably due to a problem with the n-type doping of the cladding. We have fabricated a second series of lasers with an increased doping level of the n-type-cladding layer (see Table 4-11). The serial resistance of device has been significantly reduced but the internal losses are substantially higher. Due to the wet etching in the processing the ridges are highly under-etched, which makes it difficult to estimate width and thus the current densities in the device.

In summary, we have produced edge-emitting lasers with excellent characteristics with internal efficiencies of over 90% and internal losses of below 1/cm. These values are comparable with those of devices that used to be made at the lab using the arsine process.

References

[1] Gerald B. Stringfellow, “Organometallic Vapour-Phase Epitaxy. Theory and Practice”, Academic Press, Boston (1989)

[2] M.E. O’Brien, Semicond. Environ. Safety Health Assoc. J. 15 (2001) 9.

[3] J. Derluyn, K. Dessein, G. Flamand, Y. Mols, J. Poortmans, G. Borghs, I. Moerman, J. Cryst. Growth 247/3-4, 237-244 (2003)

[4] S. Leu, F. Höhnsdorf, W. Stolz, R. Becker, S. Salzmann, A. Greiling, J. Cryst. Growth 195, 98 (1998)

[5] S. Watkins, G. Haacke, Appl. Phys. Lett. 59, 2263 (1991)

[6] T. Takeuchi, Y. Chang, A. Tandon, D. Bour, S. Corzine, R. Twist, M. Tan, H. Luan, Appl. Phys. Lett. 80, 2445 (2002)

[7] H. J. Möller, “Semiconductors for Solar Cells”, Artech House, Boston (1993)

[8] P. Modak, “Development of InAlGaP-based light-emitters on GaAs and Germanium substrates by means of MOCVD”, Ph.D. thesis, Intec - Ghent University (2001)

[9] M. D’Hondt, “Ontwikkeling van MOVPE-gebaseerde InGaAs/InP fotodetctoren en laserdioden voor golflengten boven 1.65µm”, Ph.D. thesis, Intec - Ghent University (1997)

[10] P. Zory ed., “Quantum Well Lasers”, Academic Press, Boston (1993)

CHAPTER 5

GROWTH OF DILUTE NITRIDES

5.1. Abstract

This chapter discusses the experimental data we obtained from the epitaxial growth of GaInNAs. In an introduction an overview of the growth conditions is given as they are found in literature.

Next we look into different possibilities for nitrogen precursors and argument the choice we have made for unsymmetrical di-methyl-hydrazine. The properties of this substance are summarised.

The growth study itself is subdivided in two main parts; one where we look at epitaxial growth using arsine, and one where the growth using TBAs is discussed. Each of these paragraphs starts off with the growth of GaNAs before going further towards GaInNAs quantum wells.

The paragraph on growth using arsine is devoted to the nitrogen incorporation behaviour and the effect of nitrogen on the photoluminescence efficiency. In the paragraph on growth using TBAs, we will show an anomalous nitrogen incorporation behaviour and have a look at the optical characterisation.

5.2. Introduction

We have reviewed the extraordinary properties of GaNAs and GaInNAs in chapter two. We briefly touched upon the difficulties involved concerning the epitaxial growth and mentioned the effect of nitrogen on the optical quality. This chapter summarizes the experimental results on the growth of Ga(In)NAs obtained at INTEC. A first step is the selection of a suitable nitrogen precursor.

The previous chapters discussed the development of low temperature growth and of growth using TBAs. These are useful steps in any GaInNAs programme, but the study of nitrogen-containing material was started already before these previous items had been finished. That is why a first paragraph will focus on the growth using arsine. A next paragraph is the logical evolution where we switch group V precursors to TBAs. Some interesting results concerning the nitrogen incorporation behaviour are obtained, as well as results from photoreflectance and TEM studies.

In both cases however, we will not aim for lattice matched material and instead use compressively strained quantum wells with high indium content. This is because the impact of nitrogen on the quality of the layers is just too big. In this view, the study of the low temperature growth and in particular its application to strained InGaAs quantum wells is of great interest.

From literature there are of course clues how the dilute nitrides are best grown using MOCVD ([1] [2] [3] [4] [5] [6]). The point with which they all agree is that the growth temperature should be low, i.e. below 550ºC, in order to have any nitrogen incorporation in the layers (see Figure 5-1). This is attributed to desorption of nitrogen from the surface as it has a high equilibrium vapour pressure. It is a phenomenon known from the pure nitrides, where huge V/III ratios are common (even though the properties of ammonia are also partly responsible). The desorption-process has an activation-energy of 23kcal/mole [6] to 30kcal/mole [5].

For the same reason, high V/III ratios are also beneficial for growth of Ga(In)NAs. To control the nitrogen content, the relative flows of the nitrogen and arsenic precursors are the determining factor. More specifically in literature, this relationship is expressed in terms of the DMHy over total group V ratio. A very high value is needed to obtain any nitrogen uptake, as can be seen Figure 5-2. It is also clear from the figure that adding indium to the alloy reduces the nitrogen-content. Indeed, the Ga-N bond is much stronger than an In-N bond, so increasing the possibility to have the latter bonds will stimulate desorption.

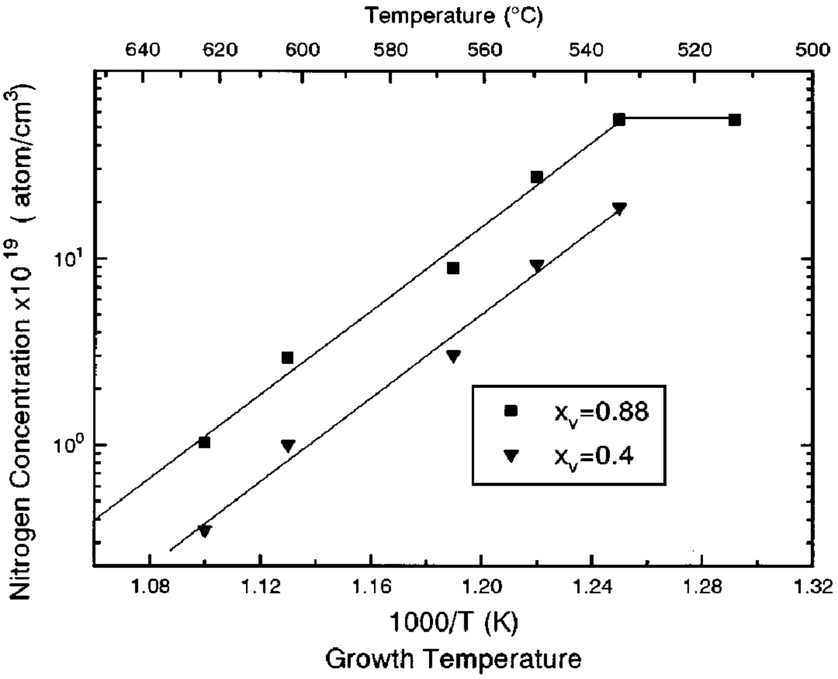

Figure 5-1 Temperature dependence of the nitrogen incorporation in GaNAs (after [6]. X_v is the relative DMHy molar flow (DMHy / DMHy + TBAs)

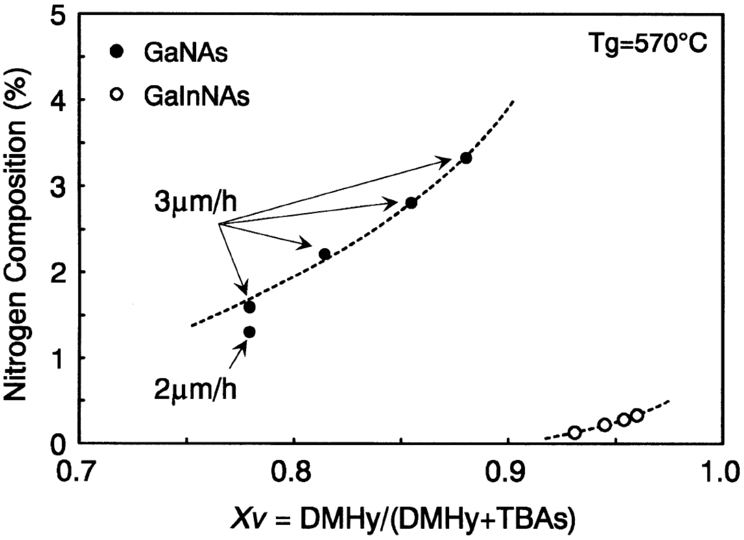

Figure 5-2 Dependence of the nitrogen content on the relative DMHy flow (X_v = DMHy/DMHy+TBAs) (after[4])

One last issue is that of the growth rate. There are reports of a nitrogen capturing effect, according to which the nitrogen incorporation increases with the growth rate (see Figure 5-2 and Figure 5-3). A high growth rate however also reduces the optical quality, through the introduction of point defects [3]. In general GaInNAs is grown at low growth rates to optimise for optical quality. This is contrary to what is done for strained InGaAs quantum wells, where a high growth rate is used to suppress relaxation.

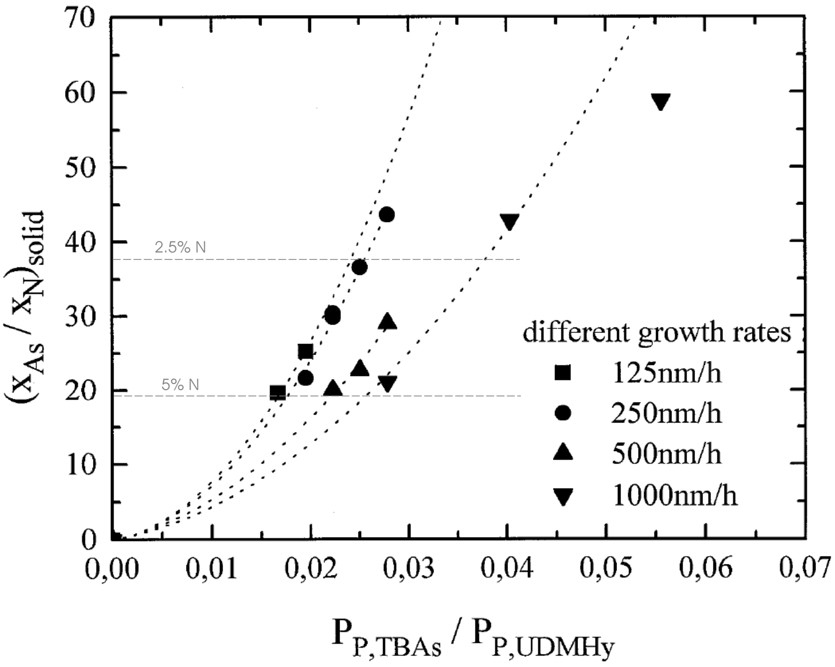

Figure 5-3 Influence of the growth rate on the nitrogen incorporation in GaNAs (after [3])

5.3. Nitrogen precursors

To add nitrogen to our epitaxial layers, we need a suitable precursor. At the time of the start of this work, there were few possibilities. The first results concerning GaNAs were obtained with gas source MBE, and in the GaN system one works predominantly with ammonia. As with arsenic precursors (see chapter 4), a nitrogen precursor has to obey a few simple rules in terms of stability, pyrolysis temperature, safety and vapour pressure. A selection of precursors is reviewed below.

- Ammonia (NH_3)

  It is the most commonly used source in the MOCVD growth of (In)(Al)GaN-material. It is chemically very stable and only dissociates at very high temperatures. Ammonia is highly corrosive, reactive and toxic. Its high pyrolysis temperature (>1000ºC) makes it unsuitable for growth on GaAs substrates [7].

- Plasma-assisted MOCVD

  This technology uses microwaves to pre-crack nitrogen or ammonia gas and produce nitrogen radicals. The plasma requires a low growth pressure. The overhead in terms of equipment is huge and the growth process complex and hard to control.

- Hydrazine (N_2H_4)

  Hydrazine is a very reactive material. It was used in the fifties as rocket fuel in the Titan rockets and explodes when brought in contact with air. At the same time, it is very toxic with a TLV value of only 0.1ppm for skin contact. On the positive side, it decomposes above 400ºC, is a fluid at room temperature and has more nitrogen-atoms per mass unit than any other source. One report shows that nitrogen incorporation is very efficient using this source [10]. These facts do not outweigh the risks this material poses.

- Unsymmetrical di-methyl-hydrazine (u-DMHy or $(CH_3)_2NNH_2$)

  The most commonly used source for the dilute nitrides is this material. Methyl groups replace two hydrogen atoms of the hydrazine molecule. This makes the molecule heavier, less stable and less reactive, but nonetheless it is corrosive, toxic and highly flammable. Its vapour pressure is lower than hydrazine's and it decomposes fully at 200ºC. The material is available commercially from three different suppliers.

- Tertiary-butyl-hydrazine $(C_4H_9)HN_2H_2$

  TBHy is another product where one of hydrazine's hydrogen atoms has been replaced by a heavier organic compound. Its vapour pressure, reactivity and toxicity are lower than hydrazine's. It is however not commercially available [8].

- Phenylhydrazine ($C_6H_5NHNH_2$)

  Phenylhydrazine has been investigated as a nitrogen source for the deposition of group III nitride based alloys by MOVPE. Its VP (0.043 @ 25°C) makes low pressure growth systems more suitable for phenylhydrazine use. Due to its low thermal stability, when compared to ammonia, reduced deposition temperatures have been demonstrated. The significant number of N-H bonds present lead to passivation of the incorporated donor and thus much reduced active nitrogen concentrations [9].

- Nitrogen trifluoride (NF_3)

  Just recently Kurtz et al. [10] reported about GaNAs growth using NF_3. It has nitrogen incorporation similar to hydrazine's. As opposed to all other sources mentioned above, it acts as an oxidising substance. In a strongly reducing hydrogen environment that is typical to MOCVD, this introduces the threat of accidental combustion inside the system. Hence, it is preferably diluted with an inert gas, such as nitrogen. The gas is commonly used as a cleaning agent in CVD reactors. It decomposes at temperatures above 300ºC, possibly releasing the toxic acid HF when in contact with other precursors.

Considering these facts, the choice for unsymmetrical di-methyl-hydrazine was made. Its molecule is shown in Figure 5-4. Some data are summarised in Table 5-1. A high vapour pressure, low pyrolysis temperature but also very high toxicity is characteristic.

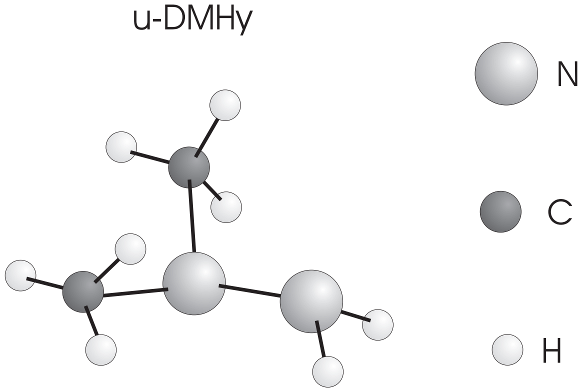

Figure 5-4 Molecule of unsymmetrical di-methyl-hydrazine

		u-DMHy
Pyrolysis temperature	[ºC]	200
Vapour pressure at 25ºC	[torr]	147
Molecular weight	[g]	60.1
Toxicity: TLV	[ppm]	0.01
Price	[€ / Mole]	600

Table 5-1 Physical properties of unsymmetrical di-methyl-hydrazine.

5.4. Initial results using arsine

5.4.1. Experimental

All samples have been grown in our close-coupled showerhead vertical rotating reactor. The growth pressure is 76Torr, although for some experiments near-atmospheric pressure (700Torr) was chosen. These latter cases will be specifically mentioned. Wafer rotation is kept constant at 300rpm and the carrier flow is 8 gas-litres per minute (slm) per manifold. The source materials are arsine, tri-methyl-gallium, tri-methyl-indium and of course the new di-methyl-hydrazine. Some experiments have been performed using tri-ethyl-gallium.

Thermal annealing is either performed ex-situ or in-situ. Some experiments were performed in a rapid thermal annealing furnace in which case a GaAs cap wafer was put on top of the wafer to stabilise it. Other wafers have been annealed in the MOCVD reactor under arsenic overpressure. Typical conditions are a ten-minute anneal at 760ºC at 76Torr.

5.4.2. GaNAs

For these experiments we focus on the incorporation of nitrogen in GaAs, so we can exclude any influence of the indium and we can easily determine the nitrogen composition from simple XRD measurements. The layers are 800nm thick bulk layers with a graded interface at the bottom to avoid the propagation of dislocations into the bulk layer [11]. The layers were morphologically perfect, except at the higher nitrogen concentrations where crosshatch patterns started to appear. The FWHM of the smooth layers is always smaller than 100 arc-seconds, indicating a good crystalline quality and a two-dimensional growth mode (Franck – van der Merwe). Combined <0 0 4> and <-1 1 5> XRD measurements (as the machine for RSM characterisation was not yet available at the time) show that the layers are fully coherently strained. This is in agreement with what is reported in literature [12].

X-ray diffraction also allows quantifying the nitrogen content of the layers. As mentioned before the two important parameters are the growth temperature and the molar DMHy flow, relative to the arsine flow. Figure 5-5 shows the temperature-sensitivity of the nitrogen incorporation. When the temperature increases beyond 530ºC, the nitrogen content starts to drop drastically, in agreement with other results ([3] [4]).

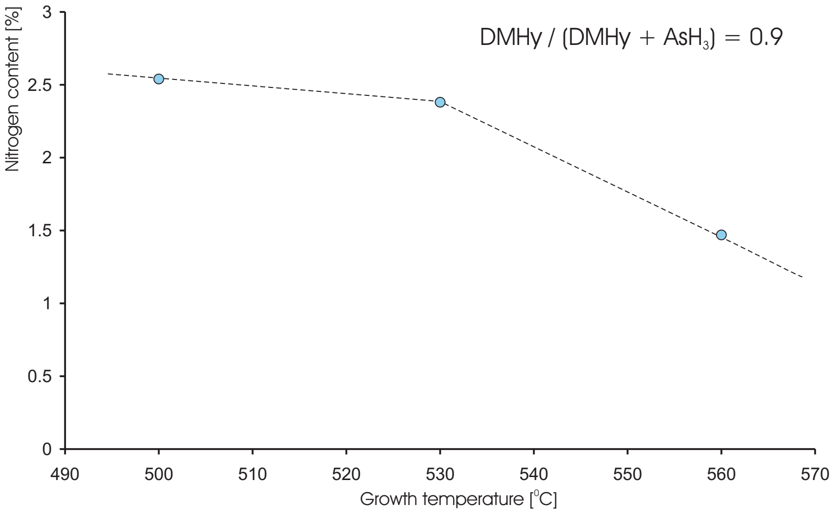

Figure 5-5 Temperature dependence of the nitrogen incorporation in GaNAs

The effect of changing the relative di-methyl-hydrazine flow is shown in Figure 5-6. The uptake of nitrogen starts only at a high value of the DMHy flow over total group V flow ratio. Because a relatively high arsine flow is needed to guarantee the quality of the grown layer, the needed DMHy flow is even higher.

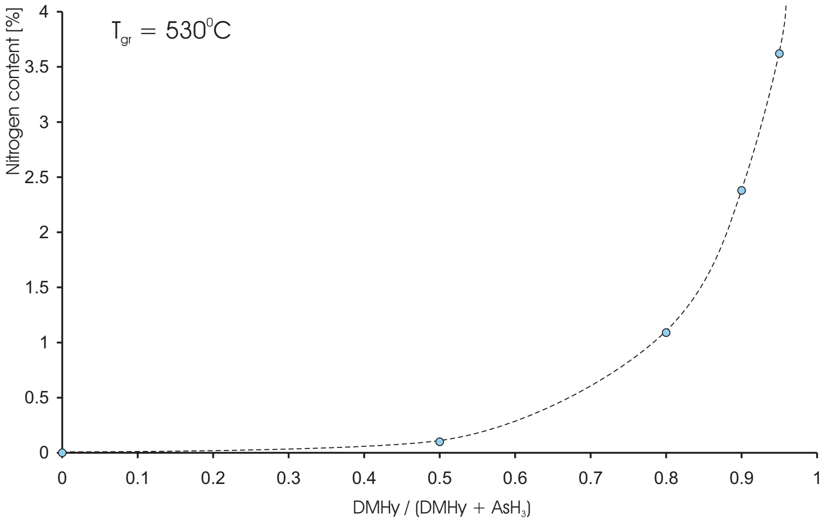

Figure 5-6 Nitrogen incorporation in GaNAs as a function of the DMHy/Group V ratio

Even though it is possible to incorporate rather high fractions of nitrogen, its effect on the photoluminescence is devastating. Figure 5-7 shows the photoluminescence of a GaNAs sample with only 0.6% of nitrogen. The intensity scale of all photoluminescence spectra in this section is normalised to the intensity a bulk GaAs layer produces. The PL efficiency is more than three orders of magnitude lower!

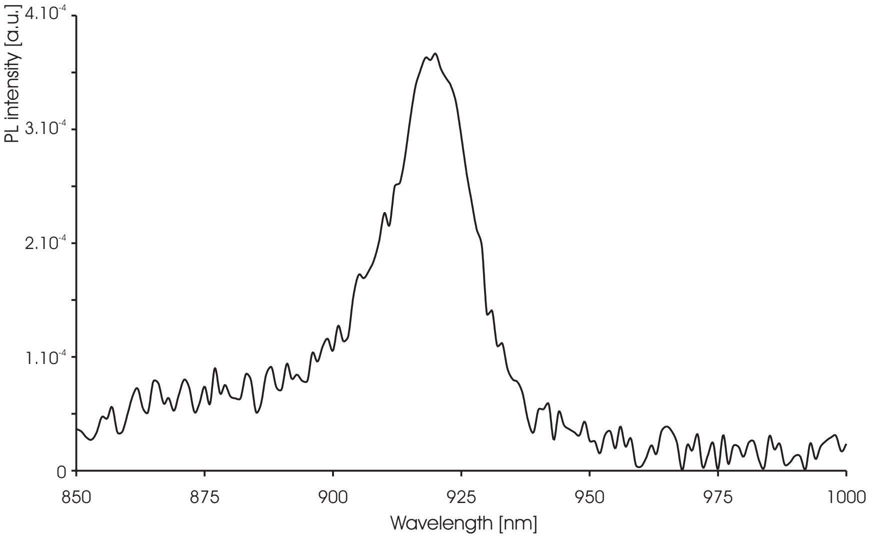

Figure 5-7 Room temperature photoluminescence of a bulk $GaN_{0.6}As_{99.4}$ *layer grown using arsine*

5.4.3. GaInNAs

The first problem we encounter when we study quaternary GaInNAs layers and specifically quantum wells is that of the determination of the exact composition of the wells. Clearly there are two degrees of freedom to eliminate, so that XRD-characterisation alone is not sufficient. When we take the thickness of the well into account, the number rises to three. This last parameter can however be fitted from XRD scans, even though the relative error is rather big.

Some reports in literature take a calibration sample as a standard and assume the indium content and well thickness remain constant, even after the introduction of DMHy into the reactor. This is a dangerous assumption because DMHy is reported to influence both growth rate and composition.

The other common solution is to use data from optical characterisation so as to determine the transition energy and then use an empirical expression to link this energy to a certain composition. We have adopted this method from [13]. Starting from an $In_xGa_{1-x}As$ quantum well with indium content equal to x with known transition energies, we introduce a nitrogen content y into the well to obtain a $Ga_xIn_{1-x}N_yAs_{1-y}$ quantum well. Let us then introduce the strain difference $\Delta e(x, y)$ as the difference in strain for the InGaAs and GaInNAs quantum wells:

$$\Delta e(x, y) = e(x, y) - e(x, 0)$$
$$\text{with } e(x, y) = [a(0, 0) - a(x, y)] / a(x, y)$$

This leads to the following expression for the band-gap energy as a function of the composition:

$$E_g(Ga_{1-x}In_xN_yAs_{1-y}) = E_g(Ga_{1-x}In_xAs) - 69\text{eV} \,.\, \Delta e(x, y)$$

This expression is illustrated in Figure 5-8 for 37.5% indium and 0.5% nitrogen.

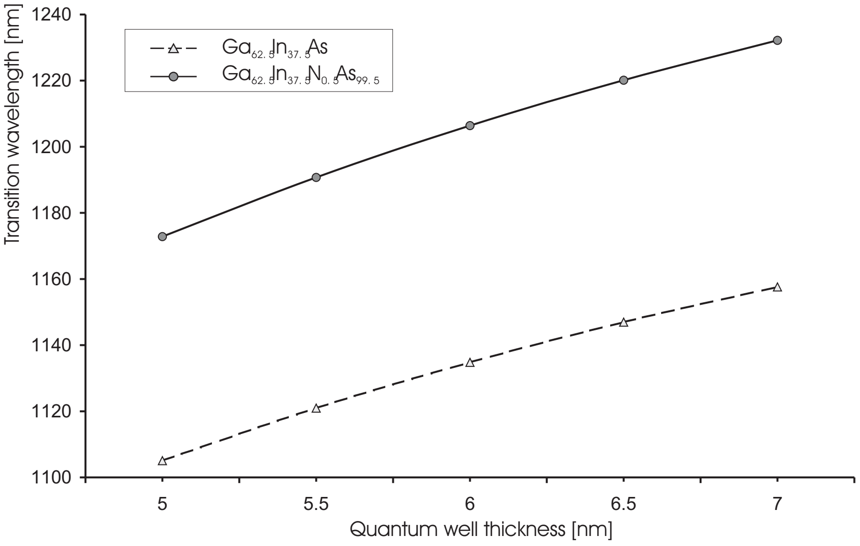

Figure 5-8 Calculation of quantum well transition energy with and without nitrogen

When we attempt to grow quantum wells two big problems remain. The first is the quenching of photoluminescence as the nitrogen content goes up even slightly; the second is the difficulty to incorporate nitrogen in sufficiently large concentrations.

Figure 5-9 shows PL-spectra of representative GaInNAs quantum well samples. We can see the effect of the nitrogen on the PL intensity. In the same picture we also notice the effect of thermal annealing on our samples. The blue shift and the recovery of the PL are clearly seen, but the resulting signal is still about two orders of magnitude less intense than the reference nitrogen-free sample.

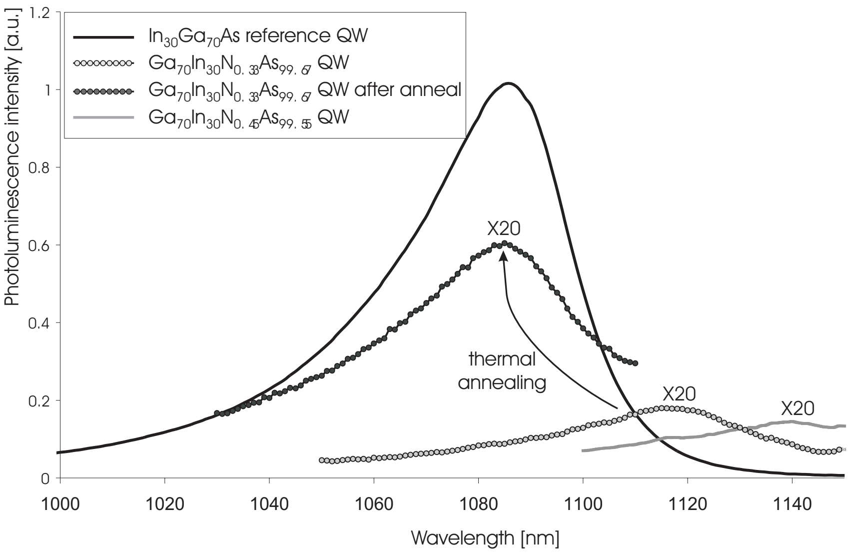

Figure 5-9 GaInNAs QW's grown at low pressure with arsine

One clue as to determine what the cause of the bad optical quality may be was discovered through transmission electron microscopy (TEM). This is shown in Figure 5-10. The samples concerned have ten GaInNAs quantum wells separated by GaAs barriers. In the samples interfacial layers appear between the quantum well and barrier layers. The growth interrupt, intended to suppress this phenomenon was ineffective.

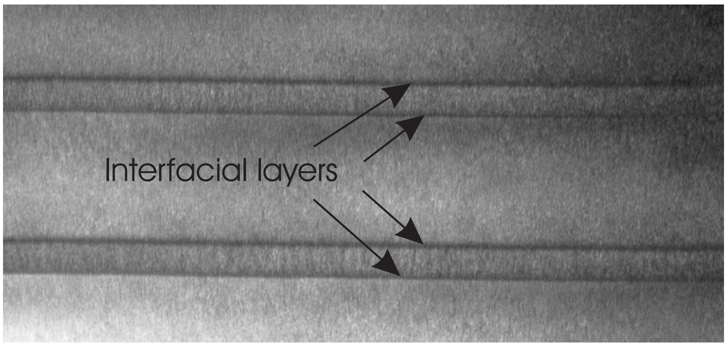

Figure 5-10 *TEM pictures of GaInNAs quantum wells grown with arsine. The growth direction is upwards.*

A side effect of the growth interrupts can be seen in Figure 5-11. The samples with the growth interrupt do not have entirely flat surfaces but have undulations. This is due to the fact that the atoms on the surface get the time to reorganise in non-two-dimensional formations to release strain.

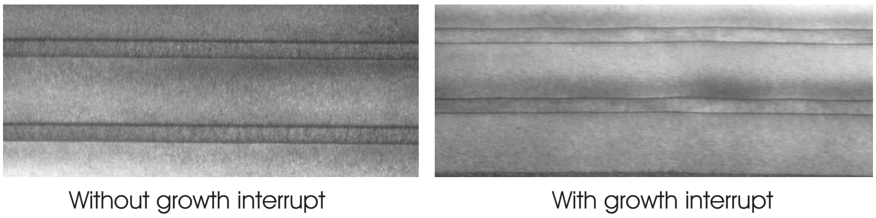

Figure 5-11 *TEM of GaInNAs quantum wells grown with and without growth interrupts. Undulations appear in the sample with growth interrupts.*

Since the optical quality remains bad after thermal annealing and no real trends are to be discerned in terms of the other growth parameters, we performed a number of experiments at atmospheric pressure. Indeed, the same molar flow at high pressure as at low pressure will induce an increased partial pressure of the source material and will thus better stabilise the semiconductor. On the other hand, higher pressure increases the chance of prereactions, as molecules have a higher probability to collide and interact.

Photoluminescence spectra of three significant samples are shown in Figure 5-12. The signals again identify the quenching of the luminescence with increasing nitrogen content of over two orders of magnitude for only 0.33% of nitrogen, which is even worse than in the low-pressure case.

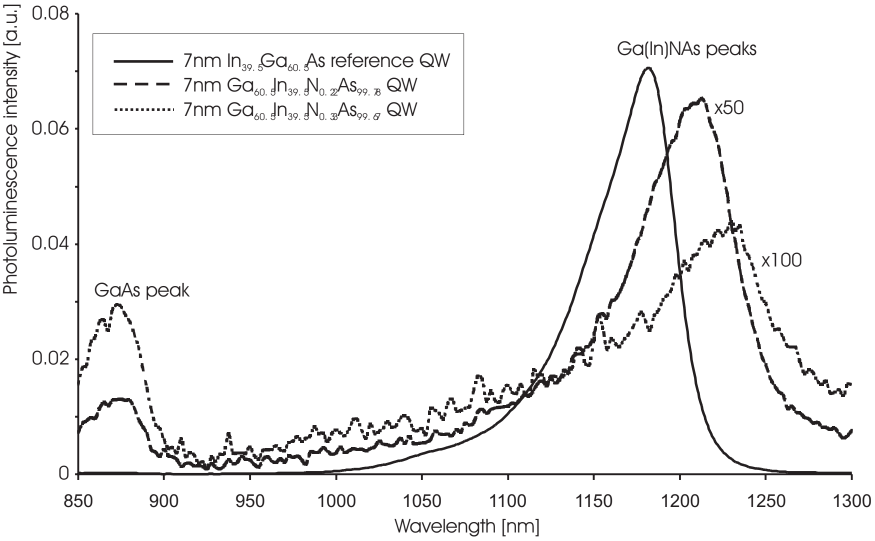

Figure 5-12 PL from GaInNAs QW's grown at atmospheric pressure

The unexpectedly low nitrogen incorporation is shown in Figure 5-13, where we plot the maximum PL wavelength for a number of different DMHy over group-V ratios. The shift of the emission wavelength as a function of the temperature is a consequence of the temperature-sensitive decomposition of TMGa in this range. Indeed, as the temperature decreases, the TMGa decomposes less efficiently and thus the material gets relatively more indium-rich. We remark that it is impossible to have larger values for the DMHy over group V ratio. This would imply reducing the arsine flow below acceptable values (because of its effect on the optical quality).

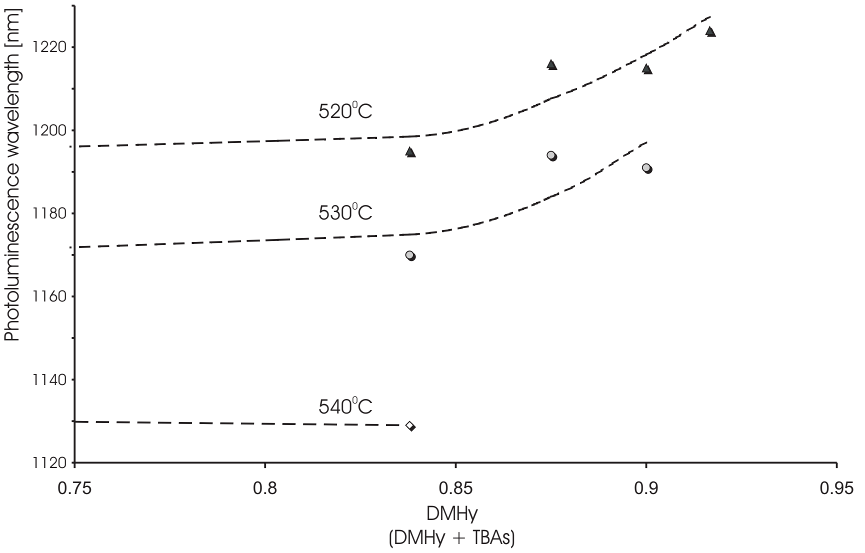

Figure 5-13 Nitrogen incorporation in GaInNAs QW's at atmospheric pressure grown using TMGa

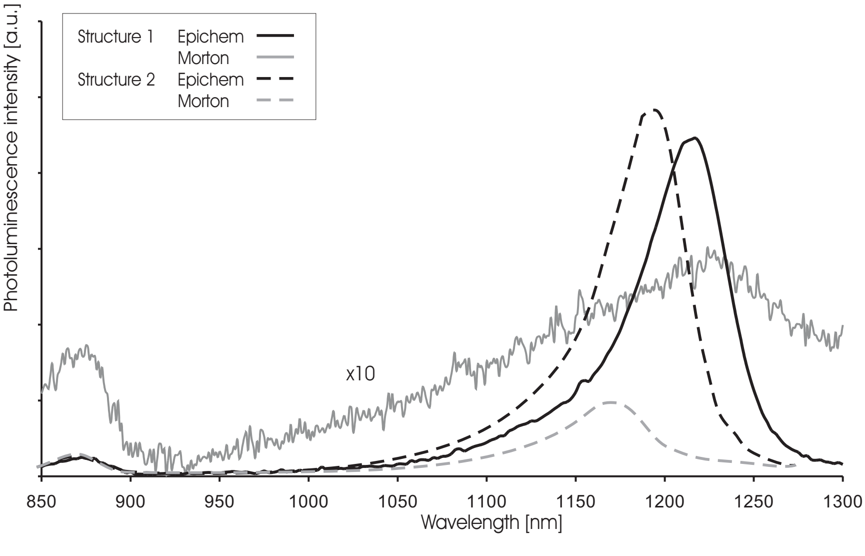

Figure 5-14 Comparison of identical structures grown under identical conditions with DMHy from different suppliers.

A last remark we would like to make in this discussion is the sometimes dubious quality of the DMHy precursor. Figure 5-14 shows two times two identical structures grown in identical conditions but with source material from two different suppliers. Clearly the optical quality is rather poor for the Morton samples, which we attribute to contamination that was induced by the source material.

5.5. Growth of dilute nitrides using TBAs

5.5.1. Experimental

All layers are grown on a Thomas Swan vertical rotating disk close-coupled showerhead reactor at a reactor pressure of 76 Torr under hydrogen carrier gas. Group III and group V source materials are switched in separate manifolds and are mixed only after the gases exit the showerhead. Source materials are tri-ethyl-gallium (TEGa), tri-methyl-indium (TMIn), tertiary-butyl-arsine (TBAs) and unsymmetrical di-methyl-hydrazine (DMHy). The growth temperature of all layers was 535ºC.

When GaInNAs quantum wells are grown a post-growth annealing step in the reactor of 10 minutes at 760ºC and 76Torr is added, in a hydrogen atmosphere with TBAs overpressure. Growth rates are 1.08µm/hr for bulk GaAs and GaNAs layers and as low as 0.07µm/hr for GaInNAs QW's.

The sample structures for GaNAs consist of semi-insulating exactly <100> oriented GaAs substrates, with a 150nm GaAs buffer layer, a 300nm GaNAs layer and a 30nm GaAs top layer. During growth of these samples the TEGa flow is held constant at 50.9µmol/min, whereas the TBAs flow was varied from 36.9µmol/min to 1181.7µmol/min. The DMHy flow was varied from 2177.2µmol/min to 6531.5µmol/min.

The GaInNAs/GaAs structures contain a single quantum well of nominally 6.5nm thick and have a 100nm GaAs top layer. They are grown on the same type of substrates. No growth interrupts are employed. For quaternary growth molar flows for TEGa, TMIn and DMHy are kept constant at 3.2µmol/min, 1.5µmol/min and 6531.5µmol/min respectively, while the TBAs molar flow was varied from 36.9µmol/min to 886.3µmol/min.

5.5.2. Nitrogen incorporation in GaNAs

The nitrogen content of GaNAs layers is studied by HR-XRD on the <0 0 4> planes using a Philips X'Pert Pro diffractometer and fitted to curves by dynamical simulation theory. Good fitting could be obtained for all samples (cf. Figure 5-15). Reciprocal space mappings around the <-1 1 5> reflection show that all layers are perfectly strained (see Figure 5-16).

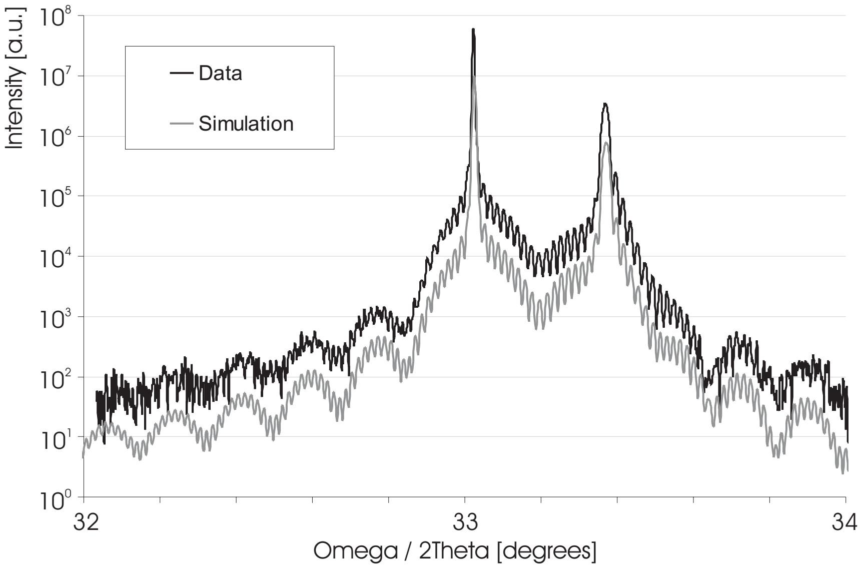

Figure 5-15 *HR-XRD <0 0 4> measurement and simulation of a 300nm $GaN_{0.024}As_{0.976}$ layer*

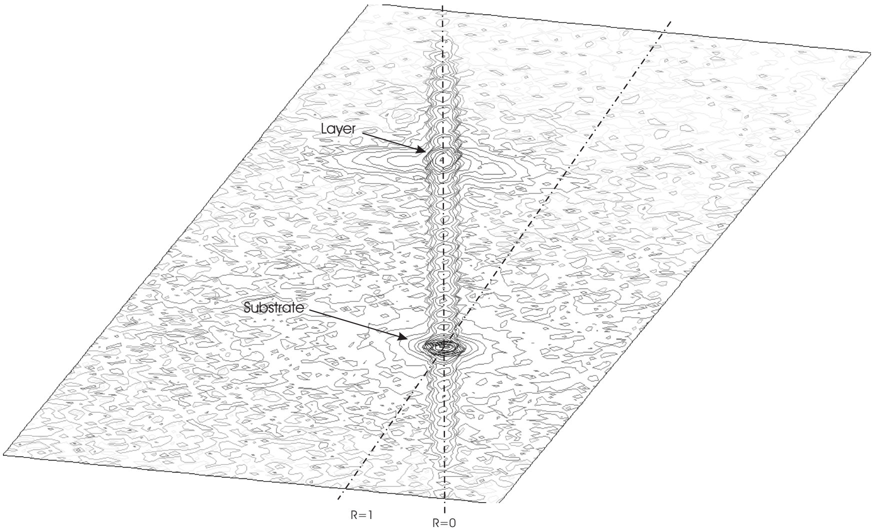

Figure 5-16 *Reciprocal space mapping around <-1 1 5> reflection of a 300nm thick $GaN_{0.015}As_{98.5}$ layer*

The first parameter under investigation is the growth temperature. We have performed a temperature sweep around the 530ºC hinge point (see Figure 5-5), where desorption of the nitrogen starts when we grow with arsine. We observe the same effect when growing using TBAs, pointing to the fact that the phenomenon is not related to any gas-phase chemical reaction, but rather physical (thermodynamical) in nature. We attribute the slight temperature shift of the hinge point to a drift in the read-out of the reactor temperature.

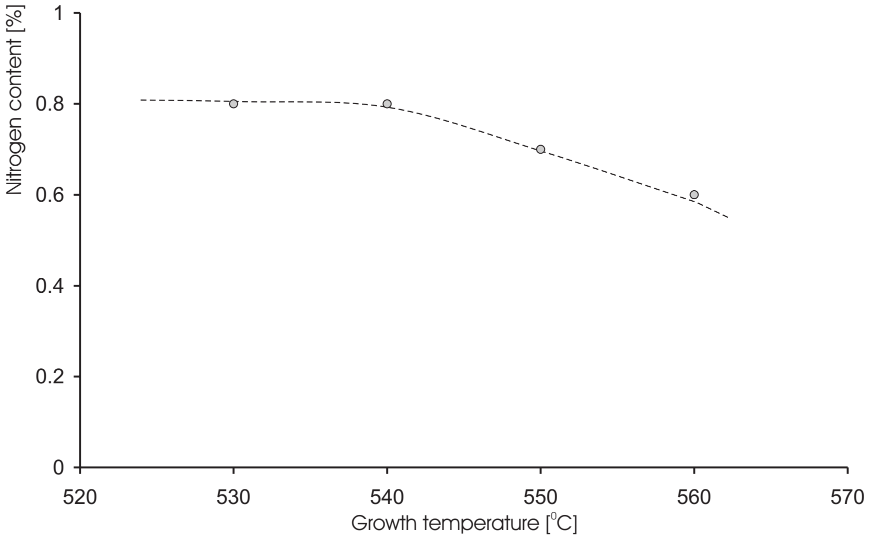

Figure 5-17 Nitrogen incorporation in GaNAs-layers grown with 73.9µmol/min TBAs and 2177µmol/min of DMHy

Contrary to what has been previously reported ([3] [4] [14]), we find that the nitrogen incorporation is not unambiguously determined by the DMHy / (DMHy + TBAs) ratio. Instead, when varying the DMHy flow and keeping the TBAs-flow constant, we find different curves that are shifted upwards with increasing TBAs-flow (cf. the black solid lines in Figure 5-18). When we keep the DMHy flow constant (grey dashed line in Figure 5-18), we see that when we decrease the TBAs flow, and thus increase the DMHy / (DMHy + TBAs) ratio, the nitrogen content actually drops.

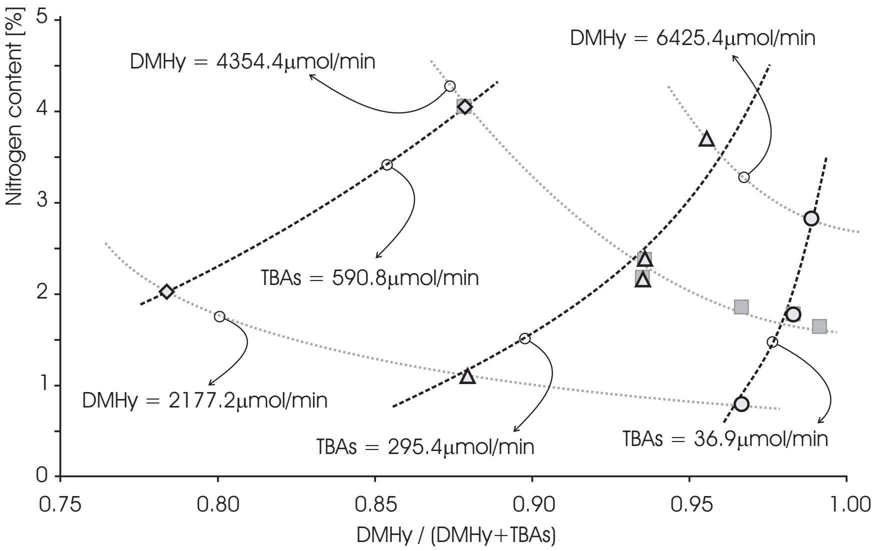

Figure 5-18 Nitrogen incorporation in GaNAs as a function of the relative DMHy molar flow, grown at 535°C and measured by XRD.

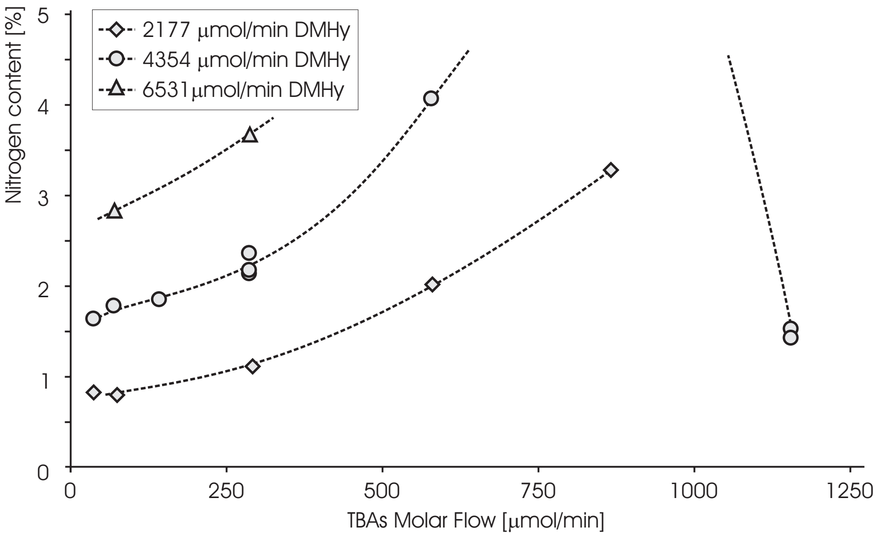

Figure 5-19 Nitrogen incorporation in GaNAs as a function of TBAs molar flow, grown at 535°C and measured by XRD

The effect of the TBAs flow on the nitrogen content of the GaNAs layers at various DMHy flows is shown in Figure 5-19. We clearly observe that nitrogen incorporation increases with the TBAs molar flow. This occurs for all investigated values of the DMHy molar flows. However, we also observe that above a certain TBAs flow the nitrogen content decreases dramatically. The composition of the samples that contained more than 4% of nitrogen could not be determined with accuracy because of severely degraded XRD-signals (due to misfit dislocations at the interface or the overall occurrence of cracks in the epilayer), even though these samples showed specular surface morphology.

We have confirmed the nitrogen incorporation by measuring the shift of the absorption edge of the GaNAs by photoreflectance[2] (see Figure 5-20). Clearly the same tendency is observed. The shift of the absorption edge of the material can only be attributed to nitrogen incorporation. The broadening of the photoreflectance transitions is between 67meV and 90meV. These are large values (typically 20meV) indicating a poor quality of the layers.

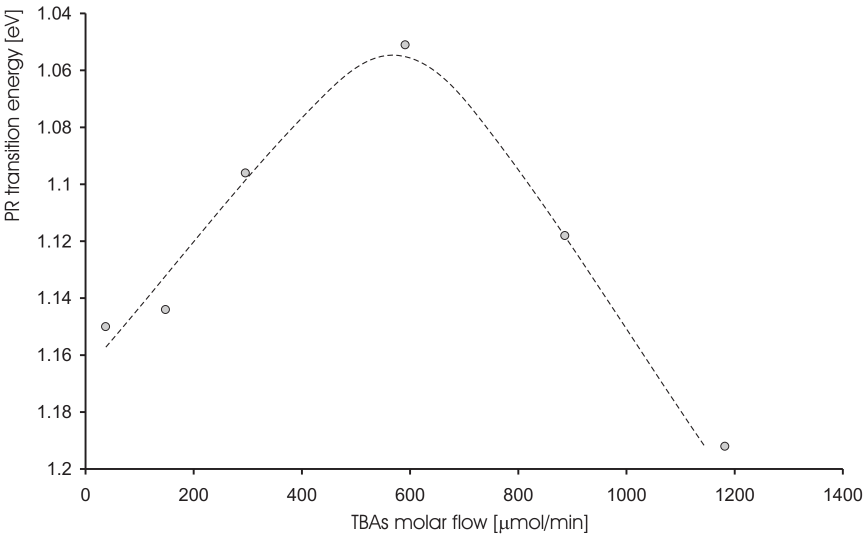

Figure 5-20 Photoreflectance transition energy as a function of TBAs molar flow, with a DMHy molar flow of 4254µmol/min

---

[2] PR is performed by G. Sęk at Wrocław University, Poland, in the framework of the IST-GIFT project.

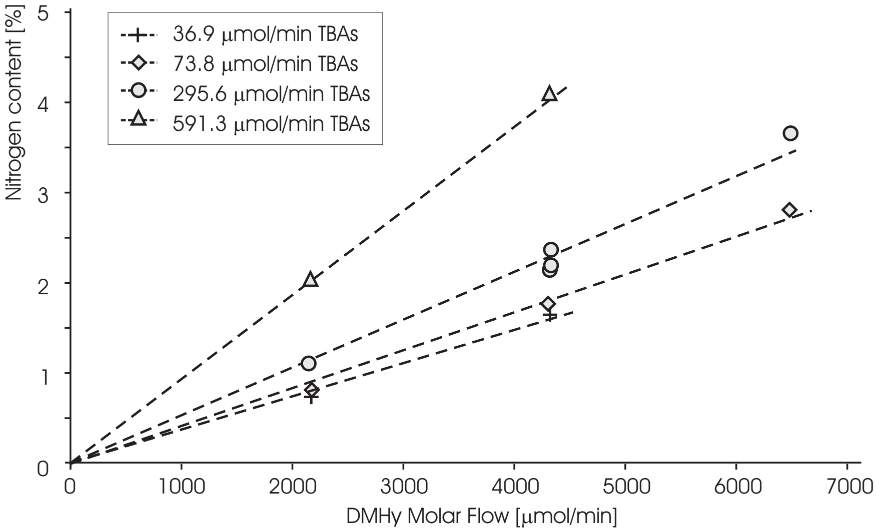

Figure 5-21 Nitrogen incorporation in GaNAs as a function of DMHy molar flow, measured from XRD

From the data obtained from XRD at TBAs flows of 36.9μmol/min and 591.3μmol/min it is clear that the nitrogen incorporation is linearly proportional with the DMHy-flow (see Figure 5-21).

This anomalous incorporation efficiency of nitrogen is certainly not due to gas phase pre-reactions so therefore must be surface related. One possible explanation is that an arsenic covered surface actually promotes the adsorption and reaction of the DMHy molecules. However, at too high surface coverage of arsenic species the DMHy molecule is readily desorbed. Our results show that GaNAs can successfully be grown under arsenic poor conditions (a TBAs/TEGa ratio of 0.7) provided that a large V_{tot}/TEGa ratio is maintained. For higher nitrogen content arsenic rich growth conditions are to be preferred. Above a certain arsenic coverage however (in our case, a TBAs/TEGa ratio of 23) the nitrogen incorporation efficiency abruptly decreases.

5.5.3. GaInNAs quantum wells

A similar investigation of the growth parameters leading to high nitrogen content GaInNAs layers was performed next. Characterization included transmission electron microscopy (TEM), high-resolution x-ray diffraction (HR-XRD) as well as photoluminescence (PL) and photoreflectance (PR).

The TEM pictures show no extended defects or quantum well variations[3]. From the 002 Dark Field images of the wells, we can extract a contrast profile with two important parameters. The first is the full width at half maximum (FWHM) that is a measure for the thickness of the well. The second is the width at the base of the profile, which is a measure for the abruptness of the interface. The profiles are not completely symmetrical with the first interface (GaAs/GaInNAs) being more abrupt than the second.

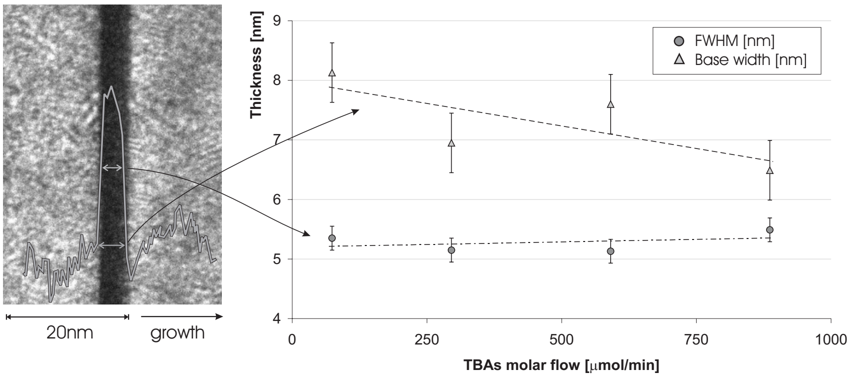

Figure 5-22 TEM pictures with extraction of quantum well interfacial parameters

Their variation as a function of the TBAs molar flow is depicted in Figure 5-22. Clearly, the quantum wells have more abrupt interfaces as the TBAs-flow increases, whereas the thickness remains approximately the same. Optical characterization was carried out using photoluminescence and photo reflectance spectroscopy[4]. The spectra as measured at room temperature are shown in Figure 5-23. The transition energies obtained by both PL and PR continuously decrease as the samples were grown with increasing TBAs flow. This is consistent with an increase in nitrogen content. Two features are shown at energy below the GaAs band edge transitions. According to their QW energy levels envelope function calculations, they are related to the fundamental heavy and light hole transitions (e_1hh_1 and e_1lh_1). The optical quality of the quantum wells is revealed clearly in Figure 5-24. The line-widths of the spectra, the FWHM of the PL peaks and the broadening of the PR features, are more or less similar for the first three samples, grown using the smaller TBAs flows. In the sample, grown with the highest TBAs flow even a third feature (e2hh2 transition) is also observed due to the higher nitrogen content and hence deeper potential well for the electrons. The relatively high (~0.9%) nitrogen content is

---

[3] TEM is performed by G. Patriarche, CNRS, France, in the framework of the IST-GIFT project.

[4] PR is performed by G. Sęk at Wrocław University, Poland, in the framework of the IST-GIFT project.

also the cause that the features of this sample are rather weak and that the linewidths increase.

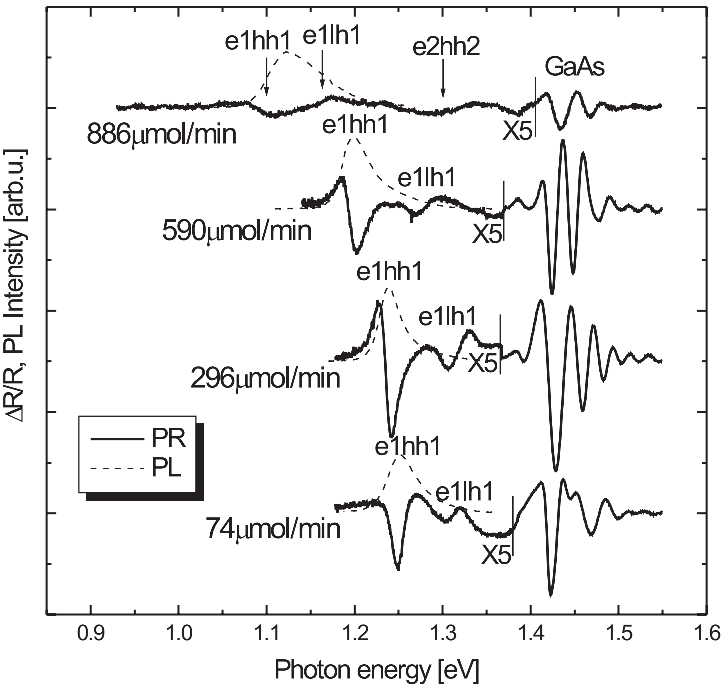

Figure 5-23 Photoreflectance and photoluminescence spectra of GaInNAs quantum wells grown with varying TBAs molar flows and a DMHy molar flow of 6531.5μmol/min.

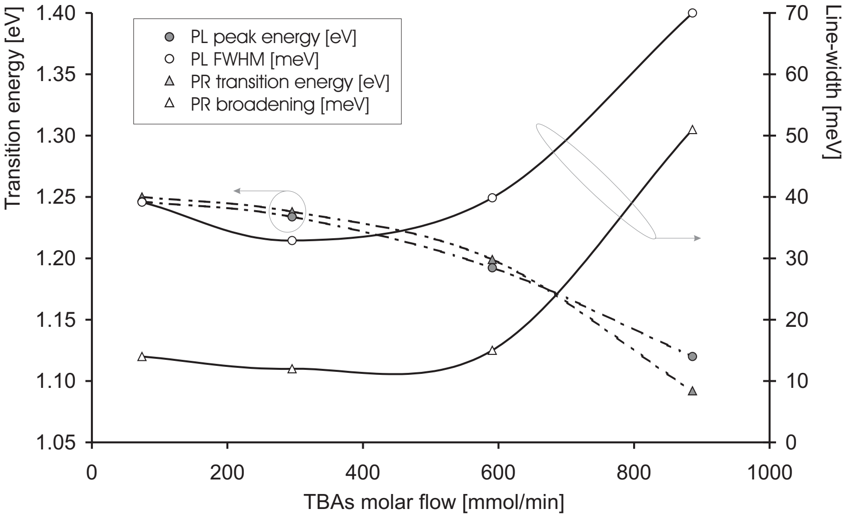

Figure 5-24 Transition energy and linewidth of the GaInNAs QW's

The same trends have been observed in low temperature optical characterisation (see Figure 5-25 and Figure 5-26). Photoluminescence and photoreflectance measurements at 10K[5] show the same decrease in transition energy with increasing TBAs molar flows. Also, the difference between the transition energies of PR and PL spectra, the Stokes' shift, is an important measure for material quality. It is caused by the fact that the absorbed light may excite the electrons into a higher energy state. Through internal conversion into vibrational energy, it can relax to the lowest excited state from before it then recombines radiatively. The larger the difference between the two levels and thus the larger the value for the Stokes' shift is indicative of worse material quality. The measured value of the Stokes' shift corresponds to what we have concluded in terms of line-widths of the room-temperature spectra, i.e. an improvement with increasing TBAs-flow until the point at which the nitrogen content becomes too high and the quality degrades again.

---

[5] LT measurements are performed by G. Sęk at Wrocław University, Poland, in the framework of the IST-GIFT project.

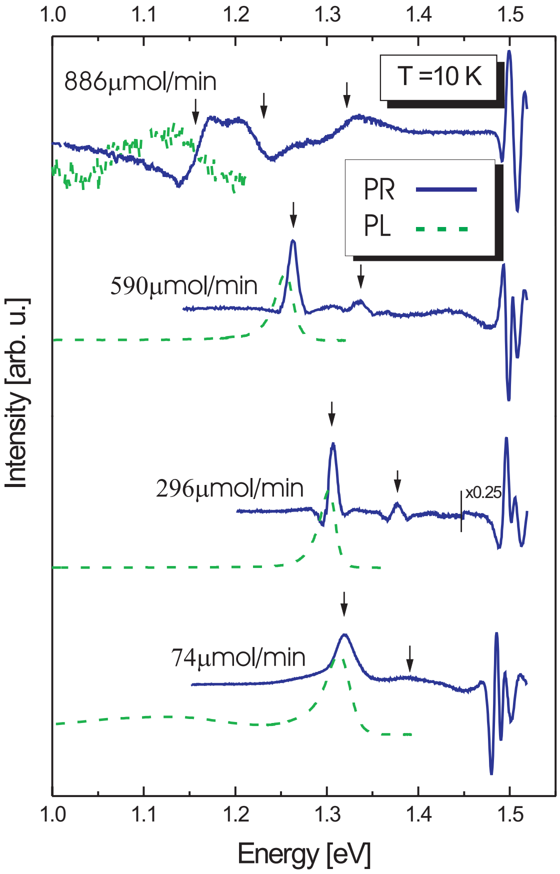

Figure 5-25 Low temperature optical characterisation of GaInNAs quantum wells

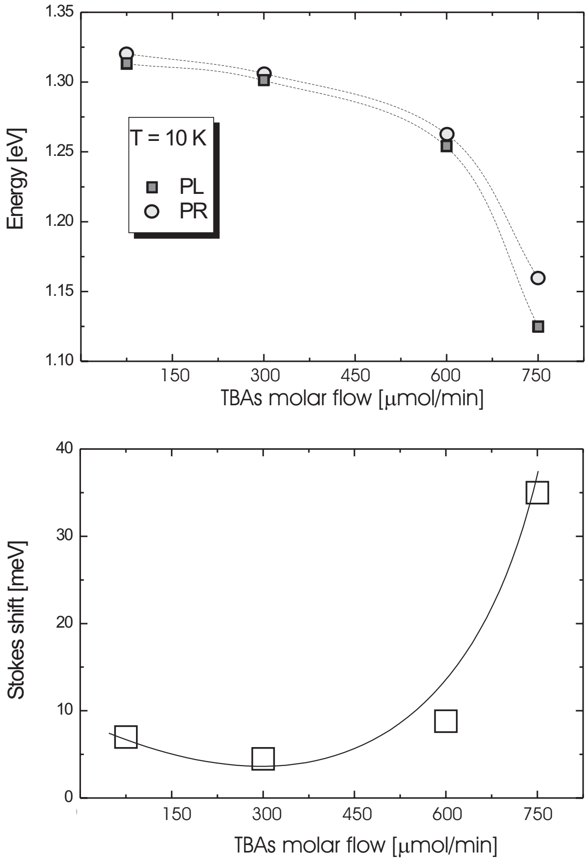

Figure 5-26 Parameters extracted from Figure 5-25

To determine the composition of the quantum wells we will combine data from the PR spectra, TEM pictures and an XRD InGaAs calibration. In our analysis we assume that the indium concentration in the wells is constant at a value of 18.5%, the value we obtain with these TEGa and TMIn flows when growing InGaAs layers. Furthermore, the run-to-run reproducibility of our reactor is rather good. A second argument to back the assumption of constant indium composition is that the DMHy-flow, which is often believed to affect the indium content of the wells, is kept constant in this particular series of samples. Then, taking the well widths from TEM and transition energies from PR into account, we can estimate the nitrogen content in the wells. The result is plotted in Figure 5-27, and shows the same tendency that is observed with the GaNAs material namely that increasing the TBAs flow causes increased nitrogen incorporation efficiency.

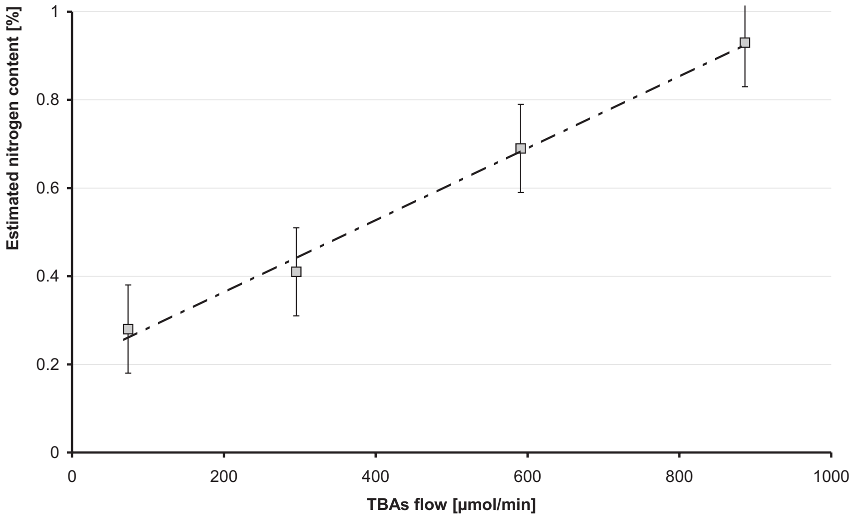

Figure 5-27 Nitrogen content estimated from TEM and PR data

We also observe the well-known effect that the nitrogen incorporation efficiency is severely decreased for the growth of indium containing quaternary layers. The simple reason is the difference in bond strength between gallium and nitrogen versus that of indium and nitrogen. To quantify the effect, we have grown a multi quantum well structure, consisting of an alternating sequence of 6nm thick $In_xGa_{1-x}As$ and $Ga_{1-x}In_xN_yAs_{1-y}$ layers separated by GaAs barriers. The structure of the superlattice is shown in Figure 5-28.

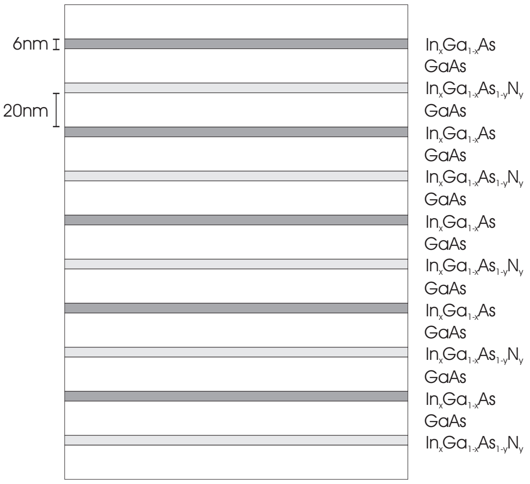

Figure 5-28 Multi quantum well superlattice to study influence of indium on the nitrogen incorporation

The structures were grown at 535ºC at 76Torr. The TEGa molar flows were varied from 17.2 to 32.8µmol/min and the TMIn molar flows from 50.4 to 102.9µmol/min to achieve indium concentrations between 10 and 35%. The DMHy was increased progressively with the indium content from 4354.4µmol/min to 7132.1µmol/min. The TBAs flows were 73.9µmol for the GaInNAs quantum wells and 1181.7µmol/min for the rest of the structure.

This structure is very well suited for analysis by HR-XRD. If the nitrogen content of the GaInNAs wells is more than zero, the periodic structure with a period of 26nm is broken and two new alternating periods are created with a period of 52nm. This will give rise to intermediary peaks in the XRD-signal, as is shown in Figure 5-29, Figure 5-30 and Figure 5-31.

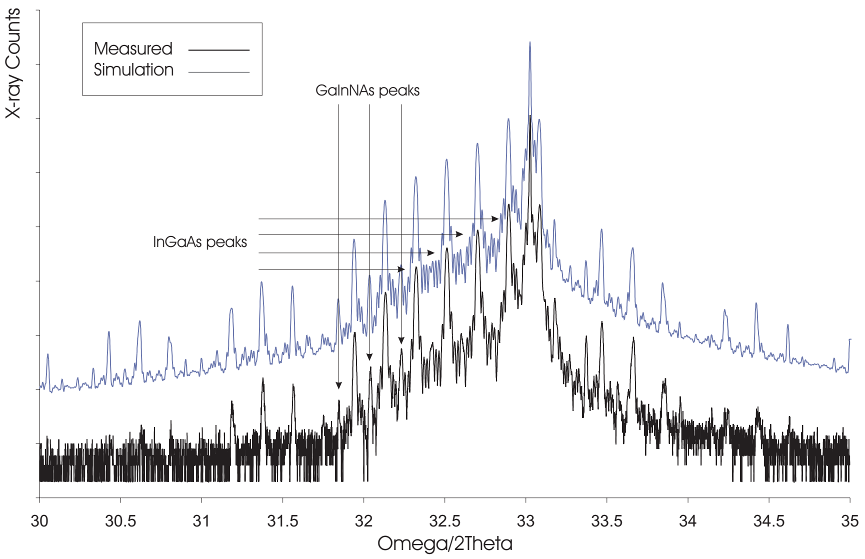

Figure 5-29 <0 0 4> XRD-reflection of the superlattice with 10% indium and 0.7% nitrogen

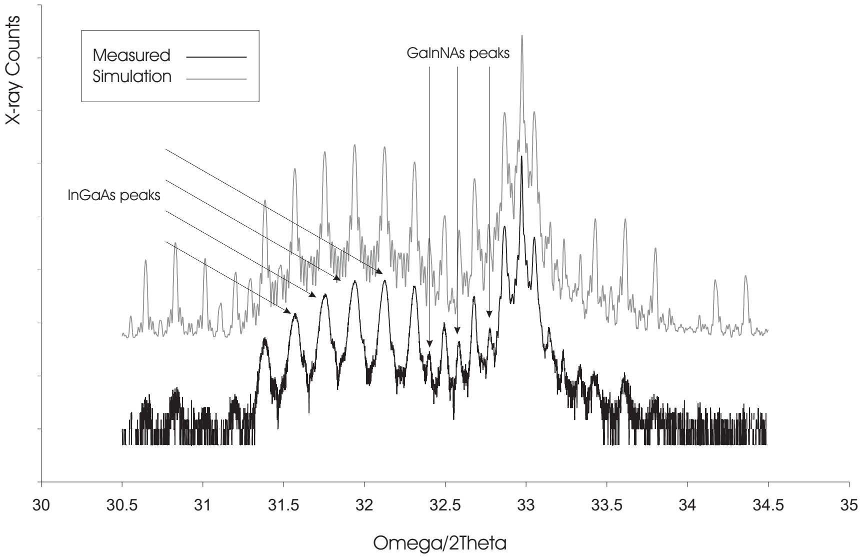

Figure 5-30 <0 0 4> XRD-reflection of the superlattice with 23% indium and 0.7% nitrogen

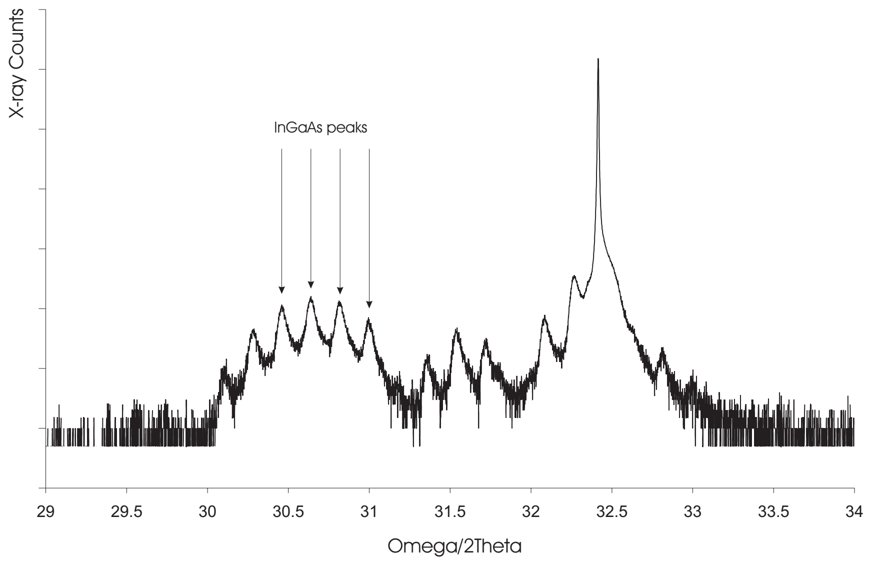

Figure 5-31 <0 0 4> XRD-reflection of the superlattice with 35% indium and an unknown nitrogen content

The XRD-signal for the high indium content is severely degraded and does not allow to determine the nitrogen content. TEM pictures of the wells show why. In the high indium content sample, the excessive strain of the multiple quantum wells leads to degraded crystallinity. Due to the high strain, the wells no longer grow two-dimensionally and undulations appear which are progressively worse the more periods are grown (see Figure 5-32). The 20nm GaAs barriers are not able to flatten the growth. Due to the high strain, no PL could be observed from any of the samples. Even the low indium content sample, which appears flat in the TEM pictures, is of an insufficient optical quality.

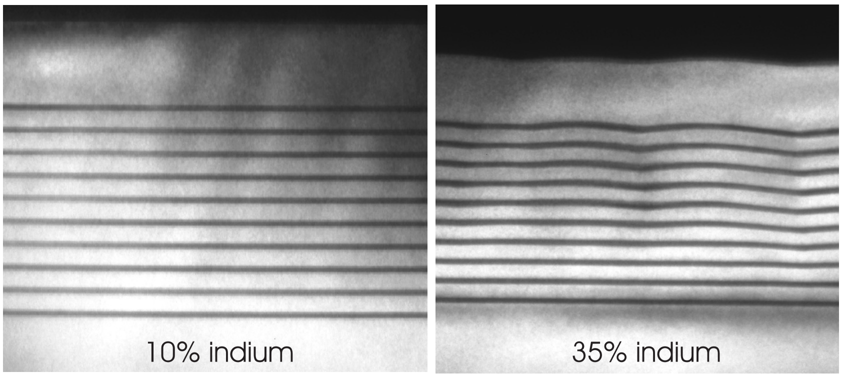

Figure 5-32 TEM pictures of the GaInNAs / InGaAs superlattice. The sample with high indium content shows heavy undulations.

From the previous we can express to what degree indium prevents the incorporation of nitrogen. This is shown in Figure 5-33. We have compared the nitrogen content of the GaInNAs layers with the nitrogen content a GaNAs layer would have when grown in similar conditions (temperature, molar flows, etc.). This is expressed as a reduction factor.

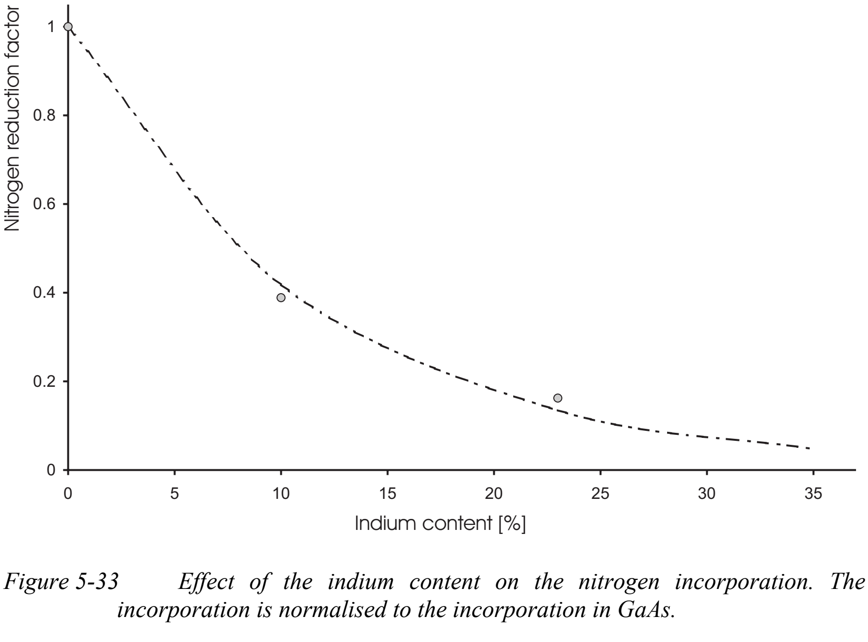

Figure 5-33 Effect of the indium content on the nitrogen incorporation. The incorporation is normalised to the incorporation in GaAs.

5.5.4. Conclusions

We have grown dilute nitrides starting from both GaAs and InGaAs material. As source material, we have used DMHy in combination with both arsine and TBAs. Whereas the observations of the arsine growth are in agreement with results from literature, this is not the case for the TBAs-grown samples, where the nitrogen incorporation behaves. It is unclear whether these literature reports have studied the nitrogen incorporation as systematically in terms of the TBAs molar flow. Unfortunately, the quenching of the luminescence efficiency is still strong even after thermal annealing, preventing us from developing a GaInNAs-based device.

References

[1] H. Saito, T. Makimoto, N. Kobayashi, J. Cryst. Growth 195, p416 (1998)

[2] S. Sato, S. Satoh, IEEE Phot. Techn. Lett. 11, p1560 (1999)

[3] F. Höhnsdorf, J. Koch, C. Agert, W. Stolz, J. Cryst. Growth 195, p391 (1998)

[4] T. Miyamoto, T. Kageyama, S. Makino, D. Schlenker, F. Koyama, K. Iga, J. Cryst. Growth 209, p339 (2000)

[5] A. Moto, S. Tanaka, N. Ikoma, T. Tanabe, S. Takagishi, M. Takahishi, T. Katsuyama, Jpn. J Appl. Phys. 38, p1015 (1999)

[6] A. Ougazzaden, Y. Le Bellego, E. Rao, M. Juhel, L. Leprince, G. Patriarche, Appl. Phys. Lett. 70, p2861 (1997)

[7] W. van der Stricht, PhD thesis, Intec, Ghent University (1998)

[8] T. Schmidtling, M. Klein, U. W. Pohl, W. Richter, MRS Fall Meeting, Boston USA (1999)

[9] G. Zhang, J. Cryst. Growth 128, p536 (1993)

[10] S. Kurtz, R. Reedy, G. Barber, J. Geisz, D. Friedman, W. McMahon, J. Olson, J. Cryst. Growth 234, p318 (2002)

[11] M. D’Hondt, PhD thesis, Intec, Ghent University (1998)

[12] R. Bhat, C. Caneau, L. Salamanca-Riba, W. Bi, C. Tu, J. Cryst. Growth 195, p427 (1998)

[13] W. Chow, E. Jones, N. Modine, A. Allerman, S. Kurtz, Appl. Phys. Lett. 75, p2891 (1999)

[14] D. Friedman, J. Geisz, S. Kurtz, J. Olson, and R. Reedy, J. Cryst. Growth 195, 438 (1998).

CHAPTER 6

CONCLUSIONS AND OUTLOOK

6.1. Conclusion

In this work we have studied the growth of dilute nitrides. Perhaps more importantly, we have first developed a growth process that is suitable for this purpose. This process includes the growth at low temperatures and the introduction of a number of alternative precursors. We have replaced two of the three standard sources for InGaAs growth (arsine and TMGa by TBAs and TEGa) and introduced a third (DMHy). For nitrogen-free material we have shown how low temperature growth allows us to overcome the theoretical strain barrier of InGaAs quantum wells ([1] [6]). This work has resulted in laser devices emitting at 1190nm.

In the course of this work we have achieved some excellent results, especially in the field of the TBAs development. Of course, we should mention the GaAs solar cells, which exhibit world record conversion efficiency for this particular type of cell of 24.5% [3]. And also the 980nm InGaAs laser diodes that were grown with the new process have very good characteristics in terms of threshold current densities and internal quantum efficiencies [8].

Less spectacular but nonetheless interesting are the results obtained from the dilute nitrides themselves. When growing with arsine, the results are in agreement with what has been reported. But when growing with TBAs, our systematic study found rather peculiar incorporation behaviour of the nitrogen as a function of the TBAs flow. Unfortunately, the optical quality of the material has remained poor, and time did not permit adding a finishing touch in the form of a functioning device.

6.2. Outlook

A work like this is of course never finished. For all of the topics we have studied a number of extensions and new road maps are possible.

An interesting direction to take in the area of low temperature growth is the deliberate use of intrinsic carbon doping using TMGa [5]. By lowering the temperature and III/V ratio, one can achieve p-type doping in the order of 10^{20}. Carbon has the extra advantage that is not very diffusive, so that very abrupt and very high doping profiles can be created. These can be exploited to form tunnel-junctions. These are commonly used in multiple junction solar cells, because they allow combining a number of single photodiodes in series. Obviously, the study of this type of solar cells is a continuation of the work that has been started in the framework of the TBAs process development.

Before the hydrides were removed from the laboratory, there was a large know-how on various material systems. Even though most of this has been transferred for the GaAs system, the materials that have phosphorous in their crystal lattice would need an alternative precursor for phosphine. The material of choice is tertiary-butyl-phosphine (TBP), which has similar properties as TBAs. Some first tests have already been performed for both the InGaAsP/InP and the InAlGaP/GaAs systems, but work is needed to bring the growth up to the old standard.

The research on long wavelength opto-electronic devices has seen a lot of progress in the last few years. Indeed, by now GaInNAs active regions have successfully been implemented in 1300nm VCSEL's [6] by a variety of research groups; initially only with MBE-techniques, but recently also with MOCVD. The fact that MOCVD has now caught up with MBE in terms of material quality and fabricated devices is an indication of the progress that has been made, not only in terms of process development but also in the quality of DMHy source material.

No doubt, as the dilute nitrides are better understood and material quality is further optimised, e.g. in the field of minority carrier diffusion length and the elimination of carrier-traps, it will be possible to find applications in various other terrains, for example as a GaInNAs layer [8] in multiple junction solar cell.

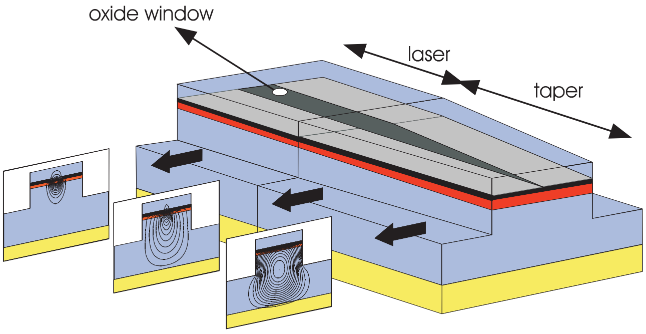

Figure 6-1 Principle of a ridge laser with an oxide-confined tapered mode-size converter (after [7])

Another interesting application is that of the edge-emitting laser diode with integrated mode-size converter (see Figure 6-1). In such device the dimensions of the laser waveguide are changed gradually so that the optical mode expands to match the mode of an optical fibre. A similar component has been fabricated with an InGaAs active region and is a proof of the inherent advantages of the GaAs material in combination with the wet lateral oxidation technique for AlGaAs [7].

References

[1] F. Bugge, M. Zorn, U. Zeimer, T. Sharma, H. Kissel, R. Hülsewede, G. Erbert, M. Weyers, J. Cryst. Growth 248, p354 (2003)

[2] D. Schlenker, T. Miyamoto, Z. Chen, F. Koyama, K. Iga, J. Cryst. Growth 209, p27 (2000)

[3] M.A.Green, Progress in Photovoltaics: Research and Applications 8 (2000), 377

[4] F. Vermaerke, "Ontwerp en realisatie van hoogperformante InGaAs/AlGaAs halfgeleider laserdiodes", Ph.D. Thesis, Intec-Ghent University (1996)

[5] M. Longo, R. Magnanini, A. Parisini, L. Tarricone, A. Carbognani, C. Bocchi, E. Gombia, J. Cryst. Growth 248, p119 (2003)

[6] G. Steinle, H. Riechert, A. Egorov, Electr. Lett. 37, p93 (2001)

[7] K. De Mesel, "Spot-size converters for photonic integrated circuits", Ph.D. Thesis, INTEC-Ghent University (2003)

[8] J. Geisz, D. Friedman, J. Olson, S. Kurtz, B. Keyes, J. Cryst. Growth 195, p401 (1998)

APPENDIX

GROWTH CONDITIONS

1. Reactor design

The reactor that was used for this work was produced by Thomas Swan Ltd. The flows enter the reactor through a showerhead-like distributor to enhance uniformity. The wafers are put on a susceptor that is brought in close proximity of the showerhead. The gas flow is vertical, that is it enters the reactor from above and exits below the susceptor. To further optimise uniformity, the susceptor rotates at high velocity. A spiralling graphite resistor heats the reactor. It is split up in three zones which each receive a fixed ratio of the total heating power so that the temperature profile can be flat across the susceptor. The heater power is controlled by a thermo-couple that nearly touches the susceptor. We can monitor the temperature profile using an optical pyrometer, calibrated to a blackbody reference, looking to through three optical view-ports, which are mounted on the showerhead.

Before the gases enter the reactor, source for group III and group V elements are kept apart and are switched in two separate manifolds. Only after the gases exit the showerhead, they are mixed so that the chance of any pre-reaction is kept small. The new source DMHy, as well as TBAs and TBP, are connected to the group V manifolds.

The waste gas at the exit of the reactor is led into a scrubber system. It consists of two columns filled with absorbing material. At first this was active charcoal, later this was replaced by a specifically designed resin. The scrubber’s main purpose is to remove all hydride-like molecules from the gas flow. These molecules are adsorbed onto the scrubber’s active material. After growth these molecules are oxidized in a more stable form. Unused group III source materials are cracked in special pyrolysis furnaces before they enter the scrubber.

2. Fixed growth parameters

A number of parameters were not changed during the work described in this thesis. The reactor pressure is kept at 76Torr during growth unless specifically mentioned otherwise. A carrier flow of 8slm of hydrogen is sent through each manifold. The susceptor rotates at 300rpm. When we grew quantum wells, the effect of switching gas flows was countered by using hydrogen make-up flows. These were programmed manually and not using the software's automatic function. To eliminate any differential pressure between manifolds and the vent line, two dedicated controllers always set the vent flow. The showerhead is water-cooled so that its temperature is stable between 35ºC and 40ºC.

3. Specific growth conditions

The standard growth conditions for different materials are summarized below. For growth conditions of the GaNAs and GaInNAs we refer to the fifth chapter.

Material		GaAs	$Al_{35}Ga_{65}As$	InGaAs (980nm)	InGaAs (1200nm)
TMGa molar flow	[µmol/min]	105	59	79	-
TEGa molar flow	[µmol/min]	-	-	-	40
TMAl molar flow	[µmol/min]	-	25	-	-
TMIn molar flow	[µmol/min]	-	-	27	43
DMHy molar flow	[µmol/min]	-	-	-	-
TBAs molar flow	[µmol/min]	990	3877	3877	-
Arsine molar flow	[µmol/min]	-	-	-	6187
V / III ratio		10	40	36	75
Growth velocity	[µm/hr]	3.97	2.99	3.65	1.56
Growth temperature	[ºC]	660	720	650	535

Table b Overview of the standard growth conditions for typical materials